

CONTENTS

	Page
INTRODUCTION	1 1/A9
I. EXPERIMENTAL METHOD.....	3 1/A11
A. Description of Detection System.....	3 1/A11
1. Scintillator detector	3 1/A11
2. Pulse shape discrimination.....	3 1/A11
3. Electronics.....	4 1/A12
4. Data storage	4 1/A12
5. Gondola	4 1/A12
B. Tests of the Detection System.....	5 1/A13
1. Temperature and pressure	5 1/A13
2. Response to sources.....	5 1/A13
3. Gain stability	6 1/A14
4. Channel 1 effect.....	6 1/A14
C. Calibration of Detectors	6 1/A14
1. Basis of calibration, ORNL detector and response functions	6 1/A14
2. Calibration at ORNL.....	7 1/B1
2a. Behaviour of ORNL detector-monitor	8 1/B2
2b. Unfolding the incident neutron spectrum from the measured pulse height distributions	8 1/B2
2c. Normalizing incident spectrum to Pu-Be above 5 MeV	9 1/B3
3. Response to neutrons >10 MeV	10 1/B4
4. Omnidirectional response	10 1/B4
5. Listing of response functions	11 1/B5
6. Cross-calibration of detectors.....	11 1/B5
7. Rejection of gammas in flight	11 1/B5
II. FLIGHT SUMMARIES	16 1/B10
A. Balloon Flights.....	16 1/B10
B. Aircraft Flights.....	19 1/C1
1. Introduction	19 1/C1
2. Solar minimum latitude survey	20 1/C2
3. Listing of aircraft flights	20 1/C2
3a. Performance of flight systems.....	20 1/C2
III. EVALUATION OF DATA	20 1/C2
A. Introduction.....	20 1/C2
B. Conversion of Counting Rates to Flux.....	34 1/D12
1. Method.....	34 1/D12
2. Contribution of the > 10 MeV neutrons to the counting rate	34 1/D12
C. Calculation of Attenuation Length.....	36 1/E1

IV. RESULTS OF OBSERVATIONS.....	36	1/E1
A. Results of Balloon Flights.....	36	1/E1
1. Flight profiles.....	36	1/E1
2. Fast neutron spectrum.....	37	1/E2
3. Attenuation length.....	37	1/E2
4. Solar modulation.....	38	1/E3
5. Time variations at floating altitude.....	38	1/E3
6. In-flight calibration of System I vs System II.....	39	1/E4
7. Flights with tissue-equivalent dome.....	39	1/E4
B. Results of Aircraft Flights	40	1/E5
1. Summary of results, free air flux.....	40	1/E5
1a. Normalization of flight systems.....	40	1/E5
2. Aircraft latitude surveys.....	41	1/E6
3. Latitude variation, near the latitude knee.....	42	1/E7
4. Time variations at the high latitude transition maximum	42	1/E8
5. Results of step flight, altitude variations	44	1/E9
V. INTERNUCLEAR CASCADE CALCULATION.....	45	1/E10
A. Introduction	45	1/E10
1. Production and transport of neutrons.....	45	1/E10
2. Previous calculations.....	46	1/E11
B. Description of the Calculation.....	47	1/E12
1. Scope of the calculation.....	47	1/E12
2. Internuclear cascade	47	1/E12
2a. LOMONTE and HIMONTE	47	1/E12
2b. References for cross sections for production of nucleons.....	48	1/E13
2c. Pion production and transport	49	1/E14
3. Neutron transport below 19 MeV, 05R	50	1/F1
4. Atmospheric flux calculation; NFLUX	51	1/F2
C. Input Data for Cascade Calculation, Galactic Cosmic Rays	51	1/F2
VI. RESULTS OF THE CALCULATION.....	52	1/F3
A. Unadjusted Calculation.....	52	1/F3
1. Monoenergetic primary protons.....	52	1/F3
2. Monoenergetic alpha particles	54	1/F6
3. Galactic cosmic rays, comparison with experiment	54	1/F6
3a. Solar minimum	55	1/F7
3b. Latitude surveys	55	1/F7
3c. Fast neutron spectrum.....	55	1/F7
B. Normalized Calculation	57	1/F9
1. Procedure	57	1/F9
2. Results	57	1/F9
2a. Fast neutron flux	57	1/F9
2b. Neutron source and products	58	1/F10
2c. Radiocarbon	58	1/F10
2d. Neutron leakage rates and fluxes.....	62	1/G1

3. Discussion.....	62	1/G1
3a. Comparison of the normalized calculation with the results of neutron experiments.....	62	1/G1
3b. Comparison with other calculations.....	70	1/G12
VII. SUMMARY OF OBSERVATIONS AND CALCULATION OF NEUTRONS FROM GALACTIC COSMIC RAYS.....	73	2/A6
VIII. NEUTRONS FROM SOLAR PROTONS	74	2/A7
A. Introduction.....	74	2/A7
B. Observations.....	75	2/A8
C. Solar Proton Spectra and Neutron Yields	78	2/A13
D. Monte Carlo Calculation.....	80	2/B1
E. Discussion.....	81	2/B2
F. Application to Other Experiments.....	84	2/B6
G. Other Flare Calculations	87	2/B9
H. Summary of Observations and Calculations	88	2/B10
I. The Geophysical Effects of Neutrons from Solar Protons..	89	2/B11
IX. COSMIC RAY MODULATION DURING 1968-1971.....	91	2/B13
A. Introduction.....	91	2/B13
B. Comparison of the Response of Neutron Monitors with Response of NYU Detector to the Primary Spectrum.	91	2/B13
C. Calculation of the Spectrum of Variation of Cosmic Rays..	92	2/B14
D. Results, Transient Cosmic Ray Decreases.....	94	2/C3
E. Results, Long Term Variation in Cosmic Ray Intensity....	99	2/C9
F. Discussion	101	2/C11
1. The spectrum of variation of Cosmic Rays.....	101	2/C11
2. The relative modulation of protons and electrons; charge splitting above 2 GV.....	102	2/C12
3. Model Calculations.....	104	2/C14
G. Conclusions and Summary.....	107	2/D3
X. APPENDIX A. ACCELERATION PROCESSES ON THE SUN ...	110	2/D6
XI. APPENDIX B. PRIMARY NEUTRONS.....	116	2/D12
XII. APPENDIX C. THE EARTH OR OTHER OBJECT AS A NEUTRON SOURCE.....	120	2/E2
REFERENCES.....	122	2/E4
FIGURES.....	133	2/F1

MAY 3 1 1979

NAS 1.26-3626

NASA Contractor Report 3126

COMPLETED

W. J. S.

Atmospheric Neutrons

Serge A. Korff, Rosalind B. Mendell,
Milton Merker, Edward S. Light,
Howard J. Verschell, and William S. Sandie

CONTRACT NAS1-10282
MAY 1979

NASA

188

NASA Contractor Report 3126

Atmospheric Neutrons

Serge A. Korff, Rosalind B. Mendell,
Milton Merker, Edward S. Light,
Howard J. Verschell, and William S. Sandie
New York University
New York, New York

Prepared for
Langley Research Center
under Contract NAS1-10282



National Aeronautics
and Space Administration

**Scientific and Technical
Information Office**

1979

CONTENTS

	Page
INTRODUCTION	1
I. EXPERIMENTAL METHOD.....	3
A. Description of Detection System	3
1. Scintillator detector	3
2. Pulse shape discrimination	3
3. Electronics.....	4
4. Data storage.....	4
5. Gondola	4
B. Tests of the Detection System.....	5
1. Temperature and pressure	5
2. Response to sources.....	5
3. Gain stability	6
4. Channel 1 effect.....	6
C. Calibration of Detectors.....	6
1. Basis of calibration, ORNL detector and response functions	6
2. Calibration at ORNL.....	7
2a. Behaviour of ORNL detector-monitor.....	8
2b. Unfolding the incident neutron spectrum from the measured pulse height distributions	8
2c. Normalizing incident spectrum to Pu-Be above 5 MeV	9
3. Response to neutrons >10 MeV	10
4. Omnidirectional response	10
5. Listing of response functions	11
6. Cross-calibration of detectors.....	11
7. Rejection of gammas in flight.....	11
II. FLIGHT SUMMARIES.....	16
A. Balloon Flights.....	16
B. Aircraft Flights.....	19
1. Introduction	19
2. Solar minimum latitude survey	20
3. Listing of aircraft flights	20
3a. Performance of flight systems.....	20
III. EVALUATION OF DATA	20
A. Introduction.....	20
B. Conversion of Counting Rates to Flux.....	34
1. Method.....	34
2. Contribution of the > 10 MeV neutrons to the counting rate	34
C. Calculation of Attenuation Length.....	36

IV.	RESULTS OF OBSERVATIONS	36
A.	Results of Balloon Flights	36
1.	Flight profiles	36
2.	Fast neutron spectrum	37
3.	Attenuation length	37
4.	Solar modulation	38
5.	Time variations at floating altitude	38
6.	In-flight calibration of System I vs System II	39
7.	Flights with tissue-equivalent dome	39
B.	Results of Aircraft Flights	40
1.	Summary of results, free air flux	40
1a.	Normalization of flight systems	40
2.	Aircraft latitude surveys	41
3.	Latitude variations near the latitude knee	42
4.	Time variations at the high latitude transition maximum	43
5.	Results of step flight, altitude variations	44
V.	INTERNUCLEAR CASCADE CALCULATION	45
A.	Introduction	45
1.	Production and transport of neutrons	45
2.	Previous calculations	46
B.	Description of the Calculation	47
1.	Scope of the calculation	47
2.	Internuclear cascade	47
2a.	LOMONTE and HIMONTE	47
2b.	References for cross sections for production of nucleons	48
2c.	Pion production and transport	49
3.	Neutron transport below 19 MeV, 05R	50
4.	Atmospheric flux calculation: NFLUX	51
C.	Input Data for Cascade Calculation. Galactic Cosmic Rays	51
VI.	RESULTS OF THE CALCULATION	52
A.	Unadjusted Calculation	52
1.	Monoenergetic primary protons	52
2.	Monoenergetic alpha particles	54
3.	Galactic cosmic rays, comparison with experiment	54
3a.	Solar minimum	55
3b.	Latitude surveys	55
3c.	Fast neutron spectrum	55
B.	Normalized Calculation	57
1.	Procedure	57
2.	Results	57
2a.	Fast neutron flux	57
2b.	Neutron source and products	58
2c.	Radiocarbon	58
2d.	Neutron leakage rates and fluxes	62

3. Discussion.....	62
3a. Comparison of the normalized calculation with the results of neutron experiments.....	62
3b. Comparison with other calculations.....	70
VII. SUMMARY OF OBSERVATIONS AND CALCULATION OF NEUTRONS FROM GALACTIC COSMIC RAYS.....	73
VIII. NEUTRONS FROM SOLAR PROTONS	74
A. Introduction.....	74
B. Observations.....	75
C. Solar Proton Spectra and Neutron Yields	78
D. Monte Carlo Calculation.....	80
E. Discussion.....	81
F. Application to Other Experiments.....	84
G. Other Flare Calculations	87
H. Summary of Observations and Calculations	88
I. The Geophysical Effects of Neutrons from Solar Protons..	89
IX. COSMIC RAY MODULATION DURING 1968-1971.....	91
A. Introduction.....	91
B. Comparison of the Response of Neutron Monitors with Response of NYU Detector to the Primary Spectrum..	91
C. Calculation of the Spectrum of Variation of Cosmic Rays..	92
D. Results, Transient Cosmic Ray Decreases.....	94
E. Results, Long Term Variation in Cosmic Ray Intensity....	99
F. Discussion	101
1. The spectrum of variation of Cosmic Rays.....	101
2. The relative modulation of protons and electrons; charge splitting above 2 GV.....	102
3. Model Calculations.....	104
G. Conclusions and Summary.....	107
X. APPENDIX A. ACCELERATION PROCESSES ON THE SUN ..	110
XI. APPENDIX B. PRIMARY NEUTRONS.....	116
XII. APPENDIX C. THE EARTH OR OTHER OBJECT AS A NEUTRON SOURCE.....	120
REFERENCES.....	122
FIGURES.....	133

INTRODUCTION

The earth's atmosphere is a great shield, absorbing the impact of cosmic debris and the radiations harmful to living things. The atmosphere receives in its upper regions a steady rain of high energy charged particles from beyond the solar system, as well as occasional penetrating bursts from the sun itself. This high energy radiation is known as the Cosmic Radiation or Cosmic Rays. It consists mostly of protons, with some alpha particles and a small number of heavy nuclei. These particles generate all kinds of secondaries upon colliding with nuclei in the atmosphere, depositing most of their energy in the first hundred grams of the top of the atmosphere. Fortunately for man, this is far above his usual environment. The situation is less propitious for passengers of high altitude aircraft, for they cruise right at the radiation maximum. For this reason, there has been much concern over the possible radiation hazards in such travel; and

several evaluations of the biological dose^{1,2} have been made. A necessary input to such an evaluation is the energetic particle distribution in the upper atmosphere, especially that of secondary cosmic ray neutrons, which make a major contribution to the radiation dose. It is part of the intent of this report to present the results of long term observations of these atmospheric neutrons.

The need for more complete information on neutron fluxes has not been reserved to the domain of health physics. The processes of production and transport of neutrons in the atmosphere have interested investigators ever

since the pioneering paper of Bethe, Korff, and Placzek in 1940.³ As director of the Cosmic Ray Project of New York University, Korff has continued his experimental observations, first developing slow neutron detectors, which were BF_3 proportional counters, enriched and depleted⁴ in B^{10} . These early experiments established the altitude and latitude

dependence of the slow neutron densities,⁵ detected time variations,⁶ and found negative results on solar neutrons.⁷ Since 1962, we have continued these investigations, employing fast neutron counters, sensitive in the 1-10 MeV energy range.

8-14
Peripheral applications of neutron measurements have continued to encourage the efforts of other investigators as well as of Korff's group. Because neutrons interact with nitrogen to yield most of the radiocarbon formed in the atmosphere, the relation of the neutron flux to the concen-

tration of this archeological dating tool has been studied.¹⁵ Neutrons have also been invoked to explain the rather stable high energy proton population of the inner radiation belts, a possible source of the protons arising from the decay of neutrons that have escaped from the top of the

atmosphere. Preliminary evidence for such a source has been reported.¹⁶ The possibility that some of the atmospheric neutrons are actually of solar origin has stimulated investigators to search for such neutrons above the cosmic ray neutron background. If found, these solar neutrons might contribute to our knowledge of processes in the solar atmosphere. So far,

17
the results have been largely negative.

In this report, we shall outline our contributions to fast neutron measurements in the atmosphere. We shall also present the results of a calculation to determine the production, distribution and final disappearance of atmospheric neutrons over the entire spectrum. In this discussion, we shall attempt to answer questions that relate to processes such as neutron

14
escape from the atmosphere and C^{14} production. In addition, since variations of secondary neutrons can be related to variations in the primary radiation, we shall have something to say about the modulation of both radiation components.

The modulation of the primary radiation is a consequence of solar activity. The sun continually exudes a plasma of charged particles, including protons, alpha particles, electrons and other particles. This plasma and the solar magnetic field, which is frozen into the plasma, modulate the flux of the charged particles coming from outside the solar system. Further dynamic effects occur when the particles interact with the earth's magnetic field. Since the sun's emission of plasma depends

largely on solar activity, we may expect to find a substantial dependence of the neutron intensity on the state of the sunspot cycle. Further, the sun occasionally emits bursts of high energy particles which reach the earth and also generate neutrons. These emissions are usually signalled by the appearance of solar flares, a complex interrelationship which we shall also discuss below.

Identification of commercial products in this report is used to adequately describe the experimental arrangement. The identification of these commercial products does not constitute official endorsement expressed or implied, of such products or manufacturers by the National Aeronautics and Space Administration.

I. EXPERIMENT METHOD

A. Description of Detection System

1. Scintillator detector.-The neutron detector flown in these experiments measures 1-10 MeV recoil-proton and heavily ionizing events produced by neutrons in an organic scintillator. Rejection of other radiation, both charged and neutral, is accomplished by employing the "phoswich"¹⁸ configuration shown in fig. 1. The detector itself is a 5 cm x 5 cm cylindrical volume of organic liquid phosphor, NE218 (also NE222). It is surrounded by a 6 mm minimum thickness of plastic scintillator NE102*, which acts as an anticoincidence shield for charged particles. The composite detector is viewed by a single 5 cm photomultiplier, the Amperex 56 AVP or, more recently, the 56 DVP and the RCA 8575.

2. Pulse shape discrimination.-Events produced in the composite scintillator by radiation other than neutrons are rejected by the detector electronics on the basis of pulse shape. In the inner phosphor, NE218, the time characteristic of a scintillation depends on the specific ionization of the particle producing the excitation. Since recoil protons in the 1-10 MeV range have a large specific ionization and electrons with the same light output are essentially minimum ionizing, the light pulses from protons and electrons differ in shape and can be separated by a circuit for pulse-shape

discrimination.¹⁹ In the same manner, electrons produced in NE218 by gamma rays and minimum ionizing charged particles passing through the scintillator assembly can also be separated from recoil-protons.

The pulse shape resulting from the passage of a charged particle through the NE102 shell is similar to that produced by minimum ionizing particles in the inner scintillator. Such pulses can be rejected by

* Nuclear Enterprises, Ltd.

increasing the rejection threshold of the circuitry that separates electrons from recoil-protons. Particles which are not minimum ionizing and which penetrate both scintillators are rejected because the excitation they deposit is greater than the upper cutoff of the spectrometer.

3. Electronics. -The circuit used for pulse shape discrimination is shown in fig. 2. It is a modification of the circuit of Daehnick and Sherr¹⁹ and was designed for improved temperature characteristic.

In balloon and airplane applications of the neutron spectrometer, the pulses produced by scintillations of recoil-protons between 1 and 10 MeV are amplified, gated as neutron events and sorted in a seven-channel pulse height analyzer. Each channel corresponds to a difference of about 1 MeV in proton-recoil energy. A block diagram of the flight system is shown in fig. 3.

4. Data storage. -The seven channels of pulse height information are binary coded and recorded on three tracks of a four track magnetic tape recorder. The fourth track contains a time signal as well as a record of all events produced in the scintillator with a light output greater than that of 1 MeV proton. Ambient pressure, the temperature of the gondola, and time are registered by a photobarograph. The photobarograph acts, in addition, as a backup system for the tape recorder, registering the counts in neutron channels 1-3 and 4-7 and in total events.

5. Gondola. -Fig. 4 is a diagram of the instrumentation rack that was used in balloon flights. The configuration shown was designed so that the mass distributed in the gondola would subtend a minimal solid angle at the scintillator. This was to prevent background neutrons, produced by high energy radiation in the local material, from reaching the detector. An exterior container housed the photobarograph and the batteries for the heaters in the gondola. Such heaters were required only during night flights, since the insulation, 10cm of polyurethane foam, and the reflectivity of the yellow fiberglass gondola were sufficient to maintain the inside temperature to within a few degrees of the pre-flight value. The container for the aircraft flights was, of necessity, more compact. It was supplied

with 200 watt heaters and maintained with thermostats between 15° and 20° C.

B. Tests of the Detection System

1. Temperature and pressure. -Each flight system was temperature-

compensated and tested between -10°C and 40°C , the lower and upper limits being imposed by the scintillator and the photomultiplier respectively. The detectors and tape recorders were also routinely checked for high altitude performance since the flight system was not pressurized. In spite of these tests, the tape recorder motors occasionally failed in balloon flights (but not aircraft flights). They were later replaced by new units which performed without failure.

2. Response to sources. -In the laboratory, the detectors were routinely tested for gain, gain stability and discrimination against gamma radiation,

the tests employing Cs^{137} , Co^{60} , and Y^{88} gamma sources and an NDA 1024 channel pulse height analyzer.* Response to neutrons was measured with a small Am-Be neutron source and checked from time to time with a 1 curie calibrated Pu-Be neutron source. In the field, pre- and post-

flight calibrations were made with a Co^{60} gamma source and a RaD-Be or Am-Be neutron source.

The rejection of gamma radiation pulses by the flight scintillator and electronics was examined with gamma sources from threshold to 2.75 MeV, corresponding to the light output of a 7 MeV neutron. At count rates below 1000/sec, the neutron identifying circuit rejected all but one or two in 10^4 counts registered in the total events output. Tests were also made with 5.3 MeV alphas incident on the outer scintillator and with sea level muons transversing the scintillator. These were also rejected.

As a further test, various combinations of outer plastic and inner liquid, with and without the fluorescing solutes, were examined with gamma and neutron sources. As a check on the rejection of protons in the anticoincidence shield, the outer scintillator was combined with a dummy

inner scintillator. It accepted less than one in 10^4 proton recoils from a Pu-Be source as a neutron. The inner scintillator yielded the same recoil spectrum with either a dummy or a scintillator as the outside shield, indicating that proton recoils from neutrons interacting in both scintillators were not counted.

* Nuclear Data Corporation

3. Gain stability. -The gain stability of the detection system has varied from phototube to phototube. The CBS tubes, CL 1004, flown in 1965, were gain stable to about 2-3% per day. The Amperex 56 AVP and 56 DVP and the RCA 8575 drifted in gain by less than 1% per day, provided they were continuously powered.

4. Channel 1 effect. -With some of the Amperex tubes, the 1-2 MeV proton recoil channel was affected by exposure to moderate amounts of radiation. The effect was always of the same nature, a decrease in counts (but not gain) in channel 1 over several hours, stabilizing to a value of as much as -10% in the most affected detectors. This drift was sometimes but not always observed with aging. Since the counts of the other channels remained unchanged by radiation exposure the channel 1 drift was related to the threshold of pulse-shape discrimination. The cause is believed to be radiation fatigue at the anode, which is involved in pulse shape discrimination. This effect was not observed with the RCA 8575 tube. The drift in channel 1 was partly compensated for by pre-and post-flight calibration, but still introduced a 10% uncertainty in the 1-2 MeV neutron flux for the earlier flights. For this reason, only the 2-10 MeV neutrons will be used in discussing time variations.

C. Calibration of Detectors

1. Basis of calibration, ORNL detector and response functions. -In the calibration of the NYU neutron detectors, we were indebted to Verbinski and Burrus of ORNL, for making available the results of an analysis of

the response of a cylindrical cell of liquid phosphor, NE213*. These results have since been extended and published.^{20,21} They include a Monte Carlo calculation of the interaction of monoenergetic neutrons with an NE213 detector, which happened to be quite similar in shape, dimensions, and content to the inner scintillator of the NYU phoswich. The Monte Carlo calculation checked and was checked by measurements, using time-of-flight and associated particle techniques, so that in the end, the authors obtained a consistent series of differential pulse height distributions from monoenergetic neutrons. The range of the calibration was from 0.2 to 22 MeV, and included only neutrons incident normal to the axis of the detector.

* NE213, used in the earlier NYU detectors differs from NE218 in its somewhat larger ratio of C/H.

These differential response functions, in tables of counts per unit light output per incident neutron, could not be used directly for the NYU detectors, because of differences imposed by use of a phoswich. The efficiency of the NYU flight instrument, especially near the threshold of the detection, was significantly decreased by: 1. attenuation in the outer anticoincidence phosphor, and 2, losses resulting from the higher bias for pulse-shape discrimination. Other differences, in volume, in composition and in resolution, were more readily correctible.

2. Calibration at ORNL. -The NYU detectors were calibrated with "monoenergetic" neutrons at the van de Graaff facility of the Oak Ridge National Laboratory in 1965 and 1967. On both occasions, Verbinski's NE213 spectrometer was used. It served both as a monitor of the flux of monoenergetic neutrons from the accelerator target and as a spectrum analyzer for whatever background neutrons might be present. Incidentally, the Verbinski detector also provided a means of comparing the response of the NYU composite scintillator with that of a bare NE213 scintillator.

The 1965 calibrations involved systems 1965-I and 1965-II, both flown in a series of neutron measurements during IQSY. All later flight systems were matched as nearly as possible to show the same response as system 1965-I to laboratory sources. In 1967, a more extensive calibration was made at ORNL with detectors 1966-II and 1966-III. These measurements form the basis of the response functions we report in this paper.

Neutrons for the calibration were produced in the reactions,

$T(p,n)He^3$, $D(d,n)He^3$, and $H^3(d,n)He^4$, covering the range from the threshold of detection, ~ 0.7 MeV, to ~ 20 MeV. During each series of measurements, the NYU and ORNL detectors were symmetrically positioned

at equal distances from the target and at equal angles, near 0° , from the axis of the beam pipe of the accelerator. Most runs were made with the axis of the NYU detector perpendicular to the beam pipe. Additional runs were made at several energies, with the axis of the NYU scintillator parallel to the beam pipe, to help determine the angular dependence of the response functions. Further observations were made with the gondola dome over the detector, as a check for possible effects of the dome on the spectrum. Also, several runs were made with the same beam energy at varying target distances. This provided an independent calculation of background neutrons.

2a. Behaviour of ORNL detector-monitor. -The ORNL detector, which served as a beam monitor, was stable in gain and gave consistent light-output spectra from .7 MeV to the upper energy limit of neutrons from the P-T reaction, i.e., around 4 MeV. However, in analyzing the data above this energy, where (D-D), (D, T), and Pu-Be neutrons were used, we found that the efficiency of the ORNL detector to neutrons tended to drift from run to run. This was observed only in the higher light output channels. It was necessary to use an independent measurement to normalize the pulse height distributions from neutrons above 5 MeV. This will be discussed in section 3.

2b. Unfolding the incident neutron spectrum from the measured pulse height distributions. -Two alternative procedures were employed to determine the incident neutron spectrum from the measured pulse height distribution in the ORNL detector. Both made use of the response functions of NE213, as reported by Verbinski. One program was the ORNL

computer code, FERDoR, developed by Burrus.²¹ In FERDoR, the pulse height spectra are unfolded using matrix inversion modified by the constraint that the recovered neutron spectrum must be everywhere non-negative. In the alternative treatment, a simple spectrum-stripping procedure was employed, based on the nature of the pulse height spectrum of

a monoenergetic neutron source.* First, the incident neutron flux at the energy of direct target neutrons was determined; it was simply the ratio of the observed counting rates in the tail of the pulse height distribution of the ORNL detector to the counts per unit neutron flux, as derived from the

* The pulse height spectrum that results from exposing the detector to monoenergetic neutrons is rather complex. The energy spectrum of the recoil-protons is flat from 0 to the end point E, the energy of the incident neutron, at the neutron energies we are considering. The light output spectrum in the scintillator differs from the proton-recoil energy spectrum because: 1, the light output from the scintillator is non-linear with proton energy; 2, multiple neutron interactions increase the number of events at larger light outputs, end effects decrease the light output; 3, neutrons interacting with carbon can eject particles which cause counts in the 1-10 MeV proton recoil region; 4, the finite resolution of the scintillator smears out the spectrum. The resulting pulse height distribution retains some of the features of the recoil-proton energy spectrum, a vestigial plateau and a descent at the upper end.

Verbinski response functions. The recoil spectrum from this neutron flux was then subtracted from the total observed pulse height distribution. This spectrum stripping procedure was then repeated, beginning with the tail of the residual pulse height distribution, until the rest of the neutron spectrum was peeled off.

In the ORNL calibration, we found that the observed pulse height distributions corresponded to those from monoenergetic neutrons from about the midpoint of the distribution to the greatest light output. Below this, background rose monotonically. Both the FERDOR and the spectral stripping procedure gave similar results, and both were later tested as a means of unfolding flight spectra observed with the NYU detector (Section III B).

2c. Normalizing incident spectrum to Pu-Be above 5 MeV. -To check the total efficiency above 5 MeV, we first noted that the NYU detector should respond more and more like a bare NE213 scintillator at increasing energy, the main residual difference at large light outputs arising from the attenuation of the anticoincidence shield. The effect of the plastic scintillator-shield can be calculated, and such a calculation was made for neutrons incident perpendicular to the axis of the empty shell. In this determination, all neutrons that would otherwise have entered the inner scintillator after collisions in the outer scintillator were considered to be counted out, i.e., as non-neutrons to the detecting circuit. The attenuation of the portion of the neutron beam that would normally enter the inner scintillator was found to be 15%, 7%, and 3% for neutrons of 1 MeV, 4 MeV and 10 MeV respectively. The effect of the outer shield was tested experimentally by exposing an NE218 scintillator, with and without the plastic shield, to Pu-Be neutrons. The attenuation of the shield was found to be $\leq 5\%$. Since the average energy of Pu-Be neutrons is about 5 MeV, the calculated shielding effect agrees with the measured value to within a per cent or two.

The total efficiency to neutrons above 5 MeV was further checked by exposing the detector to the 1-curie Pu-Be source, the absolute emission

of which was known to be 1.89×10^6 neutrons/sec to within 2-3%.* The energy spectrum of a Pu-Be neutron source was also reasonably well known,

having been measured by several methods.²²⁻²⁴ By exposing the detector to the source and using standard techniques for background elimination,

* Mound Laboratories, Monsanto Chemical Company, Miamisburg, Ohio

we obtained the pulse height distribution from a known neutron energy distribution. To determine the ratio of the observed to the calculated efficiencies, we proceeded as follows. Using the known flux at the detector and the unnormalized pulse height distributions, the counting rate in channel 7 was calculated:

$$C(7)_{\text{calc}} = \int_{E_{\text{lo}}(7)}^{E_{\text{max}}} R(t, E) n(E) dE d\mathbf{k} \quad 1$$

$$L_{\text{up}}(7) \quad L_{\text{lo}}(7)$$

Where $C(i)$ was the counting rate in the i 'th channel of the flight analyzer, $R(t, E)$, the response function of neutrons of energy, E , in the t 'th pulse height bin of the response function; $n(E)$, the differential neutron spectrum, and L_{lo} and L_{up} , the upper and lower thresholds of channel 7.

E_{max} was the end point of the Pu-Be spectrum (~11 MeV), and L_{lo} was the pulse amplitude of a proton-recoil of energy E_{lo} .

$C(7)_{\text{calc}}$ was compared with $C(7)_{\text{obs}}$. The ratio, $C(7)_{\text{calc}}/C(7)_{\text{obs}}$ was taken to be the correction factor to $R(t, E)$ for neutrons between E_{lo} and E_{max} . The counts from neutrons between E_{lo} and E_{max} in the other channels were calculated and subtracted from the observed counts. The same procedure was repeated from channel 6 to channel 1. The normalized response functions obtained in this manner were consistent with the Verbinski responses above 5 MeV, corrected for the shielding of the plastic scintillator.

3. Response to neutrons >10 MeV. -Holt⁴ calculated the pulse height distributions, in the 7 channels of the flight instrument, for neutrons between 14 MeV and 80 MeV. His results, which relied heavily on cross

sections reported by Kurz²⁵ and Bertini,²⁶ accounted for low energy stars in carbon as well as recoil-protons in hydrogen. This calculation was used to extend the response functions beyond 20 MeV.

4. Omnidirectional response. -The response of the NYU detector to an omnidirectional isotropic flux was determined on the basis of measurements at ORNL parallel and perpendicular to the detector axis of symmetry

at different incident energies. The variation of response at intermediate angles, was checked in measurements with the Pu-Be source. The correction factors for an omnidirectional flux were 0.79, 0.85 and 0.90 at 1.5, 2.5 and 4 MeV. Above 4 MeV, the correction factor was taken to be the same as that due to the outer scintillator, which is mainly responsible for the directional effects.

5. Listing of response functions. -The omnidirectional response functions of the detector to neutrons are given in Table I and fig. 5. They differ from the responses reported by Holt et al. in 1966, in that the angular response at lower energies was found to be larger than originally determined from Pu-Be alone. We have used these response functions to reevaluate the measurements previous to the 1967 calibration, and these are the fluxes we report in this paper. The results of the last ORNL calibration are believed to have an uncertainty of about 10%. The effect of errors in the calibrated response on the calculated spectrum will be discussed later.

6. Cross-calibration of detectors. -Several of the flight systems were not calibrated with monoenergetic neutrons. These included 1966-I, 1968-III, 1970-IV, and 1970-V. Gain, channel edges, and PSD* threshold and neutron response for such detectors were set with laboratory sources only. To eliminate residual differences in response to the atmospheric neutron spectrum, we attempted to cross-calibrate these detectors against the remaining systems in high altitude flights. The effect of gain and PSD threshold were also tested in flight. A 10% difference in gain was found to cause a 10% change in flight counting rates; a 10% change in neutron counts near threshold with Am-Be produced a 10% change at aircraft altitude, consistent with the calculated response functions. With this test, we were assured that the gain stability of the detector was matched by an equivalent counting rate stability in flight.

7. Rejection of gammas in flight. -The rejection of gammas by the circuit was checked with laboratory sources giving mixed neutron and radiation fields. A more meaningful check was made by observing the rejection of charged particles and gammas in the radiation at high altitude. Flight 6901 encountered a cloud of radiation. The rejection of charged particles, as a function of total counting rate in this flight is listed in Table II.

* Pulse Shape Discrimination

TABLE I

ENERGY (MEV)	CH.1	CH.2	CH.3	CH.4	CH.5	CH.6	CH.7	TOTAL RESPONSE
1.0	0.006	0.0	0.0	0.0	0.0	0.0	0.0	0.006
1.1	0.052	0.0	0.0	0.0	0.0	0.0	0.0	0.052
1.2	0.096	0.0	0.0	0.0	0.0	0.0	0.0	0.096
1.3	0.316	0.0	0.0	0.0	0.0	0.0	0.0	0.316
1.4	0.575	0.0	0.0	0.0	0.0	0.0	0.0	0.575
1.5	0.824	0.0	0.0	0.0	0.0	0.0	0.0	0.824
1.6	1.112	0.008	0.0	0.0	0.0	0.0	0.0	1.120
1.7	1.405	0.016	0.0	0.0	0.0	0.0	0.0	1.421
1.8	1.719	0.025	0.0	0.0	0.0	0.0	0.0	1.744
1.9	2.041	0.034	0.0	0.0	0.0	0.0	0.0	2.075
2.0	2.342	0.043	0.0	0.0	0.0	0.0	0.0	2.385
2.1	2.411	0.166	0.0	0.0	0.0	0.0	0.0	2.577
2.2	2.385	0.316	0.0	0.0	0.0	0.0	0.0	2.701
2.3	2.388	0.472	0.0	0.0	0.0	0.0	0.0	2.860
2.4	2.362	0.625	0.0	0.0	0.0	0.0	0.0	2.987
2.5	2.364	0.786	0.0	0.0	0.0	0.0	0.0	3.150
2.6	2.281	0.932	0.026	0.0	0.0	0.0	0.0	3.239
2.7	2.148	1.064	0.054	0.0	0.0	0.0	0.0	3.266
2.8	2.015	1.196	0.083	0.0	0.0	0.0	0.0	3.294
2.9	1.905	1.343	0.114	0.0	0.0	0.0	0.0	3.362
3.0	1.771	1.477	0.144	0.0	0.0	0.0	0.0	3.392
3.1	1.694	1.518	0.257	0.005	0.0	0.0	0.0	3.474
3.2	1.600	1.530	0.378	0.010	0.0	0.0	0.0	3.518
3.3	1.508	1.540	0.494	0.016	0.0	0.0	0.0	3.558
3.4	1.437	1.545	0.580	0.028	0.0	0.0	0.0	3.590
3.5	1.349	1.534	0.659	0.040	0.0	0.0	0.0	3.582
3.6	1.282	1.503	0.727	0.091	0.0	0.0	0.0	3.603
3.7	1.233	1.485	0.802	0.147	0.0	0.0	0.0	3.667
3.8	1.167	1.452	0.869	0.202	0.0	0.0	0.0	3.690
3.9	1.114	1.434	0.946	0.261	0.0	0.0	0.0	3.755
4.0	1.049	1.400	1.013	0.317	0.0	0.0	0.0	3.779
4.1	0.976	1.340	1.002	0.419	0.051	0.0	0.0	3.788
4.2	0.911	1.260	0.982	0.503	0.097	0.0	0.0	3.773
4.3	0.881	1.220	0.962	0.586	0.144	0.0	0.0	3.793
4.4	0.851	1.160	0.941	0.670	0.191	0.0	0.0	3.813
4.5	0.823	1.101	0.922	0.752	0.238	0.0	0.0	3.836
4.6	0.793	1.040	0.902	0.836	0.284	0.0	0.0	3.855
4.7	0.763	0.981	0.882	0.919	0.330	0.0	0.0	3.875
4.8	0.739	0.945	0.862	0.892	0.377	0.0	0.0	3.815
4.9	0.714	0.909	0.842	0.866	0.424	0.0	0.0	3.755
5.0	0.689	0.872	0.822	0.839	0.470	0.0	0.0	3.692
5.1	0.664	0.836	0.802	0.813	0.517	0.0	0.0	3.632
5.2	0.640	0.800	0.782	0.786	0.563	0.026	0.0	3.597
5.3	0.620	0.728	0.745	0.767	0.639	0.040	0.0	3.539
5.4	0.599	0.657	0.708	0.747	0.715	0.052	0.0	3.478

THE RESPONSE IN NEUTRONS PER UNIT INCIDENT FLUX

ENERGY (MEV)	CH.1	CH.2	CH.3	CH.4	CH.5	CH.6	CH.7	TOTAL RESPONSE
5.5	0.580	0.585	0.671	0.728	0.790	0.066	0.0	3.820
5.6	0.561	0.565	0.635	0.708	0.866	0.078	0.0	3.413
5.7	0.542	0.545	0.598	0.689	0.941	0.092	0.0	3.407
5.8	0.522	0.525	0.561	0.670	0.945	0.107	0.0	3.330
5.9	0.504	0.509	0.545	0.651	0.941	0.107	0.0	3.317
6.0	0.497	0.495	0.531	0.631	0.915	0.129	0.0	3.318
6.1	0.483	0.480	0.516	0.612	0.931	0.124	0.0	3.311
6.2	0.471	0.464	0.500	0.592	0.925	0.150	0.0	3.302
6.3	0.458	0.449	0.485	0.573	0.921	0.110	0.0	3.296
6.4	0.449	0.435	0.470	0.563	0.900	0.162	0.0	3.279
6.5	0.439	0.419	0.455	0.551	0.879	0.152	0.0	3.255
6.6	0.429	0.405	0.440	0.540	0.859	0.163	0.0	3.236
6.7	0.419	0.390	0.425	0.529	0.839	0.114	0.0	3.216
6.8	0.410	0.374	0.410	0.518	0.817	0.165	0.021	3.215
6.9	0.401	0.365	0.394	0.507	0.797	0.176	0.0	3.161
7.0	0.396	0.359	0.387	0.496	0.776	0.187	0.002	3.163
7.1	0.392	0.354	0.379	0.485	0.754	0.198	0.083	3.145
7.2	0.387	0.348	0.372	0.474	0.734	0.208	0.104	3.127
7.3	0.383	0.343	0.365	0.463	0.714	0.219	0.124	3.111
7.4	0.378	0.338	0.357	0.452	0.692	0.230	0.145	3.092
7.5	0.373	0.332	0.349	0.441	0.671	0.241	0.166	3.073
7.6	0.368	0.328	0.341	0.430	0.651	0.240	0.186	3.044
7.7	0.363	0.324	0.334	0.419	0.630	0.238	0.207	3.015
7.8	0.358	0.320	0.326	0.408	0.610	0.229	0.238	2.985
7.9	0.353	0.316	0.318	0.397	0.590	0.219	0.268	2.961
8.0	0.348	0.311	0.310	0.387	0.571	0.209	0.298	2.934
8.1	0.342	0.309	0.302	0.376	0.551	0.195	0.329	2.904
8.2	0.335	0.306	0.294	0.366	0.531	0.180	0.358	2.870
8.3	0.329	0.303	0.286	0.356	0.511	0.165	0.389	2.839
8.4	0.321	0.301	0.278	0.345	0.491	0.150	0.419	2.805
8.5	0.315	0.298	0.270	0.335	0.472	0.135	0.450	2.775
8.6	0.309	0.292	0.267	0.324	0.464	0.120	0.468	2.744
8.7	0.302	0.286	0.265	0.313	0.455	0.106	0.464	2.691
8.8	0.296	0.280	0.262	0.303	0.447	0.090	0.459	2.637
8.9	0.290	0.275	0.259	0.293	0.439	0.076	0.455	2.587
9.0	0.284	0.268	0.257	0.283	0.431	0.062	0.450	2.535
9.1	0.277	0.262	0.254	0.272	0.423	0.056	0.446	2.480
9.2	0.273	0.257	0.251	0.268	0.415	0.052	0.432	2.418
9.3	0.268	0.252	0.248	0.265	0.406	0.057	0.419	2.375
9.4	0.263	0.247	0.246	0.262	0.398	0.052	0.405	2.323
9.5	0.258	0.242	0.243	0.259	0.390	0.047	0.392	2.271
9.6	0.254	0.237	0.240	0.257	0.382	0.043	0.378	2.221
9.7	0.249	0.232	0.238	0.254	0.374	0.047	0.364	2.168
9.8	0.244	0.227	0.235	0.251	0.365	0.043	0.350	2.115
9.9	0.239	0.222	0.232	0.248	0.357	0.048	0.337	2.063

ENERGY (MEV)	THE RESPONSE IN NEUTRONS PER UNIT INCIDENT FLUX							TOTAL RESPONSE
	CH.1	CH.2	CH.3	CH.4	CH.5	CH.6	CH.7	
10.0	0.235	0.217	0.230	0.245	0.349	0.413	0.323	2.012
11.0	0.227	0.162	0.192	0.214	0.305	0.363	0.290	1.773
12.0	0.251	0.158	0.161	0.184	0.265	0.313	0.245	1.577
13.0	0.293	0.167	0.139	0.151	0.230	0.260	0.207	1.447
14.0	0.377	0.223	0.126	0.131	0.182	0.226	0.172	1.437
15.0	0.404	0.232	0.158	0.123	0.165	0.197	0.154	1.433
16.0	0.420	0.211	0.185	0.167	0.148	0.172	0.135	1.438
17.0	0.403	0.194	0.162	0.190	0.170	0.153	0.116	1.388
18.0	0.386	0.179	0.145	0.174	0.221	0.155	0.106	1.366
19.0	0.369	0.164	0.124	0.151	0.221	0.177	0.098	1.304
20.0	0.338	0.151	0.116	0.146	0.212	0.162	0.101	1.226
21.0	0.299	0.139	0.108	0.140	0.203	0.153	0.107	1.149
22.0	0.261	0.126	0.101	0.135	0.194	0.144	0.101	1.062
23.0	0.222	0.114	0.093	0.130	0.203	0.135	0.095	0.992
24.0	0.185	0.102	0.085	0.124	0.212	0.126	0.089	0.923
25.0	0.146	0.089	0.073	0.112	0.221	0.117	0.083	0.841
26.0	0.140	0.086	0.069	0.107	0.212	0.108	0.080	0.802
27.0	0.133	0.082	0.066	0.102	0.202	0.099	0.076	0.760
28.0	0.127	0.078	0.063	0.097	0.192	0.090	0.073	0.720
29.0	0.122	0.075	0.060	0.093	0.182	0.081	0.069	0.682
30.0	0.116	0.071	0.057	0.089	0.172	0.072	0.066	0.643
31.0	0.112	0.068	0.055	0.085	0.162	0.069	0.064	0.615
32.0	0.107	0.066	0.053	0.082	0.152	0.066	0.061	0.587
33.0	0.104	0.063	0.051	0.079	0.142	0.063	0.058	0.560
34.0	0.099	0.060	0.049	0.076	0.132	0.061	0.056	0.533
35.0	0.095	0.059	0.047	0.073	0.122	0.059	0.054	0.509
36.0	0.092	0.057	0.045	0.071	0.117	0.057	0.052	0.491
37.0	0.089	0.054	0.044	0.068	0.113	0.055	0.051	0.474
38.0	0.086	0.052	0.043	0.065	0.109	0.053	0.049	0.457
39.0	0.083	0.050	0.041	0.063	0.105	0.051	0.047	0.440
40.0	0.079	0.049	0.039	0.061	0.101	0.049	0.045	0.423
41.0	0.077	0.048	0.038	0.060	0.099	0.048	0.044	0.414
42.0	0.076	0.046	0.037	0.058	0.096	0.046	0.043	0.402
43.0	0.074	0.045	0.036	0.057	0.094	0.045	0.042	0.393
44.0	0.072	0.044	0.035	0.056	0.092	0.044	0.041	0.384
45.0	0.070	0.042	0.034	0.054	0.089	0.043	0.040	0.372
46.0	0.069	0.041	0.034	0.053	0.087	0.042	0.039	0.365
47.0	0.068	0.041	0.033	0.052	0.085	0.041	0.039	0.359
48.0	0.066	0.040	0.032	0.050	0.083	0.040	0.038	0.349
49.0	0.065	0.039	0.031	0.049	0.081	0.039	0.037	0.341
50.0	0.063	0.038	0.031	0.048	0.079	0.039	0.036	0.334
51.0	0.061	0.037	0.030	0.046	0.076	0.037	0.035	0.322
52.0	0.059	0.035	0.029	0.045	0.073	0.036	0.033	0.310
53.0	0.056	0.034	0.027	0.043	0.071	0.034	0.032	0.297
54.0	0.054	0.033	0.026	0.041	0.068	0.032	0.031	0.285

ENERGY (MEV)	THE RESPONSE IN NEUTRONS PER UNIT INCIDENT FLUX							TOTAL RESPONSE
	CH.1	CH.2	CH.3	CH.4	CH.5	CH.6	CH.7	
55.0	0.051	0.032	0.025	0.039	0.065	0.031	0.029	0.272
56.0	0.050	0.031	0.025	0.038	0.064	0.030	0.028	0.266
57.0	0.050	0.030	0.024	0.037	0.062	0.030	0.027	0.260
58.0	0.048	0.029	0.020	0.036	0.061	0.029	0.027	0.250
59.0	0.047	0.028	0.023	0.035	0.060	0.028	0.026	0.247
60.0	0.046	0.028	0.023	0.035	0.058	0.028	0.026	0.244
61.0	0.045	0.027	0.022	0.034	0.057	0.027	0.025	0.237
62.0	0.044	0.026	0.021	0.034	0.056	0.026	0.025	0.232
63.0	0.043	0.025	0.021	0.033	0.054	0.026	0.024	0.226
64.0	0.042	0.025	0.020	0.033	0.053	0.025	0.024	0.222
65.0	0.041	0.024	0.020	0.032	0.052	0.025	0.023	0.217
66.0	0.041	0.023	0.019	0.031	0.050	0.024	0.022	0.210
67.0	0.039	0.023	0.019	0.030	0.048	0.023	0.021	0.203
68.0	0.037	0.022	0.018	0.028	0.047	0.022	0.020	0.194
69.0	0.036	0.021	0.017	0.027	0.045	0.021	0.019	0.186
70.0	0.034	0.020	0.017	0.026	0.043	0.021	0.019	0.180
71.0	0.033	0.020	0.016	0.025	0.042	0.020	0.018	0.174
72.0	0.032	0.019	0.016	0.024	0.040	0.020	0.018	0.169
73.0	0.031	0.019	0.015	0.024	0.039	0.019	0.017	0.164
74.0	0.030	0.018	0.014	0.023	0.037	0.019	0.017	0.158
75.0	0.029	0.018	0.014	0.022	0.036	0.018	0.016	0.153
76.0	0.028	0.017	0.014	0.022	0.035	0.017	0.016	0.149
77.0	0.027	0.017	0.013	0.021	0.034	0.017	0.015	0.144
78.0	0.027	0.016	0.013	0.020	0.033	0.016	0.015	0.140
79.0	0.026	0.016	0.012	0.019	0.032	0.016	0.014	0.135
80.0	0.025	0.015	0.012	0.019	0.031	0.015	0.014	0.131

TABLE II
REJECTION OF CHARGED PARTICLES RECORDED IN FLIGHT 6901

Total Events, counts per second	Rejection ratio, excess neutron counts/total events	Channel 1-3	Channel 4-7
235 (pre-exposure counting rate)			
1000		1.6×10^{-4}	1×10^{-4}
2000		2×10^{-4}	
4000		6×10^{-4}	1.6×10^{-4}
6000		1.3×10^{-3}	2×10^{-4}
7000		2.9×10^{-3}	3.6×10^{-4}

II. FLIGHT SUMMARIES

A. Balloon Flights

At the beginning of the present solar cycle, when the galactic radiation was at a maximum, we initiated a series of balloon flights to measure the world wide flux of neutrons in the atmosphere. Flight 111, the first flight of the present program was the final flight of the solar minimum

^{10,11} survey. The effect of increasing solar activity on the neutron flux was determined in balloon flights from 1965-1968. Table III lists these flights along with essential flight information and the experimental results.

In addition to the free air measurements, we have included, in Table III, three balloon flights in which the detector was surrounded with a 15 cm dome of tissue-equivalent material, as requested by T. Foelsche of NASA, to assist in his evaluation of radiation doses. These are listed separately with the letter P appended.

Under the heading of Comments, unusual system performance has been indicated. In several flights, the tape recorder motor stopped at some point at floating altitude; fortunately the photobarograph record supplied

TABLE III
SUMMARY OF BALLOON FLIGHTS

NYU Flight	Date (1965)	U.T.	(hrs.)	(mb)	DRNM ¹	INUV. ²	Comments	Attenuation Length		Transition Maximum			Floating Altitude		
								Total Events	Neutrons	Neutron Flux 1-10 MeV	Neutron Flux 2-10 MeV	n	Neutron Flux 1-10 MeV	Neutron Flux 2-10 MeV	n
111	8/3	2017	26 $\frac{1}{2}$	4.6	7038	7094	ASF	162 \pm 7	162 \pm 9	2.46	1.50	1.23	1.41	0.88	1.11
112	9/2	0228	20	40	6999		MS		158 \pm 30	2.27		1.29			
(1966)															
113	7/16	1020	18	4.5	6833	6945	A2	170 \pm 1	157 \pm 5	2.12	1.32	1.14	1.21	0.75	1.06
114	7/24	0331	21 $\frac{1}{2}$	40-50	6851	6947	A1T	157 \pm 2	159 \pm 4		1.18				
116	8/3	0315	20	2.6	6826	6993	A2T	168 \pm 1	164 \pm 6	1.99	1.24	1.16	1.02	0.63	1.15
(1967)															
117	6/25	0823	15 $\frac{1}{2}$	49	6643	6752	A1	165 \pm 2	172 \pm 8 Ascent	1.11					
									1st 5 hrs	1.06					
									2nd 5 hrs	1.02					
									last 3 hrs	1.025					
118	7/15	1106	16	3.3	6644	6785	A2F	160	154	2.00	1.16	1.23	0.92	0.56	1.06
119	7/22	0845	16	46	6707	6842	A1	167	176		1.10				0.59
120(1)	9/27	1431	8	40-42	6606	6732	B1F	164	179		1.08				
120(2)	Same as 120(1), Both systems on same flight					B2F		159	159	2.00	1.04		1.15		

¹ Counting rate of the Deep River neutron monitor

² Counting rate of the Inuvik neutron monitor

NYU Flight	Date (1968)	U. T. (hrs.)	(mb)	DRNM	INUV.	Com- ments	Attenuation Length		Transition Maximum			Floating Altitude		
							Total Events	Neutrons	Neutron Flux		n	Neutron Flux		n
									1-10 MeV	2-10 MeV		1-10 MeV	2-10 MeV	
121	7/18	0905	18	5.5	6389	6503	A2F	161 ± 2	158 ± 4	1.72	0.95	1.16	0.95	0.56 1.14
122	8/21	0011	21	40-50	6409	6525	BIT	163 ± 4	161 ± 7		0.99			
123	9/12	1832	22	3.6	6361	6443	B2T	180 ± 2	185 ± 6	1.65	0.93	1.10	0.90	0.54 1.06
124	9/26	2104	25	40-50	6501	6533	B2T	167 ± 2	166 ± 5	1.73	0.96	1.10		
125	9/30	1841	12½	42-50	6355	6560	BIT	177 ± 2	183 ± 8		0.94			
(1970)														
126	8/20	1123	15	24-48	6260	6329	P5	169 ± 1.8	164.6 ± 8.8		.55 ± .03			
127	8/25	1156	15	3.75	6281	6346	P5	167.7 ± 1.8	167.6 ± 6.3		.58 ± .04			0.23
128	8/31	2027	9	27-57	6390	6495	P4	170.25 ± 2.6	210.9 ± 16		.616			
<u>Phantom Flights</u>														
(1965)														
111P	8/9	2233	20	5.5	7004		AQ	149 ± 6	144 ± 9	1.40		0.96	1.27	1.10
112P	9/8	0830	15	40-60	7018		MS	157 ± 30	158 ± 30	1.20				
(1966)														
115(P)	7/31	1200	5	50	6840		A1F	168 ± 1	164 ± 6	1.04				

* : Not cross-calibrated

+ : Ascent data inadequate

Comments: A. Fort Churchill, Manitoba, 0.2 GV

B. Lynn Lake, Manitoba, 0.4 GV

M. St. Paul, Minnesota, 1.3 GV

P. Palestine, Texas, 4.5 GV

S. System 1965--I

Q. System 1965--II

1. System 1966--I

2. System 1966--II

4. System 1970--IV

5. System 1970--V

F. Tape recorder failed after
reaching floating altitudeT. Large temperature drift
after reaching floating altitude

the remaining data. In some night flights, as listed, temperature excursions exceeded acceptable limits, and only data recorded within such limits were used. In the summer of 1970, the heater supply in the gondola was increased to 100 watts, and this appeared to be adequate during night flights.

All but two of the 22 balloons were launched successfully. All that were launched reached floating altitude. The gondola flown in flight 111P was lost in a thunderstorm at around balloon cutoff. It was found in the backwoods of Canada after a year. The equipment was corroded, but the tape was still readable and the data was retrieved.

The balloon trajectories were such that changes in cutoff rigidity did not exceed ~ 0.2 GV at high latitude. At lower latitudes, the balloon usually drifted less than 17 km, except during flights from Palestine, Texas, in 1970, when the latitude drift was appreciable and a latitude effect could be observed in the data.

B. Aircraft Flights

1. Introduction. -In airplane surveys of cosmic-ray neutrons, the measurements suffer from the presence of an appreciable quantity of matter around the detector. The free-air flux of neutrons is moderated by the airplane and its contents. The matter around the detector also acts as a target for high-energy particles in the cosmic radiation, and neutrons are produced in the airplane and its contents. Thus the neutron flux is not the free air flux and the neutron spectrum is not a free air spectrum. The effect of the vehicle can be measured for any given airplane by arranging a rendezvous flight between a balloon and an airplane, each carrying a neutron detector. It can also be approximated by comparing measurements made in an airplane with measurements made with a balloon at the same cutoff rigidity and at times when the ground based neutron monitors register

approximately the same counting rates.* Airplanes enjoy the advantage of their maneuverability and flexibility. They can fly at any given latitude or spread of latitudes during all seasons, unlike balloons. The flight paths are not wholly dependent on the whims of the winds of the upper atmosphere.

* Observations since 1969 indicate that some caution must be exercised in evaluating relative response of detectors during periods in which the interplanetary field is frequently disturbed, such as late 1969-early 1970. See section V. C.

They are less limited by surface weather. This is most important if short term variations, such as those resulting from a solar flare, are to be measured.

2. Solar minimum latitude survey. -Early in this program, we had the opportunity to test the feasibility of flying the neutron spectrometer in an airplane. Professor Korff was scientific advisor for the Rockwell Polar Flight, November 14-17, 1965, and the NYU flight instrument traveled round-the-world over both poles.

3. Listing of aircraft flights. -Table IV lists the series of aircraft flights that followed. Most of the flights were at the neutron transition maximum and north of the latitude knee. Such flights are recorded without comment in the table. Unusual flights are separately indicated, especially those involving large excursions in latitude (latitude flights), in altitude (step flights) and in the incident radiation (solar proton events and classic Forbush decreases). Table IVb summarizes the aircraft step flights.

3a. Performance of flight systems. -At most times, at least two flight systems were available in Alaska, permitting ample time for cross-calibration with overlapping flights. Only system 1970 V, flown in Palestine, was not cross-calibrated, since it lost its P.S.D. en route to Alaska.

In March, 1969, system II, which had been the best-calibrated and least problematical of the flight instruments began to lose gain in flight, thus ending three years of faithful service.

All other equipment performed satisfactorily. Even the tape recorder motors, which had performed marginally in balloon measurements, behaved well in aircraft flights.

III. EVALUATION OF DATA

A. Introduction

The raw data of each flight was processed and recorded as a function of time, in intervals of one minute. The record contained universal time, ambient pressure, the counts in the seven neutron channels and total events, as well as the photobarograph data. To convert the proton recoil spectrum to neutron flux, we employed the 7 channel response functions enumerated in Table I.

TABLE IV

 SUMMARY OF AIRCRAFT FLIGHTS
 a. ALL FLIGHTS

Flight	Date / U. T.	Sys. ¹	Loc. ²	Cruising Pressure, g/cm ²	Deep River	Inuvik	2-10 MeV Flux ³	Comments ⁴
(1967)								
6701	Apr 11/07-15 ^h	3/1966	Bed	70	6661	6816	1.083	High lat. survey
6702	June 25/17-24	3/1966	Pres	61-71	6643	6752	1.04 → 1.02	Balloon rendezvous
(1968)								
6801	Jan 16/20-23	2	En	59-71	6643	6703	1.040	
6802	" 18/19-23	1	En	62-71	6637	6713	.999	
6803	" 22/19-22	1	En	59-71	6685	6684	1.040	
6804	Mar 9/23-10/03	1	E-Anc-E	243-267	See altitude flights			Low altitude
6805	" 12/20-13/02	1	En	61-71	6428	6542	.942	Anti-G. H. depl.
6806	" 19/20-24	2	En	58-71	6568	6680	1.000	
6807	" 26/20-27/02	2	En	57-71	6462	6651	.992	
6808	Apr 13/02-07	2	En	64-71	6534	6700	1.051	Total lunar eclipse
6809	" 17/02-07	2	En	64-71	6618	6775	1.091	
6810	" 19/06-13	1	En	59-71	6628	6752	1.013	Large diurnal
6811A	" 24/08-14	1	E-Abq	71	See latitude flights			Lat. survey, N-S
6811B	" 25/19-26/01	1	Abq-E	71	See latitude flights			Lat. survey, S-N
6812	May 2/03-08	2	En	59-71	6626	6709	1.115	Hi gain
6813	" 10/03-08	1	En	62-73	6499	6604	1.013	
6814	" 13/18-23	1	En	61-74	6616	6640	1.008	
6815	" 18/16-22	2	E-Abq	68-79	See latitude survey			Latitude survey
6816A	" 30/15-21	2	Abq-Pan	62-118	See latitude survey			Latitude survey
6816B	Jun 1/15-18	2	Pan	54-71	See latitude survey			Latitude survey
6817	" 1/19-23	1	En	59-71	6453	6559	.970	
6818	" 2/19-23	1	En	118-383				Step flight
6819	" 8/19-22	1	E	45-71	6551	6647	1.036	Local flight
6820	" 10/00-05	1	En	60-74	6417	6513	1.020	P. E.
6821	" 15/16-19	1	En	60-71	6427	6484	.945	

Flight	Date / U. T.	Sys. ¹	Loc. ²	Cruising Pressure, g/cm ²	2-10 MeV			Comments ⁴
					Deep River	Inuvik	Flux ³	
6822	Oct 8/19-21 ^h	3	En	64-71	6293	6372	.906	
6823	" 17/18-24	2	En	61-71	6394	6467	.90	No tape data
6824	" 19/19-20/01	2	En	62-71	6388	6501	.896	
6825	" 29/20-30/03	2	En	59-71	5885	5972	.740	Start F. D.
6826	" 31/04-10	2	En	60-72	6012	6033	.750	F. D., N. M. 12%
6827	Nov 1/14-20	2	En	57-71	5809	5859	.670	F. D. small P. E. in flight
6828	" 2/04-11	2	En	57-71	5695	5706	.655	F. D., P. E. near background
6829	" 3/10-16	2	En	57-71	5726	5712	.659	F. D. background flight
6830	" 4/19-5/01	2	En	57-71	5998	6101	.760	P. E. near bkg., 5% neutron inc. in flight
6831	" 18/20-22	2	En	75-116	6093	6156	1.021	H. E. P. E., N. M. increase 11 U. T.
6832	" 26/02-03	2	En	68-82	6144	6245	.828	
6833	Dec 5/23-6/03	2	En	62-78	6117	6121	.834	F. D., P. E.
6834	" 10/16-20	2	En	63-76	6205	6247	.845	
6835	" 13/20-24	2	En	65-70				Logic 3
6836	" 20/20-21/01	2	En	62-75	6272	6329	.870	
 (1969)								
6901	Jan 4/21-5/02	2	En	72	6378	6525	.889	
6902	" 8/20-9/01	1	En	62-71	6480	6604	.936	
6903	" 14/20-15/01	2	En	56-71	6446	6599	.960	
6904	" 16/20-17/02	1	En	54-71	6335	6455	.925	
6905	" 25/00-05	2	En	56-75	6425	6529	.958	
6906	" 27/20-28/01	2	En	59-73	6345	6383	.908	
6907	" 31/21-24	1	En	59-71	6289	6402	.921	
6908	Feb 14/20-15/01	2	En	61-72	6420	6506	.954	
6909	" 20/21-24	2	En	63-72	6492	6570	.987	
6910	" 24/21-25/01	1	En	58-72	6489	6570	.983	
6911	" 25/14-18	2	En	62-72	6401	6561	1.529	H. E. P. E., N. M. max 0950 U. T.
6912	" 25/20-24	1	En	56-72	6504	6577	1.076	P. E.

Flight	Date / U. T.	Sys. ¹	Loc. ²	Cruising			2-10 MeV	Comments ⁴
				Pressure, g/cm ²	Deep River	Inuvik		
6913	Feb 26/02 ^h 07 ^h	2	En	60-72	6414	6502	1.029	P. E., F. D.
6914	" 26/11-16	1	En	60-72	6422	6444	1.000	P. E., F. D.
6915	" 26/19-24	2	En	59-72	6414	6450	.995	P. E., F. D.
6916	" 27/19-23	2	En	62-72	6323	6421	.918	P. E., F. D.
6917	" 28/06-10	1	En	59-72	6295	6381	.936	P. E., F. D.
6918	Mar 4/20-24	2	En	68-72				Sys. 2 fail.
6919	" 12/19-24	1	En	71	6490	6533	.944	
6920	" 13/05-10	2	En	61-72				Diff. PSD amp.
6921	" 13/12-17	1	En	63-72	6499	6562	.954	
6922	" 18/00-04	2	En	60-72				Diff. PSD amp.
6923	" 19/00-04	1	En	59-71	6418	6482	.942	Small F. D.
6924	" 20/19-24	1	En	59-72	6320	6395	.907	Small F. D.
6925	" 21/02-07	3	En	59-72	6260	6426	.908	Small F. D.
6926	" 21/10-15	1	En	59-72	6302	6367	.913	
6927	" 21/18-22	3	En	57-72	6371	6405	.941	
6928	" 22/02-07	1	En	60-70	6337	6452	.947	
6929	" 22/21-23/01	1	En	62-72	6408	6505	.953	
6930	" 23/21-24/02	1	En	59-72	6341	6469	.950	
6931	" 24/04-08	3	En	60-70	6295	6386	.937	F. D., N. M. 6%
6932	" 25/01-06	1	En	59-76	6016	6146	.856	F. D.
6933	" 27/18-23	1	En	56-72	6186	6264	.863	F. D.
6934	" 28/03-08	3	En	61-72	6227	6338	.880	F. D.
6935	" 28/14-19	1	En	59-70	6297	6364	.900	F. D.
6936A	" 30/00-01	1	E	117-192				Aircraft malfunction
6936B	" 30/13-18	1	En	60-72	6787	6800	2.128	H. E. P. E., N. M. max 1330 U. T.
6937	" 30/21-31/02	3	En	58-82	6698	6708	1.806	H. E. P. E.
6938	Apr 2/20-3/01	1	En	59-77	6416	6500	1.042	Decay P. E.
6939	" 11/20-12/01	1	En	58-73	6473	6565	.971	Begin P. E.
6940	" 12/17-21	1	En	62-72	6534	6513	1.087	P. E., F. D. begin.
6941	" 13/01-05	3	En	59-72	6374	6462	1.119	P. E., F. D.
6942	" 15/01-05	1	En	60-72	6238	6331	.908	P. E., F. D.
6943	" 15/13-18	3	En	58-79	6245	6339	.885	P. E., F. D.

<u>Flight</u>	<u>Date / U. T.</u>	<u>Sys.</u> ¹	<u>Loc.</u> ²	<u>Crusing Pressure, g/cm²</u> ²	<u>Deep River</u>	<u>Inuvik</u>	<u>2-10 MeV Flux³</u>	<u>Comments⁴</u>
6944	Apr 15/21-16/02 ^h	1	En	60-87	6269	6347	.892	
6945	" 18/14-19	3	En	61-88	6295	6373	.878	
6946	" 21/20-22/01	1	En	60-92	6420	6493	.923	
6947	" 22/12-17	3	En	60-92	6273	6318	.881	Small F. D.
6948	" 29/19-24	1	En	64-87	6285	6263	.891	F. D., N. M. 5%
6949	May 2/22-3/03	3	En	64-92	6119	6270	.848	
6950	" 8/20	3						Aborted
6951	" 9/19	1						Aborted
6952	" 12/19-24	3	En	72-92	6216	6328	.850	
6953	" 15/19-24	1	Es	72-92	5868	5977	.744	F. D., $P_C = 1$ GV
6954	" 22/19-24	1	Es	72-92	6280	6331	.889	
6955	" 23/19-23	1	Es	71-150	6257	6367	1.014(72 ms) {Hi gain test}	{gain 1.1 x}
6957	Jun 2/21 ¹ -3/00 ¹	1	En	91-72	6257	6367	.864	
6958	" 5/20 ¹ -6/00 ¹	3	En	83-64	6311	6360	.881	
6959	" 11/20-24	3	En	94-61	6062	6121	.802	F. D., N. M. 6%
6961	" 19/20-23 ¹	1	Anc	71	5992	6051	.819	1 GV
6962	" 23/20-23 ¹	1	En	74-62	6085	6204	.919	High gain test
6963	Jul 2/19-23 ¹	1	En	91-68	6195	6245	.840	
6964	" 7/23-24	3	En	71	6231	6294	.846	
6965	" 14/18-20	3	En	71-68	6087	6193	.790	
6966	" 18/20-21	1	En	75-71	6221	6267	.841	
6967	" 21/18-20 ¹	1	En	71-68	6184	6216	.851	
6968	Aug. 1/22-2/01 ¹	3	En	75-71	6248	6336	.844	
6969	" 6/20 ¹ -24	1	En	71-64	6230	6331	.840	
6970	" 8/20-23	3	En	71	6243	6368	.838	
6971	" 11/20 ¹ -23 ¹	1	En	71-62	6260	6382	.865	
6972	" 14/20 ¹ -23 ¹	1	En	71-63	6286	6401	.858	
6973	" 18/20-23	3	En	71-62	6316	6385	.875	
6974	" 21/20-23	3	En	76-65	6385	6407	.881	
6975	" 25/20-23	1	En	73-63	6357	6395	.879	
6976	" 29/20-23	3	En	72-61	6359	6415	.883	

<u>Flight</u>	<u>Date / U. T.</u>	<u>Sys.</u> ¹	<u>Loc.</u> ²	<u>Cruising Pressure, g/cm²</u>	<u>Deep River</u>	<u>Inuvik</u>	<u>2-10 MeV Flux³</u>	<u>Comments⁴</u>
6977	Sep 2/20 ¹ ₄ -23 ^h _h	1	En	71-65	6404	6470	.906	
6978	" 5/20-24	3	En	72-57	6300	6368	.883	
6980	" 11/20 ¹ ₄ -24	1	En	71-58	6389	6449	.873	
6981	" 15/18-22	1	En	71-61	6325	6439	.883	
6982	" 18/20-23 ¹ ₂	3	En	71-59	6373	6436	.857	
6983	" 23/21-23 ¹ ₂	1	En	71-68	6341	6474	.865	
6984	" 25/20-26/01	3	En	71-56	6404	6511	.897	P. E., Exp 41, >60 at bkg.
6985	" 27/21 ¹ ₂ -24	3	En	71-65	6464	6550	.911	
6986	Oct 1/20-22 ¹ ₂	3	En	71-61	6245	6323	.902	Recov. ED.(11/28-30)
6987	" 10/20-24	1	En	71	6359	6430	.883	Radiation Sampling
6988	" 17/19 ¹ ₂ -23	1	En	71	6402	6537	.906	Radiation Sampling
6989	" 20/20 ¹ ₂ -21/01	3	En	71	6433	6512	.909	
6990	" 21/20-24	1	En	71	6443	6523	.912	
6991	" 27/22-28/02	1	En	91-71	6390	6530	.875	
6992	" 29/22-30/01	1	En	91-71	6424	6502	.898	
6993	Nov 2/23-3/03	3	En	91-71	6380	6489	1.020	P. E.
6994	" 3/06-10	1	En	71	6369	6478	.939	P. E.
6995	" 5/21-6/00 ¹ ₂	1	En	71	6411	6491	.886	
6996	" 7/22-8/03	1	En	81-71	6328	6472	.891	
6997	" 14/21 ¹ ₂ -15/01 ¹ ₂	3	En	91-71	6461	6582	.899	
6998	" 18/22-19/01 ¹ ₂	1	En	91-71	6429	6582	.921	
6999	" 19/06 ¹ ₂ -11	3	En	91-71	6442	6612	.910	
69100	" 21/04 ¹ ₂ -09	1	En	71	6510	6611	.919	
69101	" 21/15-19	3	En	74-71	6537	6603	.898	
69102	" 22/01-04 ¹ ₂	1	En	71	6567	6646	.936	
69103	" 24/14-18	1	En	71	6440	6535	.910	
69104	Dec 3/21 ¹ ₂ -4/00 ¹ ₂	1	En	475-71	6299	6430	H. A. 911	Step Flight
69105	" 10/21 ¹ ₂ -11/01 ¹ ₂	3	En	71	6347	6453	.885	
69106	" 12/21 ¹ ₄ -24	3	En	475-71	6382	6462	H. A. 894	Step Flight

<u>Flight</u>	<u>Date / U. T.</u>	<u>Sys.</u> ¹	<u>Loc.</u> ²	<u>Cruising Pressure,</u> <u>g/cm²</u>	<u>Deep River</u>	<u>Inuvik</u>	<u>2-10 MeV Flux</u> ³	<u>Comments</u> ⁴
(1970)								
7001	Jan 22/21-22/01 ^h	3	En	71-56	6424	6473	.906	
7002	" 26/22-23/01	1	En	71-60	6445	6573	.923	
7003	" 29/22-30/02	3	En	71-62	6325	6410	.920	P. E.
7005	" 31/22-1/02	1	En	71-63	6329	6434	.894	P. E.
7008	Feb 4/21-3/01	3	En	71-59	6354	6466	.897	
7009	" 9/22-10/01 ^h	3	En	71-64	6448	6562	.911	
7010	" 11/21-12/01	3	En	71-62	6452	6546	.929	
7011	" 13/21-14/01	3	En	71-64	6433	6525	.915	
7012	" 20/22-21/01	1	En	71-58	6532	6633	.957	
7013	" 24/21-25/01	1	En	79-57	6489	6623	.979	
7014	" 27/20-28/01	1	En	71-	6466	6569	.947	
7015	Mar 4/21-5/01 ^h	1	En	79-	6435	6580	.910	
7018	" 27/21-28/04	1	En	71-63	6367	6457	.891	
7019	Apr 1/02-05 ^h	1	En	71-61	6100	6306	.841	F. D. (3/31)
7020	" 2/21-3/01	3	En	77-63	6296	6470	.881	F. D.
7021	" 3/22-4/01 ^h	1	En	71-59	6314	6487	.895	
7023	" 8/20-9/00 ^h	3	En	74-61	6400	6514	.906	
7024	" 11/00-01	3	En	71-68	6262	6338	.861	
7025	" 16/19-24	1	En	78-56	6237	6360	.868	
7026	" 17/20-18/01	1	En	78-59	6284	6348	.883	
7028	" 21/21-22/01	1	En	75-61	6368	6496	.900	
7030	" 27/20-24	3	En	71-50	6432	6545	.905	
7031	" 30/21-24	1	En	71-62	6435	6545	.960	
7032	May 4/20-23 ^h	1	En	71-61	6331	6433	.903	
7033	" 13/19-23 ^h	3	En	71-61	6403	6487	.901	
7035	" 20/20-24	3	En	71-62	6343	6445	.889	
7036	" 21/20-24	3	En	72-61	6334	6446	.894	
7038	" 27/20-23 ^h	1	En	71-63	6381	6486	.913	
7039	" 28/20-24	1	En	73-59	6370	6425	.913	

Flight	Date / U. T.	Sys. ¹	Loc. ²	Cruising			2-10 MeV Flux ³	Comments ⁴
				Pressure, g/cm ²	Deep River	Inuvik		
7040	Jun 1/20-24 ^h	1	En	71-61	6194	6291	.863	F. D., N. M. 4%
7041	" 3/20-24	1	En	73-61	6162	6225	.829	F. D.
7042	" 8/20-23 ¹ ₂	3	En	75-71	6198	6270	.849	
7043	" 12/20 ¹ ₂ -24	1	En	78-71	6248	6338	.839	
7044	" 17/20-23 ¹ ₂	1	En	73-71	6182	6276	.857	F. D., N. M. 4%
7045	" 19/15-17	1	En	71-65	6043	6164	.803	
7046	" 26/19 ¹ ₂ -22	1	En	91-64	6261	6352	.904	
7047	" 30/14-17	3	En	71-70	6261	6354	.898	
7048	Jul 2/20 ¹ ₂ -24	1	En	71	6083	6218	.821	
7049	" 4/21-24	1	En	75-61	6128	6275	.824	
7050	" 6/21-7/00 ¹ ₂	1	En	75-59	6166	6296	.837	
7051	" 10/21-11/01	3	En	75-59	6258	6366	.865	
7052	" 15/21-16/03	3	En	75-57	6306	6416	.891	
7053	" 17/22 ¹ ₂ -18/00 ¹ ₂	3	En	71-68	6285	6396	.882	
7054	" 20/15-17 ¹ ₂	3	En	91-71	6304	6391	.866	P. E., Expl. 41, >60 MeV bkg.
7056	" 20/23-21/01	3	En	71-64	6316	6431	.899	P. E., Expl. 41 >60 MeV bkg.
7057	" 22/02 ¹ ₄ -04	1	En	71-64	6288	6376	.875	P. E., Expl. 41 >60 MeV bkg.
7058	" 22/04-07 ¹ ₂	3	En	79-57	6296	6379	.881	P. E., Expl. 41 >60 MeV bkg.
7059	" 22/21 ¹ ₂ -23/01 ¹ ₂	3	En	75-71	6304	6433	.877	P. E., Expl. 41 >60 MeV bkg.
7060	" 23/20 ¹ ₂ -23	3	En	78-62	6185	6283	.884	F. D., N. M. 2%
7061	" 24/00 ¹ ₂ -03	1	En	71	6236	6280	.834	P. E., F. D.
7062	" 25/00-02	3	En	71-64	5976	6050	.838	F. D., declining
7063	" 25/02-06	1	En	75-61	5920	6000	.775	F. D., N. M. 7%
7065	Aug 4/22-5/02	3	En	71	6269	6390	.853	
7066	" 7/21-22/01	3	En	79-71	6370	6447	.906	
7067	" 11/21 ¹ ₂ -12/01	3	En	71	6380	6439	.880	
7068	" 14/15-19	1	En	71	6370	6434	.880	
7069	" 15/15 ¹ ₂ -19	3	En	71-63	6351	6406	.860	
7070	" 16/15-18	1	En	75-71	6259	6396	.882	
7071	" 19/19-20 ¹ ₂	3	Es	91-61	6283	6355	.822	$P_c \geq 1$ GV
7072	" 20/22-21/02	1	En	78-69	6276	6350	.860	

Flight	Date / U. T.	Sys. ¹	Loc. ²	Cruising		Deep	Inuvik	2-10 MeV	Comments ⁴
				Pressure, g/cm ²	Flux ³				
7075	Sep 23/19 $\frac{1}{2}$ -23 $\frac{1}{2}$ ^h	3	En	92-59	6466	6602		.926	
7076	" 29/18 $\frac{1}{2}$ -23 $\frac{1}{2}$	1	En	92-61	6521	6617		.969	
7077	" 30/17 $\frac{1}{2}$ -21 $\frac{1}{2}$	3	En	92-64	6514	6553		.934	
7078	Oct 7/19 $\frac{1}{4}$ -23 $\frac{1}{4}$	1	En	92-64	6440	6522		.933	
7079	" 8/20 $\frac{1}{2}$ -24	3	En	92-64	6462	6566		.921	
7080	" 12/21 $\frac{1}{4}$ -01 $\frac{1}{4}$	1	En	72-62	6514	6634		.995	
7081	" 28/20 $\frac{1}{2}$ -22 $\frac{3}{4}$	1	En	92-72	6434	6515		.962	
7082	Nov 4/20 $\frac{3}{4}$ -01	3	Es	152,118	Latitude flights			.7-1.7 GV	
7083	" 5/22-02 $\frac{1}{4}$	4	Es	92,62	Latitude flights			.7-1.7 GV	
7085	" 13/20 $\frac{1}{2}$ -22 $\frac{1}{2}$	3	E	73-62	6339	6429		.911	
7086	" 15/10 $\frac{1}{2}$ -11	3	En	75-72	6395	6473		.905	
7087	" 16/03 $\frac{1}{4}$ -05 $\frac{1}{2}$	1	En	72	6370	6498		.952	
7091	Dec 7/22 $\frac{1}{2}$ -01 $\frac{1}{2}$	4	En	78-70	6512	6527		.947	
7092	" 10/22-00 $\frac{1}{2}$	4	En	80-72	6442	6556		.953	
7093	" 14/21 $\frac{3}{4}$ -01	4	En	72-59	6312	6407		.902	F. D., N. M. 3 $\frac{1}{2}$ %
(1971)									
7101	Jan 4/22-04	1	En	71-75	6500	6604	1.000		
7102	" 8/22-01 $\frac{1}{2}$	1	En	71-75	6607	6781	.993		
7103	" 13/23-02	1	En	71-75	6634	6811	1.042		
7105	" 20/22-01 $\frac{1}{2}$	3	En	69-84	6359	6488	.919		
7106	" 22/22-01 $\frac{1}{2}$	1	En	72	6389	6528	.951		
7107	" 25/04 $\frac{1}{4}$ -08 $\frac{1}{2}$	3	En	72-118	6520	6657	2.313-1.962	H. E. P. E, N. M. 12%, 00 U. T.	
7108	" 25/08 $\frac{1}{4}$ -12 $\frac{1}{2}$	1	En	72-87	6512	6635	1.963-1.773	P. E.	
7109	Feb 2/22-01 $\frac{1}{2}$	3	En	61-72	6611	6774	1.032		
7110	" 5/22-01 $\frac{1}{2}$	1	En	72-84	6649	6746	1.036		
7111	" 9/22-02	4	En	62-72	6595	6691	1.040		
7112	" 12/22-02	3	En	59-76	6610	6770	1.037		

<u>Flight</u>	<u>Date / U. T.</u>	<u>Sys.</u> ¹	<u>Loc.</u> ²	<u>Cruising</u>		<u>Inuvik</u>	<u>2-10 MeV</u>	<u>Comments</u> ⁴
				<u>Pressure,</u> <u>g/cm²</u>	<u>Deep</u> <u>River</u>			
7114	Mar 4/22 ^{1/2} -01 ^{1/2}	1	En	69-72	6657	6767	1.044	
7115	" 9/20 ^{1/2} -24	4	En	72	6702	6800	1.049	
7116	" 11/20 ^{1/2} -24	1	En	72	6627	6728	1.029	
7117	" 18/20 ^{1/2} -23 ^{3/4}	1	En	68-72	6619	6717	1.023	
7118	" 25/20 ^{1/2} -23 ^{3/4}	1	En	68-72	6607	6707	1.038	
7119	" 26/20 ^{1/2} -21	4	En	72	6612	6719	1.028	
7120	" 27/20 ^{1/2} -23 ^{1/4}	3	En	72	6622	6748	1.058	
7121	Apr 8/20 ^{1/2} -24	3	En	65-75	6686	6846	1.103	
7122	" 9/21 ^{1/2} -00 ^{1/2}	1	En	61-72	6684	6771	1.090	
7123	" 13/20 ^{1/2} -23 ^{3/4}	1	En	72	6719	6821	1.124	Partial tape data
7124	" 14/20 ^{1/2} -24	3	En	59-68	6548	6733	1.075	F. D. during flight
7125	" 15/20 ^{1/2} -23 ^{3/4}	4	En	70-72	6506	6619	1.040	F. D. , N. M. 3%
7126	" 20/20 ^{1/2} -24	4	En	72	6629	6738	1.062	
7127	" 21/20 ^{1/2} -23 ^{1/2}	1	En	72,211,307	6651	6741 H. A.	1.078	Step flight
7128	" 22/20 ^{1/2} -23 ^{1/2}	3	En	72-92	6700	6734	1.071	
7129	May 4/19-19 ^{1/2}	1	En	72	6714	6763	1.077	
7130	" 5/19 ^{1/2} -22 ^{1/2}	3	En	72,211,307	6721	6775 H. A.	1.095	Step flight
7131	" 11/18 ^{1/2} -22 ^{1/2}	3	En	72,118,211,307	6728	6790	1.105	
7132	" 12/19 ^{1/2} -22 ^{1/2}	1	En	72,211,307	6664	6803	1.113	
7133	" 12/19 ^{1/2} -22 ^{1/2}	1	En	72,211,307	6737	6739 H. A.	1.064	Step flight
7134	" 13/21 ^{1/2} -01 ^{1/2}	3	En	66-72	6696	6720	1.096	
7135	" 18/19 ^{1/2} -21 ^{1/2}	4	En	72-92	6544	6639	1.032	
7136	" 19/18 ^{1/2} -22 ^{1/2}	3	En	72-92,211	6589	6688 H. A.	1.041	Step flight
7137	" 24/19 ^{1/2} -20 ^{1/2}	3	E	92	6779	6862	1.063	
7138	" 25/18 ^{1/2} -19 ^{1/2}	4	En	92	6792	6857	1.058	
7139	" 26/19 ^{1/2} -22 ^{1/2}	3	En	62,92	6789	6938 H. A.	1.183	Step flight
7140	Jun 1/19-23 ^{1/4}	3	En	62,92	6772	6871 H. A.	1.124	Step flight
7142	" 3/18 ^{1/2} -23 ^{1/2}	3	Es	118,152	See altitude flights			.5-1.7 GV Step flight
7143	" 9/18 ^{1/2} -21	1	En	118,307	See altitude flights			Step flight
7144	" 16/19 ^{1/2} -21 ^{1/2}	3	En	72-80,211,307	6857	6890 H. A.	1.125	Step flight
7146	" 24/19 ^{1/2} -22 ^{1/4}	1	En	72-76	6856	6913	1.180	
7147	" 25/18 ^{1/2} -22 ^{1/4}	1	En	72,118,211,307	6886	6934 H. A.	1.214	Step flight
7148	" 28/18 ^{1/2} -22 ^{1/4}	3	En	72,118,211,294	6901	7017 H. A.	1.199	Step flight
7149	" 29/18 ^{1/2} -21 ^{1/2}	1	En	72-92,118,211,307	6866	6943 H. A.	1.188	Step Flight

NOTES:

1. Flight Systems

Systems 1 = 1966-1

2 = 1966-2, 2' = detector 2 with other electronics

3 = 1968-3

3' = 1966-3

2. Symbols

Bed = Bedford, Maine to Greenland

Pres = Presque 'ile, Maine to Ft. Churchill

E = Eielson A. F. B., Alaska (P_c = 0.5 GV)En = North of Eielson (P_c between 0.0 and 0.5 GV)Es = South of Eielson (P_c between 0.5 and 1.0 GV)Anc = Anchorage, Alaska (P_c = 1.0 GV)Abq = Albuquerque, N. M. (P_c = 4.3 GV)Pan = Panama, Canal Zone (P_c = 12.0 GV)M = Loring A. F. B., Maine (P_c = 1.0 GV)Fch = Ft. Churchill, Manitoba (P_c = 0.2 GV)3. 2-10 MeV neutron flux $n/cm^2\cdot sec.$ at transition maximum

F. D. - Forbush Decrease

P. E. - Solar Proton event, observed by Explorer 34 or Explorer 41

H. E. P. E. - Proton Event during which an increase of sealevel neutron monitors has occurred

N. M. - High latitude sea-level neutron monitors. Where indicated % decrease.

H. A. - High Altitude value in step-flight

TABLE IV

b. STEP FLIGHTS

<u>Flight</u>	<u>Date / U. T.</u>	<u>Sys.</u>	<u>Pressure</u> <u>g/cm²</u>	<u>Deep</u> <u>River</u>	<u>Inuvik</u>	<u>2-10 MeV</u> <u>Flux</u>
(1968)						
6804	Mar	3/ 23 $\frac{3}{4}$ - 00 $\frac{1}{2}$	1	267	6637	.442
		4/ 01 - 01 $\frac{3}{4}$		244		.514
(1969)						
69104	Dec	3/ 21 $\frac{1}{2}$ - 22	1	72	6299	.911
		22 - 22 $\frac{1}{4}$		118		.797
		22 $\frac{1}{2}$ - 22 $\frac{3}{4}$		189		.543
		23 - 23 $\frac{3}{4}$		307		.291
		23 $\frac{3}{4}$ - 00 $\frac{1}{2}$		475		.094
69106	Dec	12/ 21 $\frac{1}{4}$ - 21 $\frac{3}{4}$	3	72	6382	.894
		22 $\frac{1}{4}$ - 22 $\frac{1}{2}$		118		.830
		22 $\frac{1}{2}$ - 23 $\frac{1}{4}$		189		.567
		23 $\frac{1}{4}$ - 24		307		.279
		13/ 00 - 00 $\frac{1}{2}$		475		.094

<u>Flight</u>		<u>Date / U. T.</u>	<u>Sys.</u>	<u>Pressure</u> <u>g/cm²</u>	<u>Deep</u> <u>River</u>	<u>Inuvik</u>	<u>2-10 MeV</u> <u>Flux</u>
		(1971)					
7127	Apr	1 / 20 $\frac{1}{4}$ - 21	1	72	6651	6741	1.085
		21 $\frac{1}{4}$ - 21 $\frac{1}{2}$		307			.346
		21 $\frac{1}{2}$ - 22 $\frac{1}{4}$		211			.590
		23 - 23 $\frac{1}{2}$		72			1.070
7130	May	5 / 19 $\frac{1}{4}$ - 20 $\frac{1}{4}$	3	307	6721	6775	.342
		20 $\frac{1}{2}$ - 21		211			.579
		21 $\frac{1}{2}$ - 22 $\frac{1}{2}$		72			1.095
7131	May	11 / 18 $\frac{3}{4}$ - 19 $\frac{1}{4}$	1	118	6728	6790	.909
		19 $\frac{1}{2}$ - 20 $\frac{1}{4}$		307			.333
		20 $\frac{1}{2}$ - 21		211			.607
		22 - 22 $\frac{3}{4}$		72			1.105
7133	May	12 / 19 - 20	1	307	6694	6739	.343
		20 $\frac{1}{4}$ - 21		211			.609
		21 $\frac{1}{4}$ - 22 $\frac{3}{4}$		72			1.064
7136	May	19 / 18 $\frac{3}{4}$ - 19 $\frac{1}{4}$	3	72-92	6589	6688	1.039
		21 - 21 $\frac{1}{2}$		211			.565
		22 - 22 $\frac{1}{2}$		72-92			1.042
7139	May	26 / 19 $\frac{1}{4}$ - 21 $\frac{1}{4}$	3	92	6789	6938	1.083
		21 $\frac{1}{2}$ - 22 $\frac{1}{2}$		72			1.183

<u>Flight</u>		<u>Date / U. T.</u>	<u>Sys.</u>	<u>Pressure</u> <u>g/cm²</u>	<u>Deep</u> <u>River</u>	<u>Inuvik</u>	<u>2-10 MeV</u> <u>Flux</u>
(1971)							
7140	Jun	1 / 19 - 21 $\frac{3}{4}$	3	92	6772	6871	1.073
		22 $\frac{1}{4}$ - 23 $\frac{1}{4}$		72			1.124
7142	Jun	3 / 18 $\frac{1}{2}$ - 21 $\frac{1}{4}$	3	152	6686	6799	.803
		21 $\frac{1}{2}$ - 23 $\frac{1}{2}$		118			.943
7143	Jun	9 / 18 $\frac{1}{2}$ - 19	1	118	6775	6855	1.003
		19 $\frac{1}{2}$ - 20		307			.361
		20 $\frac{1}{2}$ - 21		118			.992
7144	Jun	16 / 19 $\frac{1}{4}$ - 20 $\frac{1}{4}$	3	307	6857	6890	.348
		20 $\frac{1}{4}$ - 21		211			.627
		21 $\frac{1}{4}$ - 21 $\frac{3}{4}$		72-80			1.125
7147	Jun	25 / 18 - 19	1	118	6886	6934	1.014
		19 $\frac{1}{4}$ - 20		307			.358
		20 $\frac{1}{4}$ - 20 $\frac{3}{4}$		211			.643
		21 $\frac{1}{2}$ - 22 $\frac{1}{4}$		72			1.214
7148	Jun	28 / 18 $\frac{1}{2}$ - 19	3	118	6901	7017	1.041
		19 $\frac{1}{4}$ - 20		294			.381
		20 $\frac{1}{4}$ - 20 $\frac{3}{4}$		211			.721
		21 $\frac{1}{4}$ - 22 $\frac{1}{4}$		72			1.199
7149	Jun	29 / 18 - 18 $\frac{1}{2}$	1	118	6866	6943	1.012
		18 $\frac{3}{4}$ - 19 $\frac{1}{2}$		307			.379
		19 $\frac{1}{2}$ - 20		211			.627
		20 - 21 $\frac{1}{2}$		72-92			1.188

B. Conversion of Counting Rates to Flux

1. Method. - The spectral unfolding procedures that were used in the calibrations of the detector (section IC.2b) were somewhat unstable, when applied to the counting rates of a seven channel analyzer. A method which produced smaller variances began with a best fit ¹⁴_g analytic spectrum, to which were then added the residual neutrons necessary for reproducing observed counting rates. The details of this procedure follows:

The counting rates in the seven channels, C_i , were related to the differential neutron flux, $N(E)$ by

$$C_i = \int_{E_{\text{thresh}}}^{E_{\text{max}}} N(E) R_i(E) dE, \quad i=1 \text{ to } 7, \quad 2$$

where $R_i(E)$ was the response function of the i^{th} channel to neutrons of energy, E , and the upper energy cutoff, E_{max} , was taken to be 80 MeV for the atmospheric spectrum. The contribution to the counting rates was negligible past this energy. Several analytic forms for $N(E)$ were tested in a weighted least squares program operating on the seven equations, numbered 2. A power law in energy,

$$N(E) = AE^{-n} \quad 3$$

was the most satisfactory, above 2 MeV. With A and n chosen to be constant, the value of n that gave the least variance was chosen. The counting rates from the best fitting spectrum were then reconstituted and the recalculated counting rates subtracted from the observed counting rates. The neutron flux corresponding to these residual counts was then calculated and the additional neutrons added to the first neutron spectrum.

2. Contribution of the > 10 MeV neutrons to the counting rate. - Table V gives several examples of spectral analysis of the flight data. Among other things, it lists the contribution of neutrons above 10 MeV to the counting rates in the seven pulse amplitude channels. This contribution was observed to be about 18% of the total, if we assumed that the spectral shape did not change above 10 MeV. Of course, the spectral shape is not likely to remain constant, but there is no consistent indication of the actual

TABLE V

SPECTRAL ANALYSIS OF THE WEIGHTED MEAN OF ALL DATA IN THE
 SEVEN NEUTRON CHANNELS: a. TRANSITION MAXIMUM, BALLOON,
 b. HIGH ALTITUDE BALLOON, c. AIRPLANE

Pulse Ht. Channel	<u>1</u>	<u>2</u>	<u>3</u>	<u>4</u>	<u>5</u>	<u>6</u>	<u>7</u>	<u>A</u>	<u>n</u>	1-10 MeV	2-10 Flux MeV
Pfotzer Maximum											
Counts/min											
Observed:	74.7	31.9	18.6	12.8	15.6	11.6	9.4	.487	1.17	1.03	.609
Recalculated: counting rates from least squares spectrum											
1-10 MeV	57.5	29.3	15.4	11.4	10.9	6.4	2.3				
10-80 MeV	6.6	3.8	3.1	3.8	5.6	4.6	3.6				
1-1/2-2 MeV	11.4	.1									
High Altitude											
Counts/min											
Observed	69.0	31.1	18.5	12.9	16.6	12.3	9.0	.410	1.08	.96	.587
Recalculated: counting rates from least squares spectrum											
1-10 MeV	53.1	28.0	15.0	11.2	10.8	6.5	2.4				
10-80 MeV	7.2	4.1	3.4	4.2	6.2	5.1	3.9				
1-1/2-2 MeV	8.5	.1									
Airplane											
Counts/min											
Observed	75.0	33.4	19.1	12.7	15.1	11.0	8.6	.545	1.23	.93	.539
Recalculated: counting rates from least squares spectrum											
1-10 MeV	60.6	30.3	15.7	11.5	10.0	6.4	2.3				
10-80 MeV	6.2	3.5	3.0	3.5	5.3	4.4	3.4				
1-1/2-2 MeV	8.1	.1									

form above 10 MeV in the literature^{16,27-30}, and the phoswich is limited by the 10 MeV upper cutoff. To estimate the possible error in using a single n between 1 and 80 MeV, we tested the effect of changing the spectral index above 10 MeV from $n = 1.2$ to $n = 2$, an overestimate of the spread. The effect on the 1-10 MeV neutrons was to increase the flux by 4% and decrease the spectral index by 0.16.

C. Calculation of Attenuation Length

The counting rates in the region between 200 and 700 mb are reported in this paper in terms of a single exponential

$$C(p) = C_0 \exp(-p/\lambda)$$

4

A more complex spatial variation would not be observable with the statistics of balloon ascent. The constants, C_0 and λ were selected to maximize the likelihood function

$$L = \sum_{i=1}^M (C_0 \exp(-P_i/\lambda))^{C_i} \exp(-C_0 \exp(-P_i/\lambda))/C_i^! \quad 5$$

IV. RESULTS OF OBSERVATIONS

A. Results of Balloon Flights

1. Flight profiles. -In figure 6, the neutron counting rates are plotted vs atmospheric depth for several typical balloon flights. Figures 6a and 6b illustrate the decline in the counting rates with increasing solar activity, an effect most dramatic at high latitudes and in the upper atmosphere. Figure 6c, the profiles of two flights from Palestine, Texas, show the shielding effect of the earth's magnetic field, which excludes primaries below about 4.5 GV at this location. We have also plotted in figure 6, the altitude distribution of the total events channel, which more closely approximates the counting rate of a hydrocarbon-clad ion chamber.

2. Fast neutron spectrum. - In Table V, we have listed the relative counting rates of the seven pulse height channels, averaged over all high latitude flight data, at $50\text{-}90 \text{ g/cm}^2$, the transition maximum, and at 2-5 mb, floating altitude on many of the flights. The fast neutron spectrum, calculated according to the method of section IV.1., is also given. At the transition maximum, n , the index of the power law in energy,

$+1.13$

$+1.12$

was $1.17\text{-}2.20$. At high altitude, the value of n was $1.08\text{-}2.0$. In each case, there was an additional contribution from 1-2 MeV, as indicated in Table V. The difference between the high altitude and the transition maximum values was real since the relative uncertainty in the two values of n was less than the absolute uncertainty, which results from statistical spread, from goodness of fit, and from uncertainties in the calibration and in the contribution of neutrons $> 10 \text{ MeV}$. Individual fluxes for all flights as well as spectra for system I flights are shown in Table III. The value of n was not observed to change within the experimental uncertainties from solar minimum to solar maximum and from pole to equator.

3. Attenuation length. - Table III also lists the values of λ calculated from the neutron counting rates as well as from total events, which displayed similar attenuation lengths with much better statistics. Table VI summarizes the observations of attenuation length, including earlier results obtained during solar minimum.

TABLE VI

ATTENUATION LENGTH OF NEUTRONS AND OF TOTAL EVENTS
AT DIFFERENT GEOMAGNETIC CUTOFF RIGIDITIES

Location	Fort Churchill, Manitoba	Lynn Lake, Manitoba	Palestine, Texas	Hyderabad, India
P_c	0.2	0.4	4.5	1.7
Number of flights	8	6	5	2
Solar epoch	min. to max.	max.	min. to max.	min.
λ , neutrons (mb)	165 ± 10	172 ± 13	181 ± 28	215 ± 15
λ , total events (mb)	164 ± 5	168 ± 9	167 ± 5	200 ± 4

At high latitude, where time variations would be most observable, we found no consistent trend in the attenuation length with solar activity. The increase in attenuation length with cutoff rigidity, reported much earlier by the NYU group for slow neutrons⁵, was also observed for fast neutrons.

4. Solar modulation. - Fig. 7 and fig. 8 summarize the change in the high latitude neutron flux between 1965 and 1968. Fig. 7 is a series of regression curves, at different pressures, of the 2-10 MeV neutron flux vs. the counting rate of the Deep River neutron monitor (DRNM). Also shown are calculated fluxes at the top of the atmosphere, which we shall discuss later. Fig. 8 presents the same data used in deriving the curves in fig. 7, in terms of altitude profiles of the 1-10 MeV neutron flux at various values of DRNM.

Solar cycle variations at Palestine, Texas, were much smaller and more difficult to discern since there was little data at the transition maximum, where time variations can be determined without correction for the contributions from pressure differences. Between 1964 and 1970, the 1-10 MeV flux at the transition maximum declined from around

1.18 neutrons/cm²-sec, a value approximately half that at high latitude, to a flux 15±3% lower. At around 4 mb, the difference was 12±6%. These numbers have the additional uncertainty that only one of the detectors flown in Palestine was crosscalibrated in flight and none were calibrated with monoenergetic neutrons.

5. Time variations at floating altitude. - Most of the balloon flights occurred during undisturbed periods, when the earth-based neutron monitors recorded excursions of less than 1%. During some of the flights, particularly in 1968, class 1 and class 2 flares erupted on the surface of the sun, but these were not followed by proton events. The data at floating altitude was equally uneventful. For example, the total events counting rates, which were not statistically limited in accuracy, varied, in flights at the transition maximum, by less than 2%, temperature corrected, and by 3%, without correction. At high altitude, the variations were as much as 6-7%, but this is possibly because the total events channel at 2-5 mb is a better altimeter than the Wallace and Tiernan pressure gauge. Time variations, however, could not be completely excluded.

Detection of variations in the neutron channels was limited by the statistics, ~±1% per hour for channels 2-7. In two flights, 117 on a geomagnetically disturbed day, and 121, during solar maximum conditions, changes of the order of 4-6% in channels 2-7 occurred. Such changes will

also be reported for several aircraft flights, in which a more direct correlation could be found with changes in the sea level neutron monitors.

In flight 126 from Palestine, Texas, changes due to variations in latitude were observed and could be separated from altitude effects. The differential latitude effect between Palestine, $P = 4.5$ GV, and Carlsbad, New Mexico, $P_c = 5.2$ GV, was approximately 10%/GV for total events and 15%/GV for total neutrons at floating pressure of $35-55 \text{ g/cm}^2$.

6. In-flight calibration of System I vs System II. -Small differences between System 1966-I and 1966-II (System I was not calibrated at ORNL), were observed with laboratory sources. These were considerably larger for the atmospheric spectrum. In the cross-calibration flight, 120, (total events, system II)/(total events, system I), was 1.05; and the ratio, (neutrons, system II)/(neutrons, system I) was 1.19 ± 0.03 . This value was in good agreement with that deduced from aircraft flights. The remaining flight systems measured were within 0-4% of the system II counting rates, as established in aircraft flights.

7. Flights with tissue-equivalent dome. -Table III includes observations made during flights in which the gondola cover was replaced by a 15.4 cm tissue-equivalent dome. This procedure was followed for 111P, 112P, and 115P, which occurred during the same epochs as flights 111, 112, and 114 respectively.

The difference between measurements with and without the dome was most impressive in the altitude profiles, such as those illustrated in figure 9 for two flights only a week apart. It should be noted that the counting rates of the total events channel were only modestly affected by the dome and, at that, only in the upper few hundred mb; whereas the neutron counting rates were considerably attenuated (fig. 9) and the spectrum appreciably hardened (Table III). These features were, in fact, reproduced in a Monte Carlo calculation by Irving of ORNL, who examined the neutron flux inside a spherical shell of hydrocarbon, ID 15 cm,

OD 54cm, when an isotropic flux of neutrons with an E^{-1} spectrum entered the outer boundary. Both neutron flux and spectral index were reduced by the presence of the "phantom".

While attenuation length was not affected by the "phantom", the neutron profiles above the equilibrium region were altered. The neutron flux increased more towards higher altitude and decreased less rapidly toward the top of the atmosphere than the "free-air" flux. In fig. 9, the dashed

curves indicate the enhancement of neutrons above 40 mb with the tissue-equivalent dome, as determined from flight 112P (Table III) and high altitude free air flights. We interpret this enhancement as resulting from increased production of neutrons inside the tissue-equivalent dome by the radiation at these altitudes, which is more energetic on the average, than that lower in the atmosphere.

The measurements with the dome are also indicative of the effect of appreciable masses near the detector in any neutron experiment. They convince one of the complexity of the corrections to the neutron flux in both spectrum and numbers, especially when the detector and its associated shields and housing are massive.

B. Results of Aircraft Flights

1. Summary of results, free air flux. - Table IV lists the results of the aircraft measurements yielding data at the high latitude transition maximum.

The counting rates of two sea level neutron monitors³¹ are also given for each flight: Deep River ($P_c = 1.02$ GV) was used to monitor the primary

radiation, for the purpose of comparing aircraft with balloon flight results. Inuvik ($P_c = 0.18$ GV) was most appropriate for monitoring the higher energy

primaries to which the aircraft detector was exposed, since Inuvik happened to be along the path of most of the aircraft flights. The data is presented in terms of the free air flux from which we have eliminated aircraft background.

We evaluated the aircraft background by comparing the counting rates in aircraft and in balloon flights: 1, in the rendezvous between two detectors, in flight 117 (balloon) and flight 6702 (aircraft), and 2, in regression curves of fast neutron counting rates vs. DRNM. Fig. 10 shows the counting rates of system 1966-II in channels 2-7 vs. DRNM for both balloon and aircraft flights. The two sets of data fell on different curves. The aircraft data lying $10 \pm 2.5\%$ above the balloon counting rates. This additional background also caused a slightly softer spectrum than that measured in balloon flights, so that $n_{aircraft}$ was 1.23 (Table V).

1b. Normalization of flight systems. - The free air fluxes in Table IV have been normalized to system 1966-II according to the relative response of the various detectors in flight. Systems 1966 III and 1970 IV were indistinguishable in their measurements from System II. For the remaining

detectors, the free-air 2-10 MeV neutron flux, in neutrons/cm²-sec, to the counting rate of channels 2-7, in counts per minute, were:

System 1966-I	0.00654±0.00027
System 1966-II	0.00541
System 1968-III	0.00566±0.00011

The errors quoted here relate only to goodness of fit of the data to the neutron monitor regression curve. According to the flight data, System 1968-III gradually lost about 5% in counting efficiency between 1968 and late 1969. This was corroborated by the response to laboratory neutron sources.

2. Aircraft latitude surveys. - Figs. 11 and 12 summarize the results of the aircraft latitude surveys listed in Table IV. Neutron fluxes are shown vs. cutoff rigidity, which was determined from the Shea and Smart (1968)³⁴ tables of L-interpolated, trajectory derived cutoffs.

The 1965 latitude flight, which circled the globe over both poles, is represented by fig. 11. The neutron counting rates reported by

Sandie et al. (1968)¹⁴ are shown, as well as the fast neutron flux, which has been corrected and normalized to the "free-air" values measured in the solar minimum balloon flights. The normalization factor was 1.10, indicating that more 1-10 MeV neutrons were lost through moderation in the aircraft than were produced in the surrounding material.

Each leg of the pole-to-pole flight is separately indicated in fig. 11. Since most cutoff rigidities were encountered at four different geographic locations, the counting rates observed in the north and south and in the east and west should be along identical curves. The degree to which the curves coincide checks the consistency of describing the data in terms of the given values of P_c . Fig. 11 indicates that the overlap is reasonably good except between 8 and 12 GV, where the counting rates in the Northern and Southern Hemispheres differed appreciably from each other in the vicinity of 160-170° West Longitude. This is apparent in fig. 11. A possible explanation, suggested by Shea and Smart (Private communication, 1971), is that the actual effective cutoffs at low latitude might be displaced from the interpolated values used in fig. 11, as a result of large penumbral effects.

The aircraft latitude flights near the transition maximum covered a period of increasing solar activity in 1968. Figure 12 is a diagram showing the neutron fluxes averaged over the different flights and corrected for pressure and for aircraft background. The background correction, indicated in the graph, was experimentally derived at high latitude only (figure 10). At all other locations, it was necessary to estimate the fraction of the background flux at 0 cutoff that remained when a portion of the total primary incident spectrum below the local cutoff was removed. To determine this fraction, we folded the spectrum of the primaries and

their charged secondaries at the transition maximum⁺ into the cross section for producing neutrons in elements near the average mass number of the surrounding material. The latitude profile of the fractional background could then be constructed. The absolute flux distribution was derived by normalization to the known background at high latitude. The background corrections were of the order of 10%.

3. Latitude variations near the latitude knee. - Table VII summarizes observations of the fast neutron flux at the transition maximum, in the vicinity of the high latitude plateau. The location of the latitude knee, which was determined from the series of aircraft flights between 1967 and 1971, was around 0.4 GV. We recall, from Figure 11, that deeper in the atmos-

sphere, at 250 g/cm^2 , the high latitude plateau extended to 1.5 to 2 GV. This was a consequence of the rapidly diminishing neutron yield of the primaries below 2 GV deeper in the atmosphere. At the transition maximum, where the neutron yield between 0.4 and 2 GV was appreciable, it was instructive to estimate its value from the experimental data. Table VII lists the neutron yield, as well as the observed neutron flux and incident primary flux, between 0.4 and 2 GV, which we require to obtain the neutron yield. Although the latitude variation of the neutron flux vs incident primary flux was known only to within $\pm 30\%$ near the knee, the derived neutron yield could be applied quite usefully in checking calculations of neutron production and in detecting any gross discrepancies in the $< 2 \text{ GeV/nucleon}$ region of incident particle energy. As an example we show in the last column the neutron yield obtained in the indicated rigidity interval from the Monte Carlo program. The observations were well within experimental uncertainties.

⁺ Derived from the internuclear cascade calculation.

TABLE VII

LATITUDE VARIATIONS BELOW 2 GV CUTOFF RIGIDITY
AT THE NEUTRON TRANSITION MAXIMUMLatitude variations below $P_c = 2$ GV at the neutron transition maximum

Epoch	Location or Route	P_c (GV)	Latitude Knee (GV)	%*	%**	neutron yield ⁺ decrease primaries "obs" "calc"
1964-5 (balloon)	Ft. Churchill St. Paul, Minn. Sioux Falls, S. D.	0.2 1.3 1.7		9.3	25 56	1.9±1.0 1.9
5/67 (aircraft)	Greenland- Bedford, Eng.	0.1 2.0	0.6-0.4 8		44	1.1 1.4
1/68-1/71 (aircraft)	Cambridge Bay- Eielson AFB- Anchorage	0.03- 0.4- 1.3		7.2	22	0 0.08 1.4±0.4 1.4

* % of the neutron flux arising from protons below the upper values of P_c in column 2.

** % of primary nucleons between 0.4 GV and the upper value of P_c shown in column 2.

† neutron yield, neutrons/cm² per primary nucleon/cm²-sr, "obs": from neutron and primary data; "calc": derived from Monte Carlo calculation.

4. Time variations at the high latitude transition maximum. -In the broad region between 0 and 0.4 GV and from 50-80 mb, the fast neutron flux from galactic cosmic rays was essentially independent of location, and the fast neutron variations arose principally from modulation of the 1-2 GeV/nucleon

primaries (Light et al., ³²). Figure 13 shows the 2-10 MeV neutron flux vs DRNM for the period August 1965 through 1968, most of the declining phase of cosmic rays during the current solar cycle. The graph includes Forbush decreases and solar particle events, the points with solar contamination

being indicated by a star. The curve in Figure 13 is the best quadratic fit to the data, exclusive of neutrons from solar protons, and clearly indicates the greater modulation of the less energetic primaries monitored by the NYU detector. The RMS deviation from the curve, which was 3%, was somewhat larger than the combined instrumental and statistical uncertainties. It was reduced further by plotting the NYU data vs. the counting rates of neutron monitors with similar asymptotic longitudes of the incoming primaries: i.e. Deep River for the balloon flight data and Inuvik for the aircraft data. The correlation of the airborne detector with the sea-level monitor improved, but certain systematic deviations from the curve remained. These could usually be associated with transient variations and have been discussed in a preliminary paper by Verschell et al.³³, on Forbush decreases.

Following the June 1969 minimum in the monthly average of DRNM, the counting rates deviated significantly from the regression curve of Figure 13. To illustrate, we have plotted, in Figure 14, the neutron fluxes measured in aircraft flights from January 1969 to June 1971 vs. the counting rates of the Inuvik neutron monitor, Inuvik having been chosen since it was along the flight path. The regression curve for the period before June 1969 is also shown. The graph clearly indicates the lag in the recovery of the 1-2 GeV per nucleon component from the June 1969 minimum. Observations of the long term modulation previous to this period, by Simpson and Wang³⁴, tended to indicate that the spectrum of primaries near 1 AU depended only on the depth of modulation, in which event a single regression curve would describe the NYU counting rates vs. Inuvik. More recent observations by Kane and Winckler³⁵, Stoker and Carmichael³⁶, Lockwood et al.³⁷, Schmidt³⁸, and Stoker et al.³⁹, confirm our conclusion that a deviation from the single regression line can and indeed has occurred. The phenomenon was somewhat complicated by spectral variations observed in Forbush decreases and will be discussed in a separate section. Solar particle effects are also discussed later in the report.

5. Results of step flight, altitude variations. -In Figure 15, we summarize the measurements of the neutron flux at different altitudes, from balloon ascent data, taken during periods of varying solar modulation, between 1965 and 1968. Further measurements were made in aircraft in step flights (Table IV). Most of the aircraft data on altitude variations was taken between April and June, 1971. Since there was no data on the free air neutron flux near this time, we used the same background correction that we had observed at the transition maximum for locations deeper in the atmosphere. Earlier balloon measurements have also been plotted in

fig. 7. The two sets of data are not quite comparable since the balloon flights occurred during a different portion of the solar cycle than the aircraft step flights. In addition, the counting statistics in the aircraft flights were much improved over the statistics of the balloon data deep in the atmosphere. While there was some overlap in data between balloon and aircraft measured fluxes, the aircraft counting rates deeper in the atmosphere tended to be about 10% lower than the balloon rates, possibly suggesting that the original 10% correction for aircraft background was unnecessary in the equilibrium region. There is also a small indication that the recovery of the neutron flux toward the values observed in 1966 may have been incomplete in the spring of 1971, at least at the largest values of the Inuvik counting rates. Measurements of free air vs. RB57 aircraft fluxes deep in the atmosphere would be required to resolve these small effects.

In flights 69104 and 69105, where measurements were made down to 475 g/cm^2 , the neutron attenuation length between 200 and 475 g/cm^2 , was found to be 168 g/cm^2 and 160 g/cm^2 , in good agreement with the values derived from balloon flight data.

V. INTRNUCLEAR CASCADE CALCULATION

A. Introduction

1. Production and transport of neutrons. - Since the beginning of the present program, we have investigated ways of extending the scope of our fast neutron measurements by a calculation. The goal has been to develop a capability of reproducing the spatial and energy distribution of the entire flux of neutrons in the atmosphere, given an arbitrary spectrum of primary particles arriving at the earth. Such a study, which involves both the production and transport of neutrons, separates out quite naturally into two energy regions, one above and one below around 20-30 MeV.

In the first region, which begins with the energetic primary, the predominant mode of dissipating energy in nuclear collisions is by particle production. Interactions in this energy range have been successfully described in terms of the "intranuclear cascade"^{40, 41}. In this formulation the incident particle collides with one or more nucleons in the target nucleus. The struck nucleons may escape as "cascade" particles or they may engage in further collisions, leading possibly to additional particle emission. After

no more can escape, an excited nucleus remains. This, the residual nucleus, finally undergoes de-excitation, as often as not by emission of nucleons and fragments. These are the "evaporation" products; they are typically lower in energy than 20-30 MeV. The more energetic cascade particles continue to propagate in further collisions in the atmosphere until the supply is exhausted and the remaining flux of nucleons lie below the energy where production predominates, <20 MeV.

The neutrons below 20 MeV or so constitute the second group. They are the evaporation and low energy cascade products. Their mode of energy loss is mainly by elastic collision, low-level nuclear excitation, and absorption. Their propagation is readily treated by one of the many approximations for the solution of the Boltzmann equation that have been written for computers to solve problems in reactor physics.

2. Previous calculations. - When the present experiment was in its infancy, there was little detailed information on particle production in high energy interactions in air. This made it difficult to calculate the entire process of neutron production and transport in the atmosphere. Around that time,

Hess et al.⁴², Lingenfelter^{15,43}, and Newkirk⁴⁴ attempted to solve the low energy neutron transport without resorting to a calculation of the nucleonic cascade. They used, as a starting point, a trial spectral and spatial distribution of neutrons produced below 10-15 MeV (the "source"), and they examined the diffusion of this source neutrons by means of computer codes for neutron transport. The validity of the trial source was tested by the requirement that a portion of the steady state neutron flux derived from it match certain neutron measurements in the atmosphere. The calculation enabled the authors to derive such quantities as the low energy neutron flux, the production of radiocarbon from the (n, p) reaction in nitrogen, and the numbers of neutrons leaking from the top of the atmosphere.

The major uncertainty in these calculations was that they lacked the basic information on the production of the source in the atmosphere and on the neutron spectrum and spatial distribution in the evaporation region of energy.

The first neutron transport calculation that related to the NYU measurements of the fast neutron flux was the work of Sandie⁴⁵. The full Monte Carlo internuclear cascade programs were later developed independently by Merker⁴⁶ and by Light⁴⁷.

B. Description of the Calculation

1. Scope of the calculation. - The calculation we shall now describe treated both the internuclear cascade in the atmosphere and the low energy transport of neutrons, in two separate consecutive programs. The results of the calculation gave the steady state distribution of neutrons throughout the atmosphere. This included variations with latitude, altitude, and incident primary spectrum.

2. Internuclear cascade.

2a. LOMONTE and HIMONTE. - The first portion of the program treated the nucleonic cascade. A Monte Carlo computer code run on the NYU CDC-6600, determined the production and transport of particles, through a computer simulation of the random processes involved.

In this program the atmosphere was treated (everywhere) as a uniform slab of 80% N^{14} and 20% O^{16} , except for the transport of pions, where particle decay was significant. The calculation extended from 0 to 700 g/cm^2 , the limit of statistically significant data. The remaining 333 g/cm^2 were estimated by extrapolation, neglecting ground effects.

The cascade calculation was divided into two parts. HIMONTE treated interacting particles above 2 GeV per nucleon; LOMONTE treated particles that either started out or were produced at less than 2 GeV. Only non-elastic collisions were considered, since the energy drain and angular dispersion in elastic collisions at high energy are small compared with that from non-elastic collisions.

At the beginning of the calculation, monoenergetic protons or alpha particles were introduced at the top of the atmosphere. Each was chosen from an isotropic flux for angle of incidence by a uniformly distributed random variable, R , where

$$R = 2 \int_0^1 u du, \quad 0 \leq u \leq 1, \quad 6a$$

so that $u = \sqrt{R}$ $0 \leq R \leq 1$, 6b

The quantity, u , was the cosine of the angle between the velocity vector of the particle and the nadir.

Interaction path lengths, S , were similarly chosen from

$$S = \lambda \ln R,$$

where λ was the interaction length. For charged particles, energy loss from ionization was accounted for and the residual energy at S was determined. At the interaction site, outgoing particles were described in terms of identity (proton, neutron, charged pion), atmospheric depth, kinetic energy, u , and weight per incident flux (multiplicity). These quantities were selected from normalized integral probability distributions, using R , the uniformly distributed random variable.

After the first collision, each of the secondary particles was followed in its subsequent collisions, until its energy fell below 19 MeV. If the cumulative weight of an interacting particle was greater than 2, it was split into two identical particles each at 1/2 the original weight. This aided the statistics by distributing weight among a larger number of particles. When the weight entering a collision fell below 10^{-3} , the particle was ignored.

Evaporation neutrons were assumed to be emitted isotropically in the center of mass frame of the residual nucleus, the momentum distribution of which was taken from the intranuclear cascade calculations of Bertini²⁶, below 2 GeV. Altogether, about 10^5 incident primaries were processed in a complete run to determine the production spectrum and spatial distribution of the less than 19 MeV neutrons. A total of 55 proton energies was processed in the range of 20 MeV to 100 GeV. Additional runs were made to check the sensitivity of the calculation to uncertainties in the published cross section data.

2b. References for cross sections for production of nucleons. The free paths for non-elastic collision used in the calculation we report here⁴⁶, are shown in figs. 16 and 17. The discontinuities are not real, but represent averaging over reported values in different regions of particle energy^{26, 48-70}.

For the cascade and evaporation products of protons and neutrons from 20 MeV to 2 GeV, Merker used Bertini's Monte Carlo calculation of the intranuclear cascade^{47, 26}, and Light used Alsmiller's analytic fits to the Bertini data^{46, 53}, with similar results.

If the interacting particles are beyond 2 GeV, intranuclear calculations tend to overproduce nucleons^{54, 55}. For this reason, experimental data

and semi-empirical fits to experimental data were used, wherever possible. The sources used were mainly:

Ranft⁵⁶, and Liland and Pilkuhn⁵², the cascade neutron and proton energy distributions above 1 GeV;

Artykoy et al.⁵⁵, for multiplicity, angular and energy distribution of gray tracks (30-500 MeV protons) from collisions of cosmic rays with medium nuclei ($A = 14$) in emulsions;

Winzeler⁵⁴, the dependence on incident energy of the number of black tracks (< 30 MeV protons) per collision in emulsion nuclei;

Yiou⁵⁷, the relative nuclide production from 22 GeV protons vs. 2 GeV protons in carbon (also Shen⁵⁸);

Lohrmann and Teucher⁵⁹, multiplicities of particles produced in light emulsion nuclei.

The contribution of incident alpha particles was more difficult to ascertain. The sources used were: Lohrmann and Teucher⁵⁹, non-elastic cross section in air; Millburn⁶⁰, Lohrmann and Teucher⁵⁹, Jain et al.⁶¹, for the nature of particles emitted from alpha particle stars; Radin⁶², for a comparison of isotopes produced by alphas relative to protons.

2c. Pion production and transport. - The effect of charged pions on the internuclear cascade in the atmosphere was investigated. The multiplicity of emitted pions was derived from various calculations and experimental results. We mention a few in the list of references^{52, 56, 63-70}. The remaining can be found in the doctoral theses of Merker and of Light. It was found that when the primary proton or alpha particle was below 40 GeV in energy, the source production due to the interactions of secondary pions was below the statistics of the calculation and could be neglected. Above this energy, the pion interactions deep in the atmosphere had a significant effect on the attenuation of the cascade, and were processed in the program.

To simplify the calculation, pions were assumed to be emitted in the forward direction and the collision of an incident pion was treated as identical to that of an incident nucleon. Partial justification for this procedure can be found in Barashenkov's⁶³ observations in nuclear emulsions. He reports that for interacting particles from 1-20 GeV, the only difference in the outgoing particles is in the identity of the most energetic cascade product, the leading particle, which tends to be the same as the incident

pion or proton. In this sense, the program tends to overproduce protons deep in the atmosphere, but the amount is a correction to a small number.

In the calculation, the pion proper lifetime was 2.604×10^{-8} sec. dE/dx^{68} was $-1.9544 \text{ MeV/gm/cm}^2$, and λ in air was 130 gm/cm^2 ^{50,55}. Pions below 2 GeV were ignored, since their effect was negligible.

The final result of the HIMONTE and LOMONTE programs was a source tape containing, for each of the 55 primary proton energies, the spatial, energy, and angular distribution of the fast neutron source. In all, there were 13 energy bins from 0 to 19 MeV, 4 angular bins, and 36 spatial bins from the top of the atmosphere to 700 grams/cm^2 . The source tape also contained the energy and spatial distribution of the neutrons between 20 and 100 MeV, which was useful information but not required for the subsequent analysis.

3. Neutron transport below 19 MeV, O5R. - The second portion of the calculation treated the transport of neutrons that had been produced or scattered below 19 MeV. It was based on the neutron transport code, O5R, which had been developed at ORNL⁷¹. O5R is a Monte Carlo simulation of the slowing down of neutrons, proceeding from individual source energies and locations.

The calculations simulate the transport of neutrons through energy intervals called supergroups, which are defined at every integer power of 2 in neutron velocity squared, from 2^{27} to $2^{67} \text{ cm}^2/\text{sec}^2$. In order to make use of detailed differential cross section data, including sharp resonances, the supergroups in the energy region from 0.0383 ev-19 MeV were further subdivided into 128 subgroups, of equal energy interval. Within the subgroup the total cross section was considered constant.

Inelastic scattering ($n, n' \gamma$) and neutron absorption, which are not handled by O5R, were also treated, to determine, (1) outgoing neutrons in inelastic collisions and (2) the production of radiocarbon in the absorption process $N^{14}(n, p) C^{14}$. The scattering angle in the inelastic collisions were assumed to be isotropic.

The neutrons were thus followed through each supergroup, with the appropriate weighting, until they left the top of the atmosphere or fell below the 0.038 ev cutoff. The necessary parameters of all the collisions were stored on a collision tape, which was analyzed afterward by an NYU subroutine, ANALYS, which determined the differential neutron flux, the leakage angular distribution and rate, and the radiocarbon production.

The differential fluxes were printed out in 34 energy bins and 28 position bins. In addition the leakage rates were read out in 6 angular intervals. In all, about 150,000 isotropic source neutrons, at 468 energies and positions, were transported by O5R, and the results were stored on magnetic tape for processing.

An additional run, with fewer neutrons, examined the case of an anisotropic source by treating the source velocity vectors as isotropic over the lower hemisphere. A further analysis, also with fewer neutrons, examined the angular distribution of the neutron flux at the various position bins in the atmosphere.

The cross sections and the Legendre coefficients used in this calculation were obtained from the ENDF/B cross section tape⁷², supplied by the Brookhaven National Laboratories.

4. Atmospheric flux calculation: NFLUX. -Program NFLUX, listed in Light's doctoral thesis, used the O5R "results" tape to calculate the equilibrium neutron distribution produced from a given primary energy spectrum. The neutron source was obtained by summing up the contribution from each of 55 primary energy bins, this contribution having been determined from the monoenergetic sources derived in LOMONTE and HIMONTE.

C. Input Data for Cascade Calculation, Galactic Cosmic Rays

In Light's doctoral thesis⁴⁶ and for our earlier reports^{32,33}, the spectra of cosmic ray protons and alphas were assembled partly from satellite and balloon measurements, made at different solar epochs⁷³⁻⁸², and partly from the neutron monitor data at sea level. The analysis of neutron monitor data proceeded with the aid of standard^{83,84} techniques. The primary flux was later re-evaluated by⁸⁵ Verschell⁸⁶, using the composite proton and α spectra of Gloeckler and Jokipii⁸⁷ and the high energy primaries of Pinkau et al.⁷⁸ and of Ryan et al.⁷⁹, for solar minimum, and the reports of Lezniak and Webber⁷⁹ plus neutron monitor data near solar maximum. The primary spectrum thus assembled gave considerably larger fluxes above 10 GeV than those reported earlier. We show the proton and alpha spectra in fig. 18 for the most recent results. Varying degrees of solar modulation are shown. The counting rate of the DRNM is used as a measure of the modulation, although it is recognized that such a basis does not allow for spectral variations during which DRNM remains constant.

Nuclei more massive than helium were not included in the calculation. Although they constitute about 11% of the nucleons in the cosmic radiation⁸⁸, they are probably responsible for a small proportion of the secondary neutrons because of the larger role that ionization loss plays in their transport.

VI. RESULTS OF THE CALCULATION

A. Unadjusted Calculation

1. Monoenergetic primary protons. - The Monte Carlo results obtained for the 55 incident proton energies processed are shown in figs. 19-24. All diagrams refer to isotropic fluxes of incident particles and display the sensitivity of various parameters to the primary energy.

Fig. 19 shows the spatial distribution of the 0-19 MeV neutron source for incident protons between 90 MeV and 100 GeV. The total source per unit area, summed over spatial bins, is plotted vs. primary proton energy in fig. 20. As the incident energy increases to large values, the source production begins to level off. This flattening results from losses to the nucleonic cascade from pionization.

Fig. 21 is the source energy distribution, integrated over atmospheric depth, the spectrum below 20 MeV changes little with incident energy. Within statistics, the effect of atmospheric depth on the source spectrum is also negligible.

Fig. 22 presents the spatial distribution of the 1-10 MeV neutron flux for the same four primary energies as the previous graph. When folded into a given primary spectrum the quantities plotted should yield the altitude profiles of the balloon flights. Also shown on the same figure are the associated 0-19 MeV neutron sources, multiplied by an appropriate normalization factor. The curves for source and flux can be observed to have the same spatial dependence except near the top of the atmosphere where leakage of neutrons depletes the flux.

The spectra of albedo neutrons between 0.0383 ev and 100 MeV are given in fig. 23 for primary protons between 100 MeV and 100 GeV. The neutron spectra deeper in the atmosphere can be found in fig. 24. The energy spectrum of the equilibrium neutron flux, unlike that of the source, is depth dependent, largely as a result of leakage effects near the boundary. Losses through leakage are most pronounced at lower primary energy, where the cascade development is closer to the top of the atmosphere. This point is illustrated in Table VIII which shows how the fraction of the source absorbed in the atmosphere to form C¹⁴ and the fraction escaping from the top of the atmosphere change with incident primary energy.

TABLE VIII
 DISPOSITION OF 0-19 MEV SOURCE NEUTRONS
 FROM ISOTROPICALLY INCIDENT MONOENERGETIC PROTONS
 (Incident flux = 1 proton-cm⁻²-sr⁻¹-sec⁻¹)

<u>Proton K. E.</u>	<u>100 MeV</u>	<u>1 GeV</u>	<u>10 GeV</u>	<u>100 GeV</u>	
Total source production:	0.361	20.2	81.7	221	n-cm ⁻² -sec ⁻¹
Total C ¹⁴ production rate:	0.074	8.66	38.4	109	C ¹⁴ -cm ⁻² -sec ⁻¹
Total neutron leakage rate:	0.191	2.77	5.40	6.9	n-cm ⁻² -sec ⁻¹
1-10 MeV leakage rate:	0.124	1.44	2.73	3.3	n-cm ⁻² -sec ⁻¹
C ¹⁴ /total source:	20%	43%	47%	49%	
Total leakage/total source:	53%	14%	7%	3%	

Notes: The neutron source consists of neutrons up to 19 MeV.

The leakage and C¹⁴ rates are for the energy range 0.0383 ev-19 MeV.

2. Monoenergetic alpha particles. - The interactions of high energy alpha particles were deduced mainly from references listed in section VI. In a series of preliminary Monte Carlo runs, the alpha particles were allowed to collide with the nuclei with a free path of 45 g/cm^2 . Of the interacting alpha, 9.7% proceeded with the emission of an outgoing He^3 nucleus with the same energy per nucleon of the incident alpha; the remaining nucleon interacted with the same production cross sections as a single free interacting nucleon. In the remaining 90.3% of the time, 0.93 neutrons and 0.93 protons escaped with the incident energy per nucleon; the remaining 2.14 nucleons were weighted as 1.5 nucleons for producing evaporation products and 2.0 nucleons for producing cascade products. The energy and angular distributions of the cascade and evaporation products were the same as though the nucleons were interacting with the nucleus independently. Such a disposition of the incident and outgoing particles was consistent with the 7-prong alpha stars in nuclear emulsions as observed by Lohrmann and Teucher⁵⁹ and the isotope production from alpha particle interactions as reported by Radin and references therein⁶².

The preliminary runs on He^4 included energies from 100 MeV to 50 GeV. At the time, the various Monte Carlo programs were not completely debugged and only the relative source production from protons and alphas could be compared. With the assumptions which we have just described on alpha interactions, the source production from primary alphas divided by the source production by primary protons was found to be $\sim 4.4 \pm 0.4$. This was on the basis of total kinetic energy. In the later runs, incident alphas were treated as 4 protons at the same energy per nucleon.

In a recent calculation, Gabriel et al.⁸⁹ examined high energy alpha interactions. They assumed that the alpha particle nucleons entering a nucleus behaved independently. This assumption enabled them to use Bertini's cascade calculation to determine the outgoing products for alpha particle collisions. In comparing their results with experimental observations on interactions below 1 GeV, they found that they reproduced the differential distributions but were in error in absolute value by a factor between 1 and 2. The results they obtain can be seen, on analysis, to further justify the procedure we have used for alphas.

3. Galactic cosmic rays, comparison with experiment. - Fig. 25a shows the fast neutron flux that is obtained when the solar minimum galactic primary spectrum is folded into the neutron yields from monoenergetic primaries. Altitude profiles at three of the balloon launching sites are given for both the experimental and the calculated fast neutron flux. Fig. 25b shows similar

curves near solar maximum, where balloon measurements were made at 2 geomagnetic latitudes.

3a. Solar minimum. - The calculated fluxes were found to be everywhere within -20 to +30% of the experimental values except near the top of the atmosphere at 17 GV, where the calculation appears to overproduce by a larger factor. Such deviations, in both amplitude and shape, can arise (1) from uncertainties in the data reported in the literature for primary cosmic ray particle spectra and (2) at high rigidity, from the variation of cutoff rigidity with direction of arrival of the primaries. The effect of changes in the published values of the primary spectrum is particularly notable. For example, the neutron altitude profiles calculated from earlier versions of the primary spectrum, especially above 10 GeV, differed in shape from those displayed in fig. 25a, and the deviations between the observed and calculated spatial distributions reported by

Light et al.³² were everywhere < 30% and occasionally of opposite sign to that displayed in the figure. Other sources of error were uncertainties in the high energy proton cross sections, in the calculation of alpha particle cross sections, in the absolute efficiency of the neutron detector, and in the balloon ascent data, due to statistics, especially in the equilibrium region. The net effect of these errors appears to be less than the ~ 25% uncertainty in the primary proton and alpha data.

3b. Latitude surveys. - The fit of the Monte Carlo output to the experimental data is also illustrated by the latitude surveys. In the equilibrium region, at 245 g/cm², the calculation yields a latitude variation of ~ 5¹/₂ compared with ~ 6 for the observed variation, fig. 11. Near the transition maximum at 72 g/cm², illustrated in fig. 25, the latitude profile follows the experimental fluxes everywhere except at 17 GV. The observed fluxes are lower than the calculated fluxes by about 10-12 percent at solar minimum (balloon flights) and about 14% at solar maximum (aircraft latitude survey).

3c. Fast neutron spectrum. - The characteristics of the 1-10 MeV neutron spectrum observed in the NYU experiment were reproduced, on the whole, by the calculation. When the calculated fast neutron spectrum was fitted to a power law in kinetic energy, the mean spectral index, n , increased slightly with atmospheric depth, but was insensitive to geomagnetic cutoff and to solar activity. This is illustrated in Table IX, which compares the observed and the mean calculated spectral indices, n . The detailed spectral shape of the calculated fast neutron flux, in 1 MeV energy bins, can be obtained from the monoenergetic primary cases in fig. 24, since the high latitude spectrum of neutrons from galactic cosmic rays has the same shape

TABLE IX

CALCULATED AND OBSERVED MEAN SPECTRAL INDEX, n ,
OF A POWER FIT, Ae^{-n} , TO THE 1-10 MEV NEUTRON SPECTRUM

P_c (Gv)	Atmospheric		<u>Spectral index, n</u>	
	Depth, g/cm ²	Calculation	Experiment	
Solar minimum	0	Albedo rate	0.90 ± 0.09	
	4-6	1.00 ± 0.09	$1.08^{+0.12}_{-0.20}$	
	60-70	1.19 ± 0.08	$1.17^{+0.13}_{-0.20}$	
	200-700	1.23 ± 0.08	$1.17^{+0.13}_{-0.20}$	
	17	60-70	1.19 ± 0.08	$1.1 - 1.2$
Solar maximum	0	4-6	1.00 ± 0.09	$1.08^{+0.12}_{-0.20}$
	60-70	1.22 ± 0.08	$1.17^{+0.13}_{-0.20}$	

as that from 1 or 10 GeV protons and the low latitude spectrum is similar in shape to that from 10 or 100 GeV protons.

In Table V we noted that the observed spectrum dropped more steeply between 1 and 2 MeV than between 2 and 10 MeV. The calculated spectrum shows a drop at 1 MeV, as indicated in fig. 24. Such departures from a smooth spectrum depend, as noted by Wilson et al.⁹¹, on the location of maxima in the cross section data of neutrons on oxygen and nitrogen. Spectral features, also found in the 2-50 MeV differential flux in fig. 24, can be sharply defined or blurred, depending on the source of the cross section data.

B. Normalized Calculation

1. Procedure. - Those errors that arise in the calculated neutron distributions, because of uncertainties in the primary proton and alpha spectra, can be eliminated by normalizing the calculated neutron fluxes to the fast neutron observations. The procedure we followed for normalization involved making slight adjustments of the neutron source to reproduce, on transport, the neutron fluxes measured at different cutoff rigidities and at different levels of solar modulation of the primaries, where the modulation was determined from the counting rates of the Deep River neutron monitor (DRNM). Such a procedure was valid at high cutoff rigidity for most periods and at low P_c from 1964 to mid-1969, after which DRNM began to deviate by $\leq 10\%$, at times, from a single valued relationship with the neutron flux at the high-latitude transition maximum (fig. 14).

2. Results.

2a. Fast neutron flux. - Fig. 26, which shows the world-wide altitude distributions of the fast neutrons during solar minimum and during solar maximum, is the best fit of the Monte Carlo calculation to the experimental data. The standard deviation of any single experimental point from the corresponding curve is $\leq \pm 7\%$ from the top of the atmosphere to 300 g/cm^2 and 2-3 times this value at 600 g/cm^2 , a depth at which the experimental statistical fluctuations are rather large.

Using the normalized calculation, we are able to predict other features of the spectra of neutrons and their products, essentially as extrapolations from the fast neutron measurements.

2b. Neutron source and products. - The neutron source spectra from the galactic cosmic radiation are similar to those of fig. 21, which illustrates the monoenergetic primary results. The source spectra in fig. 21 differ from those of Hess et al.⁴², Newkirk⁴⁴, and Lingenfelter⁴³ in the absence of a well defined evaporation peak, so that the prominent spectral feature these authors find in the transported source, a bump located between 0.1 and 1 MeV and usually described as the softened evaporation peak, is only marginally evident in the leakage flux and is absent elsewhere (figs. 23 and 24).

The spatial distributions of the vertically integrated neutron source at different values of P_c and at 4 levels of solar modulation are listed in

Table X. The final products of the 0-19 MeV neutron source as well as the fractional contribution to each product are presented in Table XI. Of particular interest are the radiocarbon production rates and the neutron leakage flux at the top of the atmosphere. These quantities are also given in Table X for the same periods and cutoff rigidities as the neutron source.

2c. Radiocarbon. - The production rates of C^{14} , displayed in Table X, are derived from the modified O5R program, which had a lower cutoff of 0.0383 ev for processing the neutron flux. Neutrons falling below this energy were counted. They contributed an additional 10% to the radiocarbon budget (Table XI). The global average of C^{14} from neutrons >0.0383 ev, listed in Table X for each degree of solar modulation, was obtained by integrating over geomagnetic latitude, using the approximation, $P_c = 15 \cos^4 \lambda$ Gv.

Table XII shows (1) the total C^{14} production rates from the 0-19 MeV neutron flux, (2) the average Zurich sunspot number, and (3) DRNM, for each of the years, 1964-1971, the period of the NYU measurements.

The average C^{14} production from 1964-1971 was 2.21 ± 0.10 nuclides per sec per cm^2 column of air. Based on the projected sun spot numbers for the remainder of the present solar cycle, the 11 year mean rate can be as large as 2.28 ± 0.10 nuclides $cm^{-2} sec^{-1}$. The error limits on the rates apply only to the statistics of the calculation. The numbers presented in the table are of particular interest because solar cycle #20 has behaved in sunspot intensity and in time profile, much like the mean of the previous 11 solar cycles (Solar Geophysical Data, 1972).

TABLE X

DISPOSITION OF THE 0-19 MEV SOURCE NEUTRONS FROM COSMIC RAY PROTONS AND ALPHAS AT DIFFERENT LEVELS OF SOLAR MODULATION AND CUTOFF RIGIDITY. THE CONTRIBUTION OF THE >19 MEV NEUTRONS IS ALSO INDICATED.

0-19 MeV Neutron Source Production Rates (0-10³³ g/cm²)

DRNM	neutrons/cm ² -second							Glob. Aver.
	0 Gv	3.0	4.5	6.0	9.0	12.0	17.0	
6900	9.34	7.09	5.55	4.44	2.82	1.85	1.25	4.43
6700	8.30	6.66	5.21	4.19	2.70	1.79	1.22	4.09
6500	7.42	6.05	4.88	3.95	2.58	1.73	1.19	3.80
6300	6.57	5.52	4.51	3.68	2.45	1.66	1.16	3.48

Radiocarbon Production Rates (0-10³³ g/cm²)

nuclides/cm²-second from 0.038 ev to 19 MeV*.

6900	4.50	3.56	2.83	2.27	1.46	0.97	0.66	2.22
6700	4.02	3.28	2.66	2.15	1.40	0.94	0.64	2.05
6500	3.61	3.05	2.49	2.03	1.34	0.91	0.63	1.91
6300	3.21	2.77	2.30	1.89	1.26	0.87	0.60	1.76

* To determine radiocarbon from 0-19 MeV neutron flux, multiply all values above by 1.10

Neutron Leakage Rates (0.038 ev to 19 MeV)

neutrons/cm ² -second								
Neutron energy, MeV	$\leq 10^{-3}$	10^{-3} -1	1-10	10-19	19-100	100-2000		
P _c 0 Gv	0.07-	0.34	0.53	0.07-	0.36	0.27		
P _c 17 Gv	0.08	0.35	0.51	0.06	0.31	0.35		

+ $\pm 10\%$ of value shown

Ratio, Leakage Rate/Leakage Flux†

P _c 0 Gv	0.70	0.65	0.55	0.48	0.45	0.38-0.23
P _c 17 Gv	0.70	0.64	0.56	0.49	0.53	0.46-0.39

† $\pm 10\%$ of value shown

TABLE XI

FRACTION OF NEUTRON SOURCE EXPENDED IN FINAL PRODUCTS

P_c	0 Gv		17 Gv	
	Solar min.	Solar max.	Solar min.	Solar max.
<u>Effects above 0.038 ev, % of total source</u>				
Leakage Rate	8.9%	8.3%		4.7%
$N^{14}(n, p) C^{14}$	48.2	48.8	52.5	52.4
$N^{14}(n, \alpha) B^{11}$		28.6		28.4
$N^{14}(n, d) C^{13}$		3.8		3.7
$O^{16}(n, \alpha) C^{13}$		3.1		3.1
$N^{14}(n, t) C^{12}$		1.6		1.6
$N^{14}(n, \gamma) N^{15}$		1.0		1.0
$O^{16}(n, p) N^{16}$		0.2		0.1
<u>Effects under 0.038 ev</u>				
$N^{14}(n, p) C^{14}$		4.5		4.8
$N^{14}(n, \gamma) N^{15}$		0.2		0.2
Leakage rate		<.02		<.01

TABLE XII
CARBON 14 PRODUCTION RATES
AS A FUNCTION OF SOLAR ACTIVITY AND COSMIC RAY MODULATION

<u>Year</u>	<u>1964</u>	<u>1965</u>	<u>1966</u>	<u>1967</u>	<u>1968</u>	<u>1969</u>	<u>1970</u>	<u>1971</u>	<u>Average</u>
Mean SS no. ¹	~20	16	50	90	107	107	100	70	
Mean DRNM	6905	7072	6870	6618	6434	6314	6353	6757	
Total C ¹⁴ rate	2.42	2.58	2.39	2.10	2.03	1.93	1.96	2.26	2.21±.10

¹Solar Geophysical Data (1972)

2d. Neutron leakage rates and fluxes. - Several recent measurements of neutrons have been made in high altitude balloons and in satellites^{91, 92, 16} to test the hypothesis that the protons in the inner radiation belt are derived principally from the radioactive decay of the neutrons escaping from the top of the atmosphere. The 0.038 ev to 19 MeV neutron leakage rates are shown in Table X, where we define leakage rates as the number of neutrons escaping each second through a 1 cm² area parallel to the boundary. We employ the word rate rather than flux to avoid a common source of confusion; that is, the theoretical studies usually involve what we have labelled as rates, whereas the satellite and the balloon detectors measure neutron fluxes, defined in the usual manner. The conversion factors from flux to rate in the different neutron energy intervals are shown in Table X, which also lists the fraction of the neutron leakage flux in each interval. We include energies above 19 MeV from the recent work of Merker^{93, 94}. Note, in particular, that the ratio of rate to flux decreases with increasing energy in a manner which indicates that the slow neutron fluxes are peaked toward the vertical (ratio > 0.5) and the 1-10 MeV neutrons are nearly isotropic over the upper hemisphere (ratio of 0.5). At energies above 100 MeV the albedo neutrons are peaked more toward the horizontal (ratio < 0.5).

Fig. 27, reproduces fig. 2 of Merker⁹³, in which the leakage rate spectrum is continued above 100 MeV and plotted at a P_c of 4.5 Gv, the cutoff at Palestine, Texas, where measurements have been made by several groups. For comparison, the calculated spectrum is given for the epoch closest to September 1971, corresponding to the time of the neutron observations of Preszler et al.

3. Discussion.

3a. Comparison of the normalized calculation with the results of neutron experiments. - The normalization of the Monte Carlo calculation to the experimental fast neutron data, as in fig. 26, permits us to interpolate our observed 1-10 MeV fluxes as accurately as is possible, to match the conditions prevailing during measurements by other groups. Table XIII is a comparison of the fast neutron measurements made by other investigators with the interpolated values we obtain at the pressure, geomagnetic coordinates, and epoch of the observations. We have also included the measurements made with the prototype of the NYU fast neutron experiment in 1962.

TABLE XIII
COMPARISON OF RESULTS WITH THE FAST NEUTRON OBSERVATIONS OF OTHERS

Experimenter	P _c (Gv)	Depth(g/cm ²)	Energy (MeV)	Fluxes, n-cm ⁻² -sec ⁻¹		Spectral Index n
				Exp. Value	NYU Result ⁺	
Miyake ⁹⁵	1.4	760	1-10	0.022±0.009	0.018±0.004	1.22±0.76
Hess et al. ⁹⁶		200	1-10	1.7	1.06 ±0.11	1.6 ±0.17
Mendell and Korff ⁹	2	18	1-10	1.4	1.30 ±0.11	1.08±0.09
	2	76	1-10	1.9	1.79 ±0.11	1.06±0.07
	2	200	1-10	1.3	1.14 ±0.07	1.14±0.07
	2	550	1-10	0.11	0.14 ±0.02	0.79±0.12
Haymes ⁹⁷	4.8	Albedo	1-14	0.24 ±0.02	0.31 ±0.03	0.77±0.14 ^{**}
	4.8	4	1-14	0.39	0.46 ±0.07	0.85±0.13
	4.8	90	1-14	1.1	1.14 ±0.15	0.96±0.14
	4.8	200	1-14	0.74	0.83 ±0.13	0.89±0.13
	4.8	550	1-14	0.11	0.13 ±0.02	0.85±0.20
Baird and Wilson ⁹⁸	0	Albedo	1-10	1.0 ±0.4	0.92 ±0.09	0.8 ±0.3
Equil. Region >100						1.42±0.30
Tajima ⁹⁹	9-12	200	2 ^a	0.12	0.08 -0.13	1.21±0.30
	9-12	650	2 ^a	0.015	0.009 -0.011	1.51±0.15
Lockwood ³⁰	4.4	5.5	3-10	0.23	0.21 ±0.03	1.04±0.15
	4.4	100	3.5-10	0.36	0.42 ±0.04	0.86±0.08
Jenkins et al. ⁹²	0	Albedo	1-10	0.28 ±0.03	0.28 ±0.03	0.8 - 1.0
Bhatt and Parikh ¹⁰⁰	12			0.035±0.003	0.036 -0.044	0.88±0.16
Alberne and Talon ¹⁰¹	17	4-6	5.5-22	0.047±0.006	0.052±0.007	1.3 ±0.3
	3.5	Albedo (rate)	3-14	0.14 ±0.01	0.12 ±0.01	1.16±0.18
	3.5	4-6	3-14	0.39 ±0.03	0.35 ±0.04	1.14±0.21
Zobel et al. ¹⁰²	3.5	90	3-14	0.96 ±0.07	0.71 ±0.07	1.35±0.23
Wallace and Boyer ¹⁰³	4.5	9		0.15 ±0.01	0.21 ±0.02	0.71±0.11

Notes: a These values are the differential flux, neutrons/cm² second-MeV, at 2 MeV.

^{*} Spectra with changing slope or peaks; see figure 28.

^{**} Extrapolated

⁺ The NYU neutron fluxes are reduced to the solar epoch, atmospheric depth, and geomagnetic latitude of the measurements of others; the normalized Monte Carlo calculation is used for interpolating the NYU results.

The average result, experiment/normalized calculation, in Table XIII, is 1.07 ± 0.30 . The agreement is well within (1) the fitting error in the normalization, as discussed in section 2b, and (2) the calibration uncertainty of 10% in the experimental NYU fluxes, to which the Monte Carlo calculation has been normalized.

The experiment fast neutron spectra, also shown in Table XIII, have usually been fitted to a single power law in energy. The spectral index, n , at high altitude was generally reported to be between 1.0 and 1.3, comparing reasonably well with the NYU values listed in Table IX.

Zobel et al.¹⁰² of ORNL and Lockwood³⁰, each using NE 213 detectors with separate anticoincidence annulus, measured the neutron flux above 3 MeV, at balloon altitudes, from Palestine, Texas. Fig. 28 shows the spectra they reported and the fast neutron spectrum we measured at the same location. The three sets of data are normalized by the Monte Carlo calculation to the altitude and solar epoch of the ORNL observation. The differential fluxes are in fair agreement below ~ 5 MeV neutron energy. At higher energies, the values reported by Zobel et al. and by Lockwood fall, on the average, below the NYU spectrum. The Monte Carlo calculation, which follows the NYU curve with minor excursions, drops sharply at around 8-10 MeV, as we shall show later. With the usual resolution of a liquid scintillator, such a drop can be smoothed out in the unfolding procedure to yield a steeper spectrum. The NYU spectrometer, on the other hand, was insensitive to spectral features above 8-9 MeV.

At energies between 1 kev and 1 MeV, measurements have been made either with single moderated slow neutron counters or with several moderators of varying thickness, similar in principle to the Bonner spheres. The choice of a neutron spectrum from the counting rates is not unique. In such cases, the determination of the neutron flux has usually been based on the neutron spectra calculated by Lingenfelter⁴³ or by Newkirk⁴⁴.

Boella et al.^{104,105} used 3 different Boron-plastic scintillators, (not all on a single flight), in rocket and balloon measurements. The authors fitted their data to the Newkirk spectrum, which gave better agreement with experimental results than did the spectrum of Lingenfelter. Table XIV compares the NYU calculations of neutron flux with the values Boella reported for one rocket and for two balloon observations. Since the counting rates were not presented in the articles by Boella et al., it was not possible to make a direct comparison with the Monte Carlo neutron spectrum, although neutron fluxes calculated with the Newkirk spectrum are similar to the results we would obtain, as we shall find in the ensuing discussion.

TABLE XIV

COMPARISON OF CALCULATION WITH MEASUREMENTS
 MADE WITH DETECTORS SENSITIVE TO NEUTRONS BELOW 10 MEV;
 BALLOON AND ROCKET OBSERVATIONS OF BOELLA ET AL.,
 EMPLOYING BARE AND MODERATED NEUTRON COUNTERS

0-20 MeV Flux, neutrons/cm² -sec

Atmospheric Depth, mb	10/63 ^a		3/66 ^b		Near Solar Min ^c
	Boella	calc.	Boella	calc.	Intriligator ^c
Quoted error	(± 0.07)		(± 0.04)		
650	0.20	0.25 ± 0.02	0.22	0.23 ± 0.02	
200	2.50	3.2 ± 0.2	3.40	3.0 ± 0.2	
90-100	3.55	4.2 ± 0.2	4.45	3.9 ± 0.2	
4	0.61	1.14 ± 0.18	1.10	1.05 ± 0.17	0.58
Albedo	0.45	0.58 ± 0.07	0.42	0.53 ± 0.07	0.36 ± 0.06 (extrapolated)
	$0.34 \pm 0.04^*$				

a. Cutoff rigidity 4.6 Gv; DRNM, 6800 (Boella et al.¹⁰⁴)
 b. Cutoff rigidity 5.3 Gv; DRNM, 6950 (Boella et al.¹⁰⁵)
 c. 42° geomagnetic latitude¹⁰⁶
 * Boella et al.¹⁰⁵

The overall agreement between the results of the experiment and of the Monte Carlo calculation is notable. An exception is the high altitude values found in the earlier flight, which are in disagreement with those found later by the same group (Table XIV).

The authors did not account for directional anisotropies below 1 MeV or for local production in the moderator at high altitudes, but the effects may not be large and may cancel out.

Using a similar detector, a dual B^{10} -plastic, B^{11} -plastic phosphor, Intriligator¹⁰⁶ found fluxes which were low compared with the calculated values. The experimental results are shown in Table XIV, last column. The author converted from counting rate to flux, using the Lingenfelter spectrum. Above 1 MeV, where both the detector sensitivity and the Lingenfelter spectrum drop sharply, the contribution to the neutron flux was given as 1/2 that of the 0-1 MeV flux, compared with the values given in Table X, in which the flux of neutrons above 1 MeV exceeds the flux below 1 MeV by factors of 1.4 to 3 depending on the upper energy cutoff.

In an experiment on OGO 6, Lockwood's group^{91,107}, measured both the counting rates of a moderated He^3 counter and the 1-10 MeV neutron spectrum from a scintillator-modulator. They found that the 1-10 MeV could be fitted to a power law, $N(E) = AE^{-n}$, where n was 0.8 to 1.0, although the neutron spectrum calculated by Wilson⁹¹, (to be discussed later), was a better fit. The value of n that we calculated (Table IX) from the Monte Carlo spectrum was 0.9 ± 0.09 . Table XV compares the numbers that Jenkins et al. presented for the 1-10 MeV and the 0-20 MeV neutron leakage rates (called leakage flux in the paper) with the results of the Monte Carlo calculation. The total leakage rates were obtained, by Jenkins et al.¹⁰³ by folding the Newkirk spectrum into the response function of the He^3 detector to obtain the flux, and then converting from flux to leakage rate. The Monte Carlo calculation, by the same procedure, yielded a 1-10 MeV to 0-20 MeV ratio of 0.52 ± 0.05 , as compared with the mean "observed" (in the sense just described) values of 0.54 ± 0.07 at the poles and 0.52 ± 0.05 at the equator, and as compared with the spectral ratio of 0.45 derived from the Newkirk spectrum alone. The experiment thus confirms the increased ratio of the fast neutrons/total neutrons that we suggested was required to interpret the observation of Intriligator.

TABLE XV

 COMPARISON OF CALCULATION WITH MEASUREMENTS OF JENKINS ET AL.;
 SATELLITE OBSERVATIONS WITH MODERATED He^3 DETECTOR

Month (1969)	Polar Regions			Equatorial Regions 12 Gv			Ratio					
	Rates 1-10 MeV		Rates Total	Rates 1-10 MeV		Rates Total						
	obs.	calc.	obs.	calc.	obs.	calc. ^a						
June	0.30	0.26	0.56	0.50	0.54	0.52	0.034	0.039-.031	0.076	0.077-0.061	0.45	0.51
July	0.29	0.27	0.55	0.51	0.54	0.52	0.039	0.039-.031	0.077	0.077-0.061	0.51	0.51
Aug.	0.32	0.28	0.56	0.53	0.57	0.52	0.040	0.040-.032	0.077	0.078-0.062	0.53	0.51
Sept.	0.30	0.28	0.58	0.53	0.51	0.52	0.039	0.040-.032	0.079	0.078-0.062	0.50	0.51
Err.	± 0.02	$\pm 10\%$	± 0.06	$\pm 10\%$	$\pm .07$		$\pm .003$		$\pm .008$	$\pm 10\%$	$\pm .06$	

a. The calculated fluxes decline between 12 and 15 Gv

The time variations we found during the period of the satellite measurement were obtained directly from aircraft measurements at Eielson AFB; the amount of the variation was within the error bars of the satellite measurement. The latitude variation we show in the table was not observed in the satellite measurement, but the ¹⁰⁷ size of latitude effect near the equator may be due to latitude mixing. The authors report an increase in the ratio of fast to total leakage rates from the equator to the poles and state that the ¹⁰⁷ increase is in agreement with the high altitude balloon studies of Boella et al. (1965 b). In the Boella paper, it is suggested that the ratio of fast leakage to 0-20 MeV leakage can increase by as much as 270% from equator to pole. The Monte Carlo calculation indicates that such an increase must be less than or of the order of the 10% uncertainty due to statistics. The latter conclusion appears to be consistent with the tabulated values of Jenkins et al. ¹⁰⁷.

The slow neutron detectors usually employ neutron capture in nuclei having cross sections inversely proportional to velocity. The counting rates are proportional to neutron density. Table XVI compares the calculated slow neutron densities from 0.038 to 10^5 ev and from 0 to 10^5 ev (extrapolated) with the total slow neutron densities reported by Haymes ⁷ and by Miles ¹⁰⁸ at similar cutoff rigidities. The first measurement was at solar maximum and the second around the mean of the solar cycle. The measurements have been normalized to an intermediate modulation by the Monte Carlo calculation.

The errors estimated in the table include calibration uncertainties and the statistic of the most significant data point. The calculated densities are ~ 12% lower than those found by Miles; they are ~ 15% higher than Haymes except deep in the atmosphere and at high altitude, where the statistical uncertainty of the experiment increases. On the whole, the three sets of neutron densities agree in altitude distribution and absolute value well within the estimated errors.

The neutron spectrum at higher energies was presented in fig. 27, for the special case of the leakage rates at 4.5 Gv. The measurements of several experimenters are shown, along with the calculations of Lingenfelter and of the present paper, extended to high energy by Merker ⁹³. The Monte Carlo spectrum is in good agreement with the leakage rate spectra reported by Jenkins et al. ¹⁰⁷ and by Preszler et al. ¹⁶, adjusted by White et al. ⁹².

TABLE XVI

COMPARISON OF RESULTS OF CALCULATION WITH SLOW
NEUTRON DENSITIES REPORTED BY MILES AND BY HAYMES

	<u>Haymes</u>	<u>Miles</u>	<u>Normalized Calculation</u>
Cutoff rigidity, Gv	4.8	5.4	4.5
Year	1958	1962	1969-1970
Counting rate,	2000	2250	2100
Mt. Wash. neutron monitor			
Normalization:			
Cutoff	x1.04	1.12	1.00
Modulation	x1.08	0.89	1.00

Atmospheric depth g/cm ²	Neutron Density			(n/cm ³) X 10 ⁷
	<u>Haymes</u>	<u>Miles</u>	<u>Normalized Calculation</u>	
			Total	
albedo			0.078	0.098
0-1			0.18	0.23
6		0.6	0.5	0.64
27.5	1.5	2.5	1.8	2.2±15%
65	3.5	4.2	3.1	3.7
90-100	4.1±30%	4.7±25%	3.6±15%	4.3
300	2.2	2.4	1.8	2.2
500	0.8	0.8	0.6	0.72

Between 20 and 50 MeV, we note the spectral flattening, first observed by Preszler et al. and later discussed by Merker with relation to the entire Monte Carlo spectrum. This feature is caused by a depletion in the neutron flux and is associated with a maximum in the nonelastic cross section at about 15 MeV.

The neutron leakage rates calculated by Lingenfelter are observed to lie considerably lower than the Monte Carlo values. The former calculation has been used extensively as a basis of comparison of the actual neutron leakage spectrum with that required to populate the inner radiation belt with protons by the CRAND mechanism. If, as the Monte Carlo calculation finds, the neutron spectrum is more complex and the rates larger than previously assumed, it will be necessary to re-evaluate the many theoretical models of CRAND injection in terms of the new spectral shapes and increased numbers of the fast neutrons.

3b. Comparison with other calculations. - The characteristics of the equilibrium neutron spectrum below 20 MeV depend on the spatial and energy distribution of the neutron production rates (the transport source).

Hess et al.⁴², Lingenfelter^{15,43}, and Newkirk⁴⁴ began their calculations, each with different source distributions, which in turn differed in shape from the Monte Carlo results in figs. 19, 20, and 21. We have already mentioned that the source spectra of all of these calculations contain an evaporation peak which becomes a vestigial bump in the steady state neutron flux, whereas the Monte Carlo spectrum is flat below 2 MeV.

The calculated 1-10 MeV neutron spectrum depends critically on the slope of the source spectrum. At balloon altitudes, principally as a result of the shape of the neutron source they employ, the neutron spectra of Hess and of Lingenfelter both fall steeply ($\sim E^{-2}$) after a few MeV, and the neutron fluxes of Newkirk and of the present calculation fall off less steeply ($\sim E^{-1.2}$). The same situation holds above 10 MeV, where the previously mentioned steepness of the Lingenfelter spectrum (fig. 27) lies in the choice of a high energy neutron source with a steep spectrum.

The shape of the 0.1 to 10^3 ev spectrum is affected little by the differences in the fast neutron source, as diffusion theory predicts, having an approximately $E^{-0.9}$ dependence in all of the calculations. However, the altitude distribution and integrated intensity of the slow neutrons, as well as the production rates of radiocarbon, the rates of leakage from the top of the atmosphere --- all depend critically on the distribution of neutrons in the source. The earlier calculations were limited by the arbitrary character

the source distribution; the present calculation is limited by the accuracy of the cross section data, used to produce the source.

Wilson et al.⁹⁰ used a Monte Carlo calculation to determine the energy of 0.3 to 10 MeV neutrons from galactic cosmic ray protons below 10 GeV. The authors found several pronounced peaks in the spectrum, related, they reported, to minima in the cross section in air. Fig. 29 compares the spectral shape which Wilson et al. found with that of the Monte Carlo calculation. The two curves are not dissimilar, although the peaks Wilson et al. reported with 1/2 MeV bins were only weakly visible in the NYU Monte Carlo results, which had 1 MeV resolution. The main differences appear to be in the cross section data employed. The observed spectra of NYU, Haymes⁹⁷, and Lockwood³⁰ are generally featureless, but poor resolution of the liquid scintillator (~15%) might have masked small excursions from a smooth curve.

The relative agreement among the various calculations is illustrated in Table XVII, which gives the ratio, other calculation/NYU calculation. Since the NYU calculation is normalized to the measured fast neutron flux, the Table XVII values in the 1-10 MeV region can also be considered as a comparison of our observations with the calculations.

The earlier spectra of Hess, which were extrapolated from aircraft measurements at 200 g/cm² to the top of the atmosphere, suffered from overproduction, principally because the source distribution was assumed to rise exponentially to the top of the atmosphere. The upper atmosphere neutron calculation differed by factors of 0.1 to 10 from the NYU calculation. Lingenfelter repeated the Hess transport program, using a more realistic source distribution and normalizing to the slow neutron experiments. As indicated in the Table, the Monte Carlo calculation agrees in many respects with the work of Lingenfelter, the main differences arising from the shape of the spectrum. For example, Lingenfelter attributes a much greater fraction than we find to the slow neutron component. On the other hand, experimental observations of the ratio of slow to fast neutrons^{104,107} were found to be more consistent with a smaller value, such as determined in both the Monte Carlo and the Newkirk calculation.

While the Newkirk spectra differ from that which we have calculated, we find fairly good agreement in all quantities of interest. Newkirk's fast neutron spectrum is not too different from the one we measure, having an average spectral index of ~1.2-1.3 in the atmosphere and ~1.0 above the atmosphere.

BLANK PAGE

BLANK PAGE

CONTENTS

	Page
INTRODUCTION	1 1/A9
I. EXPERIMENTAL METHOD.....	3 1/A11
A. Description of Detection System.....	3 1/A11
1. Scintillator detector	3 1/A11
2. Pulse shape discrimination.....	3 1/A11
3. Electronics.....	4 1/A12
4. Data storage	4 1/A12
5. Gondola	4 1/A12
B. Tests of the Detection System.....	5 1/A13
1. Temperature and pressure	5 1/A13
2. Response to sources.....	5 1/A13
3. Gain stability	6 1/A14
4. Channel 1 effect.....	6 1/A14
C. Calibration of Detectors	6 1/A14
1. Basis of calibration, ORNL detector and response functions	6 1/A14
2. Calibration at ORNL.....	7 1/B1
2a. Behaviour of ORNL detector-monitor	8 1/B2
2b. Unfolding the incident neutron spectrum from the measured pulse height distributions	8 1/B2
2c. Normalizing incident spectrum to Pu-Be above 5 MeV	9 1/B3
3. Response to neutrons >10 MeV	10 1/B4
4. Omnidirectional response	10 1/B4
5. Listing of response functions	11 1/B5
6. Cross-calibration of detectors.....	11 1/B5
7. Rejection of gammas in flight	11 1/B5
II. FLIGHT SUMMARIES	16 1/B10
A. Balloon Flights.....	16 1/B10
B. Aircraft Flights	19 1/C1
1. Introduction	19 1/C1
2. Solar minimum latitude survey	20 1/C2
3. Listing of aircraft flights	20 1/C2
3a. Performance of flight systems.....	20 1/C2
III. EVALUATION OF DATA	20 1/C2
A. Introduction.....	20 1/C2
B. Conversion of Counting Rates to Flux.....	34 1/D12
1. Method.....	34 1/D12
2. Contribution of the > 10 MeV neutrons to the counting rate	34 1/D12
C. Calculation of Attenuation Length.....	36 1/E1

IV. RESULTS OF OBSERVATIONS	36	1/E1
A. Results of Balloon Flights	36	1/E1
1. Flight profiles	36	1/E1
2. Fast neutron spectrum	37	1/E2
3. Attenuation length	37	1/E2
4. Solar modulation	38	1/E3
5. Time variations at floating altitude	38	1/E3
6. In-flight calibration of System I vs. System II	39	1/E4
7. Flights with tissue-equivalent dome	39	1/E4
B. Results of Aircraft Flights	40	1/E5
1. Summary of results, free air flux	40	1/E5
1a. Normalization of flight systems	40	1/E5
2. Aircraft latitude surveys	41	1/E6
3. Latitude variations near the latitude knee	42	1/E7
4. Time variations at the high latitude transition maximum	43	1/E8
5. Results of step flight, altitude variations	44	1/E9
V. INTERNUCLEAR CASCADE CALCULATION	45	1/E10
A. Introduction	45	1/E10
1. Production and transport of neutrinos	45	1/E10
2. Previous calculations	46	1/E11
B. Description of the Calculation	47	1/E12
1. Scope of the calculation	47	1/E12
2. Internuclear cascade	47	1/E12
2a. LOMONTE and HIMONTE	47	1/E12
2b. References for cross sections for production of nucleons	48	1/E13
2c. Pion production and transport	49	1/E14
3. Neutron transport below 19 Mev, OSR	50	1/F1
4. Atmospheric flux calculation; NFLUX	51	1/F2
C. Input Data for Cascade Calculation: Galactic Cosmic Rays	51	1/F2
VI. RESULTS OF THE CALCULATION	52	1/F3
A. Unadjusted Calculation	52	1/F3
1. Monoenergetic primary protons	52	1/F3
2. Monoenergetic alpha particles	54	1/F6
3. Galactic cosmic rays, comparison with experiment	54	1/F6
3a. Solar minimum	55	1/F7
3b. Latitude surveys	55	1/F7
3c. Fast neutron spectrum	55	1/F7
B. Normalized Calculation	57	1/F9
1. Procedure	57	1/F9
2. Results	57	1/F9
2a. Fast neutron flux	57	1/F9
2b. Neutron source and products	58	1/F10
2c. Radiocarbon	58	1/F10
2d. Neutron leakage rates and fluxes	62	1/G1

3. Discussion.....	62	1/G1
3a. Comparison of the normalized calculation with the results of neutron experiments.....	62	1/G1
3b. Comparison with other calculations.....	70	1/G12
VII. SUMMARY OF OBSERVATIONS AND CALCULATION OF NEUTRONS FROM GALACTIC COSMIC RAYS.....	73	2/A6
VIII. NEUTRONS FROM SOLAR PROTONS	74	2/A7
A. Introduction.....	74	2/A7
B. Observations.....	75	2/A8
C. Solar Proton Spectra and Neutron Yields	78	2/A13
D. Monte Carlo Calculation.....	80	2/B1
E. Discussion.....	81	2/B2
F. Application to Other Experiments.....	84	2/B6
G. Other Flare Calculations	87	2/B9
H. Summary of Observations and Calculations	88	2/B10
I. The Geophysical Effects of Neutrons from Solar Protons..	89	2/B11
IX. COSMIC RAY MODULATION DURING 1968-1971.....	91	2/B13
A. Introduction.....	91	2/B13
B. Comparison of the Response of Neutron Monitors with Response of NYU Detector to the Primary Spectrum..	91	2/B13
C. Calculation of the Spectrum of Variation of Cosmic Rays...	92	2/B14
D. Results, Transient Cosmic Ray Decreases.....	94	2/C3
E. Results, Long Term Variation in Cosmic Ray Intensity....	99	2/C9
F. Discussion	101	2/C11
1. The spectrum of variation of Cosmic Rays.....	101	2/C11
2. The relative modulation of protons and electrons; charge splitting above 2 GV.....	102	2/C12
3. Model Calculations.....	104	2/C14
G. Conclusions and Summary.....	107	2/D3
X. APPENDIX A. ACCELERATION PROCESSES ON THE SUN ...	110	2/D6
XI. APPENDIX B. PRIMARY NEUTRONS.....	116	2/D12
XII. APPENDIX C. THE EARTH OR OTHER OBJECT AS A NEUTRON SOURCE.....	120	2/E2
REFERENCES.....	122	2/E4
FIGURES.....	133	2/F1

TABLE XVII

 COMPARISON OF MONTE CARLO
 NORMALIZED CALCULATION WITH THE RESULTS OF OTHER CALCULATIONS

P_c	$\%$	Neutrons-cm ⁻² -sec				Transition Max.		% of		
		Gv	Time	Neutron	C^{14}	Leakage	1-10 MeV	Neutrons	<1	1-10
				Monitor		<20 MeV	n	Flux	MeV	>10
<u>Hess</u>		-4.5	1956-7	~85%	6.2±1.5 0.69	3.97 0.58	1.03 0.23	2.0 1.2/2.0	~4.5 0.20	60% 33% 5%
<u>Fraction,</u> <u>NYU/Hess</u>										
<u>Newkirk</u>	1.3	7/61		~88%	7.1 0.89	4.0 0.85	0.8 0.63	1.2 1.2/1.2	1.3, 1.6** 0.85, 0.98	
<u>NYU/Newkirk</u>										
<u>Lingenfelter</u>	Global	1953-4		100%						
<u>Solar Min.</u>					4.10 1.16	2.61 1.00	0.43 0.75	1.2-1.9 ⁺	1.78 1.40	64% 30% 6%
<u>NYU/Lingenfelter</u>	Aver.									
<u>Solar Max</u>		1957-8		82% 86% 82%*	3.22 0.93 0.83	2.08 0.85 0.75	0.30 0.65 0.53	1.2-1.9 ⁺	1.20 1.14 1.00±0.04	
<u>NYU/Lingenfelter</u>	F.D.									
<u>Wilson</u>	0	Min Max						Normalized Figure 8 to NYU		
<u>NYU</u>									42% 52% 6%	

* Extrapolated from data in Forbush decreases

+ n=1.2, 1-3 MeV; n=1.9, 2-10 MeV

** From Figure 4 and Figure 5, Newkirk ⁴⁴

VII. SUMMARY OF OBSERVATIONS AND CALCULATION OF NEUTRONS FROM GALACTIC COSMIC RAYS

The distributions summarized in Figs. 8, 13, 14, 15, and 26 represent the global flux of fast neutrons from galactic cosmic rays during the first half of solar cycle 20, which is very close to the 100 year mean sunspot cycle. The observed neutron flux during this period correlated well with DRNM. This permits us to interpolate from experimental data, employing the neutron monitors only, as a guide to the depth of modulation. The shape of observed as well as of calculated altitude distributions of the neutrons were modulation dependent at high latitudes and altitudes but were modulation independent to $\pm 7\%$, in the equilibrium region. The observed neutron spectrum in the 1-10 MeV region was of the form, AE^{-n} , with n independent of modulation and rigidity, within $\pm 10\%$, but slightly dependent on altitude, in the upper atmosphere. The value of n was

$1.08^{+0.13}_{-0.20}$ at 2-5 mb and $1.17^{+0.12}_{-0.20}$ at 50-90 mb. An additional

flux of $\sim 10\%$ between 1 and 2 MeV was indicated. At sea level, the spectrum was steeper and depended on the local terrain.

Past the solar maximum of 1969 and during Forbush decreases, the neutron flux deviated from a single valued relationship to DRNM. The deviation is interpreted as a change in the proton modulation spectrum at the same DRNM.

The results of our calculations agree with our experimental measurements of the fast neutron flux to within -20% and $+30\%$ over almost the entire range of latitude, altitude, and solar cycle variations. The uncertainties associated with the experiment are principally calibration errors, except in the lower atmosphere, where statistical uncertainties predominate. The errors in the calculation arise from uncertainties in the high energy cross sections, paucity of alpha particle cross section data, uncertainties of the order of 25% in the primary spectrum, and the doubtful correctness of the assumption of a single effective cutoff rigidity. The uncertainties due to the latter two effects were reduced by normalizing the calculation to the fast neutron measurements. The normalized calculation agrees with experimental results over a wide range of neutron energy, changing solar conditions, latitude and altitude, including the leakage flux. On the basis of the correspondence between experiment and calculation, we have reported our estimates of the neutron spectra in figs. 21, 23, 24, and 27, the global production rates of C^{14} in Tables X and XII, and the neutron leakage rates

in Table X. The calculation of the high energy albedo has been confirmed by the recent observations of a larger neutron leakage flux at high energies than had previously been predicted by others, and the leakage spectrum predicted between 1 and 10 MeV has also been confirmed by satellite observations.

VIII. NEUTRONS FROM SOLAR PROTONS

A. Introduction

Although the literature on atmospheric neutron measurements is rather extensive, there have been only a handful of recorded observations of neutron enhancement during solar particle events. Two of the increases were detected by Smith et al.¹⁰⁹ and Greenhill et al.¹¹⁰ at balloon altitudes, and two were observed by Chupp et al.¹¹¹ and by Lockwood and Friling¹¹² in measurements above the atmosphere. Chupp et al., Greenhill et al., and Lockwood and Friling flew moderated slow-neutron counters, which had a broad energy response, principally below 1 MeV. The detectors lacked energy resolution, so that in order to determine the neutron flux from the counting rates recorded during the flights, it was necessary to assume the shape of the spectrum of neutrons incident on the detector. In analyzing the results of all three experiments, the investigators employed the neutron spectrum from the calculation of Lingenfelter and Flamm¹¹³.

Smith et al., used both a bare and a moderated Li^6 I scintillator, which provided an additional channel of spectral information. Their galactic cosmic ray neutron measurements were the experimental basis of the S_n calculation of Newkirk⁴⁴ and were in agreement, of necessity, with the Newkirk calculated spectrum.

The first calculation of neutrons from solar protons was that of Lingenfelter and Flamm¹¹³. As later noted by the authors (Lingenfelter and Flamm¹¹⁴), their equation (1) contained an extra factor of $1/\mu$ ($\mu = \cos$ zenith angle), which had the effect of doubling the incoming proton flux and peaking it toward the horizontal. This difficulty complicated analyses of earlier observations, based on the neutron spectra derived from the Lingenfelter calculation. Armstrong et al.², of ORNL used a Monte Carlo simulation to determine the neutron spectrum from the great proton

flare of February 23, 1956; other flare data or monoenergetic protons were not considered. The ORNL group also investigated secondary neutron production from energetic solar neutrons ¹¹⁵.

B. Observations

In the series of high-altitude aircraft measurements from Eielson AFB, over 40 of the flights (Table IV) occurred during near-earth enhancement of solar protons >10 MeV (Solar Geophysical Data, 1968-1971). In about half of these flights, the neutron counting rates at cruising altitude, 55-75 mb, rose above the galactic background. The minimum observable neutron increase corresponded to solar fluxes of at least 1 proton-cm⁻² sec⁻¹ at energies >60 MeV. Table XVIII lists the principle features of the primary proton and the secondary neutron fluxes during periods of neutron increases. Figures 30-33 illustrate the dependence of the atmospheric neutrons on the solar particle spectra. In all the figures, the contribution of neutrons from galactic cosmic radiation has been subtracted, and the data has been normalized to 65 g/cm² atmospheric depth.

Figures 30a to 33a contain the time histories of the solar protons and of the secondary neutrons during 4 representative events. The protons are displayed in several energy bins, so that the variations of different portions of the solar particle spectrum can be compared with those of the neutrons. Note the large spread in the neutron yield relative to the incident proton flux from event to event. For example, the hard proton spectrum of March 30, 1969 (figure 31) was 100 times more effective in producing neutrons at 65 g/cm² than the soft spectra encountered in events like that of April 12, 1969 (figure 32). Figures 30a to 33a clearly demonstrate that the neutrons track the more energetic components of the solar proton flux during the periods when the primary spectrum is harder, and the less energetic components when the primary spectrum is softer. There is no positive evidence of uncorrelated increases, such as one might expect if some of the neutron flux were produced by incident fluxes of energetic solar neutrons.

The error bars on the neutron data are also displayed in figures 30a to 33a. The errors include uncertainties in the background cosmic ray neutron flux and in the normalization to 65 g/cm² from other atmospheric depths.

The fast neutron spectrum was not observed to change during neutron increases, within the statistics of the measurements.

TABLE XVIII.- NEUTRON OBSERVATIONS DURING SOLAR PROTON EVENTS

Solar Flare Protons						Calculated 2-10 MeV neutrons-cm ⁻² -sec ⁻¹		Observed 2-10 MeV Neutrons-cm ⁻² -sec ⁻¹			
No.	Date	Time	Ref.	Energy Range, MeV	Energy Spectrum, p-cm ⁻² -sr ⁻¹ -GeV ⁻¹	Protons-cm ⁻² -sr ⁻¹ -sec ⁻¹	From AE ^(a)	From ν/ν_0	From Galactic and Solar Protons	From Solar Protons	From Solar Protons, Normalized to n=10 mb
1	6-10-68	00-0410	1			3.8	7.4	0.051	0.036	1.017 (F.D.)	0.02-0.05
			2	30-260	$3.9 \times 10^{-7} E^{-3.4}$ (ν_0)	3.4 3.6 3.67	7.5 6.2	0.016-0.062	0.050		
2	6-11-68	05-09	1			4.2	1.77	0.014	0.006	0.791	1.7-0.2
3a	6-11-68	15-20	Decrease beginning 1600 UT								
		15-16	1			5.5	2.51	0.007	0.006	0.668	0.0-0.008
		16-17	1			6.1	1.9	0.026	0.016	0.691	0.02-0.011
		17-18	1			6.6	1.7	0.048	0.010	0.714	0.04-0.012
		18-19	1			6.1	0.7	0.016	0.042	0.711	0.06-0.010
		19-20	1			6.1	0.41	0.044	0.061	0.719	0.04-0.010
3b	6-11-68	05-10	1			4.2	1.77	0.014	0.006	0.791	1.7-0.2
		05-06	1			5.7	2.52	0.021	0.016	0.656	
		06-10	1			6.1	1.8	0.016	0.015	0.681	1.0-0.1
4	6-11-68	20-25				400-1000					
		20-21	1			400-1000					
		22-25	1			400-1000					
5	6-11-68	2015-2115				400-1000					
		20-21	1			400-1000					
		1060	56	$\times 2 \times 10^3$	ν_0^{-5}	400-1000					
		11	3	$\times 10^3$	$\nu_0^{-6.5}$						
		1330	4	$\times 100$							
				30-60		6					
				6-10		6.4					
				6-10		6.1					
6	6-12-68	23-09	1			400-1000					
		(Peak of event)				400-1000					
				400-1000		6					
				400-1000		6.1					
				400-1000		6.0					
7a	6-25-69	14-18 (Phase 0400, UT)				6-20	6.154	6.215	6.114	6.154	6.0-0.6
		1				6-17	6.190	6.190	6.190	6.190	6.0-0.6
		4	$\times 100$								
		5	$\times 100$								
		6	$\times 1000$								
		7	$\times 1000$								
7b	6-25-69	20-01	1			6.7	6.190	6.94	6.042	1.06	0.115-0.01
		2350	5	80-1000	$0.029 E^{-2.8}$	6-6	6.195	6.195	6.195	1.06	0.115-0.01
		6	1								
		7	$\times 60$			1.4					
7c	6-26-69	02-07				6-6	6.190	6.190	6.190	0.06-0.09 ^(b)	6.0-0.6-0.05
		02-06	1			6-6	6.190	6.190	6.190	0.07 ^(b)	0.04
		6	$\times 60$			6	0.051	6.190	6.190	0.06-0.09 ^(b)	
		06-07	1			6	0.051	6.190	6.190	0.07 ^(b)	
		7	$\times 60$			6.7					
		8	$\times 100$			6.9	0.9	0.181	0.181	0.07-0.07 ^(b)	
7d	6-26-69	12-14	1			6-6	6.190	6.190	6.190	0.04-0.02	0.07-0.07
		2	$\times 60$			6	0.9	0.181	0.181	0.07-0.07 ^(b)	
		3	$\times 60$			6.0					
		4	$\times 100$			6.5					
		5	$\times 100$			6.5					
		6	$\times 100$			6.5					
		7	$\times 100$			6.5					
7e	6-26-69	12-14	1			6-6	6.190	6.190	6.190	0.04-0.02	0.07-0.07
		2	$\times 60$			6	0.9	0.181	0.181	0.07-0.07 ^(b)	
		3	$\times 60$			6.0					
		4	$\times 100$			6.5					
		5	$\times 100$			6.5					
		6	$\times 100$			6.5					
		7	$\times 100$			6.5					
7f	6-26-69	16-18	1			6-6	6.190	6.190	6.190	0.04-0.02	0.07-0.07
		2	$\times 60$			6	0.9	0.181	0.181	0.07-0.07 ^(b)	
		3	$\times 60$			6.0					
		4	$\times 100$			6.5					
		5	$\times 100$			6.5					
		6	$\times 100$			6.5					
		7	$\times 100$			6.5					
7g	6-27-69	08-10	1			6-6	6.190	6.190	6.190	0.04-0.02	0.07-0.07
		2	$\times 60$			6	0.9	0.181	0.181	0.07-0.07 ^(b)	
		3	$\times 60$			6.0					
		4	$\times 100$			6.5					
		5	$\times 100$			6.5					
		6	$\times 100$			6.5					
		7	$\times 100$			6.5					
7h	6-27-69	08-10	1			6-6	6.190	6.190	6.190	0.04-0.02	0.07-0.07
		2	$\times 60$			6	0.9	0.181	0.181	0.07-0.07 ^(b)	
		3	$\times 60$			6.0					
		4	$\times 100$			6.5					
		5	$\times 100$			6.5					
		6	$\times 100$			6.5					
		7	$\times 100$			6.5					
7i	6-27-69	1330-1730	1			6-6	6.190	6.190	6.190	0.04-0.02	0.07-0.07
		2	$\times 60$			6	0.9	0.181	0.181	0.07-0.07 ^(b)	
		3	$\times 60$			6.0					
		4	$\times 100$			6.5					
		5	$\times 100$			6.5					
		6	$\times 100$			6.5					
		7	$\times 100$			6.5					
7j	6-27-69	1537	1			6-6	6.190	6.190	6.190	0.04-0.02	0.07-0.07
		2	$\times 60$			6	0.9	0.181	0.181	0.07-0.07 ^(b)	
		3	$\times 60$			6.0					
		4	$\times 100$			6.5					
		5	$\times 100$			6.5					
		6	$\times 100$			6.5					
		7	$\times 100$			6.5					
7k	6-27-69	1537-1737	1			6-6	6.190	6.190	6.190	0.04-0.02	0.07-0.07
		2	$\times 60$			6	0.9	0.181	0.181	0.07-0.07 ^(b)	
		3	$\times 60$			6.0					
		4	$\times 100$			6.5					
		5	$\times 100$			6.5					
		6	$\times 100$			6.5					
		7	$\times 100$			6.5					
7l	6-27-69	1737	1			6-6	6.190	6.190	6.190	0.04-0.02	0.07-0.07
		2	$\times 60$			6	0.9	0.181	0.181	0.07-0.07 ^(b)	
		3	$\times 60$			6.0					
		4	$\times 100$			6.5					
		5	$\times 100$			6.5					
		6	$\times 100$			6.5					
		7	$\times 100$			6.5					
7m	6-27-69	1737-1737	1			6-6	6.190	6.190	6.190	0.04-0.02	0.07-0.07
		2	$\times 60$			6	0.9	0.181	0.181	0.07-0.07 ^(b)	
		3	$\times 60$			6.0					
		4	$\times 100$			6.5					
		5	$\times 100$			6.5					
		6	$\times 100$			6.5					
		7	$\times 100$			6.5					
7n	6-27-69	1737-1737	1			6-6	6.190	6.190	6.190	0.04-0.02	0.07-0.07
		2	$\times 60$			6	0.9	0.181	0.181	0.07-0.07 ^(b)	
		3	$\times 60$			6.0					
		4	$\times 100$			6.5					
		5	$\times 100$			6.5					
		6	$\times 100$			6.5					
		7	$\times 100$			6.5					
7o	6-27-69	1737-1737	1			6-6	6.190	6.190	6.190	0.04-0.02	0.07-0.07
		2	$\times 60$			6	0.9	0.181	0.181	0.07-0.07 ^(b)	
		3	$\times 60$			6.0					
		4	$\times 100$			6.5					
		5	$\times 100$			6.5					
		6	$\times 100$			6.5					
		7	$\times 100$			6.5					
7p	6-27-69	1737-1737	1			6-6	6.190	6.190	6.190	0.04-0.02	0.07-0.07
		2	$\times 60$			6	0.9	0.181	0.181	0.07-0.07 ^(b)	
		3	$\times 60$			6.0					
		4	$\times 100$			6.5					
		5	$\times 100$			6.5					
		6	$\times 100$			6.5					
		7	$\times $								

• Experiments

10 Flight system (system 2966-2) failure

• beginning of flight

End of flight

© 2000 by [Schaum](#)

upper limb

P. O. Forbes Dec

- Interpolated

1000 J. POLYMER SCI.: PART A

C. Solar Proton Spectra and Neutron Yields

Our best estimates of the solar proton spectra during three characteristic events are shown in figures 30b, 31b, and 33b, for the increases of February 25, 1969, March 30, 1969, and January 25, 1971. The portions of the spectra shown at energies below 1 GeV are direct measurements of solar protons by rocket, satellite, and stratospheric detectors.

The portions of the spectra above 1 GeV are based on observations of the increases in the counting rates of the world network of sea level neutron monitors. To obtain the solar proton spectrum, we compared the counting rates of monitors at various cutoff rigidities with the rates that would be observed for different power laws in rigidity and in kinetic energy. The neutron monitor counting rates from any given spectrum were determined by folding into the spectrum the relative specific yield functions of Lockwood and Webber⁸⁴, normalized to the ratio, counting rate/observed primary flux, at solar minimum. The high energy increases were extrapolated to times later in the events by use of the observed time constant of the decay of the sea level excess, shown in figures 30a, 31a, and 33a.

As the recent literature on solar proton spectra suggests, the curves in figures 30b, 31b, and 33b appear to be power laws in kinetic energy,

$$dN/dE = AE^{-n(E)}$$

7

The exponent, $n(E)$, of the differential flux, dN/dE , increases with energy, E . Such spectra are not readily exploited in predicting neutron increases, on the basis of the limited number of observations we have made.

Freier and Webber¹²⁹ observed that the solar proton fluxes during many events could be fitted to a simple exponential in rigidity over a wide spectral range, where

$$N(>P) = N_0 \exp(-P/P_0)$$

8

and N is the integral flux of protons of rigidity $>P$

N_0 is the total proton flux

P_0 is a constant, the characteristic rigidity.

We have analyzed our neutron data in terms of specific yields from exponential solar spectra (1) because of the simplicity of categorizing solar events in terms of the spectral parameter, P_o . (2) to evaluate the goodness of fit of experimental neutron yields to the exponential approximation of the observed proton spectra, and (3) to compare with the results of the other observers who examined their data vs. the neutron yields, calculated by Lingenfelter and Flamm^{113, 114}, from proton spectra exponential in rigidity.

For the incident primary spectrum, we have used the proton fluxes > 30 MeV and > 60 MeV from the Solar Proton Monitoring Experiment (SPME) on Explorers 34 and 41¹¹⁶. From the two points on the integral spectrum we obtain

$$P_o = \frac{44.17 \text{ MV}}{\log_{10}(N > 30 \text{ MeV}/N > 60 \text{ MeV})} \quad 9$$

Equation 9 neglects the departure from the exponential of the proton fluxes > 10 MeV, also measured by SPME. We found, however, that such deviations could be neglected because of the small effect that the protons in the energy region below 30 MeV had on the neutron counting rates. This conclusion is based on our observations of the neutron fluxes during very low energy events.

The solar proton spectra, derived from the SPME data and extrapolated by an exponential in rigidity, are shown in figures 30b, 31b, and 33b, where they can be compared with the proton observations at the higher energies. Note the deviations of the exponential (converted to energy spectrum) from the observed spectra above 100 MeV. Unfortunately, the observed spectra also show large differences, so that the quality of fit of the exponential to the actual proton spectra is not clearly illustrated.

Figure 34 shows the neutron flux per incident proton-cm⁻²-sec⁻¹ > 30 MeV vs P_o , as calculated in equation 9. Small increases are also shown, but only the data with less than 30% uncertainty have been included. (See Table I for error.) The points from a single event are connected by lines with arrows pointing along the flow of time. We have also joined, by a dashed line, the data points from the main phase and early decay of the solar protons of March 30, 1969 and from the early decay of the events of February 25, 1969 and January 25, 1971. All three were associated with high energy proton flares, which produced increases in the sea level neutron monitors (figures 30, 31, and 33).

We observe that while the three sets of points fall more or less on the dashed curve over the entire range of P_o , the deviations from the curve at later times in the events and during other events are appreciable. For example, at a P_o of 40-50 MeV, the yield on January 25, 1971 was a factor of 2-3 lower than that observed during the small but well correlated increase which occurred in the midst of a flight on November 1, 1968.

We conclude, therefore, that the neutron yields in the atmosphere can be predicted to within, at best, a factor of 2 or 3 with the approximation of an exponential spectrum for the solar primaries, based on SPME. On the other hand, if we examine the observed primary spectra in figures 30b, 31b, and 33b, it is apparent that the actual measurements differ frequently among themselves by factors at least as great as those we have just quoted, either at the same energy or, if the observations are in different energy intervals, in the goodness of fit of one spectral region to another. To determine the effect of the variations in spectra on the fast neutron yield at 65 g/cm^2 and to evaluate the contribution of solar protons to the total neutron distributions, we must employ the Monte Carlo calculation.

D. Monte Carlo Calculation

Figure 35 shows the fast neutron yield at various atmospheric depths vs. incident proton energy, as determined from the Monte Carlo program. The proton flux was assumed to be isotropic at the top of the atmosphere.

The depth dependence of the fast neutron flux generated by exponential solar proton spectra of varying P_o is illustrated in figure 36. The curves are normalized to an incident proton flux of $0.1 \text{ proton-cm}^{-2} \text{-sr}^{-1} \text{-sec}^{-1}$, isotropically distributed.

The dependence of the 10^{-7} - 10^2 MeV differential neutron spectrum on the mean energy of the incident protons was discussed earlier. (See figures 23 and 24.) Figure 37 shows the neutron energy distributions for two representative solar proton spectra.

In this section, we shall focus on the Monte Carlo output of the 1-10 MeV neutron spectrum at $60-70 \text{ g/cm}^2$ during solar proton events. The estimated proton spectrum during the spectacular increase of February 23, 1956¹ yielded a neutron spectrum which could be approximated by a power law in energy, with a negative exponent of 1.25 ± 0.08 , the same as that calculated for neutrons from the galactic cosmic radiation. As the solar proton spectrum softens, i. e., with decreasing P_o , the Monte Carlo

fast neutron distributions steeper above 6-7 MeV. If we attempt to fit the calculated distributions to a single power law, we find that the spectral index increases from 1.3 ± 0.1 at a P_o of 250 Mv to 1.5 ± 0.1 at a P_o of 50 Mv. The counting statistics during the low energy events were not good enough to detect changes in the neutron spectrum above 10 MeV.

The contribution of the solar protons to the total reservoir of radiocarbon and to the neutron leakage flux are given in Table XIX, which also includes the integrated 0-19 MeV neutron production rates in the atmosphere.

E. Discussion

We are now in a position to test how well the calculation of the neutrons from solar protons reproduces the observed fluxes and how sensitive the calculation is to uncertainties we have demonstrated in the solar proton spectrum. Table XIX lists the measured neutron fluxes from solar particles during each event observed and presents the theoretical neutron flux calculated in two ways. The first considers the solar proton spectra to be exponentials in rigidity. The value of P_o is based on the SPME proton fluxes during the NYU measurement. The second uses a composite proton spectrum, derived from the references listed in the table. Figure 34 compares observations made during the progress of a solar particle event with the Monte Carlo calculation of neutron production, assuming that the proton spectrum is an exponential distribution in rigidity. The actual time profiles of the calculated and of the observed neutron fluxes during a proton increase are illustrated in figure 32 for the large low energy event of April 12-15, 1969.

Examining the goodness of fit of the calculated to the experimental neutron fluxes at 65 g/cm^2 , we find:

(1) Figure 34: The experimentally derived neutron yields from protons with exponential rigidity spectra follow roughly the same shape as the curve derived from the Monte Carlo program. The experimental points are occasionally on the calculated curve but generally tend to be lower, on the average, by 40% at the highest P_o and 40-65% at the lowest P_o . Moreover the goodness of fit of the data to the calculated values varies during the progress of individual events, the relative fit often improving later in the event. Such behavior is possibly associated with increasing isotropy of the protons with time. The experimental yields from event to event, where observed, can vary by factors of 2 or more about the mean value of the neutron yield at a given P_o . At least a portion of the

TABLE XIX

CONTRIBUTION OF NEUTRONS FROM SOLAR PARTICLE EVENTS TO THE 0-19 MEV NEUTRON SOURCE, TO RADIOCARBON PRODUCTION, AND TO THE LEAKAGE FLUX. THE INTEGRAL PROTON FLUX, N , ABOVE P MV IS $N = e^{-P/P_0}$ PROTONS-CM $^{-2}$ -SR $^{-1}$ -SEC $^{-1}$.

<u>Spectrum</u>	<u>Source</u>	<u>C^{14}</u>	<u>0-20 MeV</u>	<u>1-10 MeV</u>	<u>% of Source</u>	
			<u>Leakage</u>	<u>Leakage</u>	<u>C^{14}</u>	<u>Lkg.</u>
<u>(P_0, MV)</u>	<u>(n-cm$^{-2}$-s$^{-1}$)</u>	<u>(cm$^{-2}$-s$^{-1}$)</u>	<u>(n-cm$^{-2}$-s$^{-1}$)</u>	<u>(n-cm$^{-2}$-s$^{-1}$)</u>		
20	6.44×10^{-7}	8.23×10^{-8}	4.47×10^{-7}	3.03×10^{-7}	13%	70%
50	7.75×10^{-4}	1.19×10^{-4}	4.93×10^{-4}	3.30×10^{-4}	15%	64%
100	1.89×10^{-2}	4.24×10^{-3}	9.39×10^{-3}	6.03×10^{-3}	22%	50%
250	4.51×10^{-1}	1.57×10^{-1}	1.23×10^{-1}	7.19×10^{-2}	35%	27%
500	2.62	1.05	4.69×10^{-1}	2.60×10^{-1}	40%	18%
1000	8.76	3.77	1.15	6.20×10^{-1}	43%	13%
2000	2.00×10^1	8.93	2.05	1.09	45%	10%
23 Feb. 1956, total flux, prompt upper limit:						
	5.72×10^5	2.33×10^5	9.83×10^4	5.42×10^4	41%	17%

variations can be attributed to the departure of the proton spectra from the exponential assumed in constructing the figure, as we shall now demonstrate.

(2) Table XVIII: Using more complete primary spectral data than is available from the SPME data, we find that the calculated neutron fluxes from the Monte Carlo program display large uncertainties which arise solely from the data spread in the primaries. At least part of the uncertainty comes about because the neutron yields rise rapidly with energy in the solar particle regime, so that the calculation is quite sensitive to small differences in the spectral shape of the primaries. For example, in the event of February 25, 1969, illustrated in figure 30, Green et al.¹²⁴, and Barouch et al.¹²¹, in different experiments on the same rocket found similar values for the integral proton flux above 30 MeV but the integral spectrum at the highest energies differed by a factor of ~ 5 . As a result, the neutrons calculated from the two sets of data varied by a factor of 10, as noted in Table XVIII. In general the observed values of the neutron intensity during the more energetic events ($P_o > 70$ MeV) lie within the range of calculated values when the proton measurements include the observations in the stratosphere (Table XVIII). During the softer events, ($P_o \sim 70$ MeV) notably January 25, 1971 (figure 33) and April 11, 1969 (figure 34), the calculation sometimes deviates from the observed neutron flux by a factor of 2 or more.

We now consider possible sources of the differences among the proton observations and between the calculation and the observations, especially during low energy events.

(1) The proton intensity observed in satellite measurements outside of the magnetosphere can differ from the flux reaching the earth's atmosphere during a proton event. Specifically, the calculated neutron yields derived from the stratospheric observations of primary protons by

Bayarevich et al.¹²⁰, and Bazilevskaya et al.¹¹⁸, and Bazilevskaya (1972, private communication), are in far better agreement with our atmospheric neutron measurements than the spectra derived from satellite data taken outside of the magnetosphere, (Quenby, 1972, private communication). Direct observations of differences in access of particles to the magnetosphere have been made in satellite measurements inside the magnetosphere. For example, during the February 25, 1969 event (figure 30),

Engelmann et al.¹³⁰, found an enhancement of the energetic protons (>360 MeV) in the auroral and polar cap regions as compared with protons at the latitude of the NYU flights, 70° - 77° invariant latitude, the differences

persisting up to the time of the fast neutron measurements. The effect was associated by the authors with anisotropies in the primary radiation at higher energies. The same phenomenon might be responsible in part for the differences between the stratospheric measurements of the solar protons and satellite measurements (figures 30b, 31b, and 33b).

(2) During low energy events, there are large anisotropies in the 30-60 MeV proton fluxes, particularly in the early convective phase of particle transport. Even when event integrated fluxes are examined, experiments with different directional response on the same satellite display notable differences in the proton fluxes. For example, whereas the SPME experimental uncertainty is $\sim 25\%$, the event integrated fluxes among the SPME and the two other experiments on the Explorer 34 satellite differed by as much as a factor of 2^{131} .

(3) Anisotropies of the proton flux at the top of the atmosphere can alter the altitude distribution of the secondary neutrons, since the vertically incident protons, for example, penetrate deeper into the atmosphere than protons arriving from other directions. It should be mentioned however that in the February 25, 1969 event, where access to the magnetosphere was observed to be location dependent, anisotropies were not observed inside the magnetosphere¹³⁰.

(4) Chupp et al.¹³¹ have suggested that alpha particle fluxes, not properly accounted for, can be responsible for errors in the calculated neutron yields. However, during those periods listed in Table XVIII, during which alpha and heavier particles were observed, the maximum total contribution of $Z > 1$ nuclei to the solar particle neutron yield was less than 10%. The percentage of alphas and heavier particles varies from flare to flare, but large alpha/proton ratios are a rarity in solar particle events.

F. Application to Other Experiments

The reports of Lockwood and Friling¹¹² and of Greenhill et al.¹¹⁰, present both efficiencies and counting rates of moderated counters exposed to neutrons during solar particle events. The main efficiency of their detectors was at neutron energies below 1 MeV. This allows us to test the Monte Carlo calculation in a region of the neutron spectrum different from that of the NYU detector and in regions of the atmosphere where no NYU flare observations were made.

The rocket experiment of Lockwood and Friling was launched June 7, 1967. The authors converted their observed counting rates to leakage flux using the neutron albedo spectrum calculated by Lingenfelter. We have made a similar analysis with the neutron spectrum from the Monte Carlo program.

Table XX lists the percentages contribution of neutrons of different energies to the counting rate of the Lockwood detector, first, as derived from the Lingenfelter neutron leakage spectrum and, second, as calculated from the Monte Carlo results. As we noted in Section VI B, the Lingenfelter spectrum drops much more precipitously than that of the Monte Carlo calculation at energies $> 1-2$ MeV. As a consequence of the smaller flux above 1 MeV, the ratio, counting rate/flux, is 50% higher than the Monte Carlo value; and the leakage flux is 50% less.

Section (b) of Table XX shows the intermediate steps in deriving the solar excess neutron flux from the relative counting rates of the detector during the proton event of June, 1967 and during a quiet time flight. We have used Monte Carlo leakage neutron spectra for the galactic and for the solar secondary neutrons. In Section (c), we show the results of independently calculating the neutron leakage flux from the Monte Carlo calculation of neutrons from the solar proton spectra on June 7. The hourly averages of the SPME proton fluxes were used. The Monte Carlo neutron flux for the proton spectra shown in the Table, was

$0.47 \text{n-cm}^{-2} \text{-sec}^{-1}$ at the beginning of the day, with a daily mean of 0.22. Lockwood and Friling presented a preliminary estimate of the solar proton spectrum during the flight, which matches the early and the daily average of SPME on June 7, if we discard their point below 25 MeV. We can conclude that, within the error bars of the proton spectrum, the agreement of the calculated with the observed flux is good.

Table XXc also shows the leakage rate, defined in Section VI B, and the ratio, leakage rate/leakage flux, for the solar particle spectrum and for the galactic cosmic ray spectrum. The ratio is observed to increase with increasingly energetic spectra. In fact, the increase is 40-50% between a solar particle spectrum with a $P_0 = 40$ MeV and a galactic cosmic ray spectrum. The changing ratio indicates that during soft proton events more of the neutrons between 0 and 100 MeV are leaving the atmosphere at large zenith angles. This phenomenon has been noted by Merker (1972), who has discussed it in terms of the last collision site of a particle escaping from the atmosphere. The implications of this phenomenon in terms of leakage neutron measurements is that (1) during solar events with a soft proton spectrum, the neutron leakage rates (which are the quantities reported by Lingenfelter and Newkirk above the atmosphere), are smaller relative to

TABLE XX

NEUTRON LEAKAGE RATES FROM SOLAR PROTONS,
JUNE 7, 1967; COMPARISON OF THE EXPERIMENT
OF LOCKWOOD AND FRILING WITH CALCULATION.

(a) Percent contribution of neutrons in different energy bins to the counting rates of the Lockwood detector, using the neutron leakage spectrum of (1) Lingenfelter and (2) the Monte Carlo calculation.

Neutron energy, MeV	<0.1	0.1-1	1-10	10-100
<u>% of Total Counting Rate:</u>				
(1) Lingenfelter	29.5	48.6	20.1	1.7
(2) Monte Carlo	21.0	33.0	36	10

The ratio of counting rate to neutron flux for proton spectra with P_0 of 40 MeV and 100 MeV and for the high latitude galactic cosmic ray spectrum.

	Galactic Cosmic Rays	Solar Protons	
		$P_0 = 40$	$P_0 = 100$
(1) Lingenfelter	3.65		
(2) Monte Carlo	2.5	2.6	2.2

(b) Calculation of the neutron flux for the June 7, 1967 event from the counting rates of the Lockwood detector during the proton event and during a quiet time flight on August 24, 1966 (normalization to June 1967 is shown).

DRNM	Counting Rates (sec ⁻¹)			Neutrons from Solar Protons [*]	
	Given	Normalized	Solar Excess	Lingenfelter	Monte Carlo
8/24/66 6800	2.42	1.85			
6/7/67 6420	2.98	2.98	1.13	0.31	0.48

* neutrons-cm⁻²-sec⁻¹.

(c) Calculation of the neutron flux at satellite altitude and of the neutron leakage rates, due to the solar protons observed during June 7, 1967. The neutrons are given for the proton spectrum derived from the SPME proton data. The neutron flux and rate calculated for the galactic proton and alpha particle spectra at the time of the event are also given.

Primary Spectrum	Beginning 47 exp(-P/78)	End 62 exp(-P/51)	Average	Galactic
Counting Rate/Flux	2.3	2.5		2.5
Leakage Rate/Flux	0.42	0.39	0.40	0.55
Neutron Flux	0.47	0.07	0.22	0.74 n-cm ⁻² -sec ⁻¹
Neutron Leakage Rate	0.20	0.03	0.09	0.41 n-cm ⁻² -sec ⁻¹

the neutron flux (which a detector measures) than for the galactic radiation. (2) The anisotropies in the leakage flux must be accounted for, if the detector sensitivity varies with angle of incidence. In the event of June 7, the neutron leakage rate was half of the galactic cosmic ray leakage rates.

Figure 38 shows the neutron excess, observed in the stratosphere by Greenhill et al.¹¹⁰ during a solar event on September 3, 1966. The solid curve was derived by Greenhill et al. from Lingenfelter's calculation of the depth dependence of the components of the neutron spectrum from incident protons. The P_0 of the Lingenfelter calculation was 125 Mv.

The authors report several measurements of the solar proton flux during September 3. We have taken their own estimate derived from the charged particle measurements on their vehicle, and have calculated the neutron counting rates they would observe from the efficiencies they present, folded into the Monte Carlo neutron spectrum from the flare protons. P_0 was 45 ± 15 Mv, and the flux greater than 200 Mv was 200 ± 70 protons- $cm^{-2} \cdot sr^{-1} \cdot sec^{-1}$. The Monte Carlo neutron counts for this spectrum are shown in the diagram; the error bars represent only the uncertainty in P_0 and not in the integral flux > 200 Mv. Within the very wide limits set by the estimate of error in the solar proton spectrum, the Monte Carlo results are consistent with both the shape and the magnitude of the neutron counting rates. The diagram also shows the change in the atmospheric profiles with P_0 . The depth dependence of the counting rate at a P_0 of 125 Mv would be flatter than the solid curve in figure 38. This is expected since the excess primaries introduced in the Lingenfelter calculation penetrate the atmosphere less effectively, because they enter the atmosphere at large zenith angles.

G. Other Flare Calculations

The Monte Carlo results can be compared directly with the calculation by the ORNL group² of neutron production in the flare of February 23, 1956. Both calculations involved Monte Carlo simulation and both employed the proton flare spectrum of Foelsche¹. From 10 to 200 g/cm² the ORNL calculation was $\sim 15\text{-}20\%$ below the NYU 0-100 MeV neutron flux. The energy spectrum of neutrons at 23 g/cm², shown in figure 8 of the ORNL article, was 80% to 100% of the NYU results from 10^{-7} to 10^2 MeV. The only notable difference was in the leakage flux; the ORNL value was around half the value we report. The number is consistent with the NYU calculated leakage rates.

H. Summary of Observations and Calculations

1. Measurable fluxes of fast neutrons are present at 55-75 g/cm² atmospheric depth during all solar particle events for which the proton flux above 60 MeV exceeds about 1 proton-cm⁻²-sr⁻¹-sec⁻¹.

2. Extrapolating the flare proton spectra from the SPME by an exponential in rigidity, we find that the neutron production rates per incident proton rise rapidly with characteristic rigidity, P_o ; the fast neutron yield at the cosmic ray transition maximum increases a hundred fold over the range of P_o encountered in aircraft flights near solar maximum. We also note that the observed neutron yields per incident proton flux above 30 MeV deviate from a smooth curve vs. P_o by as much as a factor of 2 in either direction.

3. When the measured fast neutron yields vs. P_o are compared with the values derived from a Monte Carlo calculation, the measurements are found to be, on the average 40% lower at high P_o and 40-65% lower at low P_o than the calculated yields although some flare flight data fall on the theoretical curve. The agreement between observation and calculation improves if primary proton data include measurements at higher energies than found in the SPME reports (used to derive P_o). In particular, if the stratosphere measurements of Bazilevskaya et al.¹¹⁹ are used in the proton integral spectral range of 200-500 MeV, the observed neutron fluxes are in agreement on the average with the calculated values for spectra with large P_o and about 50% of the calculated values at P_o of ~ 70 MeV. The differences between experiment and calculation in the low energy proton flares can be caused by the use of too high cross sections for protons below 60-100 MeV in the calculation, but other equally plausible explanations exist. In particular, anisotropies in the proton beam and preferential access of protons to the magnetosphere can cause the proton flux at the top of atmosphere to differ from that observed by satellites outside the magnetosphere.

4. Within the accuracy of the solar proton data, the Monte Carlo results are in good agreement with two observations made in the atmosphere and above the atmosphere with moderated neutron counters. Both observations were at low P_o , and both had some on-board indication of the primary spectrum. Two other measurements have not been analyzed

because of the uncertainty in geomagnetic cutoff or detector response function.

I. The Geophysical Effects of Neutrons from Solar Protons

We can now examine the fluctuations in the neutron distribution due to solar flare particles, and we can determine the long term effects on the levels of neutrons and their products. In Table XXI, we show the 0-19 MeV neutron production rates and the radiocarbon and leakage rates during the proton events in which the NYU detector flew. The January 28, 1967 event is also shown as well as the combined effect of all the other periods from 1965-1971 with solar particles near the earth.

The numbers in Table XXI are based on the exponential approximation of the proton spectra and must be thought of as an upper limit to the actual values, which can be lower by a factor of two from the listed rates during the less energetic events. At the peak of the most productive solar particle increases of cycle 20, the maximum rates of production of radiocarbon were roughly 6x those from high latitude galactic cosmic ray neutrons, and the leakage rates were a factor of 50x greater. On the other hand, the time integrated rates were 2-3 orders of magnitude below those from galactic cosmic ray neutrons. During the much more active solar cycle 19, the major event of February 23, 1956 alone produced roughly 40x the leakage rates and 150x the radiocarbon as all the solar events in solar cycle 20. Averaged over the 11 year solar cycle, this single event added approximately 10% to the radiocarbon production in solar cycle 19.

The increment from the flare of February 23, 1956, was cancelled by the depression in radiocarbon production from the galactic cosmic radiation during solar cycle 19. The exclusion of the galactic primaries was associated with the 1956 event as well as with other large but not comparable flares. As a result, the average C^{14} production was the same from both the unusually active solar cycle 19 and the average solar cycle 20.

TABLE XXI

GLOBAL AVERAGE PRODUCTION OF RADIOCARBON FROM
 SOLAR PROTONS WITH SPECTRA EXPONENTIAL IN RIGIDITY.
 THE PROTON FLUX IS 1 PROTON-CM⁻²-SEC⁻¹ AT ENERGIES
 ABOVE 30 MEV. NORMAL CUTOFFS ARE ASSUMED.

<u>P_o</u>	<u>Monte Carlo</u>	<u>Lingenfelter</u>
50	1.5×10^{-4}	4.8×10^{-4}
100	1.0×10^{-3}	1.7×10^{-3}
150	3.2×10^{-3}	4.5×10^{-3}
200	6.3×10^{-3}	9.0×10^{-3}
250	1.3×10^{-2}	1.8×10^{-2}
300	2.4×10^{-2}	3.2×10^{-2}
325	3.2×10^{-2}	4.2×10^{-2}

IX. COSMIC RAY MODULATION DURING 1968 TO MID-1971

A. Introduction

The fast neutron intensity at the high latitude transition maximum and the counting rates of high latitude neutron monitors respond, on the average, to different portions of the spectrum of primary cosmic rays. Because of the differences in response, changes in the regression relation between the counting rates of the NYU aircraft neutron detector and the counting rates of the Inuvik neutron monitor, at a given level of modulation of the neutron monitor rates, can be interpreted in terms of a change in slope of the spectrum of variation of cosmic rays, either in the declining or the recovery phase of the cosmic ray intensity variation. Such effects were observed in both transient and long term decreases in 1968 to mid-1971, and were mentioned in Section IV. B. In this section we discuss the methods employed to detect and quantify the cosmic ray spectral variations, we discuss the nature of the variations, and we summarize the implications of these variations to the solar and interplanetary parameters involved in cosmic ray modulation. The discussion will include some extensions of the work, completed after the termination of NASA Contract NASI-10282. A more detailed analysis has been

presented elsewhere¹³²⁻¹³⁶.

B. Comparison of the Response of Neutron Monitors with the Response of the NYU Detector to the Primary Spectrum

Figure 39 shows the yield functions for primary cosmic ray protons of the fast neutron detector at the high latitude transition maximum and of the neutron monitors at zero cutoff rigidity. Curve 1 is the fast neutron flux at

$60-70 \text{ g/cm}^2$ and zero cutoff. Curve 2, from Debrunner and Flueckiger¹³⁷, is the specific yield of an NM-64 neutron monitor to primary protons incident vertically at the top of the atmosphere; the derivation of the yield functions includes a calculation of the nucleonic cascade in the atmosphere. Curves 3

and 4, which are the neutron monitor yields obtained by Lockwood and Webber⁸⁴

and Mathews et al¹³⁸, were derived from an analysis of the latitude dependence of neutron monitor counting rates and the observed spectrum of cosmic ray protons and alpha particles at the time of a latitude survey with neutron monitors. In the latter two calculations, alpha particles, at the same energy per nucleon as protons, were assumed to interact in nuclear collisions as four independent nucleons.

When the primary proton and alpha spectra are folded into the

response function shown in figure 39, the time variations in the counting rates of the NYU detector are found to arise principally from 1-3 GeV protons, whereas neutron monitor variations are produced on the average, from protons and alpha particles between 10-15 GeV per nucleon, at low cutoff rigidity.

For an analysis of spectral variations based on two detectors at different locations to be valid, the incident primary radiation must be isotropic or the two detectors must measure secondaries from particles arriving from the same directions in space. The Inuvik neutron monitor was chosen as the high energy detector since the aircraft detector usually passed over Inuvik twice during a typical flight. To insure that none of the transient spectral effects arose principally from cosmic ray flow patterns, we employed several other neutron monitors with directions of viewing surrounding those along the aircraft trajectory. Table XXII lists the asymptotic directions of arrival of cosmic rays at the neutron monitors.

C. Calculation of the Spectrum of Variation of Cosmic Rays

From the neutron monitor data at varying P_c and the high latitude flux of the fast neutrons at the transition maximum between 1968 and 1971, it is possible to generate a series of monthly curves of the parameter, M , where $M = \ln(j(P_c, 1965)/j(P_c, t))$; j is the primary intensity of protons or alphas, P is rigidity. Monthly plots of M are readily converted to monthly variations in the cosmic ray spectrum using the 1965 observations of cosmic ray intensity.

To obtain the modulation parameter, M , above 2 Gv, first, the counting rates of neutron monitors at various cutoff rigidities were used to estimate of the modulation over the entire rigidity range. Then the fast neutron flux was used to correct the modulation between 2 and 4 Gv. Above 13.3 Gv, only an approximate value for M , based on the Kula neutron monitor, was obtained.

Step 1: The modulation of the primary spectrum is related to changes in the latitude dependence of neutron monitor counting rates by

$$\sum j_n(P_c, 1965) R_n(P_c) / \sum j_n(P_c, t) R_n(P_c) = (dN/dP_c)_{1965} / (dN/dP_c)_t \quad 10$$

where n is the nuclear species, dN/dP_c is the slope of the neutron monitor latitude curve, and R is the specific yield of the monitor for species n at rigidity P . In the rigidity range where the cosmic ray variations depend only on rigidity, the left hand side of equation 10 reduces to $\exp(M)$, whence

TABLE XXII
ASYMPTOTIC ARRIVAL DIRECTIONS OF INCIDENT COSMIC RAYS ⁺

	<u>Lat</u>	<u>Long</u>	1.5 GV		4.5 GV		11 GV		15 GV		25 GV	
			<u>Lat</u>	<u>Long</u>								
Inuvik [*]	68.35 ^o	-133.73 ^o	10.4,	-127	31.7,	-128	43,	-128	45 ^o ,	-125 ^o	52,	-120
Sulphur Mt.	51.20 ^o	-115.61 ^o	-5,	2.4	-14.5,	-85	7,	-97	12,	-97	26,	-92
Resolute	74.69 ^o	-94.91 ^o	59,	-92	64,	-88	67,	-86	68,	-83	72,	-82
Deep River	46.10 ^o	-77.50 ^o	-6,	45	-11,	-31	7,	-44	13,	-42	29,	-44
Alert	82.50 ^o	-62.33 ^o	83,	11	84,	-15	83,	-28	83,	-21	85,	-28
Goose Bay	53.33 ^o	-60.42 ^o	-15,	11	8.5,	-16	22,	-24	28,	-21	42,	-23
Dallas	32.78 ^o	-91.07 ^o	-----		25,	120	-29,	-29	-19,	-39	5,	-51
	<u>Lat</u>	<u>Long</u>	<u>13.5 GV</u>		<u>15 GV</u>		<u>25 GV</u>		<u>45 GV</u>		<u>95 GV</u>	
Makapuu Pt.	21.30 ^o	-157.66	23.6,	.58	-20	, -20	-12,	-95	6	, -123	16,	-140
Kula	20.44 ^o	-157										

⁺ Data from Hatton, C.J. and D.A. Carswell AECL-1824 (1963)

^{*} Private Communication

Shea and Smart Calculation- .5 - 2.6 GV asymptotic longitude at $\sim -133^{\circ}$ from 0.00 UT - 3:00 UT, and is -123° by 6:00 UT, 136° at 12:00 UT, then back; latitude varies $\sim 5^{\circ}$ at 4.6 GV, less than 2° variation for ~ 10.6 GV primaries. Less than 5° in either asymptotic latitude or longitude of arrival for angles up to 32° from the vertical.

$$N(P_c, t) = N(P_{c \text{ max}}, t) + \int_{P_c}^{P_c \text{ max}} (dN/dP)_{1965} \exp(-M(P)) dP$$

11

where $M(P)$ indicates that equation 11 is valid only in the rigidity and energy range where the dependence of M on parameters other than P is negligible. $P_{c \text{ max}}$ is the cutoff rigidity of the lowest latitude neutron monitor employed.

To evaluate M from equation 11, we employed the NM-64 neutron monitor data from Inuvik ($P_c = 0.18$ GV), Dallas (4.35 GV), Hermanus (4.90 GV), Rome (6.32

GV) and Kula (13.3 GV = $P_{c \text{ max}}$)¹¹⁶. As an additional check, data from IGY monitors at Ottawa (1.08 GV), Ushuaia (5.68 GV), and Brisbane (7.21 GV)¹¹⁶

were processed separately. Different functional forms for M were tested, including power laws and polynomials in P . The best fit in the least squares sense was generally of the form of a power law in P , of the form

$c_1 P^{-n_1}$ below 13 GV and $c_2 P^{-n_2}$ above 13 GV.

Step 2: The fast neutron flux at the transition maximum was calculated by folding into the neutron specific yield (figure 39) the modulated primary proton and alpha spectrum, derived from the cosmic ray intensities observed in 1965 and the values of M determined in step 1. The calculated neutron flux was then compared with the monthly average of the observed neutron flux and the difference was converted to an additional primary flux between 2 and 4 GV. It should be noted that the correction was usually small, rarely exceeding 4% of the neutron flux, or 60 .

Step 3: the primary cosmic ray modulation above 13.3 GV was estimated from the counting rates of the Kula monitor, by folding the specific yield of the Kula neutron monitor, as deduced by Mathews et

al¹⁴¹, illustrated in figure 39, into the best fitting modulated primary spectrum, as determined from the best fitting exponent, n_2 , of the modulation parameter above 13 GV. It should be noted that if one of the other response functions in figure 39 were employed, the modulation spectrum would exhibit spectral indices differing by roughly $\pm 20\%$, but the time variations of n_2 would be essentially the same. Effects due to variations in the upper rigidity limit of cosmic ray modulation were neglected.

D. Results, Transient Cosmic Ray Decreases

Transient cosmic ray events fell into two broad spectral classes, each

distinguished by differences in (1) the time histories of the counting rates of the neutron monitors during the decline and recovery of intensity and (2) the relation between the rate of change of the fast neutron flux and that of the neutron monitor counting rates.

Type I events were classic Forbush decreases; they are illustrated by the decrease of March 24, 1969, shown in figure 40. Their characteristics are:

- (1) The onset of the event was always preceded by or simultaneous with the sudden commencement of a geomagnetic storm (SSC).
- (2) The neutron monitor rates declined rapidly, $\geq \frac{1}{2}$ - 1% per hour in the main phase. The recovery was slow, lasting 5 to 10 days or more.
- (3) The fast neutron flux lagged the Inuvik neutron monitor counting rates both in the decline and in the recovery of intensity.

As shown in figure 40, the regression curve of the lower energy primary intensity, represented by the fast neutron flux, relative to the higher energy intensities, traces out a hysteresis loop (solid line). The dashed curve in figure 40 shows the regression relation for the months surrounding the type I event of March 1969. Also shown in figure 40 are regression curves of the fast neutron counting rates vs the counting rates of high latitude neutron monitors with different directions of viewing, as well as the counting rates of monitors at greater cutoff rigidity during the same type I event. Note that the spectral changes illustrated by the neutron intensity vs neutron monitor counting rate at Inuvik are also present when neutron monitors with different directions of viewing are employed.

Type II events were more symmetric than type I; they are illustrated in figure 41, which represents a small decrease occurring seven days before the March 24, 1969 type I event. The characteristic features of type II events were:

- (1) The onset of the decrease was slow and in only 1 case out of seven (figure 41) was the onset associated with an SSC. Generally, if an SSC occurred at all, it took place during later phases of the event.
- (2) The decline to minimum usually occurred over several days or appeared in the neutron monitor counting rates as a series of small decreases with large diurnal variations. The total duration, decline and recovery, at neutron monitor energies, rarely exceeded 10-15 days.
- (3) The fast neutron flux decreased more rapidly and recovered more rapidly (on or above the curve for the decline) than during the type I events, as is illustrated in the regression curves for the March 17 event, shown in figure 41.

Figure 42 shows the time histories of the fast neutron vs the Inuvik neutron monitor rates for a group of type I and type II decreases observed during the NYU aircraft measurements. It appears, from figure 42, that the spectral characteristics and time histories of the different classes of events were independent of solar epoch over the period 1968-1971, when the neutron monitor rates ranged from a minimum 79% to a maximum 96% of the May 1965

values at high latitude. In each type of event, the profiles of the fast neutron flux vs the counting rates of the neutron monitors displayed comparable slopes from event to event, even as the long term regression, which represented an average over the modulation period(dashed curve), occasionally overlapped and occasionally was displaced from the lines connecting the points of observation during the decreases.

As a further illustration of the spectral differences between type I and type II events, we employ the rough indices, R_d and R_r , where R_d is the ratio

of the % decline of the fast neutron flux to the % decline of the neutron monitor counting rates, and R_r is the corresponding ratio for the recovery period.

Figure 43 shows R_r vs R_d for type I and type II events for which observations were made during both the decline and recovery of intensity. The points representing the two types of events are observed to cluster in two different portions of the graph, as a result of the differences in spectral evolution of the two types of decrease. The average values of R , including events not shown in figure 43 because only the declining or recovery phase was observed, are shown in Table XXIII.

TABLE XXIII

RATIO OF PERCENTAGE CHANGE IN THE FAST NEUTRON FLUX TO PERCENTAGE CHANGE IN THE COUNTING RATES OF THE INUVIK NEUTRON MONITOR

	R_d	R_r	No. Events		R, Decline and Recov.
			Tot.	Part.	
Type I	2.4 ± 0.6	2.0 ± 0.6	8	12	
Type II	3.1 ± 0.7	3.3 ± 0.8	5	9	
Long Term					
1968					
Without FD					$3.2(\text{early})-3.1(\text{late})$
With FD					2.5
6/69 - 12/69					$2.3(\text{early})-1.7(\text{late})$

The estimated uncertainties shown in Table XXIII are upper limits and include statistical errors, the effects of incomplete coverage of events, including discrete sampling, and hybrid effects. The error limits are for individual events and are lower by a factor of ~ 3 when the events are considered by class. With the resultant upper limit to the uncertainty in R ,

the spectral difference between type I and type II events is evident. An analysis of the significance of the results shown in figure 43 is presented in

Verschell et al.¹³⁵, in which it is demonstrated that the probability that the observed characteristics of type I and type II events are uncorrelated is less than 1%.

Table XXIII also includes the "long term" coefficients, R , for all of 1968 and the latter half of 1969, which can be compared with R_d and R_r for the

transient decreases. Table XXIII illustrates the aforementioned effect, in that the spectral changes in the transient decreases of 2-12 Gv cosmic ray intensity in 1968-1971 were similar to the long term modulation shortly after cosmic ray minimum(June-December 1969); the spectral changes during type II events were similar to the steeper long term variation in the period preceding cosmic ray minimum, 1968).

There have been many attempts to determine the spectrum of the primary cosmic radiation during Forbush decreases by utilizing the counting rates of neutron monitors at different cutoff rigidities. The results have been limited by the statistics of the smaller decreases, particularly at low latitude, by the effects of persistent anisotropies on the relative counting rates of stations sampling different areas of the sky, and by the possible depression in cutoff during magnetospheric disturbances accompanying the early phases

of type I events. For example, Mathews et al.¹³⁸ found no consistent pattern for the spectra of Forbush decreases vs. the long term variation unless they compared the rates of two stations, specifically Sulphur Mountain and Calgary, at nearly the same location but with different energy response. For the stations cited, the authors found a consistent flattening of the regression curve of lower vs higher energy during large Forbush decreases. Their observation is consistent with the spectral characteristic of type I events. In Table XXIV, we list the mean ratio R , which is the % decline to minimum intensity at neutron monitors of a given P_c divided by the % decline at high

latitude neutron monitors, for type I and type II events derived from the neutron monitor data from 1965-1971. The counting rates of the northern hemisphere high latitude stations, Inuvik, Deep River, and Goose Bay have been averaged to obtain a representative high latitude neutron monitor rate at low cutoff rigidity.

The long term regression coefficients found by Mathews et al¹³⁸ for 1965-1969 are also shown as well as the yearly regression coefficients that we determined for the period 1966-1971 at low latitudes. We also list our estimates for the errors in the ratios, based on the uncertainties in individual

TABLE XXIV

RATIO OF THE % DECLINE TO MINIMUM INTENSITY AT VARIOUS
 CUTOFF RIGIDITIES TO THE % DECLINE AT HIGH LATITUDE SEA
 LEVEL NEUTRON MONITORS IN THE NORTHERN HEMISPHERE

	No. of events	Kerguelen ⁺	Sulphur Mountain [*]	Leeds	Munich Dallas	Rome	Kula Hermanus
P_c , Gv		1.19	1.14	2.20	4.14, 4.35, 4.90	6.32	13.3
Type I < 3%	6	0.90 ± 0.23	1.00 ± 0.03	0.92 ± 0.22	0.70 ± 0.23	0.62 ± 0.12	0.27 ± 0.1
> 3%	19	0.94 ± 0.19	1.20 ± 0.03	0.98 ± 0.11	0.78 ± 0.13	0.64 ± 0.14	0.38 ± 0.1
Type II < 3%	20	1.00 ± 0.23	1.26 ± 0.16	0.98 ± 0.17	0.79 ± 0.14	0.62 ± 0.21	0.44 ± 0.11
> 3%	15	1.06 ± 0.14	1.18 ± 0.17	0.94 ± 0.11	0.79 ± 0.14	0.64 ± 0.11	0.47 ± 0.13
Monthly av. 1965-69 **			1.27 ± 0.01	1.02 ± 0.01	0.82 ± 0.01		0.28 ± 0.02
Years: 1966-7						0.55	0.23
1968						0.56	0.21
1969						0.87	0.31
1970						0.65	0.25
1971						0.41	0.21

* High Altitude, lowest effective rigidity

** The data on this line is from Mathews et al¹⁴¹

+ Southern hemisphere station, illustrates effect of NS anisotropies

events.

At neutron monitor energies, there are no detectable differences between type I and type II events (Table XXIV) within the uncertainties in the neutron monitor data, except at the highest cutoff rigidity. The cosmic ray intensity at ~ 30 GV (13.3 GV cutoff at Kula) appears to have declined more steeply than the intensity at 10-15 GV (atmospheric cutoff at three northern high latitude neutron monitors) in type II events as opposed to type I events or to the long term modulation. Since the high energy behavior appears to differ from that between 2 and 10-15 GV, an additional check of the rigidity

dependence of the regression coefficient was made in Verschell et al¹³³ by Roelof, who used variational coefficients for neutron monitors to estimate the spectrum of variation, assuming a power law in rigidity for the regression coefficient. Because of the nature of the variational coefficients and the location of the neutron monitors, the Kula data dominated in the fitting procedure. The value found for the spectral index n was ≈ 0.8 for type I and ≈ 0.4 for type II events, consistent with the trend shown in Table XXIV. This enhanced sensitivity of the high energy radiation to symmetrical as opposed to Forbush type events is also found in investigations of the counting rate

histories of meson monitors. Antonucci et al¹³⁹, for example, showed that the meson monitor rates declined earlier and with a steeper profile than that usually observed with relation to the rates of high latitude neutron monitors during small symmetrical events, around 1-2% in the neutron monitor rates.

Hysteresis effects, such as those observed below 10 GV during type I events were found in the data from neutron monitors and meson monitors at the same geographic location, but only for the most statistically significant events. These were the largest decrease, October 1968, and the decrease with the longest uninterrupted recovery, June 1969.

E. Results, Long Term Variation in Cosmic Ray Intensity

In addition to the transient effects we have just summarized, there were several abrupt, persistent changes in the regression relation between the fast neutron flux and the counting rates of the Inuvik neutron monitor. We have divided the data into seven periods for which the regression relation, including transients, was reasonably independent of time; that is, the standard deviation of points were typically 0.033 in 1968 and 0.004 to 0.023 in 1969-1971. The regression curve for each of the 7 periods is shown in figure 44a. To indicate the spectral variations that were involved, we show similar curves for the fast neutron flux vs the counting rates of neutron monitors at lower and higher effective rigidity than Inuvik, from Sulphur Mountain (high altitude and latitude) to Kula at a P_c of 13.3 GV. The greater the cutoff of the neutron monitor relative to the cutoff at Inuvik, the larger the effect displayed in fig. 44.

The abrupt changes followed the decline to minimum of transient events during active periods and sudden recoveries of the neutron flux relative to the Inuvik neutron monitor counting rates during quiet times. Periods 2, 3, and 5 in figure 44a followed the type I Forbush decreases of 10/31/68 to 12/5/68, 5/15/69 and 6/5/69, and 11/7/70. Period 4 followed the mixed type I and type II events of 6/70. Periods 6 and 7 followed the sudden partial recoveries of the fast neutron flux in 1/71 and 4/71.

The most notable features of figure 44a are (1) the successive displacements of the regression curves relative to that for 1968(dashed line). The net effect was a decrease in slope, that is, a lag in recovery of the fast neutron intensity, as the higher rigidity cosmic rays were demodulated beyond a characteristic point for each period; (2) the higher the effective rigidity of the neutron monitor, the greater the lag in the decline and recovery of the fast neutron flux.

To check the contribution of transient decreases to the observed phase lags of the neutron intensity, the main phase of Forbush decreases (~ 10 days) was removed from the data set and the regression relations were recalculated (figure 44b). Removing transient effects does not substantially alter the conclusions drawn when all data is included, according to figure 44b. Using fast neutron data from balloon flights prior to 1968, as shown in curve C of figures 44a and 44b, we observe that the long term hysteresis persisted at least to mid-1971, in that the neutron flux lagged the recovery of Inuvik monitor rates to 1966 levels after the neutron flux recovered above the 1968 regression curve in early 1971.

The transient decreases which initiated the changes in the modulation spectrum above 2 GV produced corresponding effects below 2 GV and in the electron spectrum. The spectral variations have been reported by Lockwood

³⁷ et al, Van Hollebeke et al ¹⁴⁰, Burger and Swanenburg ¹⁴¹, and others. In the three papers cited, the low energy counting rates were compared with the counting rates of the high latitude neutron monitors and the integral proton intensity above 60 Mev, the differential proton and alpha intensities at 60 Mev per nucleon and the integral proton intensity above 1 GV, respectively, were shown by the authors to exhibit large hysteresis effects with respect to the 10-15 GV primaries which the neutron monitors track. Figure 45 shows the monthly averages of the fast neutron flux (effective rigidity ~ 3 GV) vs the monthly averages of (1) the Inuvik neutron monitor counting rates(10-15 GV), (2) primary protons above 60 MeV, (3) protons and alphas at 60 MeV per nucleon. The four cases shown illustrate that changes in the regression relation between higher and lower rigidity particles occurred over the range of rigidities from 0.3 to 15 GV; the results shown in figure 44 extend the rigidities which were affected to still higher values. In both figure 44 and figure 45, the lower

rigidity particles lag the higher rigidity particles in the recovery of intensity. At the lowest rigidity, 0.34 GV, the cosmic ray proton intensity decreased in period 4 (figure 44) while the fast neutrons (2-4 GV) were recovering. A similar behavior was found in the spectrum of cosmic ray electrons by Burger

¹⁴¹ and Swanenburg. Above 2 GV, we have shown that the lower rigidity particles lagged in both the decline and in the recovery of the events initiating the modulation periods.

F. Discussion

1. The spectrum of variation of cosmic rays. Figure 46 shows the monthly plots of the parameter M , derived according to the method outlined in this

section by Verschell et al¹³⁵. In Verschell et al, the additional modulation required by the fast neutron excess was indicated by a segment between 2 and 4 GV. Also given in figure 46 are the time histories of the modulation parameter, M , plotted for the differential and integral proton intensities shown in figure 45 as well as integral intensities of protons above 1 GV,

reported by Burger and Swanenburg¹⁴¹. If a single normalization factor, 0.34, is added to the modulation parameter of > 60 MeV protons, the values of M join smoothly to the curves above 2 GV up to the beginning of 1971, when the integral fluxes above 60 MeV and above 1 GV lag increasingly from the continuation of the smooth curve for the modulation parameters above 2 GV. If the effective rigidity of the integral proton spectra did not change drastically this behavior implies that there was an abrupt change in the proton spectrum at the beginning of 1971 and occurring between 1 and 3 GeV. This tendency for one portion of the energy or charge spectrum to recover while a lower energy or the electron portion remains depressed has been alternatively interpreted as a true time lag or as a change in the scattering properties of the medium.

In the present study, the small residual modulation found from the fast neutron counting rates was treated as a multiplicative correction to M between 2 and 4 GV, the spectral form being that which gave the best correlation with all the primary data to be found above 2 GV over the period studied. The form used for the correction was $(1 + \delta/P)$. Figure 47 shows, among derived values of quantities to be discussed later in this exposition, c_1 , n_1 , and δ for each

month between 1968 and mid-1971, with gaps in δ for months with no aircraft fast neutron data. Note that the spectral exponent, n_1 , which relates primarily to intermediate rigidities (4-13 GV), goes through several minima, corresponding to times of abrupt changes in the modulation spectrum after transient decreases. Such minima are observed as a flattening of the modulation

spectrum on the decline and a steepening on recovery of intensity. This characteristic of the hysteresis effect above 2 GV was noted in Verschell et

al³³; it has recently been observed near solar minimum in observations of the intensity of 40-90 MeV protons vs neutron monitor counting rates by

Garcia Munoz et al¹⁴², who found that the low energy component lagged the high energy component in the decline and recovery of intensity during a "mini-hysteresis" loop in 1974. Note also that δ tends to peak during the time when the hysteresis effect was largest at low rigidity, as expected from a positive correction to the modulation parameter at lower, relative to higher, rigidities.

Before proceeding with this analysis, we are required to re-emphasize and note the justification and the limitations of the principal assumption on which the analysis of the neutron monitor data, to yield the spectrum of variation, is based. This assumption, discussed with respect to equations 10 and 11, was that protons and alpha particles suffered the same intensity modulation at neutron monitor rigidities. Below 4 GV, this limitation can be relaxed, since we depend principally on the fast neutron data between 2 and 4 GV, a rigidity range in which the alpha particle variations are a second order correction to the modulation parameter of protons. The validity of the aforementioned assumption has been tested on the basis of current modulation theory and the conclusions are illustrated in figure 48. Figure 48 shows that within the context of conventional modulation theory differences between proton, alpha, and electron modulation above 2 GV are negligible at the depths of modulation encountered in the course of a solar cycle.

Experimental verification of the assumption of no charge-splitting in M above 2 GV as well as experimental verification of the neutron monitor analysis of M is limited by a paucity of data, particularly proton data. Figure 49 compares the modulated spectrum of hydrogen and helium nuclei with that obtained by direct observation of the primary intensities. In the helium spectrum for which there is some information above 2 GV, and for the proton integral spectra down to 1.37 GV, the primary and secondary observations agree within the error bars of the measurements. At 1.6 GV, where the calculation is below the limit of sensitivity of the neutron detector, the two sets of results still agree except at the deepest modulation for helium, but the proton modulation is not as deep as would be inferred if the neutron data were to be extrapolated. Thus, within experimental uncertainties, M , as obtained from the fast neutron and the neutron monitor data, appears to be a valid measure of the proton and alpha intensities above 2 GV.

2. The relative modulation of protons and electrons; charge splitting above

2 GV. We shall show that the time variations of proton intensity during 1968-1971 differed considerably from the time variations of electron intensity in the same rigidity intervals. Current theoretical models of cosmic ray transport can account for such "charge splitting" in the modulation of particles below 2 GV, where differences in particle velocity at the same rigidity become significant for electrons vs protons. Above 2 GV, "charge-splitting" in the modulation becomes negligible in solutions of cosmic ray transport equations. The results of numerical calculations are illustrated in figure 48, which will be discussed later.

Figure 50 shows experimental and theoretical observations of the time variations in the fluxes of electrons and of protons during 1968-1971. First, we consider the experimental results. The electron fluxes (thin solid lines)

were reported by Burger and Swanenburg¹⁴¹ and were based on observations of electrons above 0.5 GV on OGO5, beginning in March 1968. Thirty day averages are plotted in rigidity intervals, 2-3 GV, 3-5 GV, and 5-7 GV. The proton intensities shown in figure 50 were determined by the method described in part C of this section. The heavy solid represent intensities which were calculated using the neutron monitor data, the fast neutron data, and the 1965 proton spectrum for the solar minimum intensity. For comparison, we show the modulated proton intensities obtained without the fast neutron data (dashed line). The fluxes are plotted logarithmically and are superimposed at the beginning of the OGO 5 data, using the average of the first three months for normalization.

Figure 50 shows that beginning in June 1968, the electron intensities(1) lagged the proton intensities in recovery, (2) showed a smaller response to transient effects, such as the October-December events in 1968, and (3) declined steadily during modulation period 2 (figure 44) while the proton intensity was recovering, and (4) remained depressed below the proton intensities during later modulation periods. Burger and Swanenburg found that the low energy electrons lagged the intensity variations of the higher energy electrons as well as the counting rate variations of the Sulphur mountain neutron monitor during the same period.

Moraal and Stoker¹⁴³ deduced the spectrum of variation of protons and alphas from neutron monitor data. Using the "force field" approximation to the cosmic ray transport equation, they found that the transport parameters that generated the proton modulation differed from the transport parameters for the electron modulation at neutron monitor energies. They attributed the discrepancy to possible uncorrected drifts in the OGO-5 electron counting rates. As illustrated in figure 50, the failure of electrons to track the proton intensities extended to energies below the region of sensitivity of the neutron monitors and in the direction of increasing hysteresis at lower rigidity, as

has been observed for the nucleonic component. Verschell (private communication) has found that the counting rates of electrons as energetic as 5 GeV remained depressed relative to the rates of protons above 1 GV, both quantities being observed in the OGO-5 experiment. Rockstroh and

Webber¹⁴⁴ and the Chicago group¹⁴⁵ have made balloon observations of the electron spectrum. The observations of Rockstroh and Webber were usually limited to one per year and may not therefore be representative of the average monthly intensity; whereas the Chicago data is an average based on several balloon flights during a month. Both sets of observations are shown in figure 50. Although there does appear to be a considerable divergence in the results reported, the hysteresis effect is clearly displayed in figure 50, at all of the rigidities plotted. In the 2-3 GV intensities, where the hysteresis is most pronounced, the data of the Chicago balloon observations and the satellite observations from OGO-5 are in excellent agreement. Thus the hysteresis of electron, relative to proton, intensities is confirmed at comparable rigidities, although uncertainties in the data do not permit an exact quantification of the effect. In the section which follows, we shall describe calculations of cosmic ray transport, specifically those calculations which attempt to reproduce the hysteresis effects in the proton, electron, and alpha spectra, and we shall discuss the goodness of fit of the results of the calculations to the observations we have summarized.

3. Model calculations. The cosmic ray spectrum near 1 AU differs from the

spectrum at greater distances from the sun¹⁴⁶, presumably as a result of the scattering of the cosmic ray particles in the expanding solar plasma by the disordered magnetic fields carried by the solar wind. According to presently accepted theory, the distribution function of cosmic rays satisfies a transport equation that includes diffusion in the modulating region, convection by the solar wind, and energy loss due to the expansion of the solar wind. Such an

equation (Moraal and Gleeson¹⁴⁷ and references therein), reduced to the case of quasistationary transport with spherical symmetry, is

$$\frac{1}{r^2} \frac{\partial}{\partial r} \left(r^2 V F - r^2 k \frac{\partial F}{\partial r} \right) - \frac{1}{3r^2} \frac{\partial}{\partial r} \left(r^2 V \right) \frac{1}{p^2} \frac{\partial}{\partial p} \left(p^3 F \right) = 0 \quad 12$$

where $F(r, p)$ is the distribution function of cosmic rays of momentum, p , at a distance, r , from the sun, V is the solar wind velocity, assumed to be constant in most studies, and k is the diffusion coefficient, generally considered to be of the form $vk(r, P)$. P is the particle magnetic rigidity and v is the particle velocity. In recent studies in which the anomalous cosmic ray effects we have discussed were investigated, solutions to the three dimensional Fokker Planck equation were examined (Moraal and

Gleeson¹⁴⁷) for heliolatitude effects that were reasonable and capable of

producing the observed hysteresis. O'Gallagher¹⁴⁸ found that time-dependent solutions contained transport time lags of the lower rigidity particles, and such solutions were capable of reproducing features of the anomalous cosmic ray recoveries, particularly if the modulating cavity turned out to be 30-50 AU in extent. Using numerical solutions to equation

12 or to an equivalent formulation, Garrard et al¹⁴⁹, Fulks¹⁴⁵, and Winckler

and Bedijn¹⁵⁰ and their co-workers have attempted to find reasonable input parameters that would satisfy the electron modulation and also reproduce the variations in the proton and helium intensities.

Using numerical solutions to the Fokker Planck equation, we have examined the implications of the results that we have reported in the rigidity spectrum of cosmic rays above 2 GV to the calculations which were most compatible with the low energy spectrum of protons and alphas and the energy spectrum of electrons to 10 GeV, specifically the calculations in references 145, 149, and 150. To generate solutions to the transport equation, we used

a modified version of the numerical code of Fisk¹⁵¹, solving equation 12, with various assumptions for the diffusion coefficient and the boundary conditions. At the sun, the boundary condition was that the differential current density,

$$S = -4\pi p^2 \left(k \frac{\partial F}{\partial r} + \frac{1}{3} pV \frac{\partial F}{\partial p} \right) \quad 13$$

vanish; i.e. $S=0$ at $r=0$. The radial dependence of k was varied, and included a radially independent coefficient, as in reference 149, an exponentially

decaying radial factor with a 50 AU cavity of modulation¹⁴⁵, a non-separable

k below a given rigidity, which changed with solar epoch¹⁵⁰, and others. The rigidity dependence of k was a power law, with the exponent varying in different rigidity intervals and, in the case of the non-separable k , varying with distance from the sun. The assumed galactic flux varied from model to model.

None of the models employed provided appreciable charge splitting for the modulation parameter, M , above 2 GV, a situation which we noted in the discussion of figure 48, whereas the observations indicate a considerable

difference in the evolution of M for protons vs electrons, as was illustrated in the discussion of figure 50. Figure 50 shows the calculated proton intensities (triangles), which were obtained from numerical solutions that employed the diffusion coefficients from the paper of Winckler and Bedijn. As was illustrated for the calculations of Garrard et al and of Fulks in figure 48, the numerically derived proton intensities track the electron intensities quite well on the basis of rigidity, whereas the experimentally derived electron and proton intensities show considerable divergence as time progresses. Good tracking is found for both models in which separable diffusion coefficients are assumed and for models in which k cannot be separated into radial and rigidity components. The electron models do not work for protons.

By generating a family of solutions to equation 12, we can determine the temporal behavior of the cosmic ray diffusion coefficient that is required to generate the proton variations above 2 GV. We can then establish whether it is possible to reproduce the electron variations, within the uncertainties that exist in the electron and in the interplanetary parameters as well as in the proton parameters. The greatest uncertainty in the proton parameters is the interstellar intensity near the solar system or, equivalently, the values of the parameters of the interplanetary medium to be employed in demodulating the galactic spectrum. As it happens, any choice of a reasonable demodulated proton spectrum is adequate to explore the behavior, if not the exact numbers, to be expected of the cosmic ray diffusion coefficient. Moreover, if we confine our calculations to values of k separable in r and P , for a given input proton spectrum, there is \approx one-to-one correspondence between the rigidity dependence of the diffusion coefficient and the rigidity dependence of the proton modulation parameter above 2 GV. From solutions to equation 12, using the input proton spectrum studied by Bedijn and Winkler, we have constructed a grid that gives a one-to-one correspondence between c_1 and n_1 and the parameters $K_1(r)$ and x of a diffusion coefficient of the form $k = \beta K_1(r)P^x$. Figure 47 shows the values of $K_1(1 \text{ AU})$ and of x , superposed on c_1 and n_1 for the period, 1968-mid-1971. The spectral exponent, x , is a constant over a large rigidity range, usually < 3 to > 10 GV, in most of the period sampled.

As figure 47 suggests, there is good correlation between n_1 and x and anticorrelation between K_1 and c_1 over the entire time interval of the observations. This behavior was insensitive to changes in the demodulated proton spectrum. In figure 47, the spectral exponent of the diffusion coefficient has a smaller range of variation than the spectral exponent of the modulation parameter, which it tracks quite well. As in the case of the type I decreases,

the spectrum of variation hardens during the onset of a modulation period and softens in later phases, as has been shown for the type I transient decreases which appeared to be associated with most of the modulation periods studied.

Formulations such as the one above in which the proton time variations are satisfied are quite different from formulations in which one attempts to satisfy the electron variations while remaining consistent with the observed particle and field data. For the electrons above 2 GV, the diffusion coefficient must steepen during the recovery from cosmic ray minimum and remain steeper than in 1968 through mid-1971, as is indeed found in calculations. For the protons above 2 GV, the spectral exponent decreases and recovers in each modulation period.

G. Conclusions and Summary

1. The intensity distribution of atmospheric neutrons cannot be inferred from neutron monitor rates only, because the regression relation between the two quantities is not single valued. This situation arises because the charge and energy components of the spectrum of variation of cosmic rays can differ during the various phases of the cosmic ray variation; secondary radiation having different response functions to the primary spectrum will therefore exhibit different rates of decline and recovery of intensity. Changes in the spectrum of variation of cosmic rays occur both during transient cosmic ray decreases and over periods greater than a few solar rotations.

2. During 1968 to mid-1971, two different classes of transient cosmic ray decrease were found, based on a comparison of stratospheric neutron intensities with neutron monitor counting rates. In type I events, the lower energy cosmic rays lagged the higher energies in the decline and recovery of intensity; in type II events, the lower energy cosmic ray intensities declined more steeply than in type I events and did not lag the variations at higher energy. The solar and interplanetary associations of the different types of decrease are still being investigated, following a preliminary analysis in

Verschell et al¹³³; as type I and type II events appear to differ not only in spectrum but also in the solar and interplanetary phenomena which cause them. The investigation in progress will carry the analysis of the cosmic ray spectra and the solar parameters to solar minimum conditions. A further discussion is beyond the scope of this report.

3. During 1968 to mid-1971, a combination of neutron and neutron monitor data was employed to detect changes in the long-term spectrum of modulation of cosmic rays. The spectrum of variation of protons > 2 GV changed several times during this period, the onset of change corresponding to a cosmic ray decrease in which the lower energy component lagged in both the decline and

recovery of intensity. We have explored one possible mechanism for producing the observed effect, namely, changes in the spectrum of the cosmic ray diffusion coefficient due to the variations in solar activity. Numerical solutions to the cosmic ray transport equation were employed to determine the nature of the changes in k required to produce the cosmic ray spectrum of variation. We find that the spectral index of the diffusion coefficient above 2 GV must decrease and recover in each modulation period, corresponding to the observed effect in the spectral index of the modulation parameter between 2 and 10 GV. In a paper in preparation, we show that the proton intensities below 2 GV can be reproduced with less stringent criteria for the shape of the diffusion coefficient.

When the transport parameters derived from the proton intensities are used to calculate the intensity variations in electrons, the calculated electron modulation past 1968 is much smaller than the observed modulation. In the case of electrons, the spectral index of the diffusion coefficient would have to be greater during 1970 - 1971 recovery than it was during cosmic ray minimum to account for the depressed intensity at lower rigidities during the recovery phase. This discrepancy between observation and calculation appears to be incapable of resolution for the case of spherical symmetric solutions to the Fokker Planck equation. The reasoning behind so strong a statement is that the observed electron modulation does not track the proton modulation in the same rigidity intervals, whereas in a model in which only the velocity and the rigidity enter in both the transport equation and the diffusion parameter, relativistic electrons and protons have almost identical transport characteristics; thus the electrons track the protons above 2 GV at any give rigidity, according to the theoretical model. Jokipii, in a recent preprint, has suggested that curvature and gradient drifts, which are not treated in the model we have employed, are the charge-dependent features in cosmic ray transport which may account for the different behavior of electrons and protons after 1969. Verschell

¹⁵² and Bercovitch ¹⁵², in a paper in preparation, have reached a similar conclusion. Indeed, the spectral variations in the electron vs proton spectrum occurred around the solar epoch when the large scale poloidal magnetic fields on the sun were reversing sign.

We have only begun to explore the complex relationships between the spectrum of variation of the transient decreases and the solar and interplanetary configurations with which cosmic ray events are associated.

Verschell et al¹³³ found that type I decreases were always rapidly evolving large scale structures and type II decreases tended to be associated with corotating structures. The long term hysteresis effect above 2 GV was clearly associated with the decay of regions active in type I activity, i.e. type 2 and 4 radio bursts, flare-generated shock waves; but without further

analysis of transients and persistent trends in the cosmic ray variation during different solar epochs, it is not possible to determine (1) whether a similar physical mechanism governed the time lags observed in the type I transients and in the long term recoveries of 1968-1971; (2) Whether the type I recoveries generated the features of the anomalous long term recovery of 1969-1972 or vice versa or neither is the case; (3) the role of large scale solar and interplanetary structures on the spectrum of variation, including both quasistationary and evolving structures and solar azimuthal and latitudinal effects; and (4) the complex interrelation of the cosmic ray effect with the near and distant solar-interplanetary phenomena, the least explored and most promising of which involves cosmic ray distributions and flow in the regions above and below the ecliptic plane.

The questions on the origin and nature of cosmic ray variations are of great importance to the study of atmospheric neutrons. When we become better informed on the spectrum of the primary radiation beyond the influence of the sun and its emissions and when we have a better understanding of the effect of different solar-interplanetary configurations on the propagation of the primary radiation, we will have gained a clearer picture of the role of the secondary atmospheric neutrons and their products in archeology, health physics, planetary science, and the history of solar emissions.

X. APPENDIX A

Acceleration Processes in the Sun

Let us consider the possible processes by which charged particles may be accelerated to high energies. Such processes might be resonant accelerations as in cyclotrons, or single passages across high potential differences, or inductive accelerations. It is clear that the first is unlikely as it would require multiple passages under resonant conditions, and the second would require the maintenance of large potentials, and thus also be improbable. This leaves the various forms of inductive acceleration as the most likely.

In essence inductive acceleration means that a particle should be moving in an orbit, and if the number of flux-linkages through that orbit increase with time, the particle will gain energy from the field. In an electric generator, the particles are the conduction electrons and they are confined to the wires. In the astrophysical case the particles are free to move in whatever direction the forces acting on them impel them. There may be many different geometrical shapes to the magnetic field, and many different particle orbits. These various systems have been from time to time discussed by various persons, and are called by various names. Examples are "The betatron mechanisms, the Fermi acceleration", etc. All have the common feature of inductive acceleration. What differs is the initial conditions and the geometry, both in time and in space, of the fields. All assume that the particle is not starting from rest, but is already moving along at a good speed when it enters the accelerating region. This initial speed may result from thermal motion, or from some unspecified other action.

During such accelerations, in order for the particle to have a net gain in energy it must experience fewer energy-losing actions than gaining actions. Such losses may be due to (a) fields with negative time-derivatives, in which the particle energy is lost to the field, or (b) to collisions in which the particle's kinetic energy is shared with other particles. Magnetic fields, in turn, may be generated by turbulent motions in partly or wholly ionized gases, since the necessary condition is movement of charges. In the sun we know that turbulence exists, that ionization exists, and that magnetic fields exist. The fields may range from a few gauss at the surface, up to many thousand gauss in large sunspot fields. Further we know that large sunspots both come into being and disappear in intervals of a few hours to a few days, so we know that time-dependent magnetic fields exist.

If a particle of mass m and charge e , moves with velocity v at right angles to a uniform magnetic field H in a region where we may take the permeability to be unity, so that the field H and the induction B are the same, it will describe a circular orbit of radius r .

The equilibrium conditions are:

$$mv^2/r = Hev \quad (A-1)$$

or, designating the momentum by p ,

$$Hr = mv/e = p/e \quad (A-2)$$

Following the usual custom, we shall call Hr the magnetic rigidity. Thus the particle will in this case describe a circle of radius p/eH at right angles to the field. If we designate by t the time to go around one circle of radius r , so that $v = 2\pi r/t$, then the period t is $2\pi m/He$, the well-known cyclotron condition in which the radius vanishes. The reciprocal of this, $He/2\pi m$, we shall call the cyclotron frequency. Note that the charge e must be in units to match the magnetic field H . If e is in electrostatic units and H in electromagnetic, then the cyclotron frequency is $He/2\pi mc$.

If the velocity vector of the particle has a component along the field, and one at right angles to the field, still assuming the field to be uniform (no gradient, or derivative with respect to coordinate) then the particle will describe a helix, since the component along the field will draw the circle out, and the pitch angle of the helix, σ , will be:

$$\sin \sigma = v_t/v \quad (A-3)$$

where v_t is the component of velocity v , transverse to the field. It is clear that the velocity v will be related to v_t through $v^2 = v_t^2 + v_a^2$ where v_a is the component along the field. The radius of the helix will be mv_t/He and its pitch angle σ will be $v_t/v \sin \sigma$. Since the energy is $\frac{1}{2}mv_t^2 = H \times \text{const}$, we may write $v^2 \sin^2 \sigma / H = \text{const}$, and call it the first adiabatic invariant.

In general, fields in the sun will not be uniform, so that the lines of flux will converge or diverge as the particle moves. The converging case leads to "magnetic mirroring". The pitch angle becomes steeper until it becomes at right angles to the field direction. The familiar case of the field at which the mirroring occurs is given by:

$$H_m = \text{const } v^2 \quad (A-4)$$

On the other hand, if we consider time-variations in the field, assuming first a uniform field and a particle moving around the field lines as in eq. A-2, then we would have:

$$(d/dt) Hr = (d/dt) p/e \quad (A-5)$$

which is the well-known betatron case, in which the particle picks up energy from the field, gaining momentum. In the betatron case, the orbit radius stays constant, but in the more general case in astrophysics, this is not a necessary condition. Thus in the betatron case we may rewrite A-5 as:

$$re dH/dt = dp/dt \quad (A-6)$$

If we designate by H_0 the field at the start of a time interval dt during which acceleration takes place, the radius r by (A-2) will be mv/eH_0 and the momentum at the same initial instant p_0 , then (A-6) becomes

$$(p_0/eH_0) e dH/dt = dp/dt \quad (A-7)$$

Note also that in the fully relativistic case, in which momentum and energy are linearly related, i.e., $E = pc$, if the initial energy at the instant acceleration starts is $E_0 = p_0 c$, then (A-7) becomes

$$dE/dt = (E_0/H_0) (dH/dt) \quad (A-8)$$

or in other words the rate at which a particle gains energy depends on its initial energy, as well as on the time rate-of-change of the magnetic field. Thus the high energy particles are accelerated to still higher energies. This situation is presumably the source of the very steep spectra observed in high energy particles of solar origin.

Consider next the field conditions necessary for the particle to leave the sun. If the general field of the sun produces a Stormer diagram such as is shown in fig. A-1, then the spot belts, being in middle latitudes are very likely to be in the forbidden regions, shown by the dark cross-hatching. Now if these regions represent areas into which particles from outside cannot enter, then they also represent regions from which particles inside cannot leave. However, the spot or flare field is now superposed on the general field, and it in turn may, as shown in fig. A-2 generate a "tunnel" or path in space through which particles can leave. It should also be clear that a field configuration such as depicted in A-2 is an exceptional rather than a usual event, and that therefore by no means all flares will have configurations such that particles can leave. Actually most flares do not produce particle fluxes that reach the earth. The field situation necessary is one of the reasons.

Still another consideration is that of the energy-loss mechanism. Inductive processes are relatively slow, and require relatively long times during which the particles gain energy. On the other hand, collisions are energy-losing processes, and a single collision may undo the gain from a long acceleration rather fast. Consider therefore the free times at various levels in the solar atmosphere.

The classical mean free path L of a particle is given by:

$$L = 1/n\pi r^2 \quad (A-9)$$

where n is the number of centers per cc with which such energy-losing collisions may take place, and r is the effective collision radius of the particle.

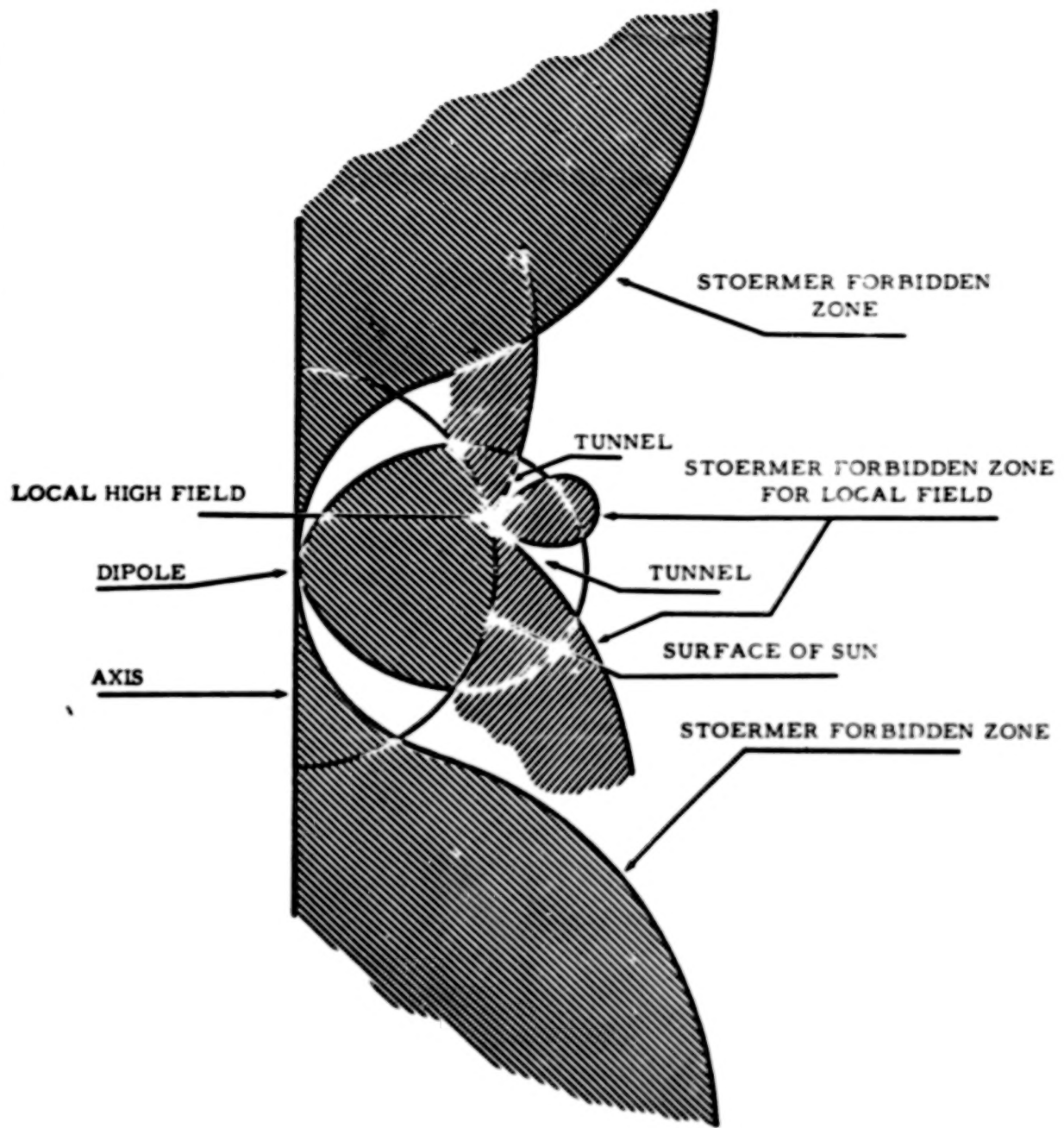
The free time t between collisions is similarly given by:

$$t = L/v$$

which for particles travelling with nearly the speed of light is approximately:

$$t = 1/c n \sigma \quad (A-10)$$

where σ is the cross section for the collisions in question. For atomic collisions the values of σ run in the neighborhood of 10^{-16} sq cms, while for nuclear collisions they are nearer 10^{-24} cm^2 . The larger cross sections involve collisions in which the projectile particle plows through the



Tunnel in Stoermer Forbidden region in Dipole Field (After Vallarta)

Figure A1.

cloud of electrons about a nucleus, whereas the nuclear cross sections are appropriate to actual collisions with the nuclei themselves. Collisions with the extranuclear electrons generate ionization, and cause losses of the order of the ionization potential, i.e., a few tens of e.v. per collision, while nuclear collisions may cause a loss of anything up to the entire energy of the moving particle. If the projectile energy is large, the ionizing collisions will not deplete its energy by very much, but the nuclear collisions will.

Solar flares are phenomena that appear quite far down in the solar atmosphere, i.e., only just above the photosphere. If the assumption is made that the pressures at this level are of the order of 0.1 to .001 atm,

then n will be of the order of 10^{18} to 10^{16} per cc. Atomic collisions would have free paths of a cm or so, whereas nuclear collisions would have free paths of the order of tens of kms. Since the particle must traverse some

10^4 kms to get out of the chromosphere, nuclear collisions would prevent this. On the other hand if the acceleration takes place far up above the

chromosphere where the pressures are down to n values of 10^{12} or so, nuclear collisions will be negligible. The particle can then both have a long enough free time, so that the rather slow inductive acceleration has a chance to work, and a particle at high energy can leave the sun without

undergoing further collisions. In the case cited, if n is 10^{12} , σ being 10^{-24} sq cms, c being 3×10^{10} cm/sec, the free time will be 30 seconds.

The free paths that correspond are of the order of 10^7 kms.

We are therefore led to the conclusion that the acceleration mechanisms in the sun must take place at fairly high elevations above an actual flare, in order that the particles can (a) be free long enough to be accelerated to high energies, and (b) have a chance of escaping from the sun without making a nuclear collision after being accelerated.

XI. APPENDIX B

Primary Neutrons

As we have mentioned before, the neutrons in the earth's atmosphere are secondaries. We may ask whether it is possible for primary neutrons to arrive at the earth. By primary neutrons we mean neutrons generated elsewhere and propagated as neutrons. Such neutrons might arrive from two sources, (a) outside the solar system, and (b) from the sun.

At first glance the answer to (a) should be negative. Neutrons are radioactive particles, with half-lives of the order of 1000 seconds, so that none might be expected from regions much further than a thousand light-seconds away. But the time-dilation of Special Relativity will increase the lifetime and allow greater distances for highly energetic neutrons.

According to Special Relativity, the lifetime of a neutron coming toward an observer on the earth will seem to him to be lengthened in the amount:

$$t = \gamma t_0 \quad (B-1)$$

where γ is the so-called Lorentz Factor,

$$\gamma = 1 / (1 - v^2/c^2)^{\frac{1}{2}} \quad (B-2)$$

If we express the energy of an incident neutron by E , then

$$E = E_0 \gamma \quad (940 \text{ MeV}) \quad (B-3)$$

or approximately, taking E_0 as 1 GeV, the value of E in GeV is gamma.

Thus for example a neutron of 10^{16} electron volts or 10^7 GeV energy would have a gamma of 10^7 and its lifetime would be 10^{10} seconds, or three hundred years. Such a neutron could arrive at the earth from a few hundred light years distance. However at this distance, there is a very small amount of matter in our portion of the universe and no potential source at present known. Even such interesting objects as the Crab Nebula with its pulsar is further away, and one would have to postulate neutrons of very high energy to survive. Whereas there are some very high energy particles in the cosmic radiation, these are very few compared to the flux at lower energies. In theory a very high energy proton could, by charge-exchange scattering, make a very high energy neutron. However the probability of this is small, and when taken in conjunction with an already small flux of high energy

particles, does not suggest that high energy neutrons from outer space should be more than an occasional event.

The situation is quite different with regards to the possibility of neutrons from the sun. The sun is only about 500 light seconds away, so that neutrons moving at half the speed of light would be expected to reach the earth. This speed corresponds to an energy of 137 MeV.

For help in thinking about the problem of neutrons of solar origin we append herewith a table showing the speeds of neutrons at various energies, and the survival probability of such neutrons reaching the earth.

As for generation processes, several have been suggested, of which we mention again charge-exchange scattering. This has been discussed for at least fifteen years, and an experiment to seek such neutrons was proposed by our group to the IGY Committee in 1956. That experiment consisted in flying a neutron detector at high and constant elevation, say top balloon altitudes, into the night hemisphere. Neutrons, coming from the sun in straight lines, unaffected by the magnetic fields they traverse, would be expected to show a geometrical shadow effect, modified by atmospheric scattering. Several flights were made and no neutrons were detected. A similar experiment was later reported by Haymes who also found no flux of solar neutrons above his lowest observable limit. We may therefore conclude that the sun does not, under normal circumstances, exude many neutrons.

However, at times of solar disturbances, the possibility still remains that neutrons might be generated on the sun. Indeed, since we know that at such times the sun does generate protons and accelerate them to energies of more than 15 GeV it would be astonishing indeed if there were no neutrons produced in the same event. The complicating factor is clearly that 15 GeV protons can generate neutrons in the earth's atmosphere or upon striking the material of which any detector in free space is made. The fact that one does actually see occasional large bursts of neutrons at times of solar disturbances must be understood in the light of secondary processes. No simple experiment to disentangle true solar neutrons from such secondary neutrons has yet been activated, although some satellite experiments are hopeful.

The disturbances on the sun are usually accompanied by a solar flare, and this terminology is loosely used in describing the high energy particles. We speak of "flare protons". However, it should be pointed out that in all probability the actual flare, a strong emission of ultraviolet, is not in itself the source of the particles, but merely a simultaneous signal. The flare occurs too low down in the solar atmosphere, and protons in the flare would

Table A-I
Neutron Kinetic Energy, Velocity, Time Dilation, Decay, etc.

Kinetic Energy	Vel. Km/sec	"Beta" (v/c)	"Gamma" $1/\sqrt{1-v^2/c^2}$	Mean Life		Fraction Surviving to 1 A. U.	
				$t = \gamma t_0$	vt	A. U.	e^{-vt}
1 KeV	437	.001459	1.000001	933	.00273	2×10^{-160}	
10 "	1383	.004614	1.000011	933	.00863	4.6×10^{-51}	
100 "	4374	.014589	1.000106	933	.02728	1.2×10^{-16}	
1 MeV	13821	.046101	1.001064	934	.08629	.00000927	
2 "	19530	.065144	1.002129	935	.12206	.000277	
3 "	23900	.079722	1.003193	936	.14953	.001246	
4 "	27575	.091982	1.004257	937	.17271	.003058	
5 "	30806	.102757	1.005322	938	.19315	.005643	
6 "	33719	.112476	1.006386	939	.21164	.008871	
7 "	36392	.121391	1.007450	940	.22866	.01261	
8 "	38874	.129670	1.008515	941	.24451	.01674	
9 "	41200	.137427	1.009579	942	.25941	.02117	
10 "	43394	.144747	1.010643	943	.27351	.02583	
15 "	52938	.176583	1.015965	948	.33543	.05073	
20 "	60889	.203105	1.021287	953	.38783	.07589	
25 "	67813	.226199	1.026608	958	.43418	.09994	
30 "	73999	.246834	1.031930	963	.47624	.1225	
40 "	84795	.282847	1.042574	973	.55135	.1630	
50 "	94090	.313852	1.053217	983	.61804	.1983	
60 "	102304	.341249	1.063860	993	.67878	.2292	
70 "	109688	.365880	1.074504	1003	.73505	.2565	
80 "	116409	.388298	1.085147	1012	.78782	.2810	
90 "	122582	.408891	1.095791	1022	.83773	.3031	
100 "	128295	.427946	1.106434	1032	.88529	.3232	
125. 943	141390	.471627	1.134046	1058	1.00000	.3679	
150 "	151800	.506349	1.159651	1082	1.09785	.4022	
200 "	169644	.565873	1.212868	1132	1.28123	.4587	
300 "	195549	.652282	1.319302	1231	1.60898	.5371	
400 "	213685	.712775	1.425736	1330	1.90004	.5908	
500 "	227136	.757643	1.532170	1430	2.17040	.6308	
700 "	245685	.819518	1.745038	1628	2.67383	.6880	
1 GeV	262270	.874838	2.064339	1926	3.3766	.7437	
2 "	284067	.947545	3.128679	2919	5.5428	.8349	
5 "	296018	.987409	6.321697	5898	11.6709	.9179	
10 "	298685	.996305	11.643393	10863	21.6892	.9550	
20 "	299491	.998993	22.286786	20794	41.6275	.9763	
50 "	299742	.999830	54.216966	50584	101.352	.9902	
100 "	299780	.999957	107.433931	100236	200.879	.9950	

Constants assumed (from "Particle Properties", Lawrence Radiation Labs., 1969)

Neutron mass = 939.550 MeV, Proper mean lifetime = 933 seconds.

Other constants assumed: $c = 299792.5$ km/sec, and 1 A. U. = 149,600,000 km

have small opportunity of escaping. Yet above the flare the magnetic fields are varying in a manner which can cause inductive acceleration of charged particles. All this has been pointed out some time ago⁸⁷ but needs repetition. Thus the flare is an optical signal of a disturbance, in which magnetic fields thousands of kilometers above the flare itself can accelerate particles, and therefore also can generate neutrons.

Indeed most flares are not evidenced by high energy particles reaching the earth. The magnetic fields must have certain characteristics to permit the particles generated to escape. These conditions have been discussed, and can occur occasionally but evidently do not occur often. Thus a large flare, in itself rare, will rarely possess the right field configuration. Only about a dozen major events are known, plus a sprinkling of minor ones.

The spectrum of the protons emitted in such events has been studied and it is known that this spectrum is very steep. It is usually represented by an exponential, with an exponent from one to four greater than the usual one describing the cosmic ray spectrum. Different flares have different spectra, so we will not give a specific number which may wrongly influence our thinking. The energy spectrum of the neutrons generated in such an event we may expect also to be very steep. Because of the steep spectrum, the atmosphere will greatly attenuate flare neutrons. To detect flare effect neutrons, we would like to have a neutron detector at a high elevation. It would have to remain at the high elevation for a long time, in order to have any probability of intercepting such an event. We have no way at present of predicting flares. We can occasionally say that the situation is such that a flare might occur. A flare breaks out quickly, and the effect is soon over. Usually there is not time to get an airplane or balloon ready, and the two hours it takes to get to altitude is enough to spoil the chances of success. We come therefore to the continuous monitoring problem. We can make a lot of flights hoping to catch a flare when the equipment is up, or design a detector which will fly in a satellite. We have actually had airplane or balloon flights in the air when small events have occurred or in some cases just after one. These are presented elsewhere in this text. Much remains to be done on this interesting problem. The monitoring satellites are one approach. The other is to make an airplane or balloon flights when conditions appear favorable.

XII. APPENDIX C

The Earth or Other Object as a Neutron Source

It has been obvious for some years that the earth, or any other object such as the moon or other planet is being continually bombarded by a flux of high energy cosmic radiation which generates neutrons as well as other secondaries, and therefore is a source of neutrons as measured in the surrounding space. In the case of the earth this is called the neutron leakage and has already been studied by various observers, both as to the amount of the flux and the energy spectrum of the leaking neutrons. Some of the considerations are discussed in earlier portions of this report.

As the neutrons leave the planet, they will disappear by decay into protons and electrons. At a great distance they will have vanished. Under special circumstances, if they have an energy which lies within certain limits and decay in certain regions of the earth's magnetic field, the resulting protons and electrons may add to the population of the radiation belts. This possibility has been widely discussed and the bibliography will not be reviewed here. Nor will we, in this appendix, concern ourselves with the other secondary entities produced and radiated.

Several considerations are of interest. First, we note that the spectrum of the emerging neutrons will depend on the chemical composition of the radiating volume. In the case of the earth, this volume consists of an atmosphere of nitrogen and oxygen. The spectrum of the leakage neutrons has been discussed in previous portions of this report. In the case of the moon, the radiating volume will be the silicate rocks and other components of the upper meter or so of lunar surface material. The spectrum will clearly be slightly different from that leaking out from the earth. In the case of the planet Mars or Venus, the neutron spectrum will again be different and its exact evaluation will require a good knowledge of the chemical composition of the atmosphere of the planet in question. Clearly this will not be the same for Jupiter as for Venus. In programming any measurement, one must also recall that the space vehicle carrying any measuring instrument, will itself be bombarded by the cosmic radiation and will itself generate some neutrons, so that a background due to the measuring instrument and its vehicle will have to be allowed for.

Close to the earth, the fluxes being known, a flat-earth approximation may be used, while at great distances, i.e., distances large compared to the radius of the earth, the earth will appear to be a point source of neutrons. The neutrons at great distances will show an inverse square diminution in intensity, to which decay-loss must be added. The probability of decay in

any cubic cm., will clearly be given by:

$$\exp - (t/T)$$

where t is the time spent by the neutron in passing through that cm, and T the decay constant of the neutron. If T , the mean life is taken as 1000 seconds, a neutron at 53 MeV which is moving at 10^{10} cm/sec will spend 10^{-10} seconds in any cc, so that the exponential decay probability is 10^{-13} . Thus if we know the flux and the energy spectrum of the neutrons, we can calculate the number to be expected at any distance from the earth or other body. It is possible that a neutron detector might serve as a warning device for a space ship approaching a planet far from a star or other source of visible light.

REFERENCES

1. Foelsche, T.: The Ionizing Radiations in Supersonic Transport Flights. Proc. Second Symposium on Protection against Radiation Hazards in Space (Gatlinburg, Tennessee), NASA SP-71, pp. 287-299, 1965.
2. Armstrong, T. W.; Alsmiller Jr., R. G.; and Barish, J.: Calculation of the Radiation Hazard at Supersonic Aircraft Altitudes Produced by an Energetic Solar Flare. *Nucl. Sci. Engin.*, vol. 37, pp. 337-342, 1969.
3. Bethe, H. A.; Korff, S. A.; and Placzek, G.: On the Interpretation of Neutron Measurements in Cosmic Radiation. *Phys. Rev.*, vol. 57, pp. 573-587, 1940.
4. Korff, S. A.: Electron and Nuclear Counters, Second ed. The D. Van Nostrand Co., New York, 1955.
5. Soberman, R.: High Altitude Cosmic Ray Neutron Intensity Variations. *Phys. Rev.*, vol. 102, pp. 1399-1409, 1956.
6. Haymes, R. C.; and Korff, S. A.: Slow Neutron Intensity at High Balloon Altitudes. *Phys. Rev.*, vol. 120, pp. 1460-1462, 1962.
7. Haymes, R. C.: High Altitude Neutron Intensity Diurnal Variations. *Phys. Rev.*, vol. 116, pp. 1231-1237, 1959.
8. Mendell, R. B.; and Korff, S. A.: Fast-Neutron Detector with Discrimination Against Background Radiation. *Rev. Sci. Instr.*, vol. 34, pp. 1356-1360, 1963.
9. Mendell, R. B.; and Korff, S. A.: Fast Neutron Flux in the Atmosphere. *J. Geophys. Res.*, vol. 68, pp. 5487-5495, 1963.
10. Korff, S. A.; Mendell, R. B.; and Holt, S. S.: Measurement of Neutrons Produced by the Cosmic Radiation. Proc. Ninth Intern. Conf. on Cosmic Rays (London), vol. 1, pp. 573-576, 1965.
11. Holt, S. S.; Mendell, R. B.; and Korff, S. A.: Fast Neutron Latitude Variations in the Atmosphere at Solar Minimum. *J. Geophys. Res.*, vol. 71, pp. 5109-5116, 1966.
12. Korff, S. A.; Mendell, R. B.; Merker, M.; and Sandie, W.: Cosmic Ray Fast Neutron Flux Measurements in the Atmosphere at Various Latitudes. Proc. Eleventh Intern. Conf. on Cosmic Rays (Calgary), Can. J. Phys., Vol. 46, pp. S1023-1026, 1968.
13. Korff, S. A.; Mendell, R. B.; and Sandie, W. G.: Cosmic Ray Neutron Studies. Air Force Report, AFCRL 68-0006, 1967.
14. Sandie, W. G.; Mendell, R. B.; and Korff, S. A.: Latitude Variations of Fast and Slow Neutrons at Aircraft Altitudes during Solar Minimum. The Scientific Report of the Rockwell Polar Flight, pp. 36-49, 1965.
15. Lingenfelter, R. E.: Production of Carbon 14 by Cosmic-Ray Neutrons. *Rev. Geophys.*, vol. 1, pp. 35-55, 1963.
16. Preszler, A. M.; Simnett, G. M.; and White, R. S.: Earth Albedo Neutrons from 10-100 MeV. *Phys. Rev. Letters*, vol. 28, pp. 982-984, 1972.

17. Eyles, C. J.; Linney, A. D.; and Rochester, G. K.: A Search for Neutrons of Solar Origin Using Balloon Borne Detectors. Proc. Twelfth Intern. Conf. on Cosmic Rays (Hobart, Tasmania), vol. 2, pp. 462-467, 1971.
18. Wilkinson, D. H.: The Phoswich-A Multiple Phosphor. Rev. Sci. Instr., vol. 23, pp. 414-417, 1952.
19. Daehnick, W.; and Sherr, R.: Pulse Shape Discrimination in Stilbene Scintillators. Rev. Sci. Instr., vol. 23, pp. 666-670, 1961.
20. Verbinski, V. V.; Burrus, W. R.; and Love, T. A., et al.: Calibration of an Organic Scintillator for Neutron Spectrometry. Nucl. Instr. Meth., vol. 65, pp. 8-25, 1968.
21. Burrus, W. R.; and Verbinski, V. V.: Fast-Neutron Spectroscopy with Thick Organic Scintillators. Nucl. Instr. Meth., vol. 67, pp. 181-196, 1969.
22. Stewart, L.: Neutron Spectrum and Absolute Yield of a Plutonium-Beryllium Source. Phys. Rev., vol. 98, pp. 740-743, 1955.
23. Broek, H. W.; and Anderson, L. E.: The Stilbene Scintillation Crystal as a Spectrometer for Continuous Fast-Neutron Spectra. Rev. Sci. Instr., vol. 31, pp. 1063-1069, 1960.
24. Anderson, M. E.; and Bond, W. H.: Neutron Spectrum of a Plutonium-Beryllium Source. Nucl. Phys., vol. 43, pp. 330-338, 1963.
25. Kurz, R. J.: A 709/7090 Fortran II Program to Compute the Neutron-Detection Efficiency of Plastic Scintillator for Neutron Energies from 1 to 300 Mev. UCRL-1139, 1964.
26. Bertini, H. W.: Intranuclear-Cascade Calculation of the Secondary Nucleon Spectra from Nucleon-Nucleus Interactions in the Energy Range 340-2900 Mev and Comparisons with Experiment. Phys. Rev., vol. 188, pp. 1711-1730, 1969.
27. Zych, A. D.: Altitude Variation of High Energy Neutrons Near the Top of the Atmosphere. Bull. Am. Phys. Soc., vol. 14, p. 500, 1969.
28. Heidbreder, E., et al.: Measurement of the Distribution in Energy and Angle of High-Energy Albedo Neutrons and Determination of an Upper Limit for the Solar Neutron Flux. J. Geophys. Res., vol. 75, pp. 6347-6349, 1970.
29. Sydor, M.: The Atmospheric Neutron Spectrum at High Altitudes. Ph.D. Thesis, University of New Mexico, 1965.
30. Lockwood, J. A.; St. Onge, R. N.; Klumper, D.; and Schow, D.: The Energy Spectrum of Fast Neutrons in the Atmosphere. Acta Physica Academiae Scientiarum Hungaricae, vol. 29, suppl. 2, pp. 703-708, 1970.
31. Steljes, J. F.: Cosmic-Ray NM-64 Neutron Monitor. Atomic Energy of Canada Limited, Chalk River, Ontario, 1963-1971.

32. Light, E. S.; Merker, M.; Korff, S. A.; and Mendell, R. B.: Solar Modulation of Atmospheric Neutron Flux, Experiment and Calculation. *Proc. Twelfth Intern. Conf. on Cosmic Rays (Hobart, Tasmania)*, MOD 107, vol. 3, pp. 903-908, 1971.
33. Verschell, H. J.; Mendell, R. B.; and Korff, S. A.: Observations of the Cosmic Ray Modulation from Neutron Measurements at the High Latitude Transition Maximum. *Proc. Twelfth Intern. Conf. on Cosmic Rays (Hobart, Tasmania)*, MOD 61, vol. 2, pp. 752-757, 1971.
34. Simpson, J. A.; and Wang, J. R.: The Eleven-Year and Residual Solar Modulation of Cosmic Rays (1952-1969). *Astrophys. J.*, vol. 161, pp. 265-288, 1970.
35. Kane, S. R.; and Winckler, J. R.: Hysteresis Effect in Cosmic Ray Modulation and the Cosmic Ray Gradient Near Solar Minimum. *J. Geophys. Res.*, vol. 74, pp. 6247-6255, 1969.
36. Stoker, P. H.; and Carmichael, H.: Steplike Changes in the Long-Term Modulation of Cosmic Rays. *Astrophys. J.*, vol. 169, pp. 357-368, 1971.
37. Lockwood, J. A.; Lezniak, J. A.; and Webber, W. R.: Change in the Eleventh-Year Modulation at the Time of the June 8, 1969 Forbush Decrease. *J. Geophys. Res.*, vol. 77, pp. 4839-4844, 1972.
38. Schmidt, P. J.: Cosmic-Ray Electron Spectrum and Its Modulation Near Solar Maximum. *J. Geophys. Res.*, vol. 77, pp. 3295-3310, 1972.
39. Stoker, P. H.; Raubenheimer, B. C.; and van der Walt, A. J.: Rigidity Dependence of Cosmic Ray Modulation at Rigidities > 2 GV in August 1969. *J. Geophys. Res.*, vol. 77, pp. 3575-3582, 1972.
40. Metropolis, N., et al.: Monte Carlo Calculations on Intranuclear Cascades. 1. Low-Energy Studies. *Phys. Rev.*, vol. 110, pp. 185-204, 1958.
41. Dostrovski, I.; Rabinowitz, P.; and Bivins, R.: Monte Carlo Calculations of High-Energy Nuclear Interactions. 1. Systematics of Nuclear Evaporation. *Phys. Rev.*, vol. 111, pp. 1659-1676, 1958.
42. Hess, W. N.; Canfield, E. H.; and Lingenfelter, R. E.: Cosmic-Ray Neutron Demography. *J. Geophys. Res.*, vol. 66, pp. 665-678, 1961.
43. Lingenfelter, R. E.: The Cosmic Ray Neutron Leakage Flux. *J. Geophys. Res.*, vol. 68, pp. 5633-5639, 1963.
44. Newkirk, L. L.: Calculation of Low-Energy Neutron Flux in the Atmosphere by the S_n Method. *J. Geophys. Res.*, vol. 68, 1825-1833, 1963.
45. Sandie, W. G.: Neutrons Produced in the Earth's Atmosphere by the Cosmic Radiation. *Ph.D. Thesis, New York University*, 1967.
46. Light, E. S.: Fast Neutrons in the Atmosphere During Periods of Solar Activity. *Ph.D. Thesis, New York University*, 1971.
47. Merker, M.: Solar Cycle Modulation of Fast Neutrons in the Atmosphere. *Ph.D. Thesis, New York University*, 1970.

48. Alsmiller, Jr., R. G.; Leimdorfer, M.; and Barish, J.: Analytic Representation of Non-Elastic Cross-Sections and Particle-Emission Spectra from Nucleon-Nucleus Collisions in the Energy Range 25 to 400 MeV., ORNL 4046, 1967. (Available as NASA CR-83981.)
49. Bugg, D. V.; Salter, D. C.; Stafford, G. H.; George, R. F.; Riley, K. F.; and Tapper, R. J.: Nucleon-Nucleon Total Cross Sections from 1.1 to 8 Gev/c. Phys. Rev., vol. 146, pp. 980-992. 1966.
50. Adair, R. K.: Diffraction-Disassocation Model of Very-High Energy Nucleon Nucleon Interactions and Diffusion of Cosmic Rays Through the atmosphere. Phys. Rev., vol. 172, pp. 1370-1380, 1968.
51. Akimov, V. V.; Grigorov, N. L.; Mamontova, N. A.; Nesterov, V. E.; Prokhan, V. L.; Rapoport, I. D.; and Savenko, I. A.: Measurements of the inelastic proton-proton and proton-carbon cross-sections at energies 10^{10} - 10^{12} eV on board the Satellites Proton 1, 2, and 3. Acta Physica, vol. 29, Supplement 3, 1970.
52. Liland, A.; and Pilkuhn, H.: Scaling Law for Fast Pion Production by 20-70 GeV Protons. Phys. Letters, vol. 29B, pp. 663-665, 1969.
53. Alsmiller, Jr., R. G.; Leimdorfer, M.; and Barish, J.: Analytic Representation of Non Elastic Cross Sections and Particle Emission Spectra from Nucleon Nucleus Collisions in the Energy Range 25 to 400 MeV. ORNL 4046, 1967. (Available as NASA CR-83981.)
54. Winzeler, H.: Proton-Nucleus Collisions in the Multi-GeV Region. Nucl. Phys., vol. 69, pp. 661-694, 1965.
55. Artykov, I. Z.; Barashenkov, V. S.; and Eliseev, S. M.: Intranuclear Cascades with Many-Particle Interactions. Nucl. Phys., vol. B6, pp. 11-31, 1968.
56. Ranft, J.: Improved Monte-Carlo Calculation of the Nucleon-Meson Cascade in Shielding Material, I. Description of the Method of Calculation. Nucl. Inst. Meth., vol. 48, pp. 133-140, 1967.
57. Yiou, F.; Baril, M.; Dufaure de Citres, J.; Fontes, P.; Gradsztajn, E.; and Bernas, R.: Mass-Spectrometric Measurement of Lithium, Beryllium, and Boron Isotopes Produced in ^{16}O by High-Energy Protons, and Some Astrophysical Implications. Phys. Rev., vol. 166, pp. 968-974, 1968.
58. Shen, B. S. P.: High Energy Nuclear Reactions in Astrophysics. W. A. Benjamin Inc., New York, 1967.
59. Lohrmann, E.; and Teucher, M. W.: Heavy Nuclei and Alpha Particles Between 7 and 100 Bev/Nucleon. I. Interaction Mean Free Paths and Fragmentation Probabilities. Phys. Rev., vol. 115, pp. 636-642, 1959.
60. Milburn, G. P.; Birnbaum, W.; Crandall, W. E.; and Schecter, L.: Nuclear Radii from Inelastic Cross-Section Measurements. Phys. Rev., vol. 95, pp. 1268-1278, 1954.

61. Jain, P. L.; Lohrmann, E.; and Teucher, M. W.: Heavy Nuclei and Alpha Particles Between 7 and 100 Bev/Nucleon, II Fragmentation and Meson Production. *Phys. Rev.*, vol. 115, pp. 643-654, 1959.
62. Radin, J.: Cross Section for $C^{12}(n, \alpha)C^{11}$ at 920 MeV. *Phys. Rev. C*, Vol. 2, pp. 793-798, 1970.
63. Barashenkov, V. S.; Gudima, K. K.; and Toneev, V. D.: Inelastic Interactions of High-Energy Protons with Atomic Nuclei. *JINR-P2-4402*.
64. Bushnin, Yu. B., et al.: Negative Particle Production at the 70 Gev IHEP Acceleration. *Physics Letters*, vol. 29B, pp. 48-57, 1969.
65. Cocconi, G., et al.: Calculation of Particle Fluxes from Proton Synchrotrons of Energy 10-1000 GeV. *Berkeley High-Energy Physics Study*, 1961. UCID-1444, no. 28, part 2. August 11, 1961.
66. Piroue, P. A.; Smith, A. J. S.: Particle Production by 2.9 Bev Protons on Beryllium and Platinum. *Phys. Rev.*, vol. 148, pp. 1315-1326, 1966.
67. Binon, F., et al.: Further Measurements on the Production of π^- and K^- Mesons and Antiprotons at the 70 Gev IHEP Accelerator. *Physics Letters*, vol. 30B, pp. 506-509, 1969.
68. Rich, M.; and Madey, R.: Range-Energy Tables. *UCRL-2301*, 1954.
69. Gibbs, R. E.; et. al: Intranuclear Cascading in Photographic Emulsion at Accelerator and Cosmic-ray Energies. *Phys. Rev.*, vol. D10, pp. 783-790, 1974.
70. Fomin, Yu. A.; and Khristiansen, G. B.: A Three-Dimensional Monte Carlo Simulation of the Nuclear Active Component of Extensive Air Showers. *Acta Physica Academiae Scientiarum Hungaricae*, vol. 29, suppl. 3, pp. 435-438, 1970.
71. Irving, D. C.; Freestone, Jr., R. M.; and Kam, F. B. K.: 05R, A general-purpose Monte Carlo Neutron Transport Code, ORNL-3622, Oak Ridge National Laboratory, 1965.
72. Honeck, H. C.: ENDF/B, Specifications for an Evaluated Nuclear Data File for Reactor Applications. BNL 50066 (T-467) ENDF 102, Brookhaven National Laboratory, New York 1966 (1969 version).
73. Webber, W. R.: The Spectrum and Charge Composition of the Primary Cosmic Radiation. *Handbuch der Physik*, vol. XLVI/2, pp. 181-264, 1967.
74. Balasubrahmanyam, V. K., et al.: Solar Modulation of Galactic Cosmic Rays Near Solar Minimum (1965-1969). *Can. J. Phys.*, vol. 46, pp. 887-891, 1968.
75. Freier, P. S.; and Waddington, C. J.: Singly and Doubly Charged Particles in the Primary Cosmic Radiation. *J. Geophys. Res.*, vol. 73, pp. 4261-4271, 1968.
76. Ormes, J. F.; and Webber, W. R.: Proton and Helium Nuclei Cosmic-Ray Spectra and Modulation Between 100 and 2000 MeV/Nucleon. *J. Geophys. Res.*, vol. 73, pp. 4231-4245, 1968.

77. Badhwar, G. D., et al.: Flux of Hydrogen, Helium, and Electrons at Fort Churchill in 1967. *J. Geophys. Res.*, vol. 74, pp. 369-371, 1969.
78. Pinkau, K.; Polvogt, U.; Schmidt, W. K. H.; and Huggett, R. W.: Measurement of the Primary Cosmic Ray Proton and Alpha-Particle Spectra Above 10 Gev/Nucleon. *Acta Physica Academiae Scientiarum Hungaricae*, vol. 29, suppl. 1, pp. 291-296, 1970.
79. Lezniak, J. A.; and Webber, W. R.: Solar Modulation of Cosmic Ray Protons, Helium, Nuclei, and Electrons, a Comparison of Experiment with Theory. *J. Geophys. Res.*, vol. 76, pp. 1605-1624, 1971.
80. Rygg, T. A.: Cosmic Ray Proton and Helium Measurement Over Half a Solar Cycle. *Tech. Report, University of Maryland*, pp. 70-111, 1970. (Available as NASA CR-119013.)
81. Puri, R. K.; and Aditya, P. K.: Flux of Primary Helium Nuclei Near Hyderabad During 1965. *J. Geophys. Res.*, vol. 73, pp. 4393-4395, 1968.
82. Lommen, P. W.; Deney, C. L.; and Kaplon, M. F.: Balloon Measurement of Proton and Alpha Particle Fluxes from Palestine, Texas. *J. Geophys. Res.*, vol. 74, pp. 2319-2326, 1969.
83. Bertsch, D. L.; and Fody, S. A.: Solar Modulation of Primary Cosmic Rays as Deduced from Neutron Monitor Data. *J. Geophys. Res.*, vol. 72, pp. 5347-5356, 1967.
84. Lockwood, J. A.; and Webber, W. R.: Differential Response and Specific Yield Functions of Cosmic Ray Neutron Monitors. *J. Geophys. Res.*, vol. 72, pp. 3395-3402, 1967.
85. Verschell, H.: Observations of the Cosmic Ray Modulation from Neutron Measurements at the High Latitude Transition Maximum. *Ph.D. Thesis, New York University*, 1972.
86. Gloeckler, G.; and Jokipii, J. R.: Solar Modulation and the Energy Density of Galactic Cosmic Rays. *Astrophys. J.*, vol. 148, pp. L 41-L 46, 1967.
87. Ryan, M. J.; Ormes, J. F.; and Balasubrahmanyam, V. K.: Cosmic-Ray Proton and Helium Spectra Above 50 GeV. *Phys. Rev. Letters*, vol. 28, pp. 985-988, 1972.
88. Shapiro, M. M.; and Silberberg, R.: Heavy Cosmic Ray Nuclei. *Annual Review of Nuclear Science*, vol. 20, pp. 323-392, 1970.
89. Gabriel, T. A.; Santoro, R. T.; and Alsmiller, Jr., R. G.: Approximate High-Energy Alpha-Particle Nucleus Collision Model. *ORNL-TM-3153*, 1970. (Available as NASA CR-118026.)
90. Wilson, J. W.; Lambotte, J. J.; and Foelsche, T.: Structure in the Fast Spectra of Atmospheric Neutrons. *J. Geophys. Res.*, vol. 74, pp. 6494-6496, 1969.
91. Jenkins, R. W.; Lockwood, J. A.; Ifedili, S. O.; and Chupp, E. L.: Latitude and Altitude Dependence of the Cosmic Ray Albedo Neutron Flux. *J. Geophys. Res.*, vol. 75, pp. 4197-4204, 1970.

92. White, R. S.; Moon, S.; Preszler, A.M.; and Sinnett, G. M.: Earth Albedo and Solar Neutrons. ICPP-UCR-72-16, 1972. (Available as NASA CR-153878.)
93. Merker, M.: Energetic Neutrons Leaking from the Top of the Atmosphere. *Phys. Rev. Letters*, vol. 29, pp. 1531-1534, 1972.
94. Merker, M.: The Contribution of Galactic Cosmic Rays to the Atmospheric Neutron Maximum Dose Equivalent as a function of Neutron Energy and Altitude. *Health Physics*, vol. 25, no. 5, Nov. 1973, pp. 524-527.
95. Miyake, S.; Hinotani, K.; and Nunogaki, K.: Intensity and Energy Spectrum of Fast Neutrons in Cosmic Radiation. *J. Phys. Soc. Japan*, vol. 12, pp. 113-121, 1957.
96. Hess, W. N.; Patterson, H. W.; Wallace, R. W.; and Chupp, E. L.: The Cosmic Ray Neutron Spectrum. *Phys. Rev.*, vol. 116, pp. 445-457, 1959.
97. Haymes, R. C.: Fast Neutrons in the Earth's Atmosphere, I, Variation with Depth. *J. Geophys. Res.*, vol. 69, pp. 841-852, 1964.
98. Baird, G. A.; and Wilson, B. G.: Solar Minimum Measurement of Fast Neutrons at High Altitude. *Can. J. Phys.*, vol. 44, pp. 2131-2136, 1966.
99. Tajima, E.; Adachi, M.; Doke, T.; Kubota, S.; and Tsukuda, M.: Spectrum of Cosmic Ray Produced Neutrons. *J. Phys. Soc. Japan*, vol. 22, pp. 355-360, 1967.
100. Bhatt, V. L.; and Parikh, V. R.: The Energy Spectrum of Fast Neutrons in the Upper Atmosphere Using Recoil Proton Techniques in Nuclear Emulsion. *Acta Physica Academiae Scientiarum Hungaricae*, vol. 29, suppl. 2, pp. 721-726, 1970.
101. Alberne, F.; and Talon, R.: Determination du Spectre et du Flux de Neutrons Atmospheriques Rapides en Période de Soleil Calme et à une Latitude Géomagnétique de 46° Nord. *Ann. Geophys.*, t25, fasc. 1, pp. 99-102, 1969.
102. Zobel, W.; Love, T. A.; Delorenzo, J. T.; and McNew, C. O.: Neutron Spectral Measurements in the Upper Atmosphere. *Proc. Nat. Symposium on Natural and Manmade Radiation in Space*, NASA TM-X-2400, pp. 922-925, 1972.
103. Wallace, R.; and Boyer, M. F.: An Experimental Measurement of Galactic Cosmic Radiation Dose in Conventional Aircraft between San Francisco and London Compared to Theoretical Values for Conventional and Supersonic Aircraft. *Proc. Nat. Symposium on Natural and Manmade Radiation in Space*, NASA TM X-2440, pp. 884-893, 1971.
104. Boella, G.; Degli Antoni, G.; Dillworth, C.; Panetti, M.; Scarsi, L.; and Intriligator, D. S.: Measurement of the Cosmic Ray Neutron Flux at 4.6 Billion Volts Geomagnetic Cutoff. *J. Geophys. Res.*, vol. 70, pp. 1019-1030, 1965.
105. Boella, G.; Dillworth, D.; Panetti, M.; and Scarsi, L.: The Atmospheric and Leakage Flux of Neutrons Produced in the Atmosphere by Cosmic Ray Interactions. *Earth and Planetary Science Letters*, vol. 4, pp. 393-398, 1968.

106. Intriligator, D. S.: Albedo Neutron Source for High-Energy Protons Trapped in the Geomagnetic Field. *Phys. Rev. Letters*, vol. 20, pp. 1048-1049, 1968.
107. Jenkins, R. W.; Ifedili, S. O.; Lockwood, J. A.; and Razdan, H.: The Energy Dependence of the Cosmic-Ray Neutron Leakage Flux in the Range 0.01-10 MeV. *J. Geophys. Res.*, vol. 76, pp. 7470-7478, 1971.
108. Miles, R. F.: Density of Cosmic-Ray Neutrons in the Atmosphere. *J. Geophys. Res.*, vol. 69, 1277-1284, 1964.
109. Smith, R. V.; Chase, F.; Imhof, W. L.; Reagan, J. B.; and Walt, M.: Radiation Measurements with Balloons. *ARL-TDR-62-2*, Res. Lab., Holloman A. F. B., New Mexico, 1962.
110. Greenhill, J. G.; Fenton, K. B.; Fenton, A. G.; and White, K. S.: The Neutron Flux at Balloon Altitudes During a Solar Proton Event. *J. Geophys. Res.*, vol. 75, 4595-4603, 1970.
111. Chupp, E. L.; Hess, W. N.; Curry, C.: The Neutron Flux in Space After the November 15, 1960, Polar Cap Neutron Event. *J. Geophys. Res.*, vol. 72, 3809-3816, 1967.
112. Lockwood, J. A.; and Friling, L. A.: Cosmic Ray Neutron Flux Measurements Above the Atmosphere. *J. Geophys. Res.*, vol. 73, pp. 6649-6663, 1968.
113. Lingenfelter, R. E.; and Flamm, E. J.: Neutron Leakage Flux from Interactions of Solar Protons in the Atmosphere. *J. Geophys. Res.*, vol. 69, 2199-2207, 1964.
114. Lingenfelter, R. E.; and Flamm, E. J.: Correction. *J. Geophys. Res.*, vol. 69, p. 4201, 1964.
115. Alsmiller, Jr., R. G.; and Boughner, R. F.: Solar Neutron Transport in the Earth's Atmosphere. *J. Geophys. Res.*, vol. 73, pp. 4935-4942, 1968.
116. Solar Geophysical Data. U. S. Department of Commerce, Boulder, Colorado, 1968-1971.
117. Engelmann, J.; Hautdidier, A.; and Koch, L.: Energy Spectra and Time Profile of Protons Emitted During the Solar Flare of June 9, 1968. *Acta Physica Academiae Scientiarum Hungaricae*, vol. 29, suppl. 2, pp. 487-491, 1970.
118. Smart, D. F.; Shea, M. A.; and Tanskanen, P. J.: A Determination of the Spectra, Spatial Anisotropy, and Propagation Characteristics of the Relativistic Solar Cosmic-Ray Flux on November 18, 1968. *Proceedings of the 12th International Cosmic Ray Conf. Papers*, vol. II, pp. 483-488, 1971.
119. Bazilevskaya, G. A.; Charakhchyan, A. N.; Charakhchyan, T. N.; Lazutin, L. L.; and Stozhkov, Yu. I.: Data on Solar Proton Events, Recorded in the Stratosphere During the 20th Solar Cycle. *Proc. Twelfth Intern. Conf. on Cosmic Rays (Hobart, Tasmania)*, vol. 5, pp. 1825-1836, 1971.

120. Bayarevich, V. V.; Basilevskaya, G. A.; Svirzhevsky, N. S.; Stozkov, Yu.; Charakhchyan, A. N.; Charakhchyan, T. N.: *Cosmic Ray Bursts in February-April, 1969: The Investigation of Galactic and Solar Cosmic Rays in the Stratosphere.* P. N. Lebedev Physical Institute Moscow, pp. 68-81, 1969.
121. Barouch, E.; Engelmann, J.; Gros, M.; Koch, L.; and Masse, P.: *Simultaneous Satellite and Rocket Observations of the February 25th, 1969 Solar Proton Event.* *Acta Physica Academiae Scientiarum Hungaricae*, vol. 29, suppl. 2, pp. 493-499, 1970.
122. Duggal, S. P.; and Pomerantz, M. A.: *The Propagation of Energetic Solar Particles During Highly Anisotropic Ground Level Events.* *Proc. Twelfth Intern. Conf. on Cosmic Rays (Hobart, Tasmania)*, vol. 2, pp. 533-537, 1971.
123. Engel, A. R.; Balogh, A.; Elliot, H.; Hynds, R. J.; and Quenby, J. J.: *The Solar Proton Events of February 25 and 27, 1969, 1. Particle Fluxes in Interplanetary Space.* *Acta Physica Academiae Scientiarum Hungaricae*, Budapest, vol. 29, suppl. 2, pp. 439-444, 1970.
124. Green, G.; Krieger, R.; Wibberenz, G.; and Witte, M.: *Energy Spectra of Protons and Alpha Particles During the February 25, 1969 Solar Event.* *Acta Physica Academiae Scientiarum Hungaricae*, Budapest, vol. 29, suppl. 2, pp. 393-399, 1970.
125. Palmeira, R. A. R.; Bukata, R. P.; and Gronstal, P. T.: *The March 30, 1969 Solar Flare Event.* *VI Interamerican Seminar on Cosmic Rays, La Paz, Bolivia*, vol. 1, pp. 231-245, 1970.
126. Balogh, A.; Dyer, C. S.; Engel, A. R.; Hynds, R. J.; and Quenby, J. J.: *The March 30, 1969 Solar Proton Event: Directional Measurements of Solar Proton Fluxes in Interplanetary Space.* *Proc. Twelfth Intern. Conf. on Cosmic Rays (Hobart, Tasmania)*, vol. 5, pp. 1819-1824, 1971.
127. Quenby, J. J.; Balogh, A.; Engel, A. R.; Elliot, H.; Hedgecock, P. C.; Hynds, R. J.; and Sear, J. R.: *The Solar Proton Events of February 25 and 27, 1969, 2. Interpretation of Correlated Interplanetary Magnetic Field and Particle Measurements.* *Acta Physica Academiae Scientiarum Hungaricae*, vol. 29, suppl. 2, pp. 445-451, 1970.
128. Masley, A. J.; and Satterblom, P. R.: *Solar Cosmic Ray Observations During the September and November 1969 Events.* *Proc. Twelfth Intern. Conf. on Cosmic Rays (Hobart, Tasmania)*, vol. 5, pp. 1849-1852, 1971.
129. Freier, P. S.; and Webber, W. R.: *Exponential Rigidity Spectrums for Solar-Flare Cosmic Rays.* *J. Geophys. Res.*, vol. 68, pp. 1605-1629, 1963.

130. Engelmann, J.; Hynds, R. J.; Morfill, G.; Axisa, F.; Bewick, A.; Durney, A. C.; and Koch, L.: Penetration of Solar Protons Over the Polar Cap During the February 25, 1969, Event. *J. Geophys. Res.*, vol. 76, pp. 4245-4261, 1971.

131. King, J. H.: Solar Cycle 20 Proton Event Integrations and Intercomparisons of Three Imp-F Solar Proton Data Sets. *Lunar Science Institute Conference on Modern and Ancient Energetic Particles from the Sun*, Houston, Texas, 1971.

132. Verschell, H. J.; Mendell, R. B.; Korff, S. A.; and Roelof, E. C.: Two Classes of Forbush Decrease. *Proc. Twelfth International Conference on Cosmic Rays (Hobart, Tasmania)*, vol. 2, pp. 764-770, 1971.

133. Verschell, H. J.; Mendell, R. B.; Korff, S. A.; and Roelof, E. C.: Two Classes of Cosmic Ray Decrease. *J. Geophys. Res.*, vol. 80, pp. 1189-1201, 1975.

134. Roelof, E. C.; Verschell, H. J.; and Mendell, R. B.: Implications of a Long-Lived Recovery of Cosmic Ray Intensity. *Proc. Twelfth International Conference on Cosmic Rays (Hobart, Tasmania)*, vol. 2, pp. 764-770, 1971.

135. Verschell, H. J.; Mendell, R. B.; and Korff, S. A.: A Hysteresis Effect in the Cosmic Ray Modulation. *Proc. Thirteenth International Conference on Cosmic Rays (Denver)*, vol. 2, pp. 1317-1322, 1973.

136. Mendell, R. B.; and Korff, S. A.: The Observed Spectrum of Variation of Cosmic Ray Intensity Above 1 GeV/Nucleon and Models of Cosmic Ray Modulation. *Proc. Fifteenth International Conference on Cosmic Rays (Plovdiv, Bulgaria)*, Paper MG-45, 1977.

137. Debrunner, H.; and Flueckiger, E.: Calculation of the Multiplicity Yield Function of the NM-64 Monitor. *Proc. Twelfth International Conference on Cosmic Rays (Hobart)*, vol. 3, pp. 911-916, 1971.

138. Mathews, T.; Stoker, P. H.; and Wilson, B. G.: A Comparative Study of the Dependence of Forbush Decreases and the 11-Year Variation in Cosmic Ray Intensity. *Planet. Space. Sci.*, vol. 19, pp. 981-991, 1971.

139. Antonucci, E. G.; Castagnoli, G. C.; and Dodero, M. A.: Underground Cosmic Ray Intensity Modulation and Interplanetary Structures during 1970-1971. *Proc. 12th Int. Conf. on Cosmic Rays*, vol. 2, pp. 629-634, 1971.

140. Van Hollebeke, M. A. I.; Wang, J. R.; and McDonald, F. B.: Modulation of Low Energy Galactic Cosmic Rays Over Solar Maximum (Cycle 20). *J. Geophys. Res.*, vol. 77, pp. 6881-6885, 1972.

141. Burger, J. J.; and Swanenburg, B. N.: Energy Dependent Time Lag in the Long Term Modulation of Cosmic Rays. *J. Geophys. Res.*, vol. 78, pp. 292-305, 1973.

142. Garcia Munoz, M.; Mason, G. M.; and Simpson, J. A.: New Aspects of the Cosmic-Ray Modulation in 1974-1975 Near Solar Minimum. *Astrophys. J.*, vol. 213, pp. 263-268, 1977.

143. Moraal, H.; and Stoker, P. H.: The Force Field Approach to the 11-Year Cosmic Ray Modulation Cycle as Observed By Stationary Neutron Monitors. *J. Geophys. Res.*, vol. 80, pp. 3253-3263, 1975.

144. Rockstroh, J. M.; and Webber, W. R.: Cosmic Ray Electrons of $E > 1$ GeV-Some New Measurements and Interpretations. *J. Geophys. Res.*, vol. 78, pp. 1-11, 1973.
145. Fulks, G. J.: Solar Modulation of Galactic Cosmic Ray Electrons, Protons, and Alphas. *J. Geophys. Res.*, vol. 80, pp. 1701-1714, 1975.
146. McKibben, R. B.: Cosmic Ray Intensity Gradients in the Solar System. *Rev. Geophys. and Space Phys.*, vol. 13, pp. 1088-1099, 1975.
147. Moraal, H.; and Gleeson, L. J.: Three-Dimensional Models of the Galactic Cosmic Ray Modulation. *Proc. Fourteenth International Conf. on Cosmic Rays*, vol. 12, pp. 4189-4194, 1975.
148. O'Gallagher, J. J.: A Time-Dependent Diffusion-Convection Model for the Long Term Modulation of Cosmic Rays. *Astrophys. J.*, vol. 197, pp. 495-507, 1975.
149. Garrard, T. L.; Stone, E. C.; and Vogt, R. E.: Solar Modulation of Cosmic Ray Protons and He Nuclei. *Proc. Thirteenth International Conf. on Cosmic Rays*, vol. 2, pp. 732-737, 1973.
150. Winckler, C. N.; and Bedijn, P. J.: Long-Term Cosmic Ray Modulation in the Period 1966-1972 and Interplanetary Magnetic Fields. *J. Geophys. Res.*, vol. 81, pp. 3198-3206, 1976.
151. Fisk, L. A.: Solar Modulation of Galactic Cosmic Rays, 2: *J. Geophys. Res.*, vol. 76, pp. 221-227, 1971.
152. Verschell, H. J.; and Bercovitch, M.: Charge Dependent Effect in the Solar Modulation of Cosmic Rays (Abstract). *Proc. Fifteenth International Conf. on Cosmic Rays*, vol. 3, p. 193, 1977.

COMPOSITE SCINTILLATOR

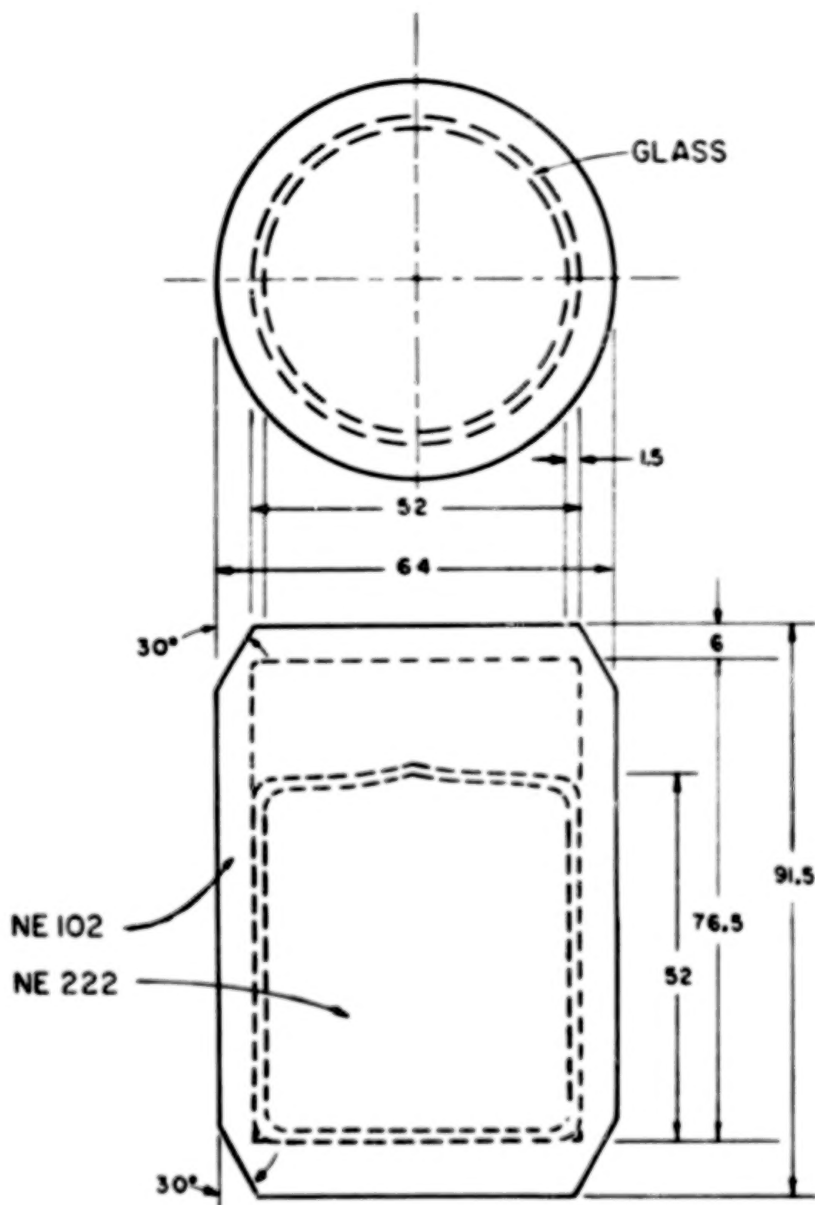


Figure 1. - Composite scintillator for flight detector, dimensions in mm.

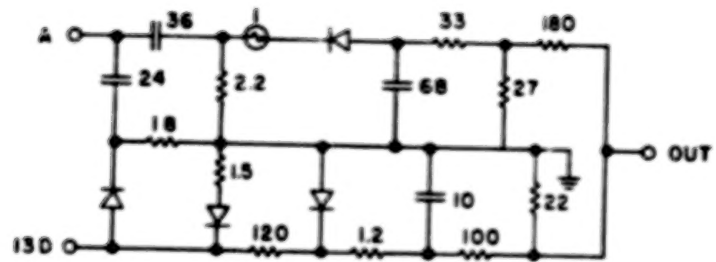


Figure 2. - Pulse shape discrimination circuit.

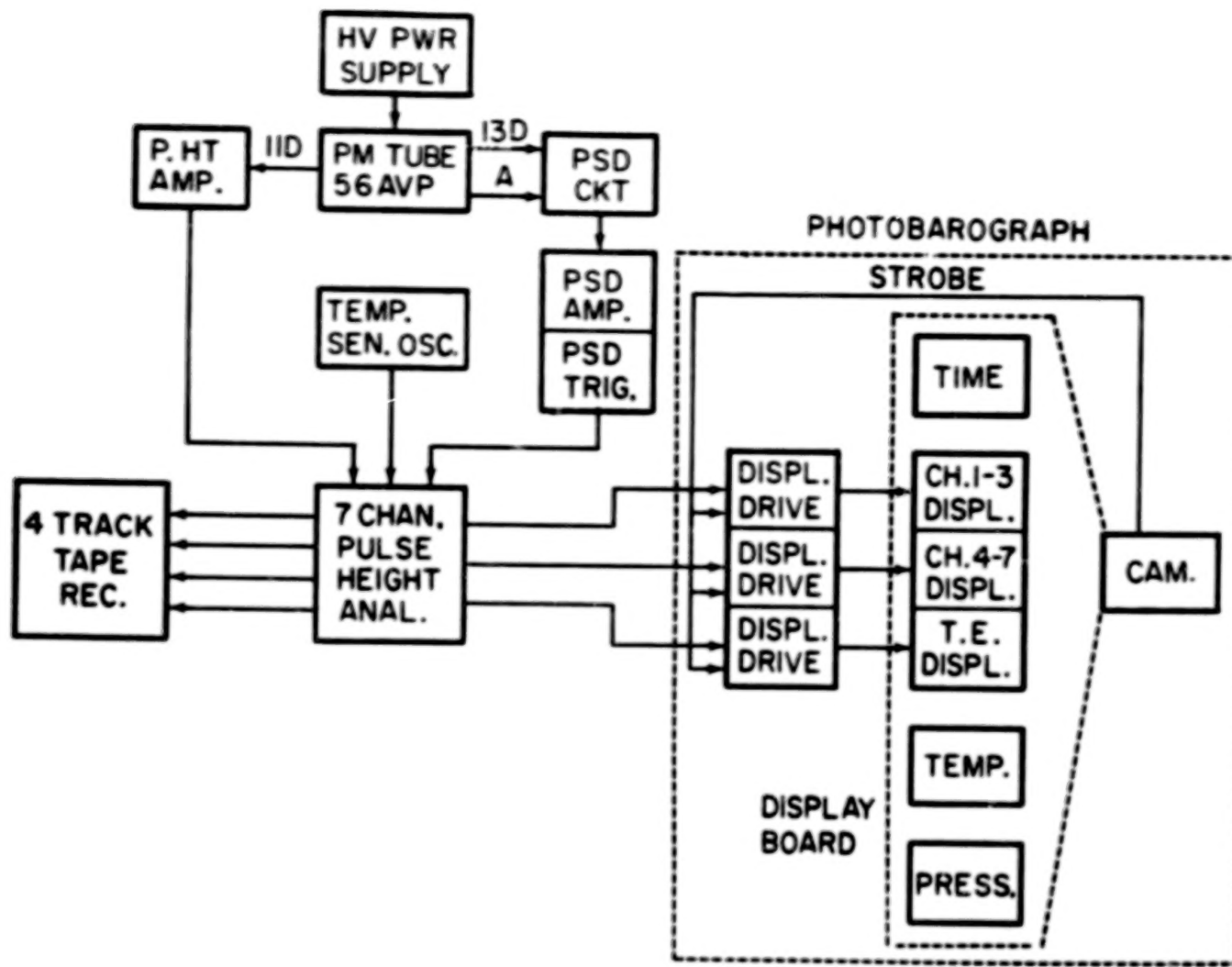


Figure 3. - Block diagram of flight system.

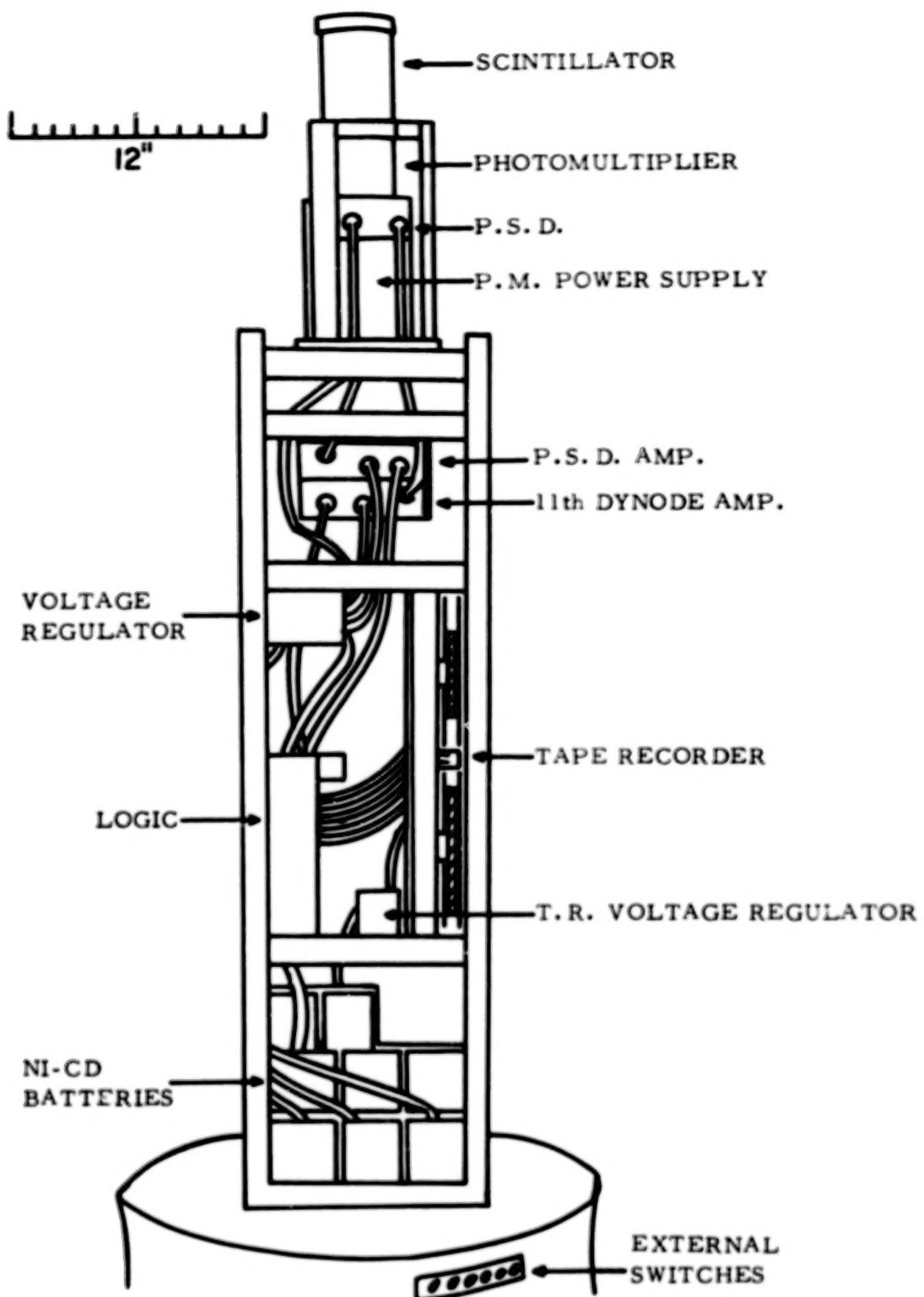


Figure 4. - Instrumentation rack for balloon gondola.

RESPONSE FUNCTIONS

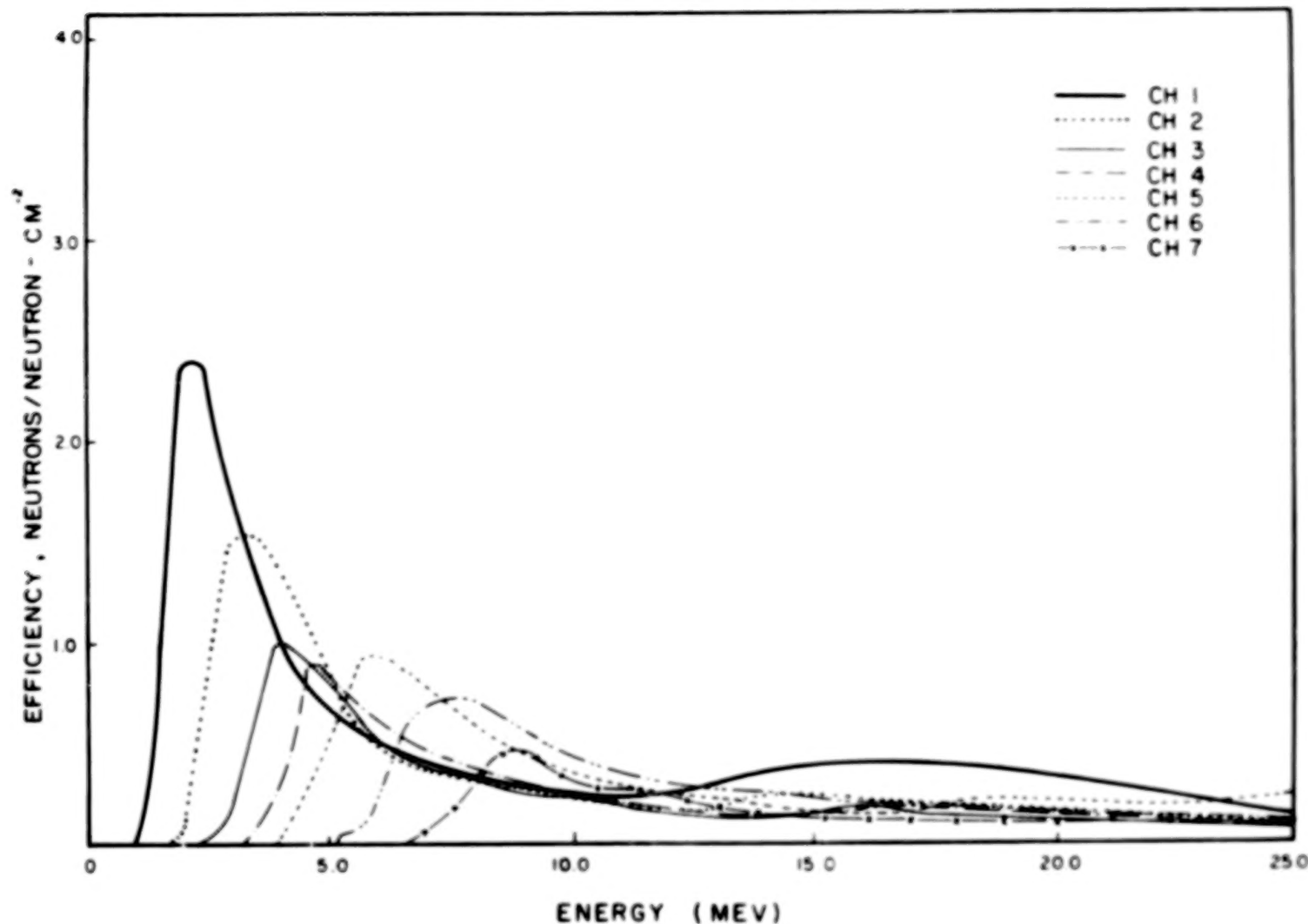


Figure 5. - Response of the seven channels of the neutron detector to neutrons from 1-25 MeV

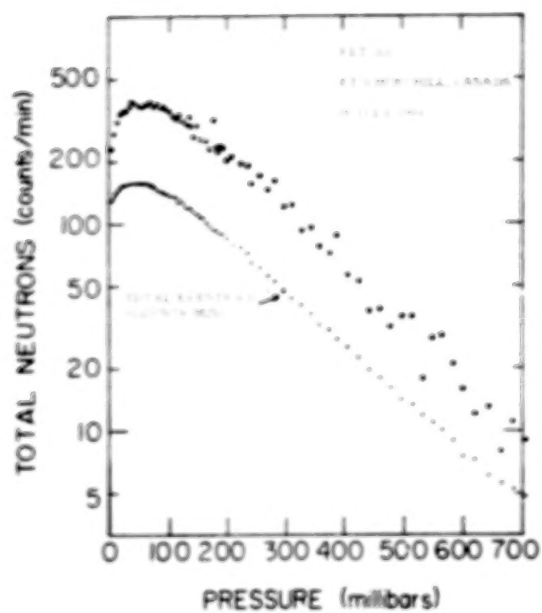


Fig. 6a

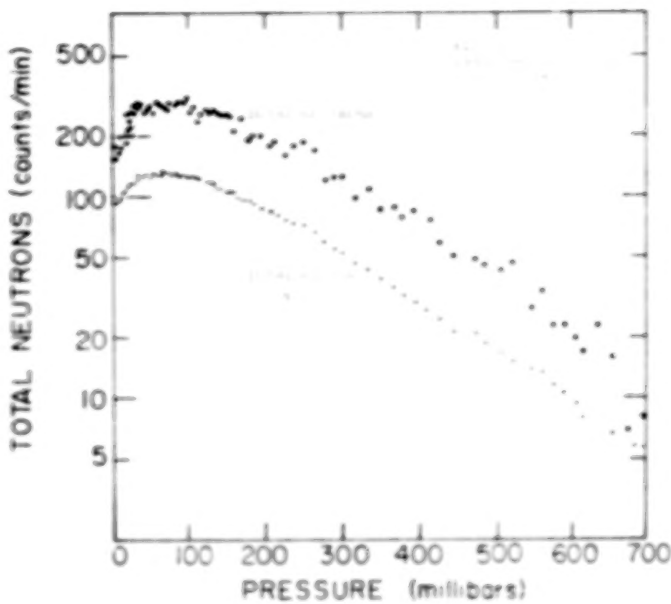


Fig. 6b

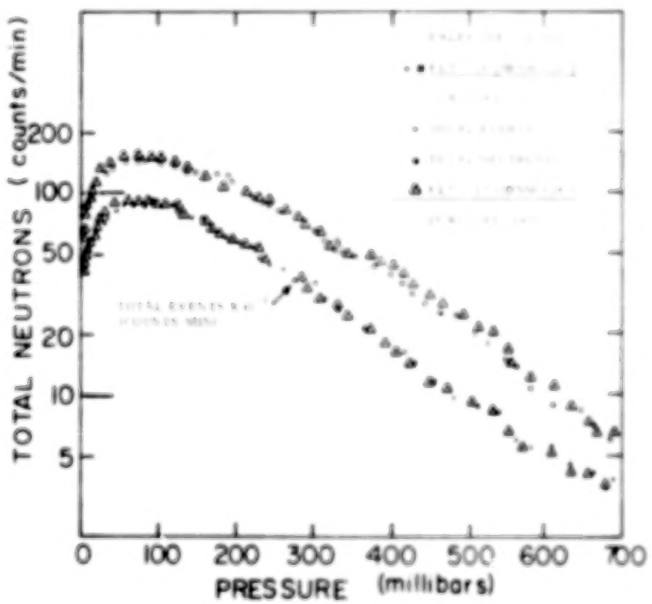


Fig. 6c

Figure 6. - Fast neutron counting rates and total events counting rates vs atmospheric depth, from balloon flights at different solar epochs and at different geomagnetic latitudes

- (a) Flight 113 near cosmic ray maximum, at high latitude
- (b) Flight 123 near cosmic ray minimum, at high latitude
- (c) Flights 126 and 127 near cosmic ray minimum, at 4.5 GV cutoff rigidity. To improve statistics, five minute running averages are plotted

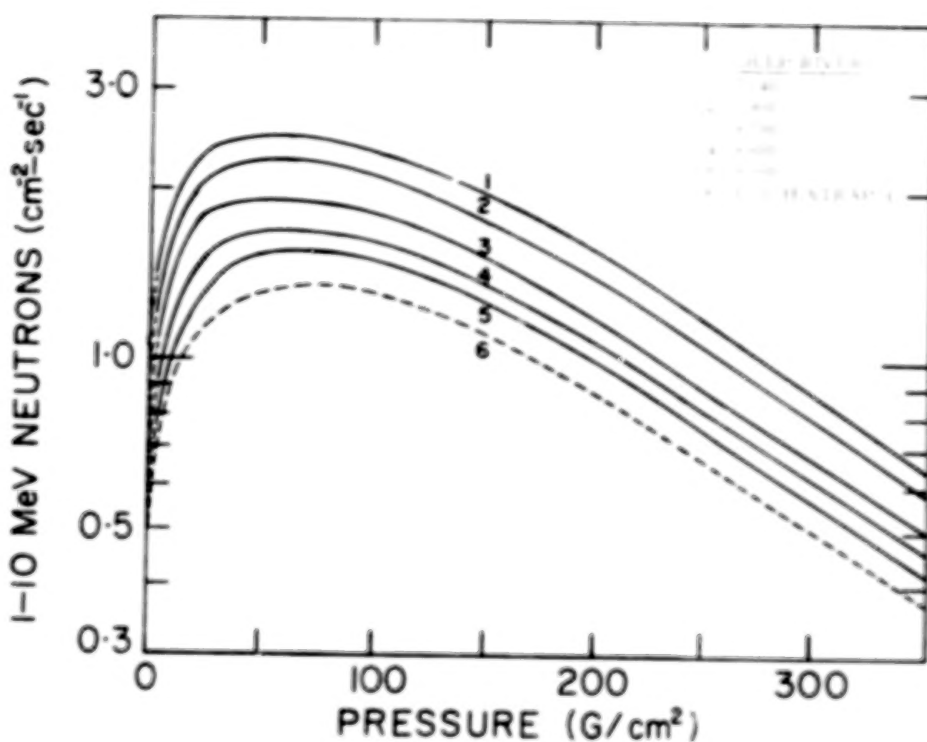


Figure 7. - Regression curves of the 2-10 MeV neutron flux vs DRNM at different atmospheric depths, from balloon flights between 1965 and 1968 at high latitude. The dashed lines are extrapolated from the experimental data using the results of the Monte Carlo calculation. To convert to 1-10 MeV flux, use Table V.

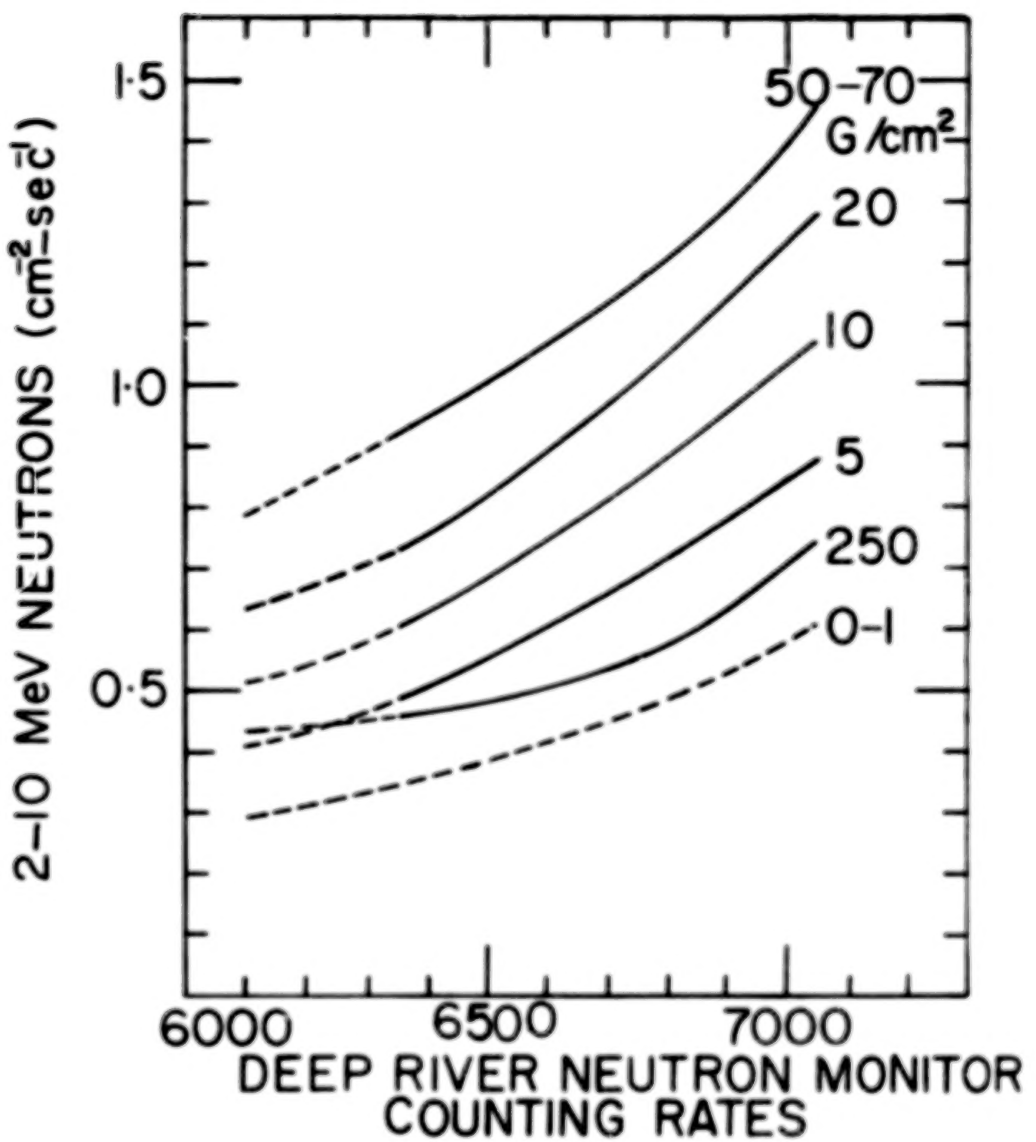


Figure 8. - Fast neutron flux vs atmospheric depth at varying degrees of solar modulation, from balloon flight data. Dashed lines are extrapolations using Monte Carlo calculation.

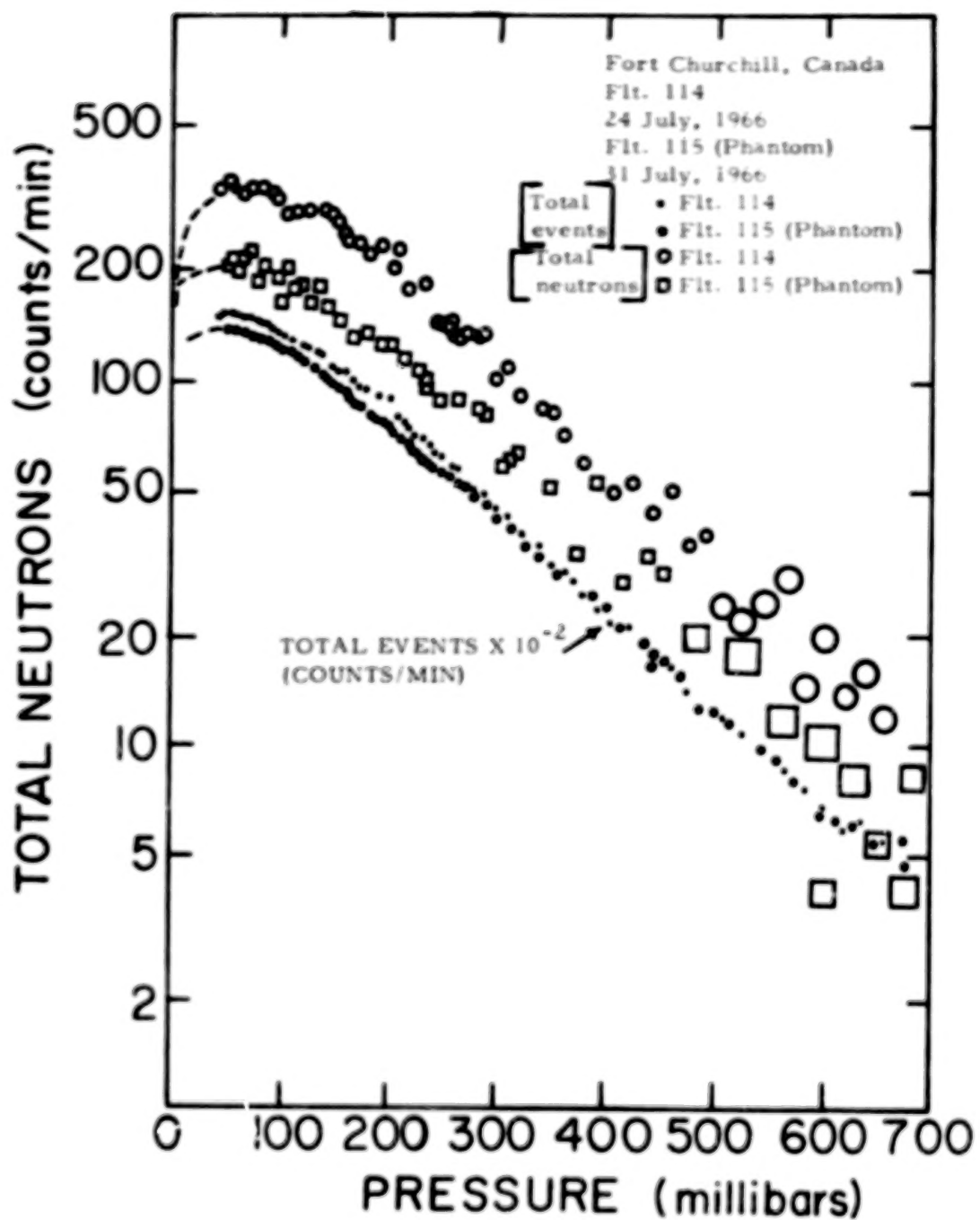


Figure 9. - Comparison of counting rates during a normal balloon flight with counting rates during a balloon flight with tissue equivalent dome on the gondola.

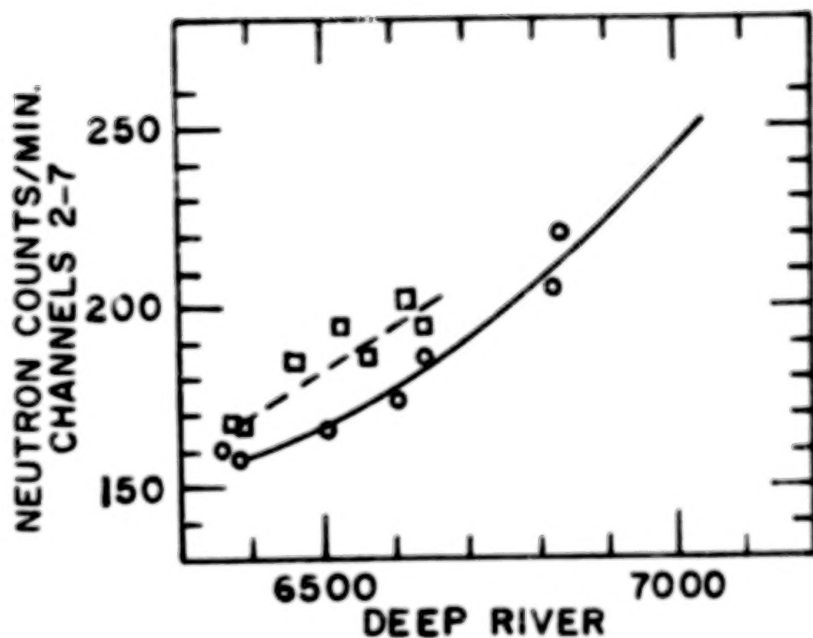


Figure 10. - Counting rates of neutron channels 2-7 in system 1966-11 balloon flights (circles) and aircraft flights (squares). The effect of the material of the aircraft on neutron counting rates is illustrated.

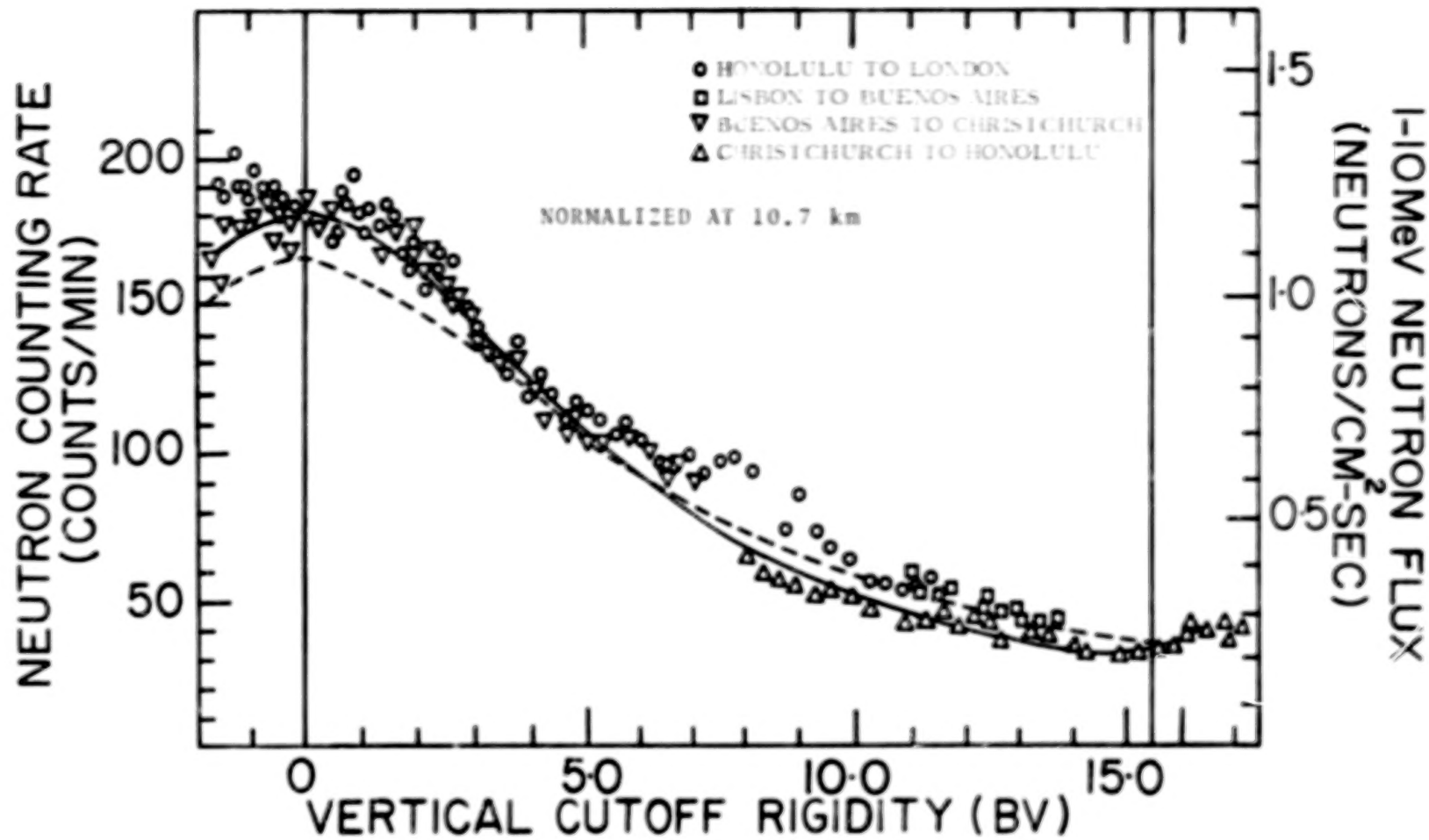


Figure 11. - Latitude survey of fast neutrons in aircraft flight which circled the earth over both poles, November 14-16, 1965. All data has been normalized to the atmospheric depth of 245 g/cm^2

----- Monte Carlo calculation

— Monte Carlo normalized calculation

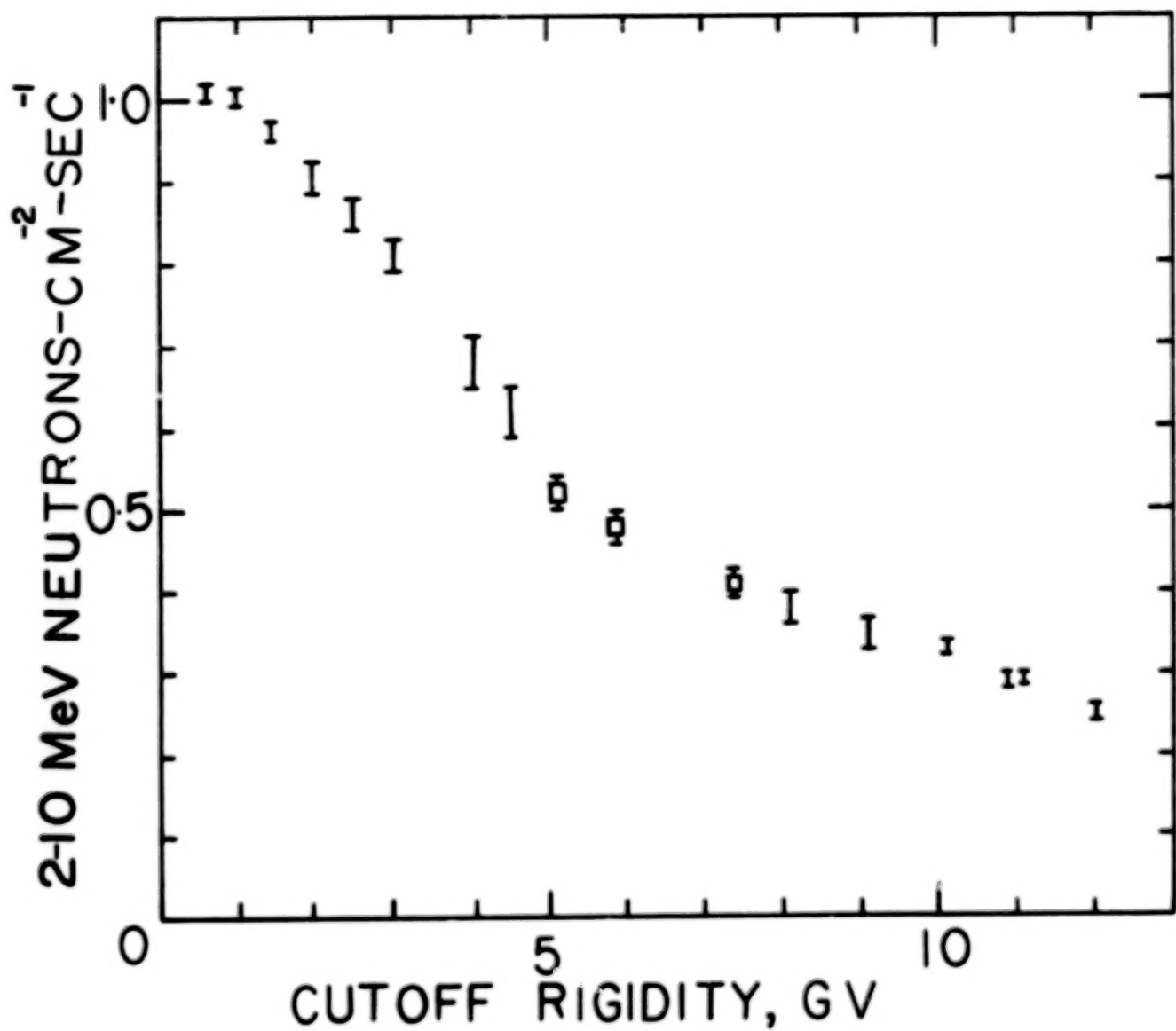


Figure 12. - Aircraft latitude survey of fast neutrons near the transition maximum, May-June 1968. Error bars include correction for background

Data at 72 g/cm² atmospheric depth

Data at 118 g/cm² atmospheric depth, normalized to 72 g/cm²

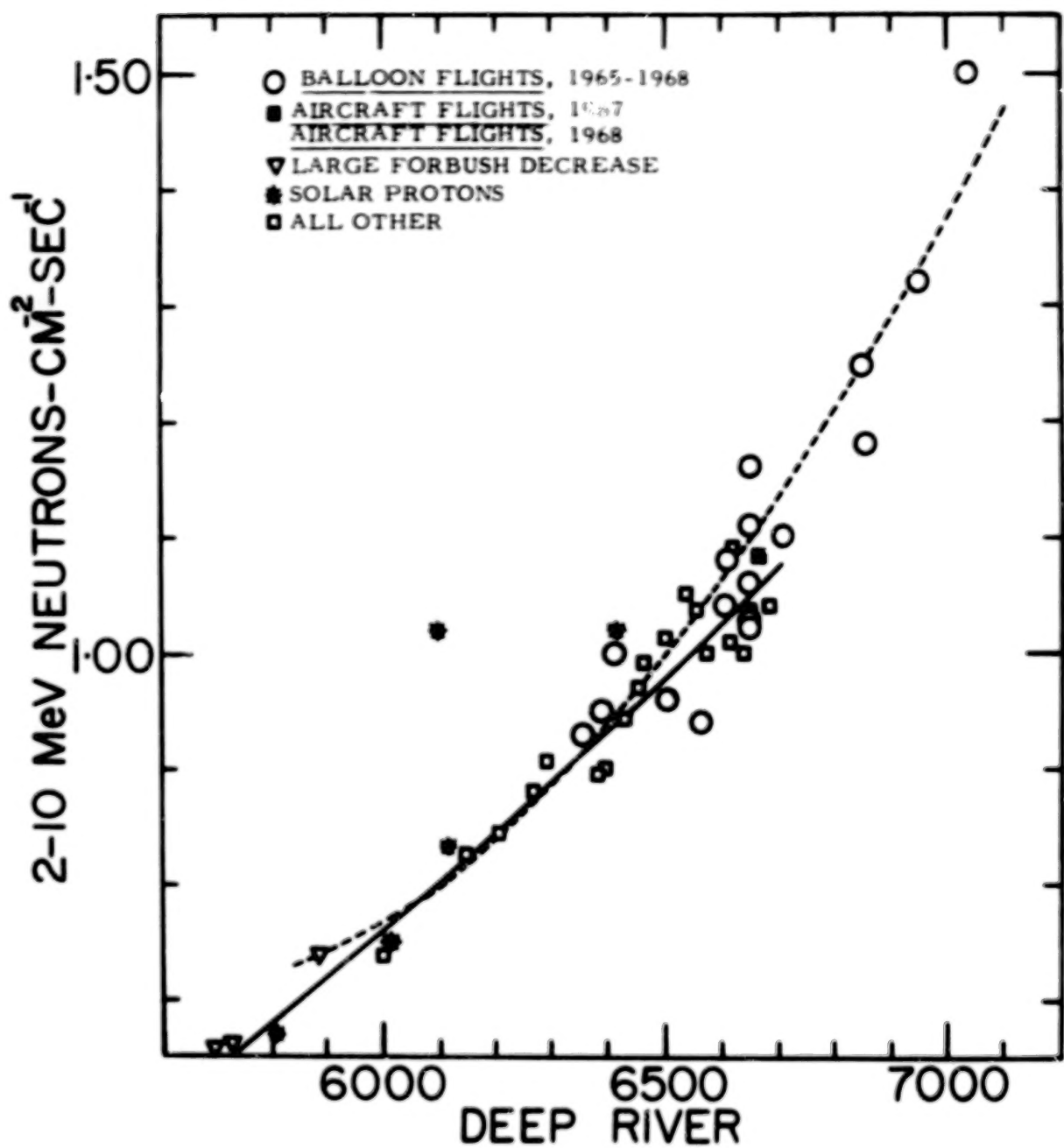


Figure 13. - Regression curves of the 2-10 MeV neutron flux at the high latitude transition maximum vs the counting rate of the Deep River neutron monitor, from 8/ 65 to 12/ 31/ 68. Dashed curve is best parabolic fit to the data from balloon and aircraft flights. Solid line is the best parabolic fit to the aircraft flight data only. To obtain 1-10 MeV neutron flux, multiply ordinate by 1. 70.

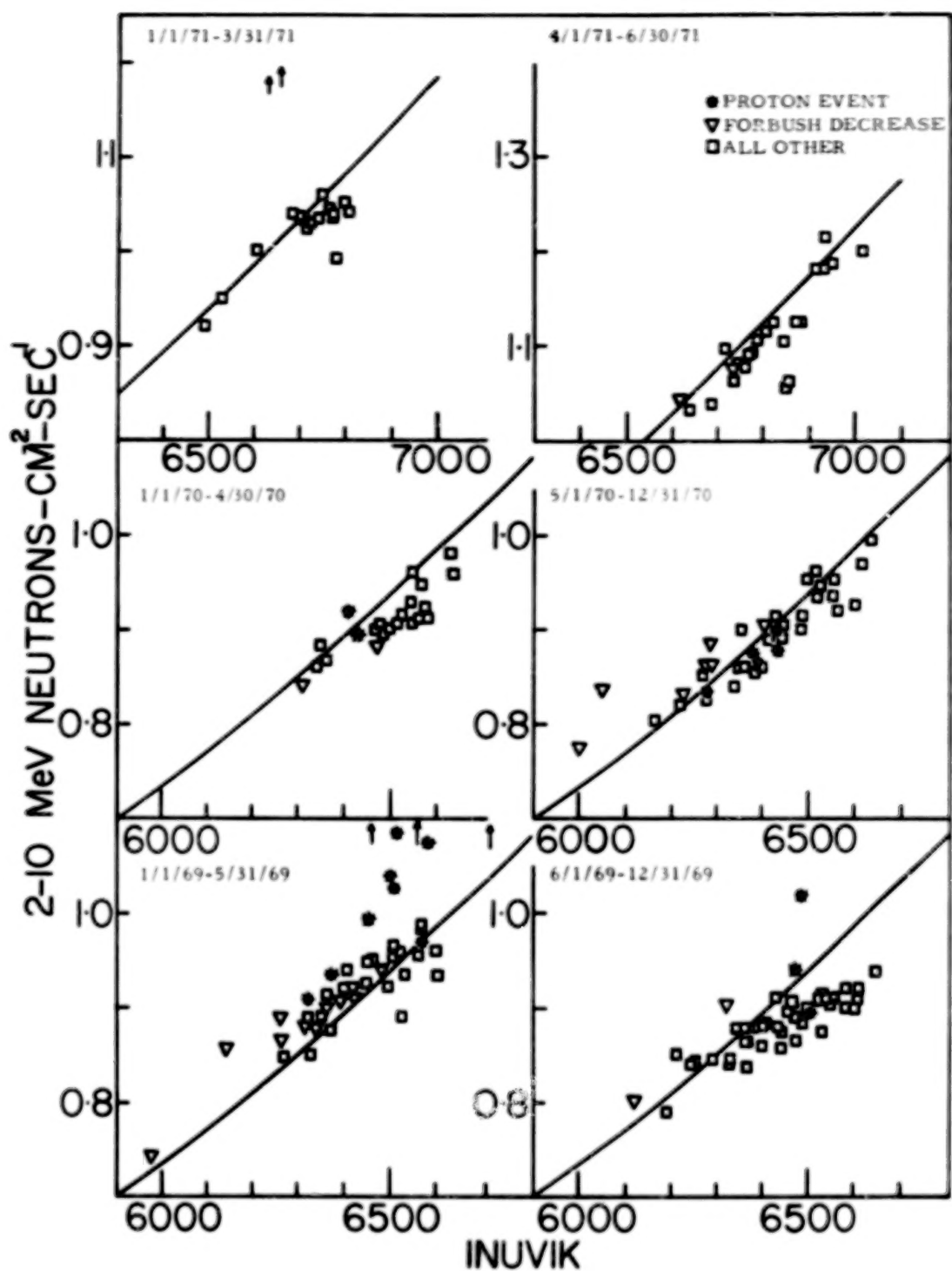


Figure 14. - Regression curves of the 2-10 MeV neutron flux vs counting rate of the Inuvik neutron monitor, for 6 periods between 1/69 and 6/30/71. Solid line, regression curve for the period before 1969; triangles, Forbush decreases; asterisks, solar proton events, arrows point to proton events above the highest flux on the diagram.

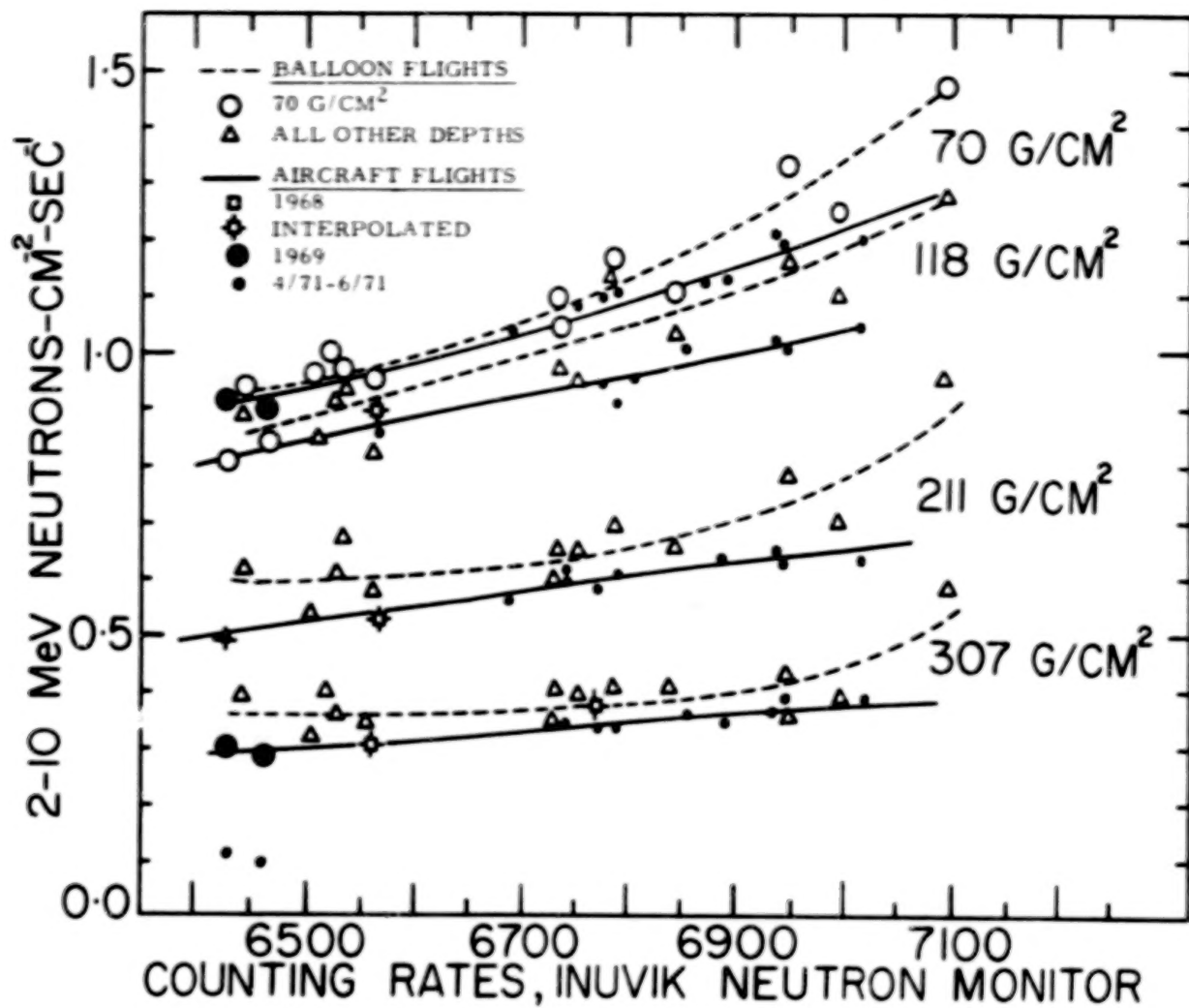


Figure 15. - Regression curves of neutron fluxes measured at different atmospheric depths vs the counting rates of the Inuvik neutron monitor. The results of the aircraft step flights are compared with balloon ascent data. The actual data points are also shown. The aircraft data taken in 1971, when compared to balloon data near solar minimum, 1965-1966 are lower at the same neutron monitor counting rate, indicating that the lower energy primaries had not yet recovered in 1971 to the solar minimum values.

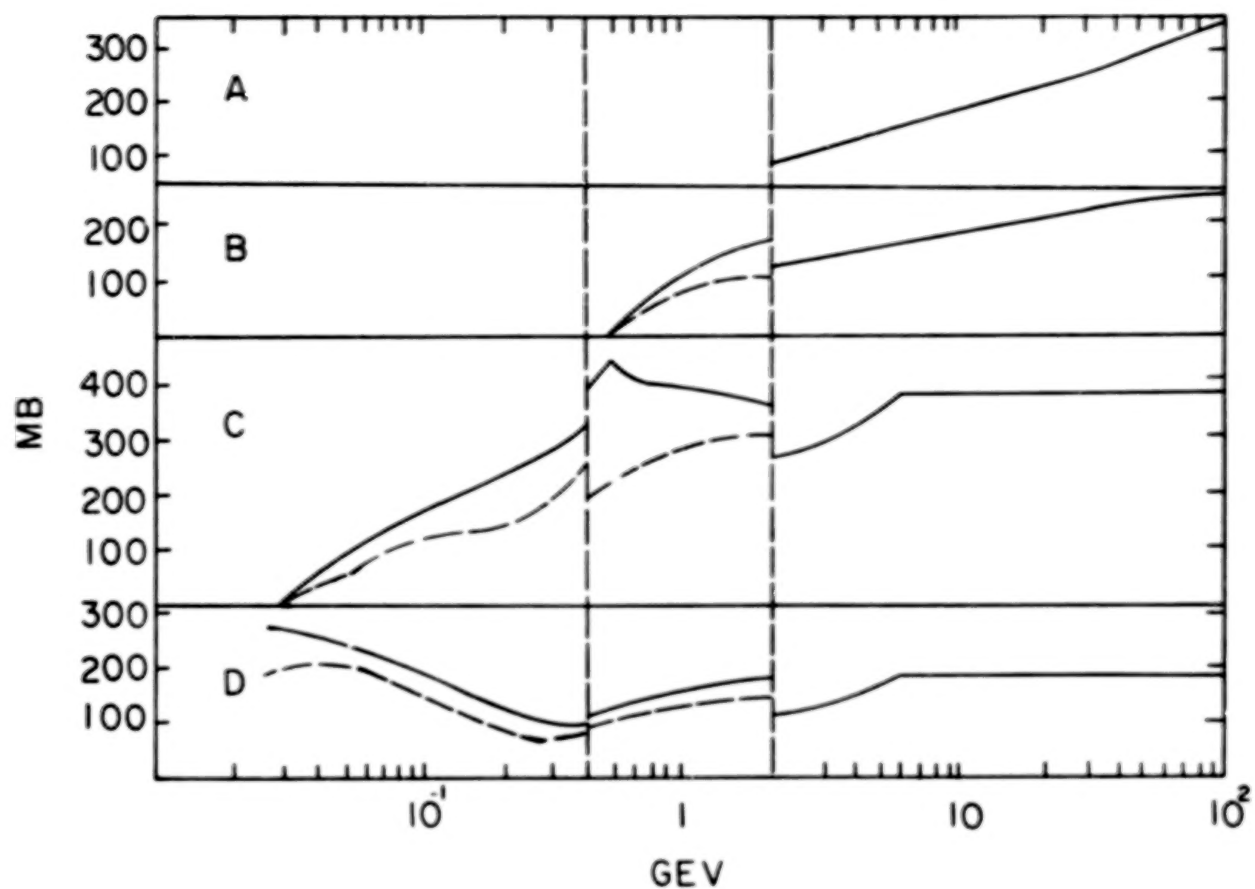


Figure 16. - Production cross sections of cascade nucleons and pions used in Monte Carlo calculation.

- (a) Charged pions
- (b) Nucleons above 500 MeV
- (c) Nucleons 30-500 MeV
- (d) Nucleons below 30 MeV

For nucleons below 2 GeV, solid curves are n-n or p-p;
 dashed curves are n-p or p-n

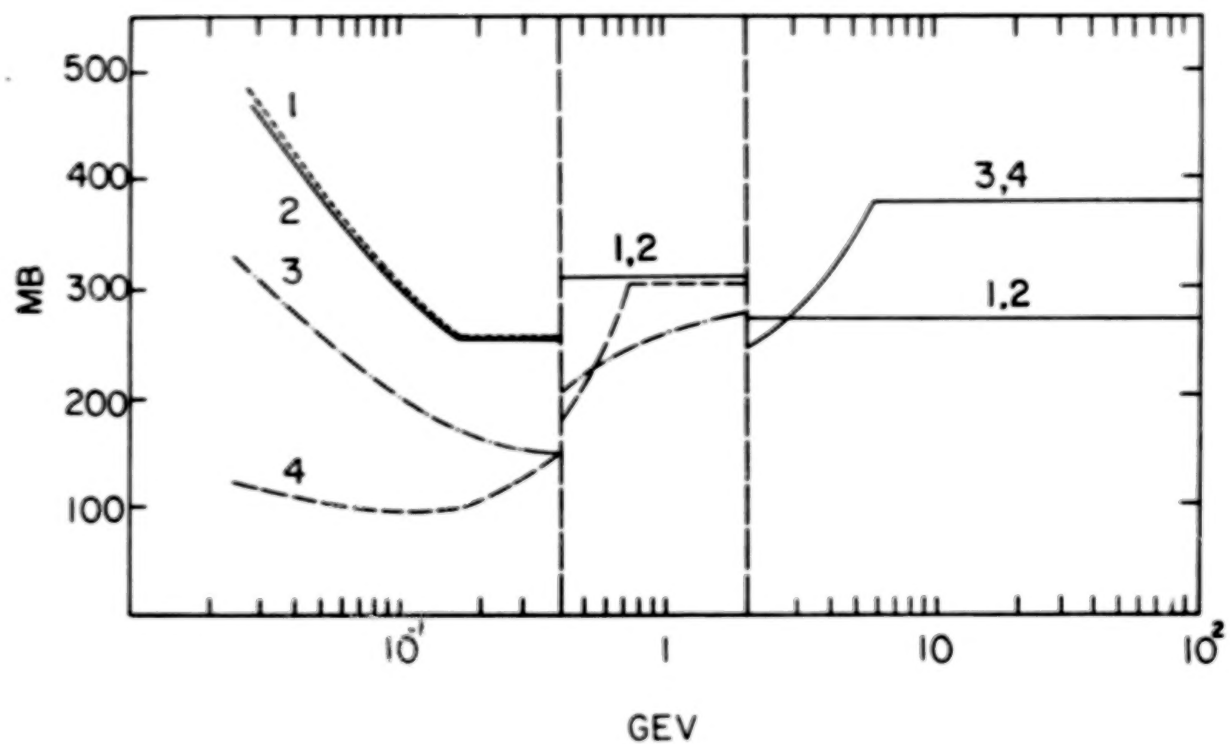


Figure 17. - Total inelastic cross section and cross section for producing evaporation neutrons.

1. Inelastic cross section, protons incident
2. Inelastic cross section, neutrons incident
3. Evaporation neutron production cross section, neutrons incident
4. Evaporation neutron production cross section, protons incident

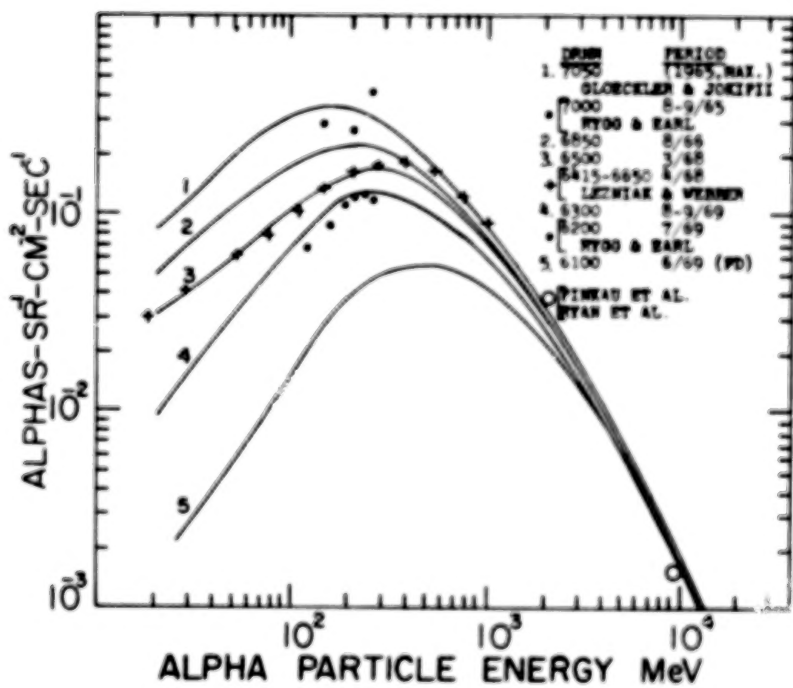
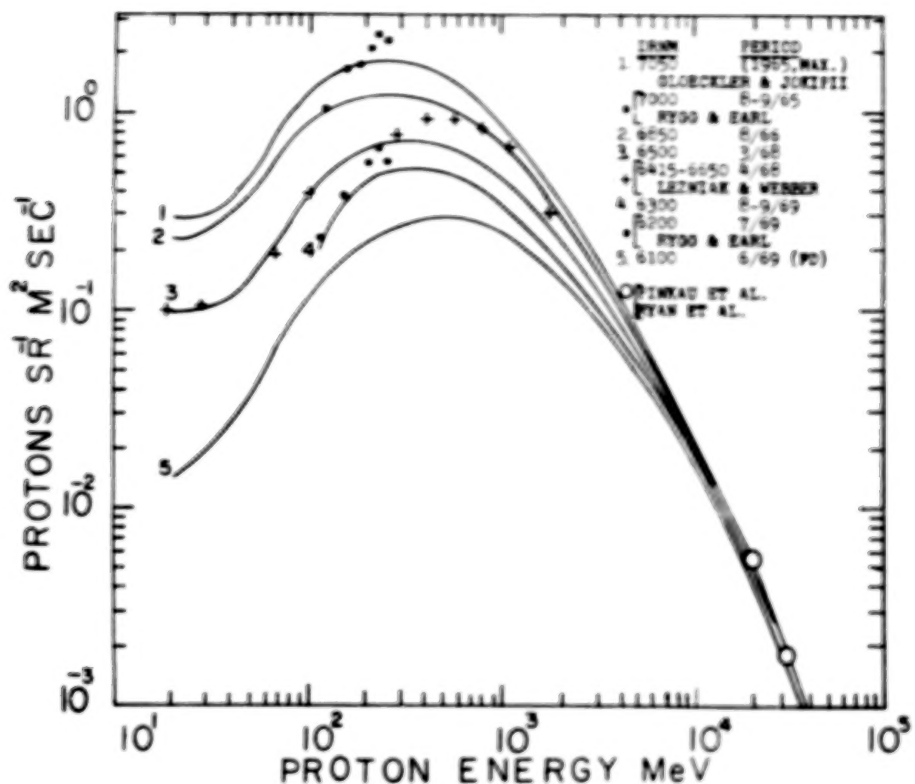


Figure 18. - Differential energy spectra of galactic primaries as a function of the DRNM counting rate, as used in the Monte Carlo calculation.

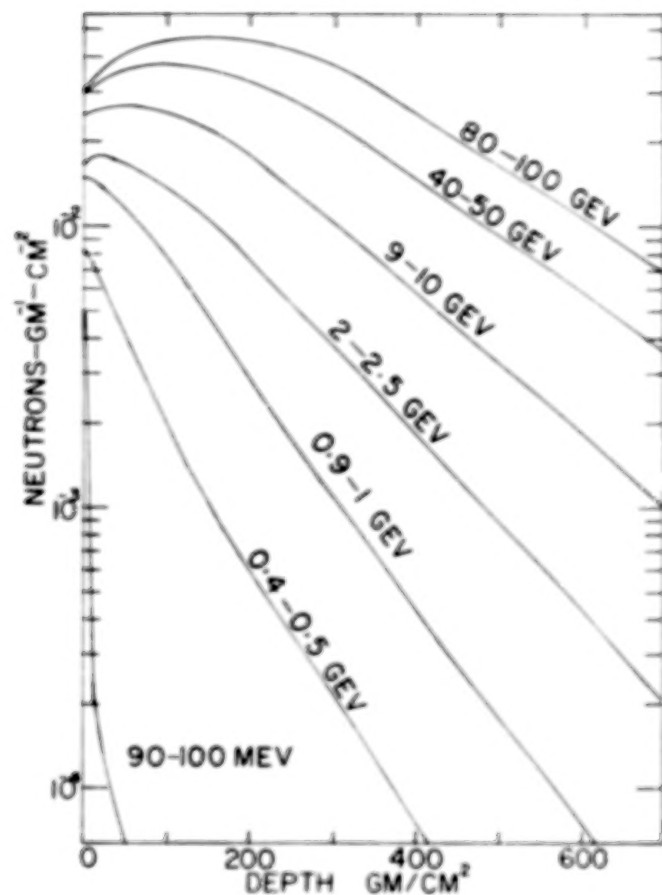


Figure 19. - Calculated spatial distribution of source neutron production for isotropic incident proton fluxes at several energies; 1000 incident protons $\text{-m}^{-2}\text{-sr}^{-1}\text{-sec}^{-1}$

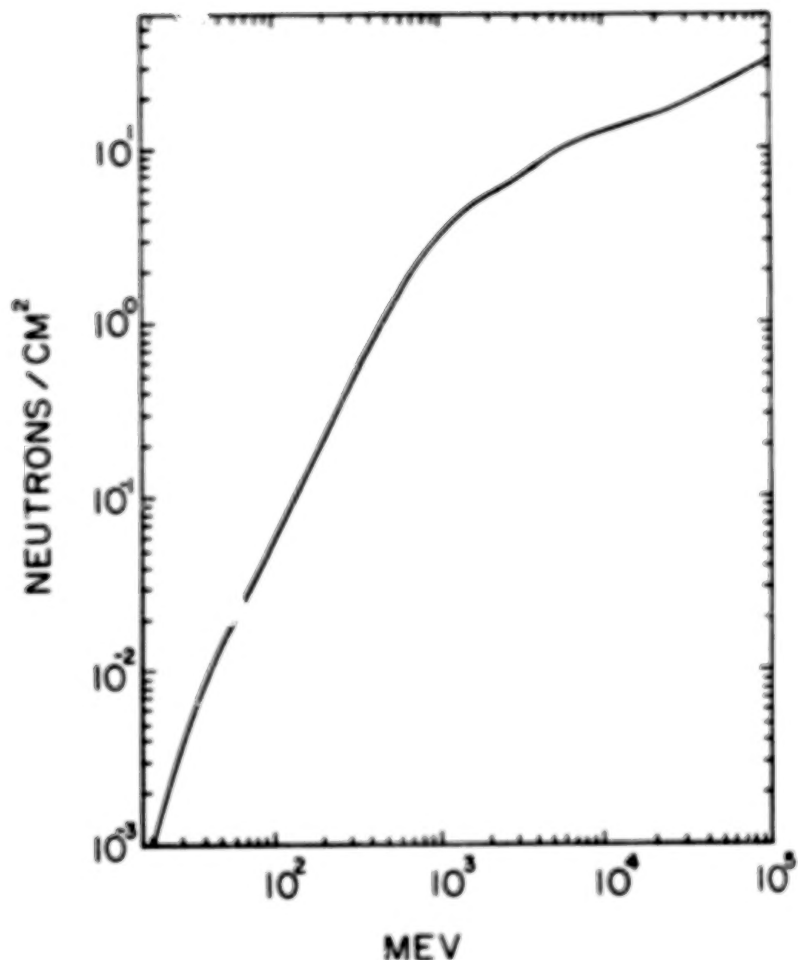


Figure 20. - Total source neutron production for a unit atmospheric column (depth 0-1033 g/cm²), from 1 incident proton -cm⁻²-sec⁻¹, isotropically distributed vs proton energy (neutrons per incident proton)

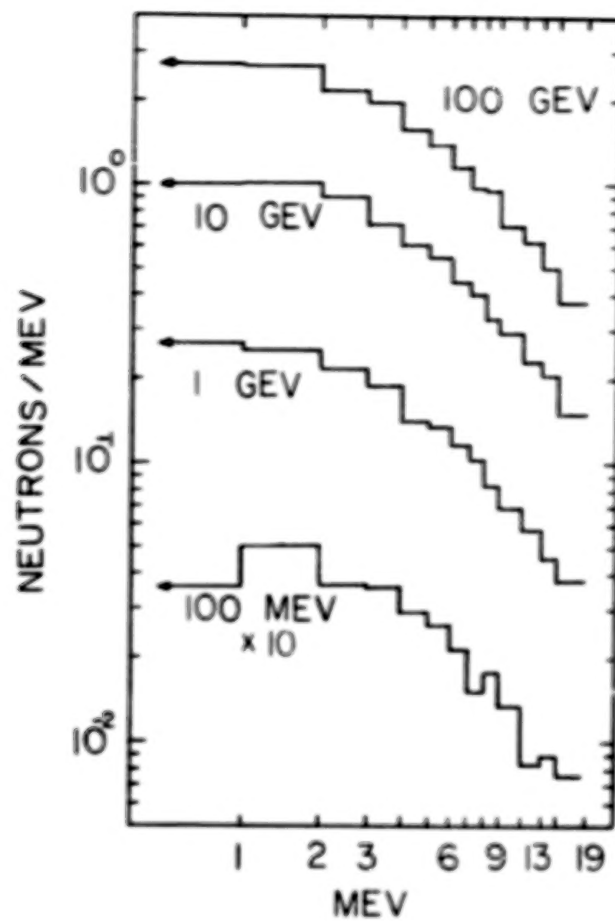


Figure 21. - Differential energy spectra of source neutrons ($0-700 \text{ g/cm}^2$) resulting from incident isotropic monoenergetic fluxes of $1000 \text{ protons/m}^2\text{-sec-ster}$, for four proton energies

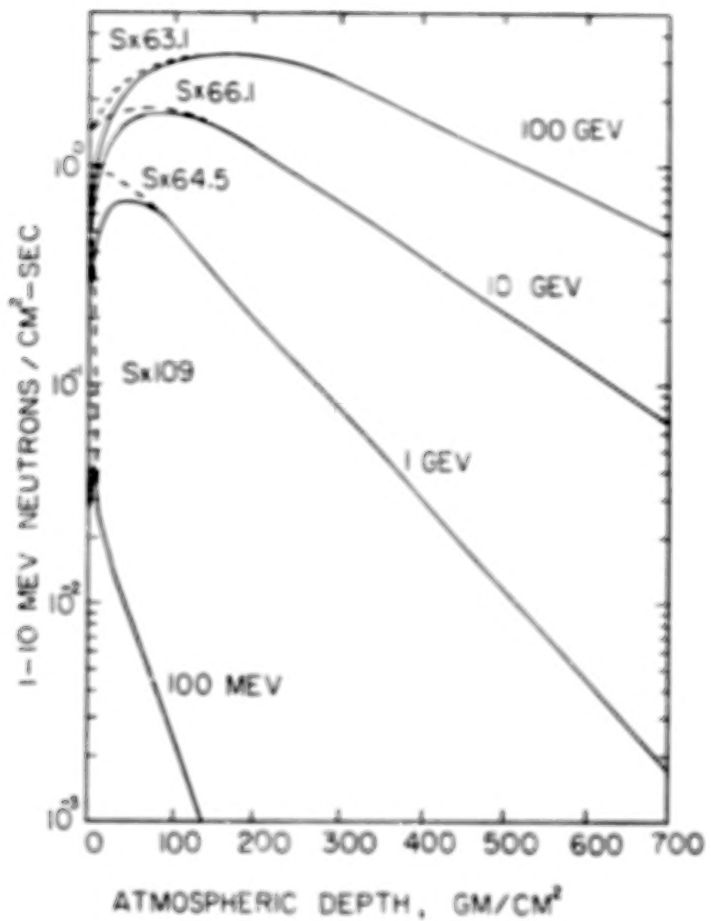


Figure 22. - Spatial distribution of 1-10 MeV neutron fluxes for the four incident proton spectra. The corresponding source production rates appear as dashed lines; the equilibrium region flux to source ratios used are indicated

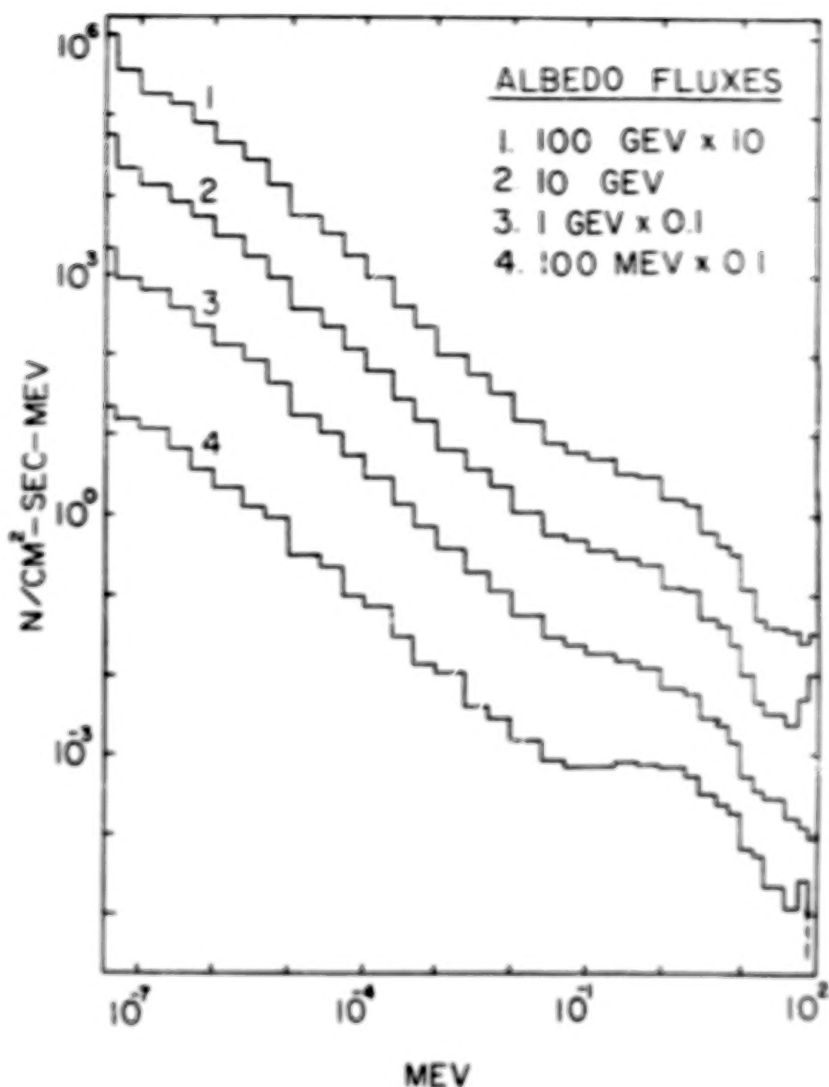


Figure 23. - Differential energy spectra of the albedo neutron flux from four incident monoenergetic proton fluxes

CONTENTS

	Page
INTRODUCTION	1 1/A9
I. EXPERIMENTAL METHOD.....	3 1/A11
A. Description of Detection System.....	3 1/A11
1. Scintillator detector	3 1/A11
2. Pulse shape discrimination.....	3 1/A11
3. Electronics.....	4 1/A12
4. Data storage.....	4 1/A12
5. Gondola	4 1/A12
B. Tests of the Detection System.....	5 1/A13
1. Temperature and pressure	5 1/A13
2. Response to sources.....	5 1/A13
3. Gain stability	6 1/A14
4. Channel 1 effect.....	6 1/A14
C. Calibration of Detectors.....	6 1/A14
1. Basis of calibration, ORNL detector and response functions	6 1/A14
2. Calibration at ORNL.....	7 1/B1
2a. Behaviour of ORNL detector-monitor	8 1/B2
2b. Unfolding the incident neutron spectrum from the measured pulse height distributions	8 1/B2
2c. Normalizing incident spectrum to Pu-Be above 5 MeV	9 1/B3
3. Response to neutrons >10 MeV	10 1/B4
4. Omnidirectional response	10 1/B4
5. Listing of response functions	11 1/B5
6. Cross-calibration of detectors.....	11 1/B5
7. Rejection of gammas in flight.....	11 1/B5
II. FLIGHT SUMMARIES.....	16 1/B10
A. Balloon Flights.....	16 1/B10
B. Aircraft Flights.....	19 1/C1
1. Introduction	19 1/C1
2. Solar minimum latitude survey	20 1/C2
3. Listing of aircraft flights	20 1/C2
3a. Performance of flight systems.....	20 1/C2
III. EVALUATION OF DATA	20 1/C2
A. Introduction.....	20 1/C2
B. Conversion of Counting Rates to Flux.....	34 1/D12
1. Method.....	34 1/D12
2. Contribution of the >10 MeV neutrons to the counting rate	34 1/D12
C. Calculation of Attenuation Length.....	36 1/E1

IV. RESULTS OF OBSERVATIONS	36	1/E1
A. Results of Balloon Flights	36	1/E1
1. Flight profiles	36	1/E1
2. Fast neutron spectrum	37	1/E2
3. Attenuation length	37	1/E2
4. Solar modulation	38	1/E3
5. Time variations at floating altitude	38	1/E3
6. In-flight calibration of System I vs System II	39	1/E4
7. Flights with tissue-equivalent dome	39	1/E4
B. Results of Aircraft Flights	40	1/E5
1. Summary of results, free air flux	40	1/E5
1a. Normalization of flight systems	40	1/E5
2. Aircraft latitude surveys	41	1/E6
3. Latitude variations near the latitude knee	42	1/E7
4. Time variations at the high latitude transition maximum	43	1/E8
5. Results of step flight, altitude variations	44	1/E9
V. INTERNUCLEAR CASCADE CALCULATION	45	1/E10
A. Introduction	45	1/E10
1. Production and transport of neutrons	45	1/E10
2. Previous calculations	46	1/E11
B. Description of the Calculation	47	1/E12
1. Scope of the calculation	47	1/E12
2. Internuclear cascade	47	1/E12
2a. LOMONTE and HIMONTE	47	1/E12
2b. References for cross sections for production of nucleons	48	1/E13
2c. Pion production and transport	49	1/E14
3. Neutron transport below 19 MeV, 05R	50	1/F1
4. Atmospheric flux calculation; NFLUX	51	1/F2
C. Input Data for Cascade Calculation. Galactic Cosmic Rays	51	1/F2
VI. RESULTS OF THE CALCULATION	52	1/F3
A. Unadjusted Calculation	52	1/F3
1. Monoenergetic primary protons	52	1/F3
2. Monoenergetic alpha particles	54	1/F6
3. Galactic cosmic rays, comparison with experiment	54	1/F6
3a. Solar minimum	55	1/F7
3b. Latitude surveys	55	1/F7
3c. Fast neutron spectrum	55	1/F7
B. Normalized Calculation	57	1/F9
1. Procedure	57	1/F9
2. Results	57	1/F9
2a. Fast neutron flux	57	1/F9
2b. Neutron source and products	58	1/F10
2c. Radiocarbon	58	1/F10
2d. Neutron leakage rates and fluxes	62	1/G1

3. Discussion.....	62	1/G1
3a. Comparison of the normalized calculation with the results of neutron experiments.....	62	1/G1
3b. Comparison with other calculations.....	70	1/G12
VII. SUMMARY OF OBSERVATIONS AND CALCULATION OF NEUTRONS FROM GALACTIC COSMIC RAYS.....	73	2/A6
VIII. NEUTRONS FROM SOLAR PROTONS	74	2/A7
A. Introduction.....	74	2/A7
B. Observations.....	75	2/A8
C. Solar Proton Spectra and Neutron Yields	78	2/A13
D. Monte Carlo Calculation.....	80	2/B1
E. Discussion.....	81	2/B2
F. Application to Other Experiments.....	84	2/B6
G. Other Flare Calculations	87	2/B9
H. Summary of Observations and Calculations	88	2/B10
I. The Geophysical Effects of Neutrons from Solar Protons..	89	2/B11
IX. COSMIC RAY MODULATION DURING 1968-1971.....	91	2/B13
A. Introduction.....	91	2/B13
B. Comparison of the Response of Neutron Monitors with Response of NYU Detector to the Primary Spectrum..	91	2/B13
C. Calculation of the Spectrum of Variation of Cosmic Rays..	92	2/B14
D. Results, Transient Cosmic Ray Decreases.....	94	2/C3
E. Results, Long Term Variation in Cosmic Ray Intensity....	99	2/C9
F. Discussion	101	2/C11
1. The spectrum of variation of Cosmic Rays.....	101	2/C11
2. The relative modulation of protons and electrons; charge splitting above 2 GV.....	102	2/C12
3. Model Calculations.....	104	2/C14
G. Conclusions and Summary.....	107	2/D3
X. APPENDIX A. ACCELERATION PROCESSES ON THE SUN ...	110	2/D6
XI. APPENDIX B. PRIMARY NEUTRONS.....	116	2/D12
XII. APPENDIX C. THE EARTH OR OTHER OBJECT AS A NEUTRON SOURCE.....	120	2/E2
REFERENCES.....	122	2/E4
FIGURES.....	133	2/F1

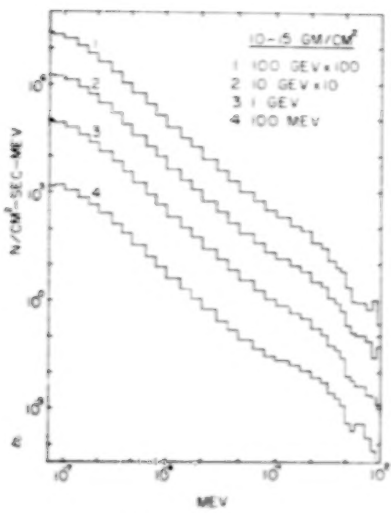


Fig. 24a

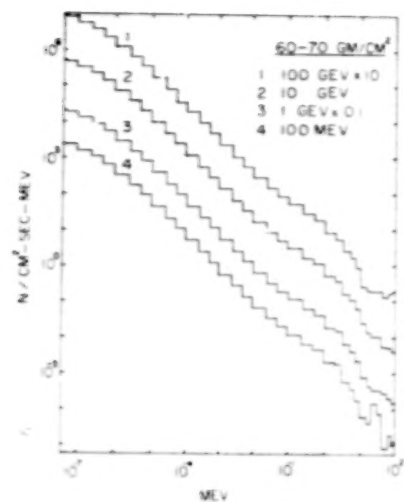


Fig. 24b

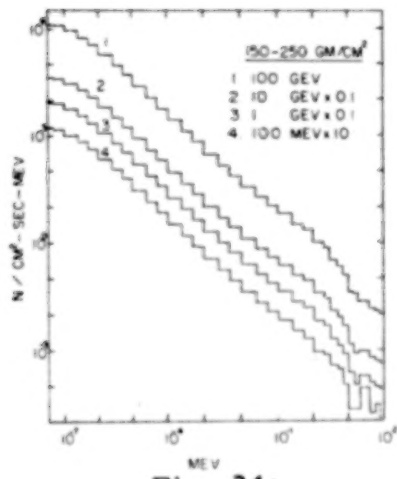


Fig. 24c

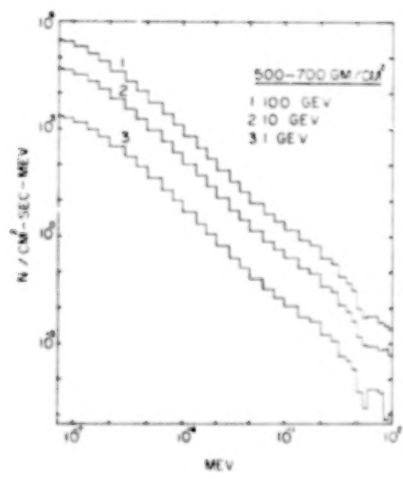


Fig. 24d

Figure 24. - Differential energy spectra of the atmospheric neutron flux from four incident monoenergetic proton fluxes

- 10-15 g/cm² atmospheric depth
- 60-70 g/cm² atmospheric depth
- 150-250 g/cm² atmospheric depth
- 500-700 g/cm² atmospheric depth

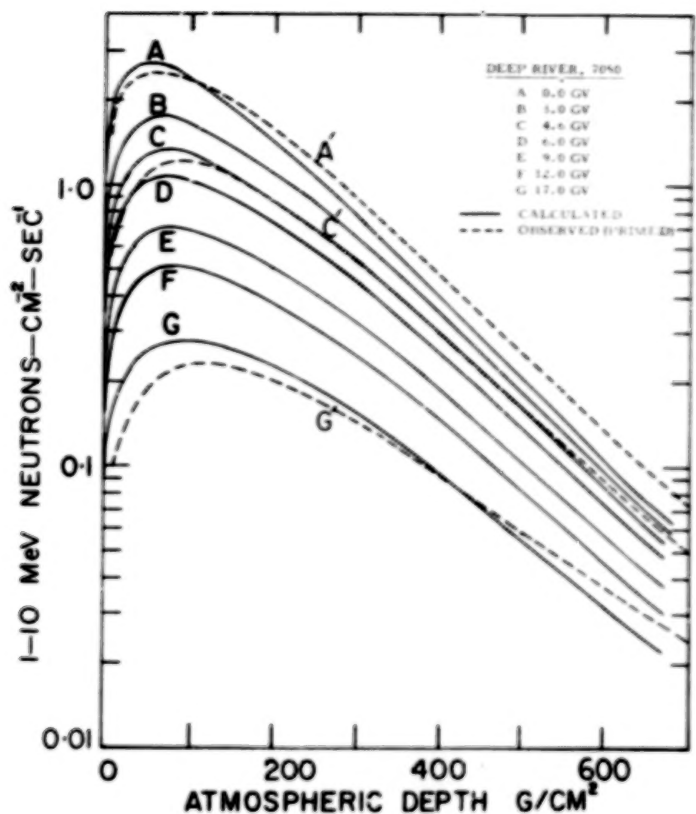


Fig. 25a

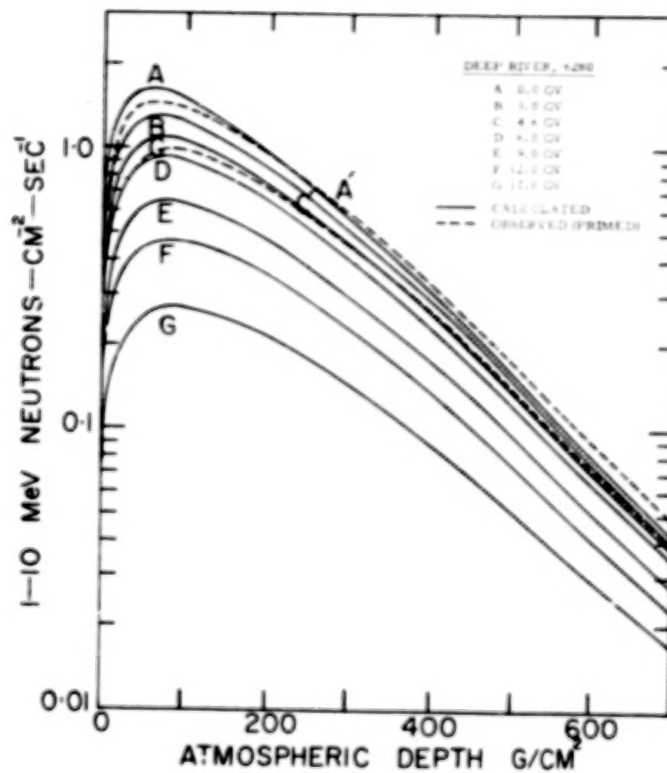


Fig. 25b

Figure 25. - Fast neutron flux vs atmospheric depth at various cutoff rigidities:
Balloon observations compared with Monte Carlo calculation

a. Solar minimum
b. Solar maximum

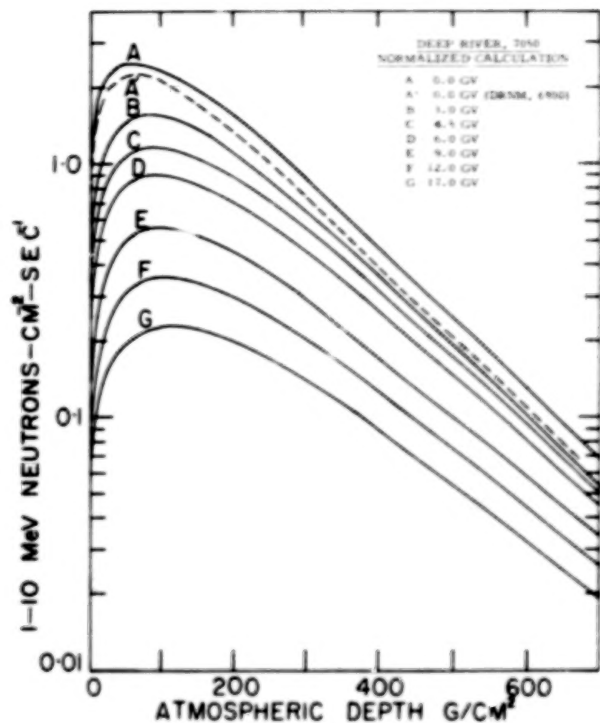


Fig. 26a

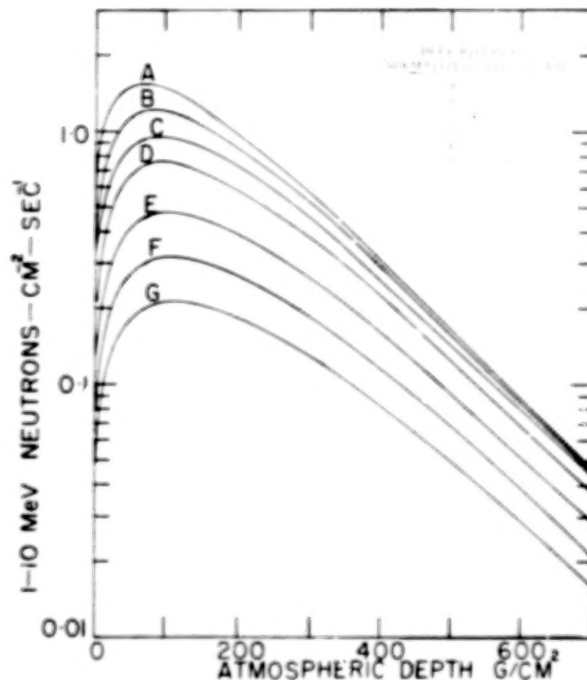


Fig. 26b

Figure 26. - Fast neutron flux vs atmospheric depth over the range of cutoff rigidity. The interpolations of experimental results have been made with normalized Monte Carlo calculation

- Near solar minimum
- Near solar maximum

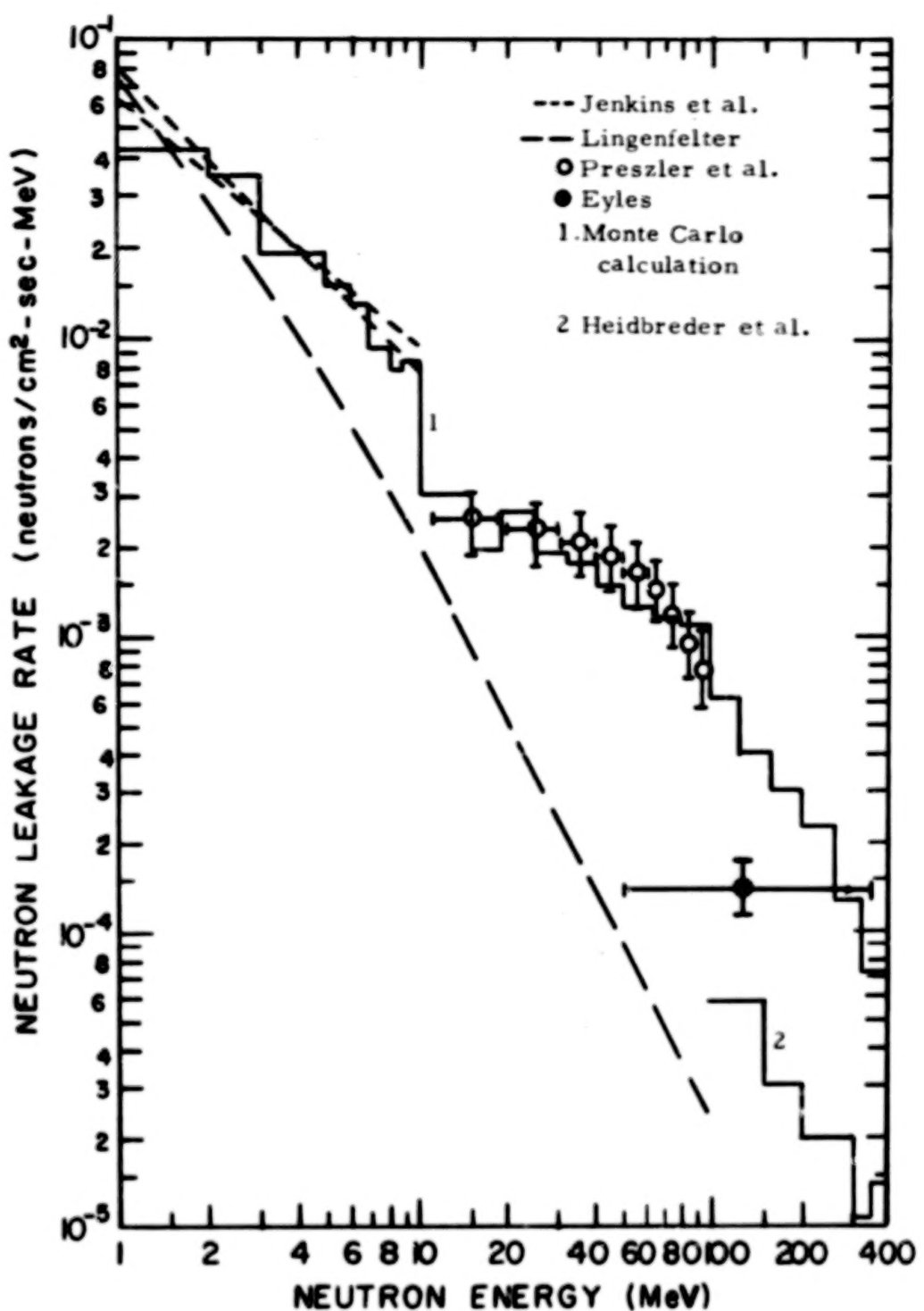


Figure 27. - Neutron leakage rate spectrum at Palestine, Texas, normalized to solar modulation during September 1971, from Figure 2 of Merker (1972)

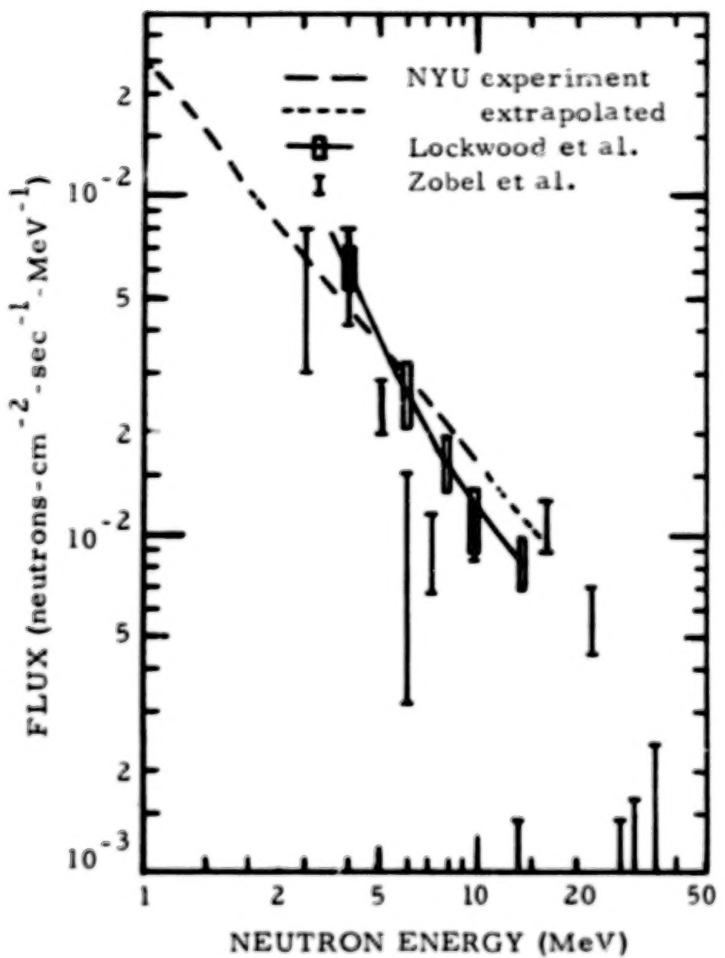


Figure 28. - Comparison of observations from Palestine, Texas, of NYU group, Lockwood et al., and Zobel et al., normalized to DRNM 6050 - and 9 g/cm^2 atmospheric depth, to approximate the conditions of the ORNL balloon flight. The results of other experiments are listed in Table 13

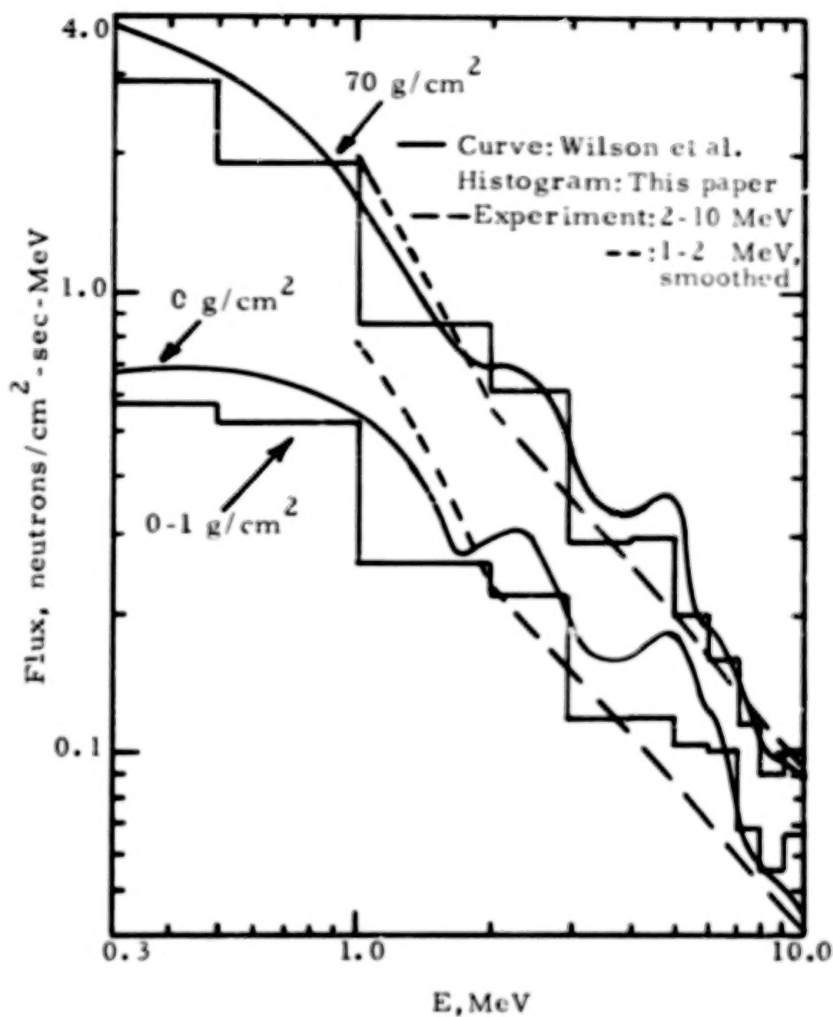


Figure 29. - Neutron spectrum between 0.3 and 10 MeV. Wilson et al., the present calculation, and the NYU observation at solar minimum are shown. The observed values at $4-5 \text{ g/cm}^2$ are extrapolated to $0-1 \text{ g/cm}^2$

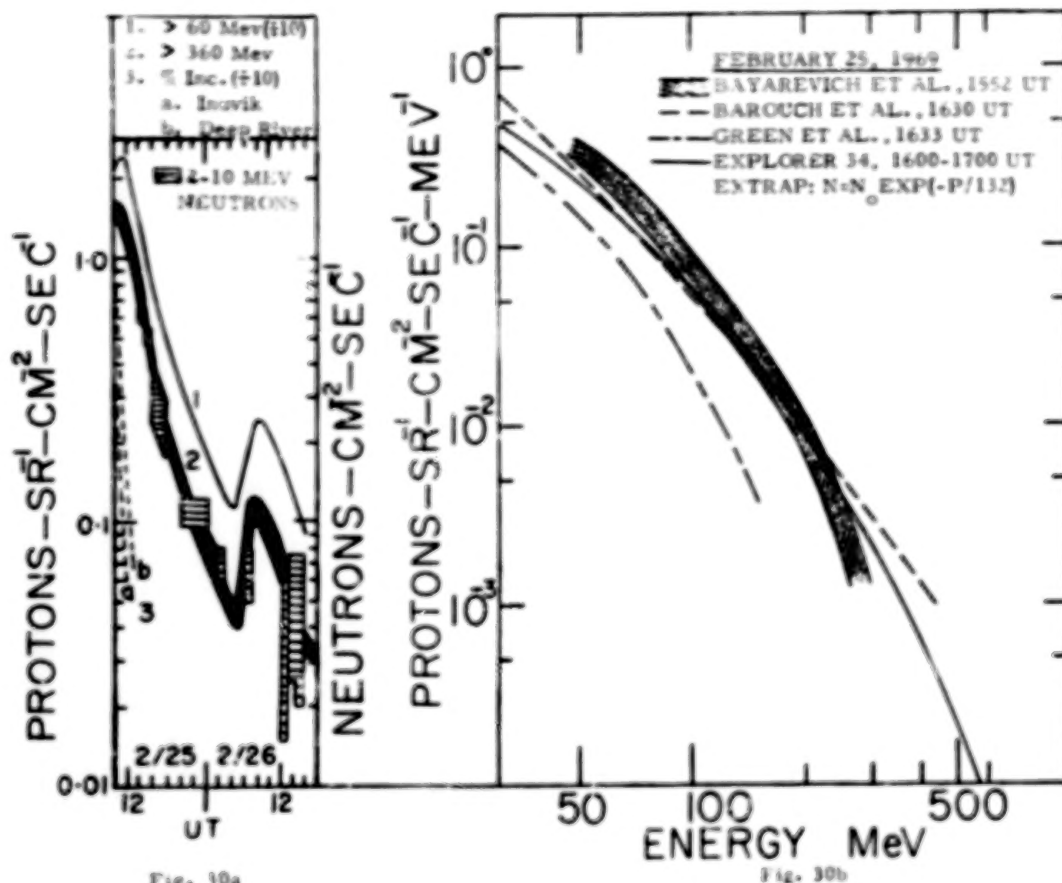


Figure 30. - Solar particle event of February 25, 1969

- Histories of the solar protons and of the secondary neutrons, February 25-26. The observed excess: flight duration, horizontal bar; uncertainties, vertical. Integral fluxes of solar protons: (1) SPME measurements, (2) Engel et al. (1970), axial and radial telescope, indicating anisotropies, (3) Steljes (1969)
- Solar proton spectrum. The Explorer 34 data (SPME) > 30 MeV and > 60 MeV, has been fitted to an exponential in rigidity, the differential energy spectrum is shown.

BLANK PAGE

BLANK PAGE

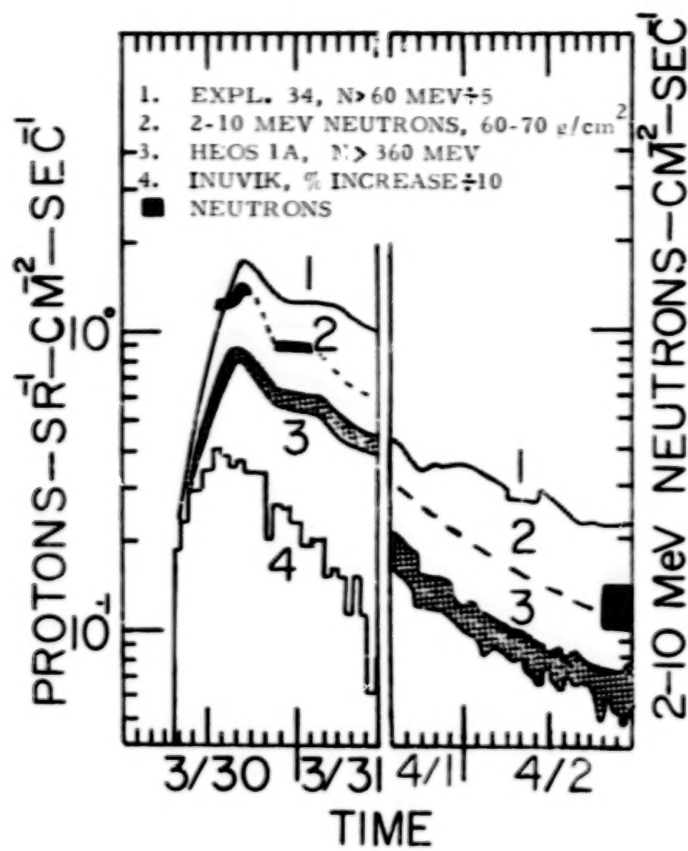


Fig. 31a

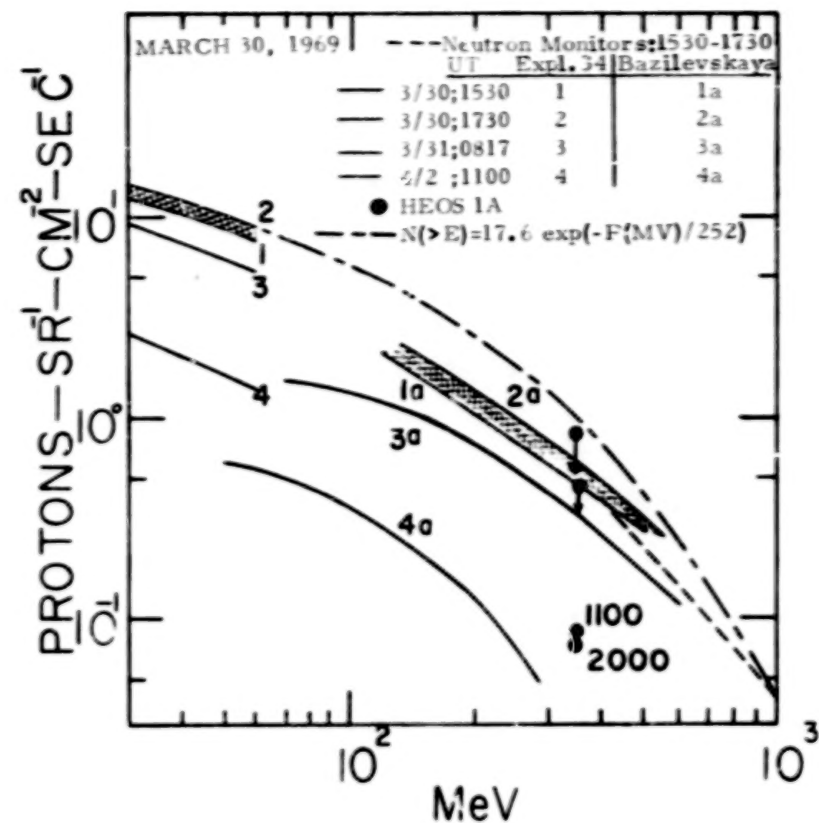


Fig. 31b

Figure 31. - Solar proton event of March 30, 1969

a. Histories of the protons and of the secondary neutrons, March 30-31, April 1-2. The neutron excess: In the observed data, the blackened area includes time at altitude (horizontal) and uncertainties in galactic background (vertical). The dashed line (2) is an interpolation from the Monte Carlo calculation. Integral fluxes of solar protons: (1) SPME measurements, (3) Balogh et al. (1971); anisotropy is indicated by the counts of radial and axial telescopes, (4) Steljes (1969)

b. Solar proton spectrum: The integral curves of Bazilevskaya et al. (1971) and Bayarevich et al. (1969) are differentiated; the Explorer data (SPME) > 30 MeV and > 60 MeV have been fitted to an exponential in rigidity, the energy dependence is shown

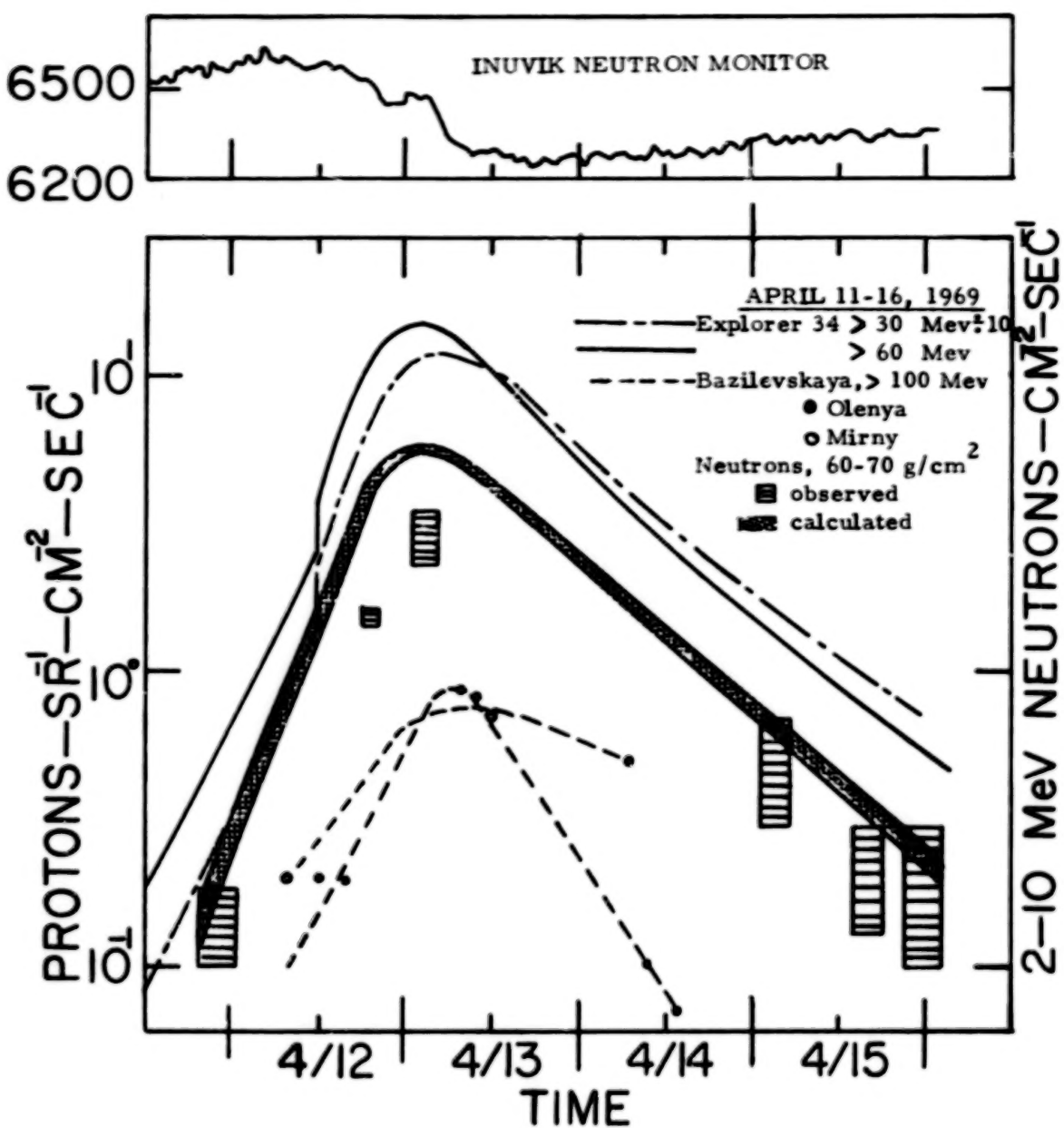


Figure 32. - The histories of solar protons and secondary neutrons, April 11-16, 1969

The neutron flux is multiplied by 10. At the peak of this low energy event, the calculation overestimates the neutron flux. Bazilevskaya et al. (1971, 1972, private communication) observed differences in solar proton spectra between Olenya and Mirny

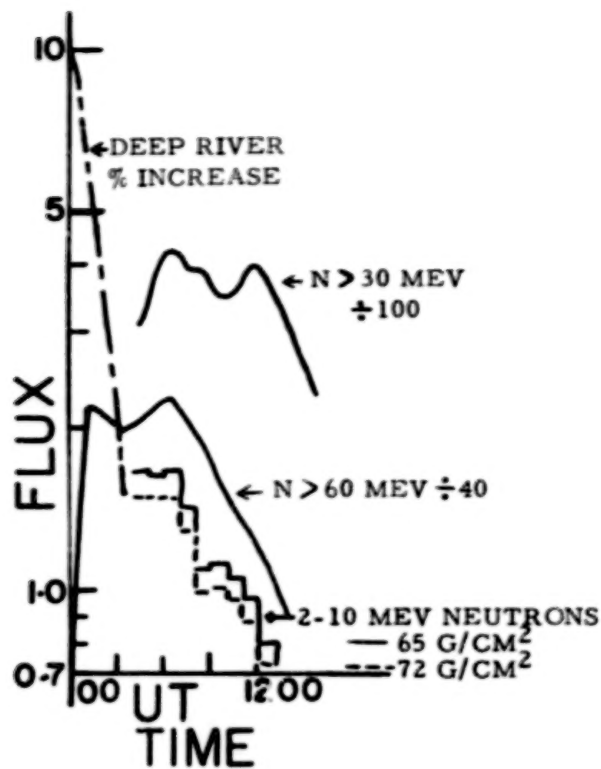


Fig. 33a

Figure 33. - Solar particle event of January, 1971

- The histories of solar protons and secondary neutrons. The neutron observations are shown at 72 g/cm^2 and are also normalized to 65 g/cm^2 . Solar protons: The 30 MeV and 60 MeV protons are SPME measurements on Explorer 41; DRNM data, from Steljes (1971).
- Solar protons spectrum: The SPME data are extended by an exponential in rigidity and continued at high energy by the spectrum calculated from neutron monitor data

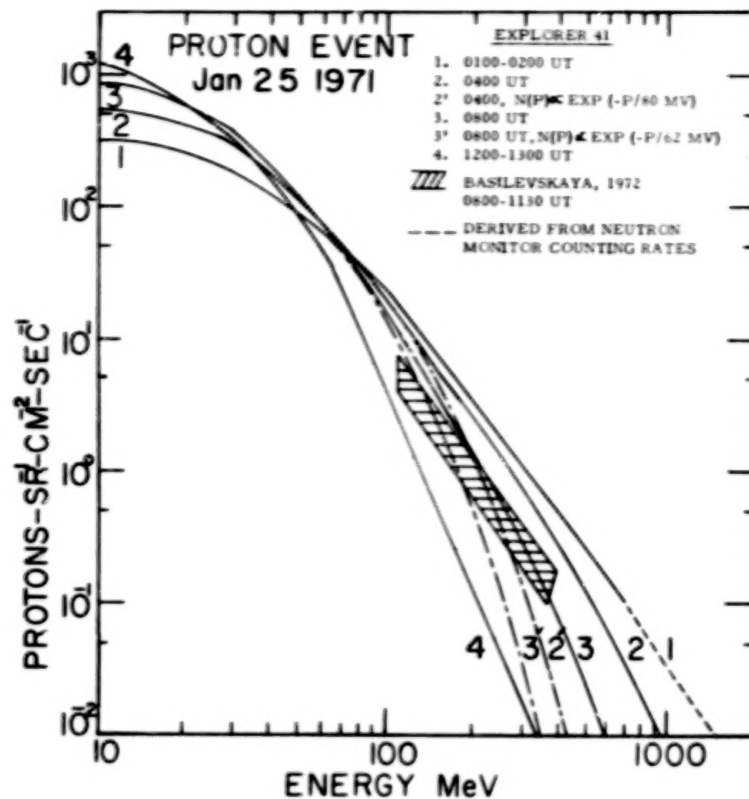


Fig. 33b

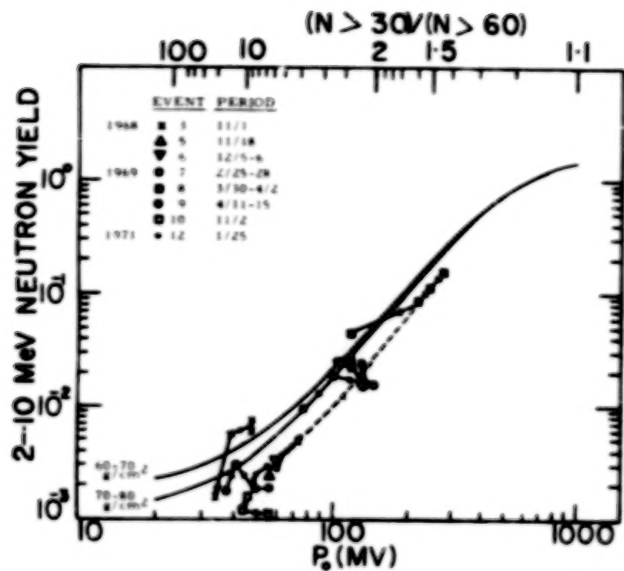


Figure 34. - The neutron specific yield at 65 g/cm^2 atmospheric depth (2-10 MeV neutron flux per incident proton- $\text{cm}^{-2} \cdot \text{sr}^{-1} \cdot \text{sec}^{-1}$ above 30 MeV). The arrows join experimental data points in the direction of increasing time. The solid line shows the results of the Monte Carlo calculation. The dashed line joins points during the main phase and/ or early decay of 3 sea level events.

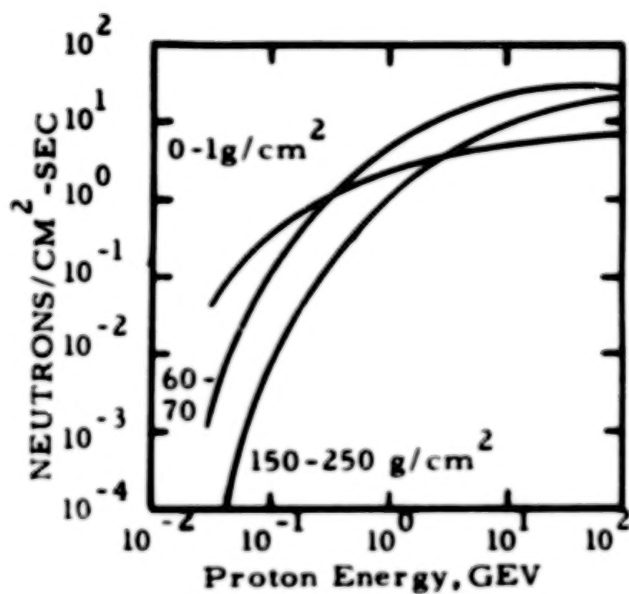


Figure 35. - The 1-10 MeV neutron flux at several atmospheric depths versus incident proton energy; normalized to 1 incident proton-cm⁻² -sr⁻¹ -sec⁻¹

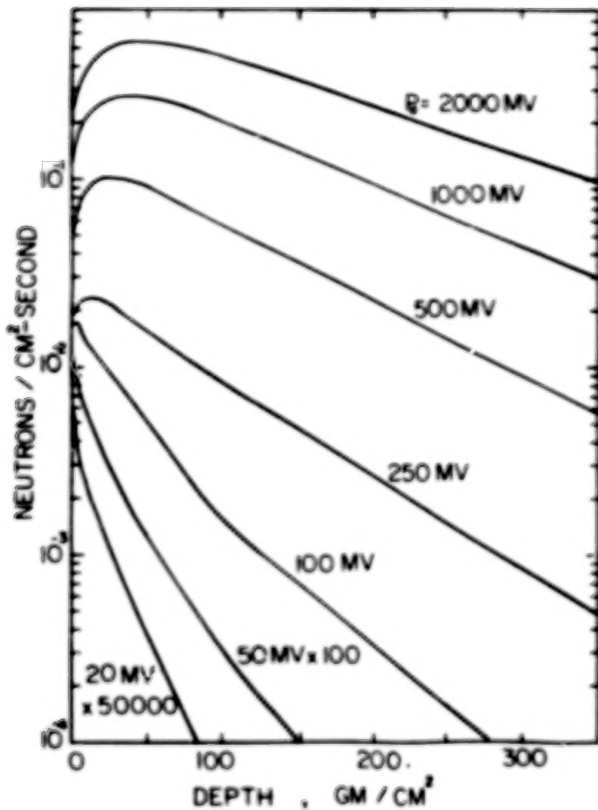


Figure 36. - The 1-10 MeV neutron flux vs. atmospheric depth for solar proton spectra of the form: $N(P) = 1000 \exp(-P/P_0)$ protons $\text{-m}^{-2} \text{-sr}^{-1} \text{- sec}^{-1}$; Monte Carlo calculation

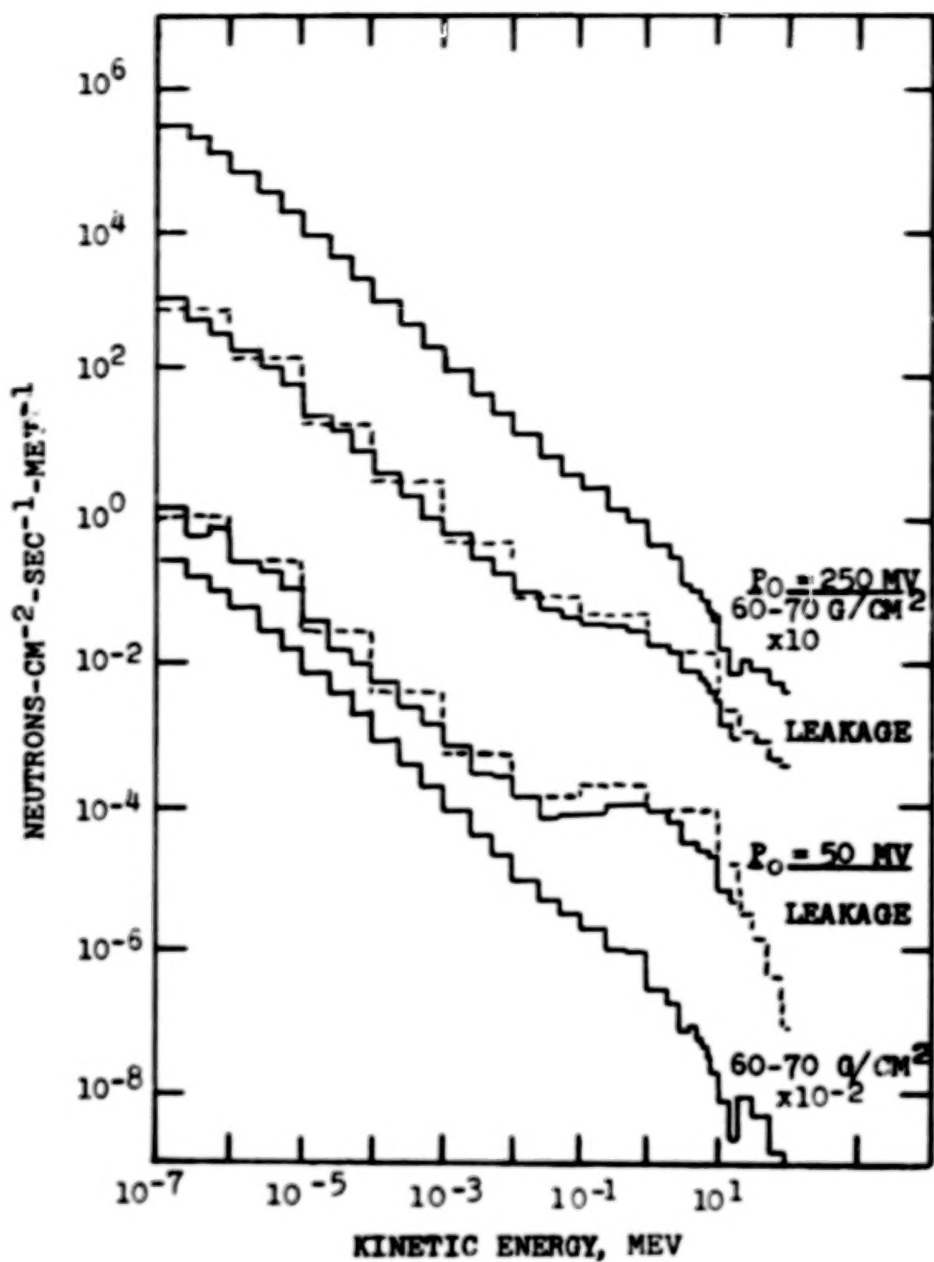


Figure 37. - Monte Carlo calculation of the neutron differential energy distributions, between 10^{-7} and 10^{-2} MeV, from solar protons with spectra exponential in rigidity; normalized to 1 incident proton $\text{cm}^{-2} \text{-sr}^{-1} \text{-sec}^{-1}$. The leakage fluxes are shown as dotted lines to 100 MeV, the leakage rates as solid lines to 20 MeV. Note the change in rate/flux ratio with neutron energy. The neutron flux at $60-70 \text{ g/cm}^2$ includes the 1-10 MeV region, where NYU measurements were made

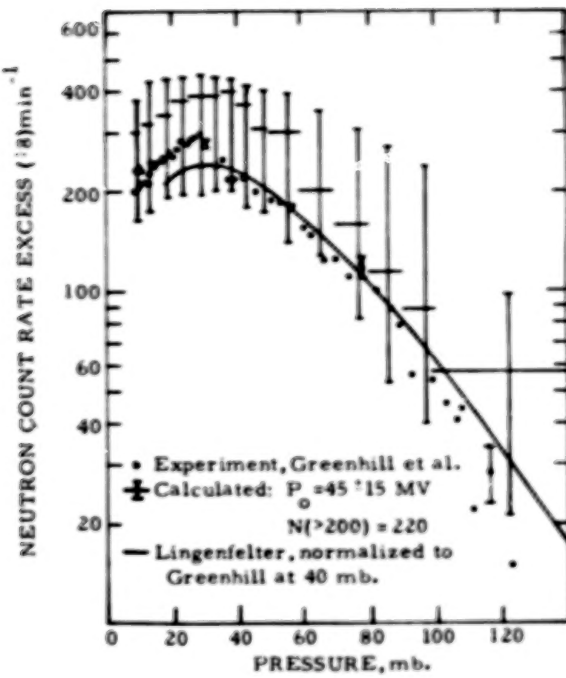


Figure 38. - Neutron counting excess observed during solar proton event of September 3, 1966 by Greenhill et al. (1970). The solid line is from the calculation of Lingenfelter for a P_0 of 125 MV, normalized to the experiment at 40 mb. The Monte Carlo calculation is for $P_0 = 45 \pm 15$ MV and the proton flux >200 MV = 220 ± 70 $\text{cm}^{-2} \cdot \text{sr}^{-1} \cdot \text{sec}^{-1}$. The error bars are shown only for the uncertainty in P_0 . Note the change in the shape of the depth distribution with P_0 .

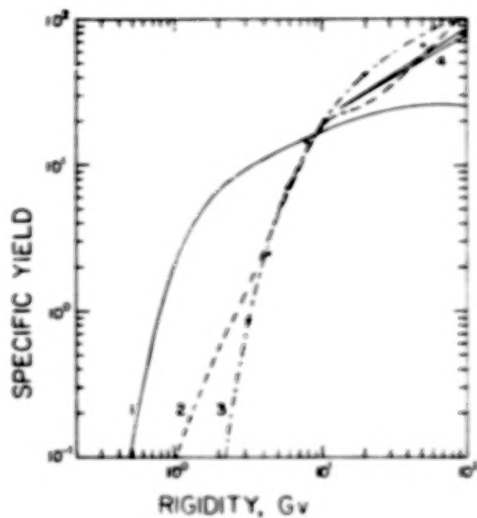


Figure 39. - The response of the NYU detector and the sea level neutron monitor to monoenergetic primary protons. Curve 1, the fast neutron flux at $60-70 \text{ g/cm}^2$ and $P_c \approx 0$. Curves 2, 3, 4, the neutron monitor yield function for an NM-64 monitor: Curve 2, Debrunner and Flueckiger¹⁴⁰; Curve 3, Lockwood and Webber⁸⁴; Curve 4, Mathews et al¹⁴¹

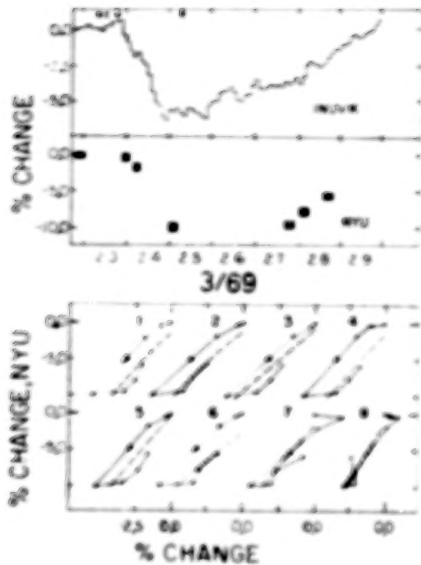


Figure 40. - Forbush Decrease of March 24, 1969 (Type I)

- a. % decrease of Inuvik neutron monitor counting rate and the flight average of the 2-10 MeV neutron flux (NYU measurement) with time (March 23 = 0%)
- b. Regression curves of the flight average of the 2 - 10 MeV neutron flux vs several neutron monitors: (1) Inuvik (2) Sulphur Mountain, (3) Resolute, (4) Deep River Neutron Monitor, (5) Alert, (6) Goose Bay, (7) Dallas, (8) Kula -- Long term variation

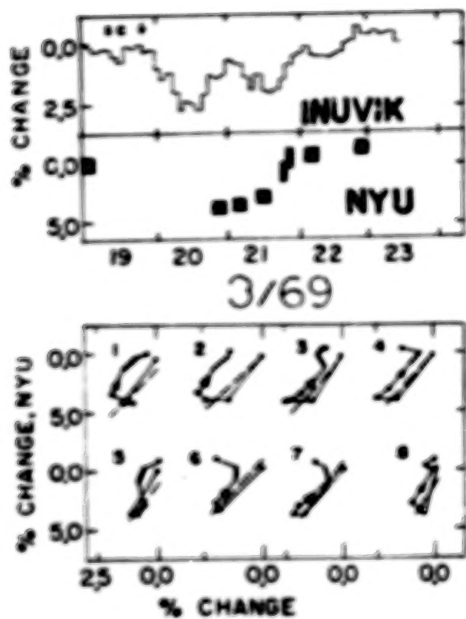


Figure 41. - Symmetric event of March 19, 1969 (Type II)

- % decrease of Inuvik neutron monitor counting rate vs the flight average of the 2-10 MeV neutron flux (NYU measurement) with time March 17-18 = 0%**
- Regression curve of the flight average of the 2-10 MeV neutron flux vs the counting rates of several neutron monitors: (1) Inuvik, (2) Sulphur Mountain, (3) Resolute, (4) Deep River Neutron Monitor, (5) Alert, (6) Goose Bay, (7) Dallas, (8) Kula**

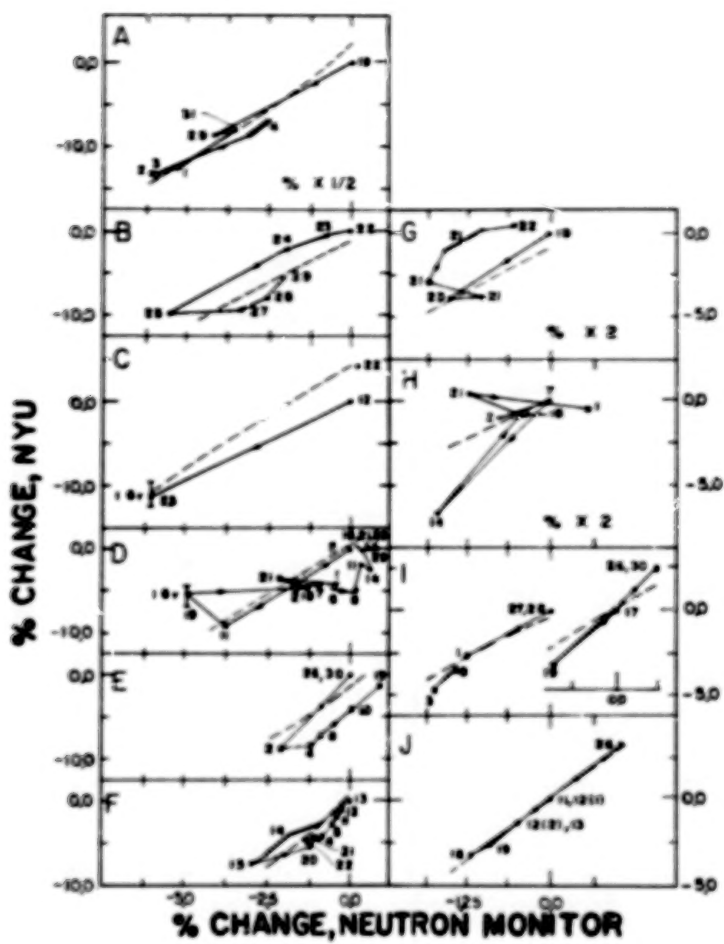


Figure 42. - Comparison of Type I vs Type II regression curves of the flight averaged 2-10 MeV neutron flux (NYU) vs the counting rate of the Inuvik neutron monitor during the flight, for several short term decreases.

Type I: A. October 29, 1968, B. March 24, 1969, C. May 15, 1969,
 D. June 7, 1969, E. July 2, 1970, F. April 14, 1971.

Type II: G. March 19, 1969, H. July 7, 1969, I. Twin event, May 29 -
 June 24, 1970, J. May 27, 1971

same month as start of event, one month later, two months later, long term regression

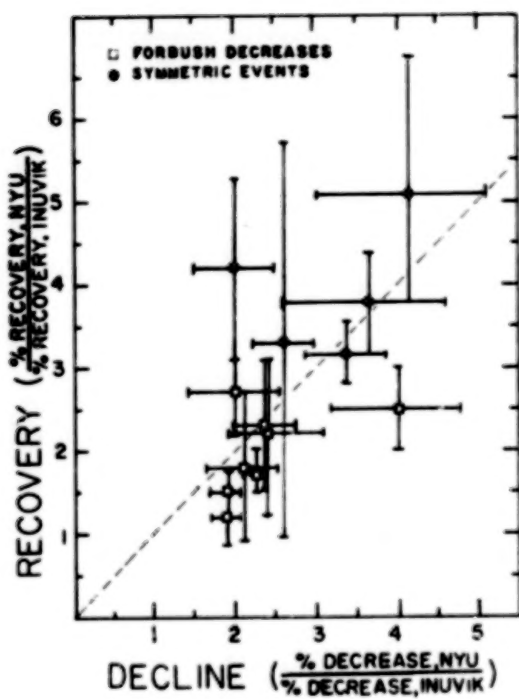


Figure 43. - Comparison of % Recovery (NYU) / % Recovery (Inuvik) to the % Decrease (NYU) / % Decrease (Inuvik) for Forbush decreases and symmetric events.

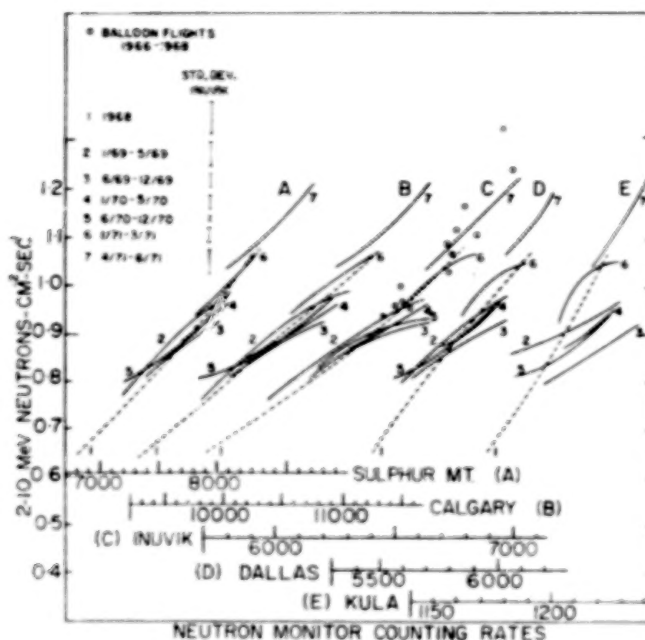


Fig. 44a

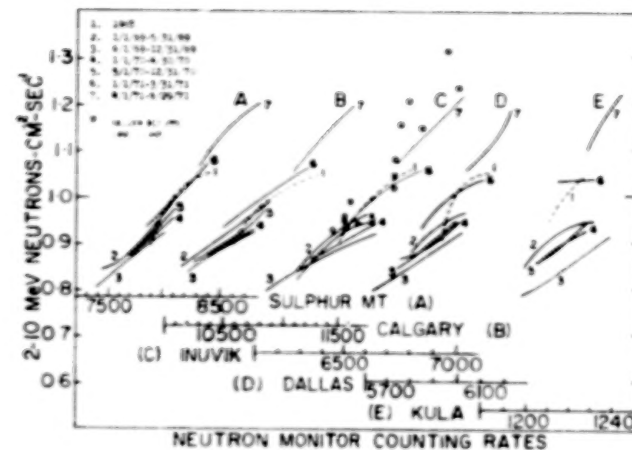


Fig. 44b

Figure 44. - Regression curves of NYU 2-10 MeV neutron flux vs the counting rates of several neutron monitor at increasing effective cutoff rigidity: A. Sulphur Mountain ($P_C = 1.08$, High alt. - 2283 m), B. Calgary ($P_C = 1.08$, High alt. - 1110 m), C. Inuvik ($P_C = .18$), D. Dallas ($P_C = 4.35$), E. Kula ($P_C = 13.30$), for seven time periods.

Fig. 44(a) all high latitude data

Fig. 44(b) Forbush decrease effects removed

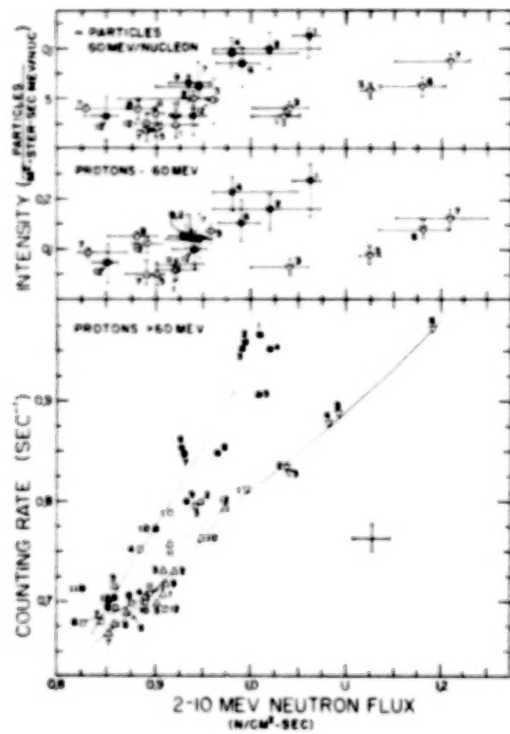


Figure 45. - Regression relation, monthly averaged 2-10 MeV neutron flux vs: (1) 60 MeV/Nucleon α particles (Van Hollebeke), (2) 60 MeV proton, (3) 60 MeV Proton (Lockwood et al).

1968: closed circles

1969: open squares

1970: triangles

1971: inverted triangles

1971 - Standard deviation

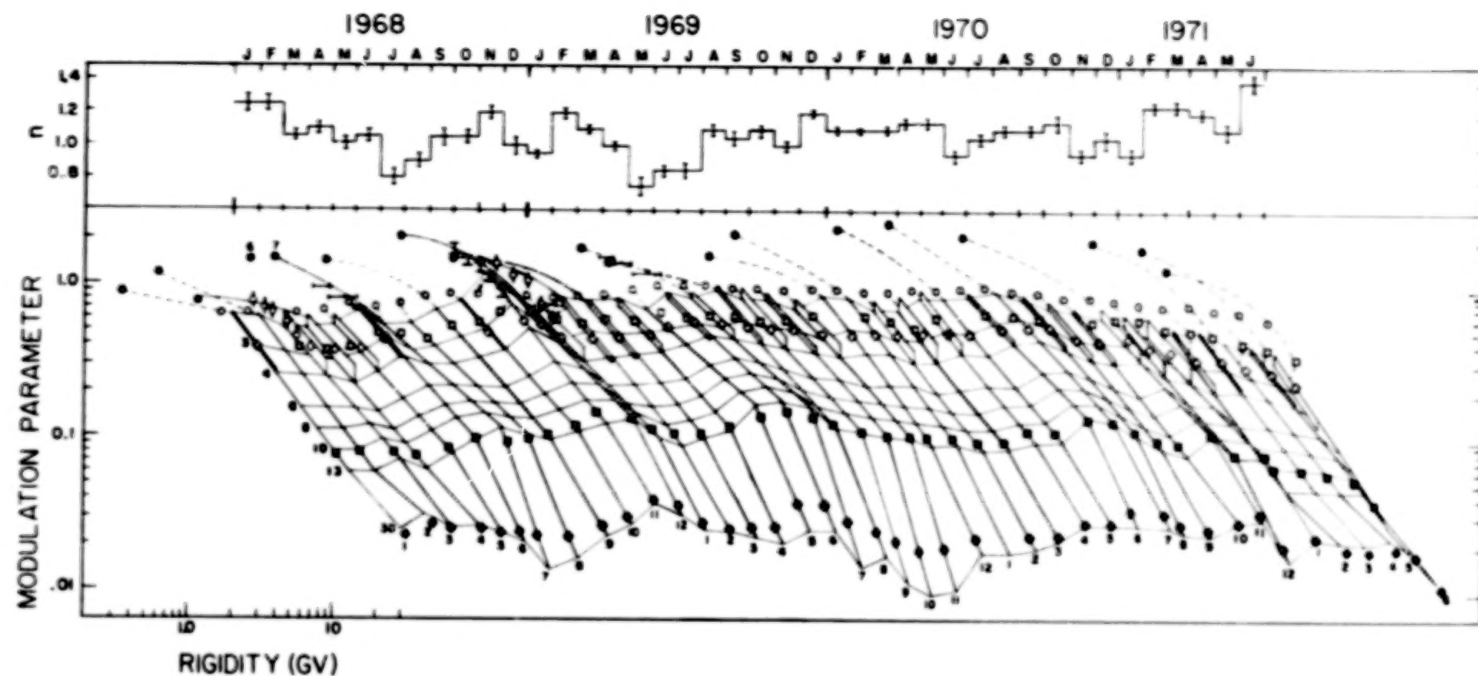


Figure 46. - Spectrum of the modulation parameter, M , monthly averages, between 1/68 and 6/71.
 $M = \ln(J_{1965}/J_t)$.

- Spectral index of M between 2 and 13.3 GV, n_1 in the text.
- Rigidity dependence of M . Solid lines: M derived from secondary atmospheric neutrons and counting rates of 5 neutron monitors, >60 MeV protons, Van Hollebeke et al. (1972) protons between 0.6 and 1.4 GV, 7/68 and 7/69, Rygg and Earl (1971). 60 MeV protons: constant 0.34 added for normalization; Lockwood et al, 1972, protons, 0.8 - 1.9 GV, Webber and Lezniak (1973). >1 GV protons, shown at 2.7 GV, Burger and Swanenburg (1972). 2-10 MeV neutron flux, 60-70 gm/cm², high latitude, this experiment counting rates, Inuvik neutron monitor counting rates, Kula neutron monitor, $P_C = 13.3$ GV

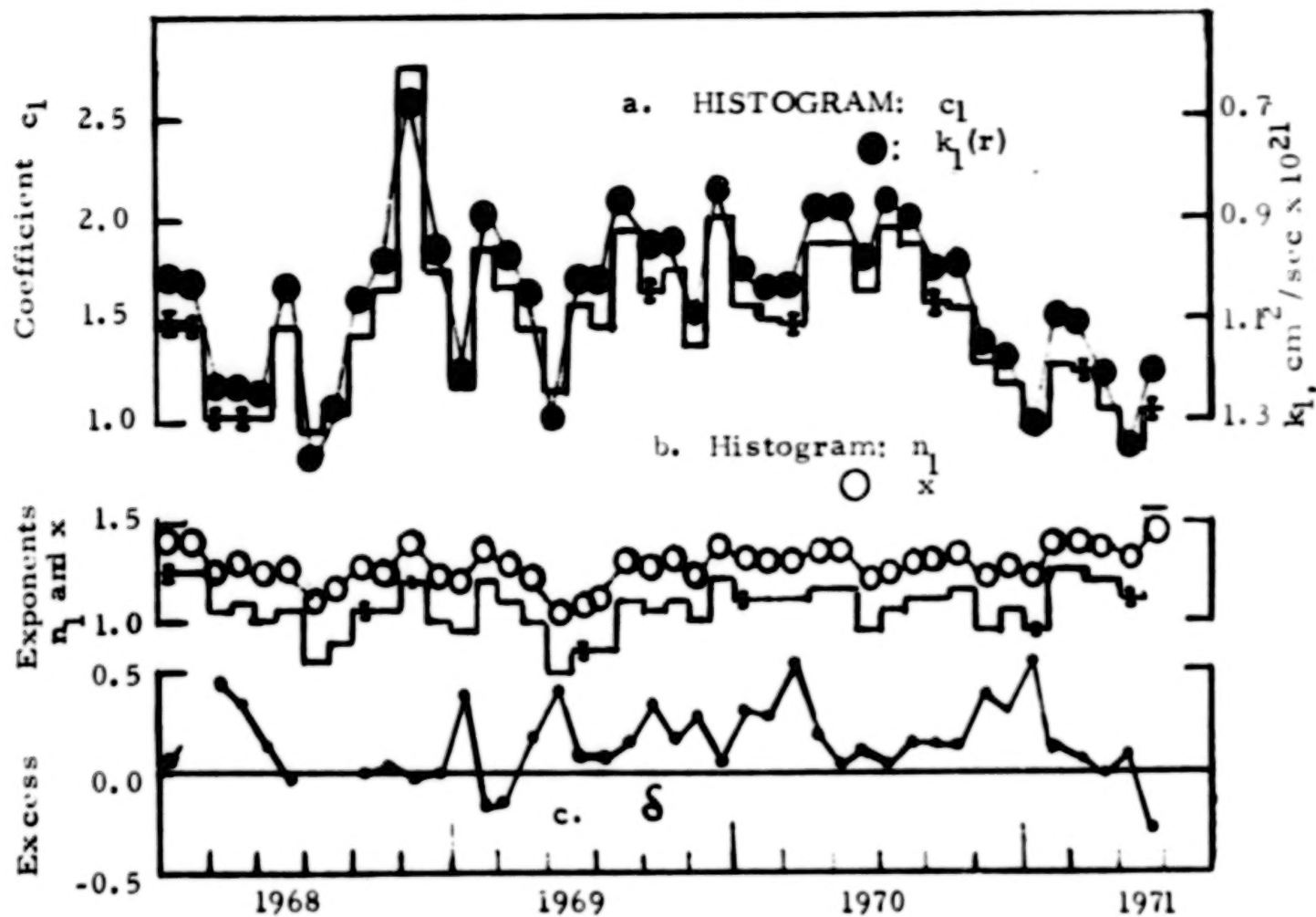


Figure 47. - Time variation of the modulation parameter, $M = c_1 P^{n_1} (1 + \delta/P)$ for protons above 2 GV. For $P > 5 \text{ GV}$, $\delta = 0$. Also shown, for comparison, is the time variation of the spectral index, x , and the coefficient, k_1 , of the diffusion coefficient at 1 AU, using the formulation of Winckler and Bedijn (1976) and the parameters that reproduce the proton modulation above 2 GV.

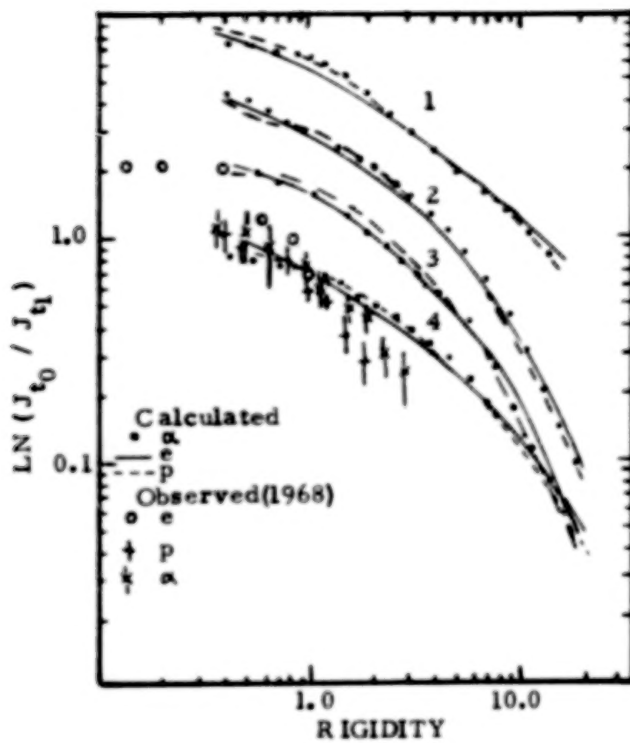


Figure 48. - A comparison of the modulation parameters of protons, electrons and alphas from a numerical calculation which uses the transport parameters and galactic spectra from Fulks (1975) and Garrard et al (1973). The time of maximum modulation was chosen because the maximum charge splitting occurs in the calculations of M above 2 GV.

1. $\ln(J_{\text{galac}} / J_{1970}) \times 4$, using parameters of Garrard et al
2. $\ln(J_{\text{galac}} / J_{1970})$, using parameters of Fulks
3. $\ln(J_{1965} / J_{1970})$, using parameters of Fulks
4. $\ln(J_{1965} / J_{1968})$, using parameters of Fulks. Also shown are experimental results from the U of NH.

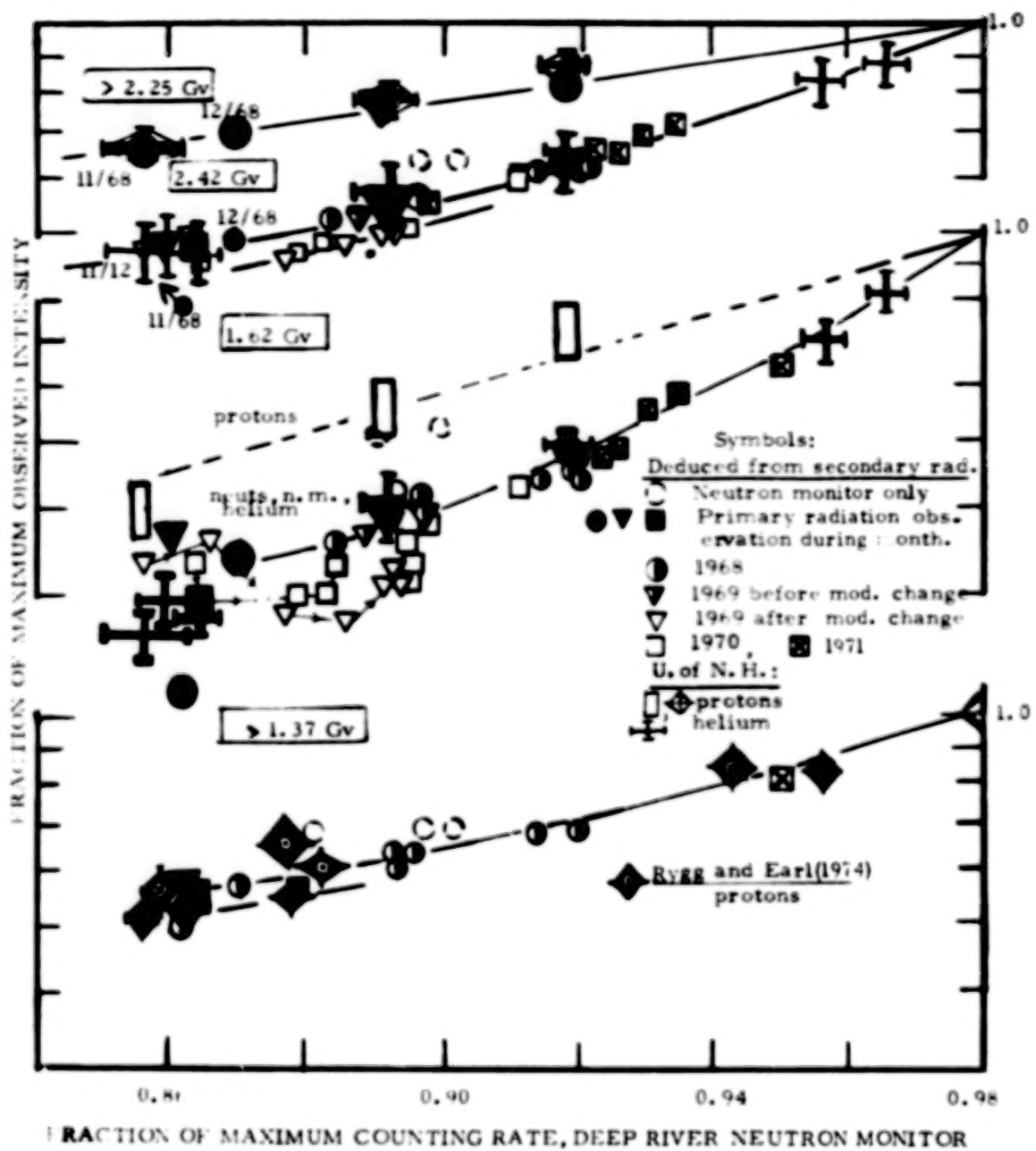


Figure 49. - A comparison of the proton and alpha intensities deduced from the modulation parameters reported in this paper with integral and differential fluxes found in balloon observations. Note that the agreement between observed primary intensities and intensities deduced from the secondary component is excellent if the fast neutron data is used to extrapolate neutron monitor data and if the comparison is not extrapolated below the 2 GV limit of validity. All data is normalized to 1.0 at solar minimum.

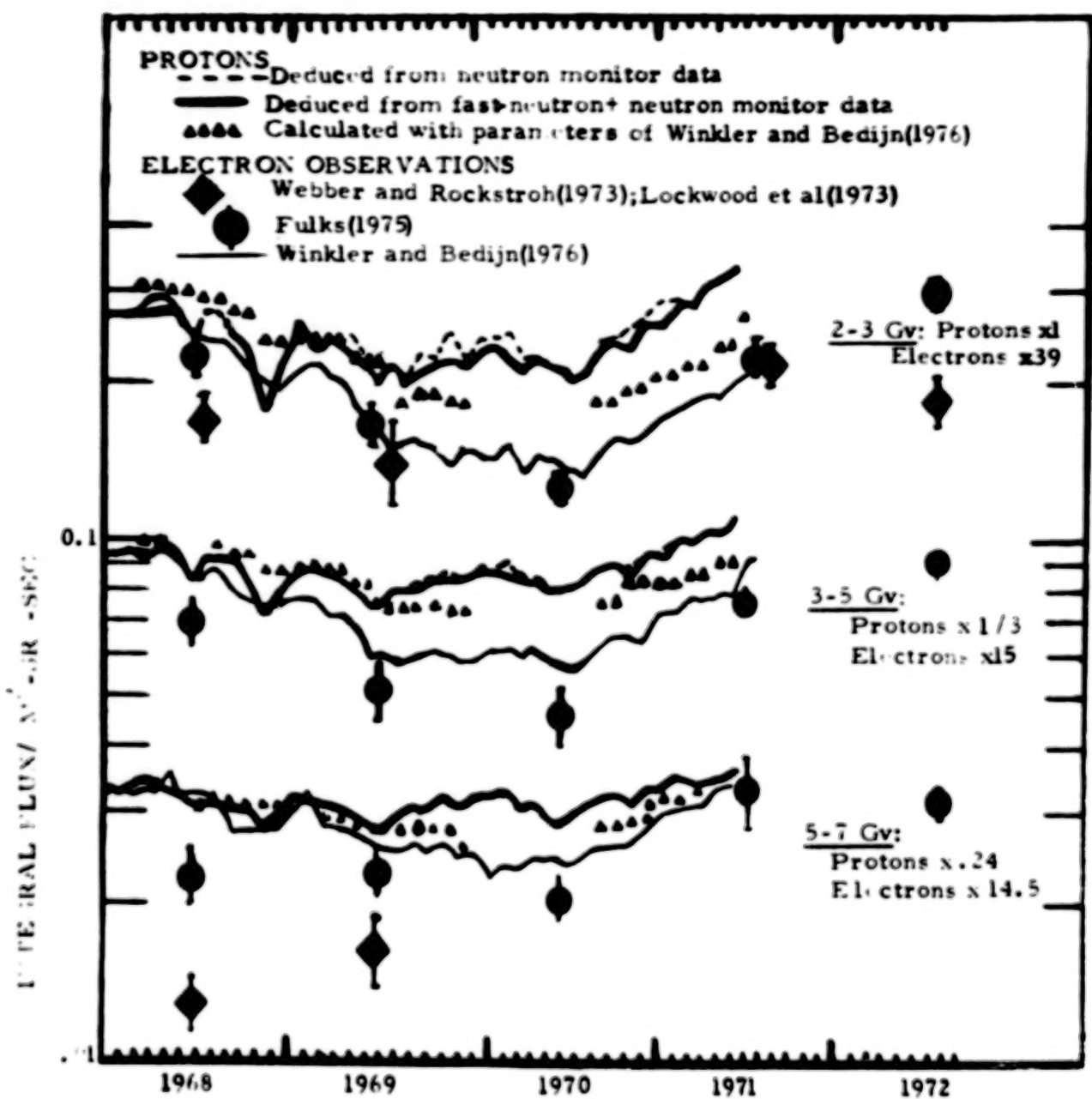
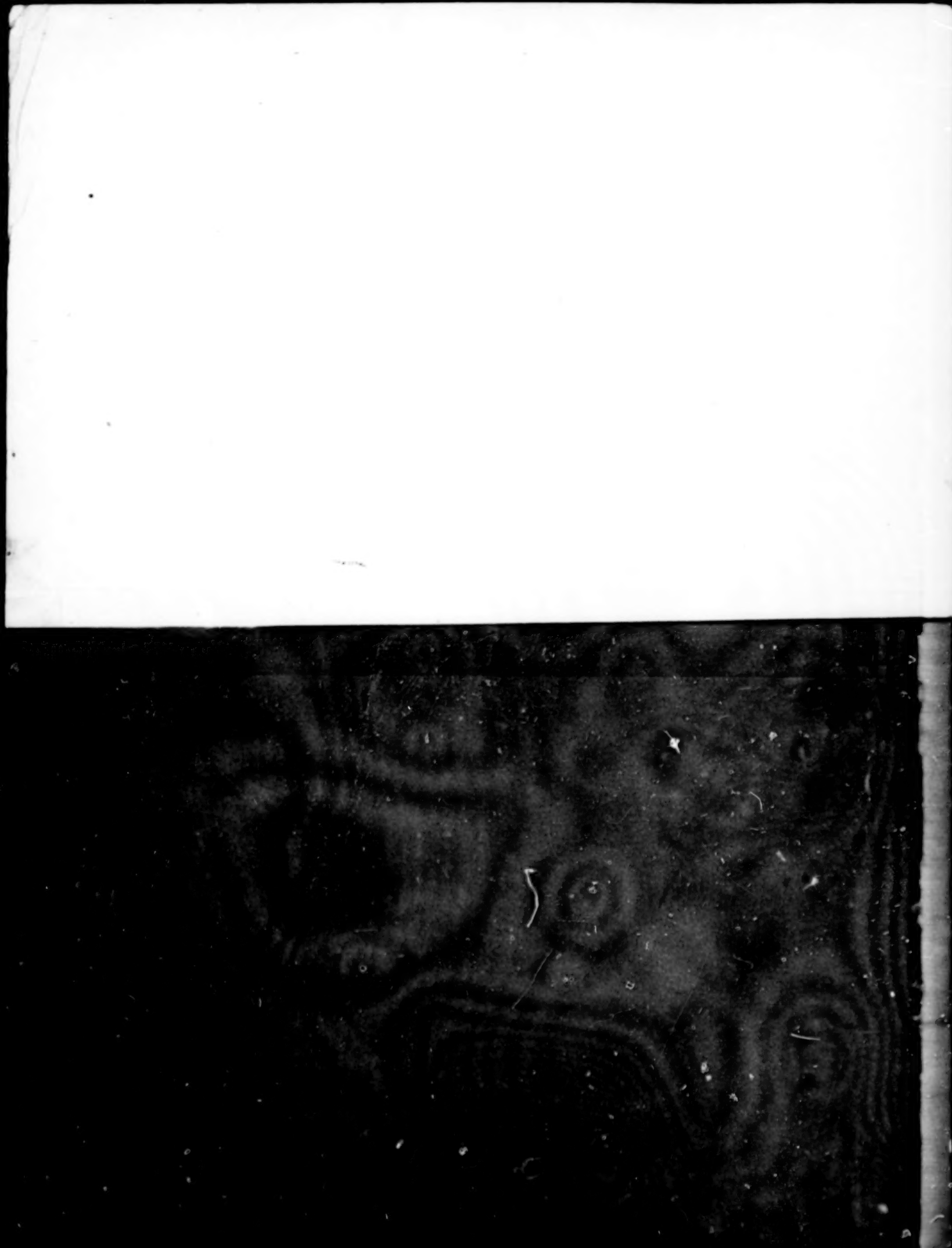


Figure 50. - A comparison of the time variations in the spectrum of electrons and protons.

1. Report No. NASA CR-3126	2. Government Accesion No.	3. Recipient's Catalog No.	
4. Title and Subtitle Atmospheric Neutrons		5. Report Date May 1979	
7. Author(s) Serge A. Korff, Rosalind B. Mendell, Milton Merker, Edward S. Light, Howard J. Verschell, and William S. Sandie		6. Performing Organization Code	
9. Performing Organization Name and Address New York University Department of Physics 4 Washington Place New York, NY 10003		8. Performing Organization Report No.	
12. Sponsoring Agency Name and Address National Aeronautics and Space Administration Washington, DC 20546		10. Work Unit No. 501-08-10-02	
15. Supplementary Notes Langley Technical Monitors: T. Foelsche and John W. Wilson Final Report		11. Contract or Grant No. NAS1-10282	
16. Abstract The Earth's atmosphere is a great shield, absorbing the impact of cosmic debris and the radiations harmful to living things. The atmosphere receives in its upper regions a steady rain of high energy charged particles from beyond the solar system, as well as occasional penetrating bursts from the sun itself. These particles generate all kinds of secondaries upon colliding with nuclei in the atmosphere, depositing most of their energy in the first hundred grams of the top of the atmosphere. Fortunately for man, this is far above his usual environment. The situation is less propitious for passengers of high altitude aircraft, for they cruise at the radiation maximum. The need for more complete information on neutron flux is not reserved to the domain of health physics.			
In this report, we outline our contributions to fast neutron measurements in the atmosphere. We also present the results of a calculation to determine the production, distribution and final disappearance of atmospheric neutrons over the entire spectrum. In this discussion, we attempt to answer questions that relate to processes such as neutron escape from the atmosphere and C^{14} production. In addition, since variations of secondary neutrons can be related to variations in the primary radiation, we comment on the modulation of both radiation components.			
17. Key Words (Suggested by Author(s)) Space Radiation Radiation doses at high altitudes Radiation environments in SST and subsonic altitudes Neutron spectra in atmosphere and solar modulation	18. Distribution Statement Unclassified-Unlimited Subject Category 52		
19. Security Classif. (of this report) Unclassified	20. Security Classif. (of this page) Unclassified	21. No. of Pages 186	22. Price* \$9.00

* For sale by the National Technical Information Service, Springfield, Virginia 22161

NASA-Langley, 1979



END

June 17, 1981